Design and large deformation response of additively-manufactured shell-lattices

by

Colin Bonatti

Ingénieur diplômé de l'École Polytechnique (2013)

Master of Science, Massachusetts Institute of Technology (2015)

Submitted to the Department of Mechanical Engineering in partial fulfillment of the requirements for the degree of

Doctor of Philosophy in Mechanical Engineering

at the

MASSACHUSETTS INSTITUTE OF TECHNOLOGY

February 2019

Signature redacted

Author.....

Colin Bonatti
Department of Mechanical Engineering
December 18th, 2018

Signature redacted

Certified by.....

Tomasz Wierzbicki
Professor of Applied Mechanics
Thesis Supervisor

Signature redacted

Certified by....

Dirk Mohr
Professor, ETH Zurich
Thesis Supervisor

Signature redacted

Accepted by.....

Nicolas Hadjiconstantinou
Professor, Graduate Officer
Department of Mechanical Engineering

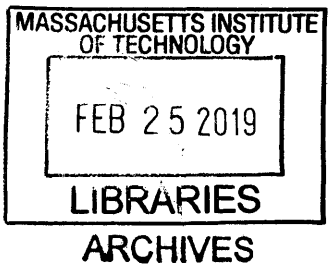

Design and large deformation response of additively-manufactured shell-lattices

by

Colin Bonatti

Submitted to the Department of Mechanical Engineering
on December 18th 2018 in partial fulfillment of the requirements for the degree of
Doctor of Philosophy in Mechanical Engineering

Abstract

Open-cell cellular solids are porous structures with a large variety of applications, from energy absorption to medical engineering. In an attempt to identify isotropic configurations with high low and large strain mechanical properties, detailed numerical simulations are conducted on a wide range of mesostructures of cubic symmetry. Results are partially validated through uniaxial compression of specimens made of 316L stainless steel via selective laser melting. In a first study the large deformation responses of four different mesostructures of relative density 20% are compared: an octet truss-lattice, tube-lattice, a sphere assembly and a tube/sphere hybrid. It is concluded that periodic shell structures provide superior strength and energy absorption capacity for the same weight, as compared to truss-lattices. Another conclusion is that to avoid concentrations of plastic strains that are detrimental to the overall energy absorption of the structure, it is best to avoid peaks in curvature. Based on these conclusions, a shell-lattice is developed that resembles a smoothened Triply Periodic Minimal Surface of FCC symmetry. Its properties are compared to those of the octet-truss for a wide range of relative densities, revealing the shell-lattice as superior to the octet-truss in almost all cases. The FCC shell-lattice is then compared to its BCC and SC equivalents. It is found that the structures all present high anisotropic properties. For a given structure, directional difference factors of up to 4.1 in uniaxial stiffness, 2 in yield strength and 1.8 in specific energy absorption are observed. However the directional averages of their properties are very similar. Irrespective of the specific type of cubic symmetry, the shell-lattices are remarkably stiff, strong and energy-absorbing, particularly at relative densities above 0.1. To address the problem of anisotropy, novel families of shell-lattices that contain the previous examples are proposed. Design maps are established and reveal that the elastic anisotropy of shell-lattices can be conveniently tailored. As a result, isotropic topologies are identified. The elastically-isotropic shell-lattices feature similar overall performance that their TPMS-like counterparts as well as a significantly reduced plastic anisotropy. The structures obtained are believed to be the best performing open-cell topologies to date.

Acknowledgements

I would like to thank my two advisors, Professor Tomasz Wierzbicki and Professor Dirk Mohr, for their support and their guidance during the years I spent as a Graduate Student at MIT. I appreciate the trust they showed in my abilities, and the fantastic opportunity they gave me to pursue and develop my own ideas. I appreciate the guidance and help I received from them when I found myself in need of it.

I am grateful Professor Katia Bertoldi, Professor Lallit Anand and Professor John Hart for agreeing to sit on my committee and discuss my research.

None of this would have been possible without the help, the support and the friendship of my colleagues: Professor Yong Xia, Professor Dr. Marcelo Paredes, Professor Vincent Grolleau, Dr. Christian Roth, Dr. Maysam Gorji, Dr. Matthieu Dunand, Dr. Stéphane Marcadet, Dr. Kai Wang, Dr. Xiaowei Zhang, Dr. Keunhwan Pack, Dr. Chus Pérez-Martín, Dr. Borja Erice, Dr. Michal Bardadyn, Mr. Rami Abi Akl, Mr. Thomas Tancogne-Dejean, Ms. Marianna Diamantopoulou, Mr. Charles Boubert, Mr. Alexis Leautier, Mr. Hailing Luo, Mr. Kyle Miller, Mrs. Brandy Dixon, Mr. Yannik Sparrer, Mr. Benoît Jordan, Mr. Julian Heindenreich, Mr. Thomas Beerli, and Ms. Franziska Siebenbrock.

Thank you to Leslie Regan and Barbara Smith for making my life so much easier here.

Finally, I would like to thank my friends and my family for supporting me during all these years.

The financial support of the MIT Fracture Consortium and the Swiss National Foundation, are gratefully acknowledged.

Table of Contents

1. Introduction

1.1.Micro, macro and meso-structure

Material properties are a function not only of the material's chemical composition but also its internal structure. Perhaps the most striking example of is that of carbon, which exists in nature as two different materials, graphite and diamond, with vast differences in their properties. Another famous example is the grain boundary strengthening (or Hall-Petch effect) observed in polycrystalline metals: as crystal grains grow smaller the overall material grows stronger. It should be noted that the two afore-mentioned examples relate two different length-scales: typical grain sizes in polycrystalline metals are typically expressed in micrometers while the lattice constant for diamond is a few angstroms. However they both refer to the microstructure of the material. As pointed out by Lee et al. (2010), tailoring the microstructure of materials is one of two original strategies that mankind has used to modify their properties, as exemplified by the manufacturing of amorphous glass windows or of special steels with highly anisotropic microstructures. The other approach is at a completely different scale: that of the macrostructure of an application, best exemplified by the use of beams and arches by architects. As manufacturing techniques advanced, mankind was able to produce composite materials, such as concrete blocks reinforced by metal fiber. At a scale larger than that of the microstructure of either of its constituent materials, and smaller scale than that of the macrostructure of the building and the beams, plates or staircases it composes, the arrangement of steel bars in the concrete matrix is referred to as the mesostructure. The mesoscale, is that of the arrangement of the different materials within the composite. In more recent developments, materials whose mesostructure allows them do develop uncommon sets of properties have been referred to as metamaterials. A common goal of metamaterial design is to advantageously combine the properties of two different materials.

1.2.Cellular materials

Cellular materials constitute one special class of metamaterials, where one of the constituents is air (or void). They are porous solids, but with high porosities that often make

up for most of the material volume. Because of this cellular solids are in essence clusters of cells of air (hence their name), delimited by a solid structure composed of either beams or shells. Note that while simpler, cellular materials with prismatic cells (2D cellular materials) escape the scope of this thesis. The reference text on cellular materials is the book *Cellular solids: structure and properties* by Gibson and Ashby (1999). As they point out, cellular solids are widespread in nature and among the oldest materials used by man: examples include wood, cork, and sponge. Man-made cellular solids include widespread examples such as honeycombs used as sandwich cores for lightweight applications, and polymeric foams used in packaging. Less straightforward applications of cellular materials rely on mutltifunctionality and include metal foam coatings designed for orthopedic implants, heat exchangers, and the development of porous scaffolds for tissue engineering, among others (Gibson and Ashby 1999, Gibson et al. 2010). It should be noted that the last two mentioned examples imply permeability of the cellular material to a fluid.

1.3.Mechanical properties

1.3.1 Relative density

Due to the high porosity of cellular materials it is often more relevant describe them in terms of their relative density, instead of their porosity, i.e. the ratio of their density to the density of the constituent material. For a cellular solid of porosity ϕ, its relative density is equal to:

$$\bar{\rho} = \frac{\rho}{\rho_s} = 1 - \phi \tag{1.1}$$

In fact, any given topology is usually referred to independent of its relative density, where it is understood that one parameter – the shell-thickness to length ratio, or the beam diameter to length ratio – controls the relative density of what is now a family of structures.

1.3.2 Linear properties

This thesis is mostly concerned with the determination of the mechanical, quasi-static properties of certain families of metallic cellular materials, notably under uniaxial compression. As such there are essentially three parameters that we are in interested in

determining: the stiffness, the strength and the specific energy absorption. Their respective scaling is expressed in terms of the relative density. The elastic moduli of isotropic composite solids are bound in terms of the stiffness of the constituent materials. From variational principles, Hashin and Shtrikman (1963) derived inequalities that in the case of porous materials reduce to:

$$0 \leq K \leq K_s + (1-\bar{\rho}) \cdot \left(\frac{-1}{K_s} + \frac{3\bar{\rho}}{3K_s + 4G_s} \right)^{-1} \tag{1.2}$$

$$0 \leq G \leq G_s + (1-\bar{\rho}) \cdot \left(-\frac{1}{G_s} + \frac{\frac{6}{5}(K_s + 2G_s)\bar{\rho}}{(3K_s + 4G_s)\mu_s} \right)^{-1} \tag{1.3}$$

Where K and G are the bulk and shear moduli of the cellular material, and K_s and G_s are those of the constituent material. Given that the isotropy of the composite, a similar bound can be obtained for the Young's modulus E, using the relation:

$$E = \frac{9KG}{3K + G} \tag{1.4}$$

For demonstrations the reader is referred to Walpole (1966) or Willis (1977). Equivalents for strength exist (e.g. Suquet 1993). Stiffness and strength of cellular materials are essentially linear properties, and they are easily obtained from elastic simulations. As such they are fairly easy to obtain, and the results (their scalings) are essentially independent of the constituent material.

1.3.3 Energy absorption

This generality is lost for specific energy absorption which is on the contrary, intrinsically nonlinear. Energy absorption relates to mechanical energy effectively dissipated by the material through either plastic work (metals), viscous effects (polymers) or fracture (ceramics) – this property relates to large-deformation, inherently non-linear behaviors of both the structure and the constituent material. As a consequence, it is useful to explore some concepts drawing from a couple of uniaxial examples.

1.3.3.1 Uniaxial examples

Figure 1.1a presents a typical engineering stress-strain curve corresponding to uniaxial compression for a bulk steel. Past the yield point there is a constant increase in the engineering stress, due to both strain hardening and the increase in area. Figure 1.1b presents the typical response of structural elements used in practice for crashworthiness, in this case a prismatic column. It is a convenient prototype structure to study because the apparently straight plate assembly is converted upon crush into a double curvature shell assembly. Figure 1.1c presents a view of a honeycomb, along with a diagram of the cross-section and a typical force displacement curve. A photo of a partial crushed column, along with a diagram of the cross-section are presented next to a typical load displacement curve. In both cases after reaching a peak load due to elastic or plastic buckling, the force drops down and then fluctuates around an average value, where the mean crushing force P_m is defined by:

$$P_m = \frac{1}{\delta_f}\int_0^{\delta_f} P(\delta)d\delta \tag{1.5}$$

Where δ_f is the final crush distance of the compressed column. The energy effectively absorbed, through plastic flow, during crushing is approximately equal to:

$$D = P_m\delta_f \tag{1.6}$$

The energy per unit mass is thus:

$$\psi = \frac{D}{\rho V} \tag{1.7}$$

Where V is the volume of the prismatic column and ρ is the density of its constituent material. Similar load-displacement curves are obtained for various cross-sectional shapes such as circular, rectangular, single hat, double hat and hexagonal cross-section with flanges. The average crushing stress is defined as the mean average crushing force divided by the tributary area:

$$\sigma_m = \frac{P_m}{A_t} \tag{1.8}$$

Where the tributary area A_t is the cross-sectional area effectively occupied by the structure or honeycomb, included void areas. The honeycomb is a very efficient energy absorbent material in axial crushing. The crushing force in the lateral (in-plane) direction

is one or two orders of magnitude smaller depending on the aspect ratio. This gives rise to the very pronounced anisotropy of honeycombs. There is a large body of literature on predicting the mean crushing strength of simple prismatic columns subjected to axial compression. For example, for a square cross-section with a wall thickness t, and the width of a flange b, assuming a constituent material of density ρ and the energy equivalent flow stress σ_0, the closed form solution for the mean crushing form is:

$$F = 12\sigma_0 t^{5/3} b^{1/3} \tag{1.9}$$

The range of validity of the above simple equation is $10t < b < 100t$. For such a column the relative density (portion of space effectively occupied by the constituent material) reads:

$$\bar{\rho} = \frac{4bt}{b^2} = \frac{4t}{b} \tag{1.10}$$

The energy per unit mass therefore reads:

$$\psi = \frac{F\varepsilon_m}{4\rho bt} = 3\varepsilon_m\sigma_0\left(\frac{t}{b}\right)^{\frac{2}{3}}\frac{1}{\rho} = \frac{3}{4^{2/3}}\varepsilon_m\sigma_0\bar{\rho}^{\frac{2}{3}} \tag{1.11}$$

The scaling is valid up to relative densities of 20%, up from which the column reacts through bulging rather than through crushing. This simple result illustrates that scalings of specific energy absorption with relative density in the power 2 / 3 emerge naturally when crushing modes are the dominant response.

Another useful measure of the energy absorption capabilities is the engineering stress:

$$\sigma = \frac{F}{A} = 3\sigma_0\left(\frac{t}{b}\right)^{2/3} \tag{1.12}$$

Where $A = 4bt$ is the actual area of the cross-section of the prismatic column (and not of the tributary area). The upper limit of the engineering stress is the so-called squash stress $\sigma = \sigma_0$, which occurs when $b = 5.2t$. Such a thick-walled tube will flow plastically with no elastic or plastic buckling. The maximum stress is the in-plane compressive membrane stress. Thinner columns ($b > 10t$) will buckle plastically. The structure then finds a new bending-dominated equilibrium path, with local areas of tensile and compressive membrane stresses. While not discussed in the core of the thesis, a numerical investigation into the respective contributions to plastic dissipation of membrane and bending actions for the structures developed herein, was conducted. Its results are presented in Appendix

3, revealing similar trends: membrane action is dominant (70% to 80% of energy dissipation) for thick, stable structures, while for thinner structures the associated buckling leads to even contributions of membrane and bending actions to the dissipation.

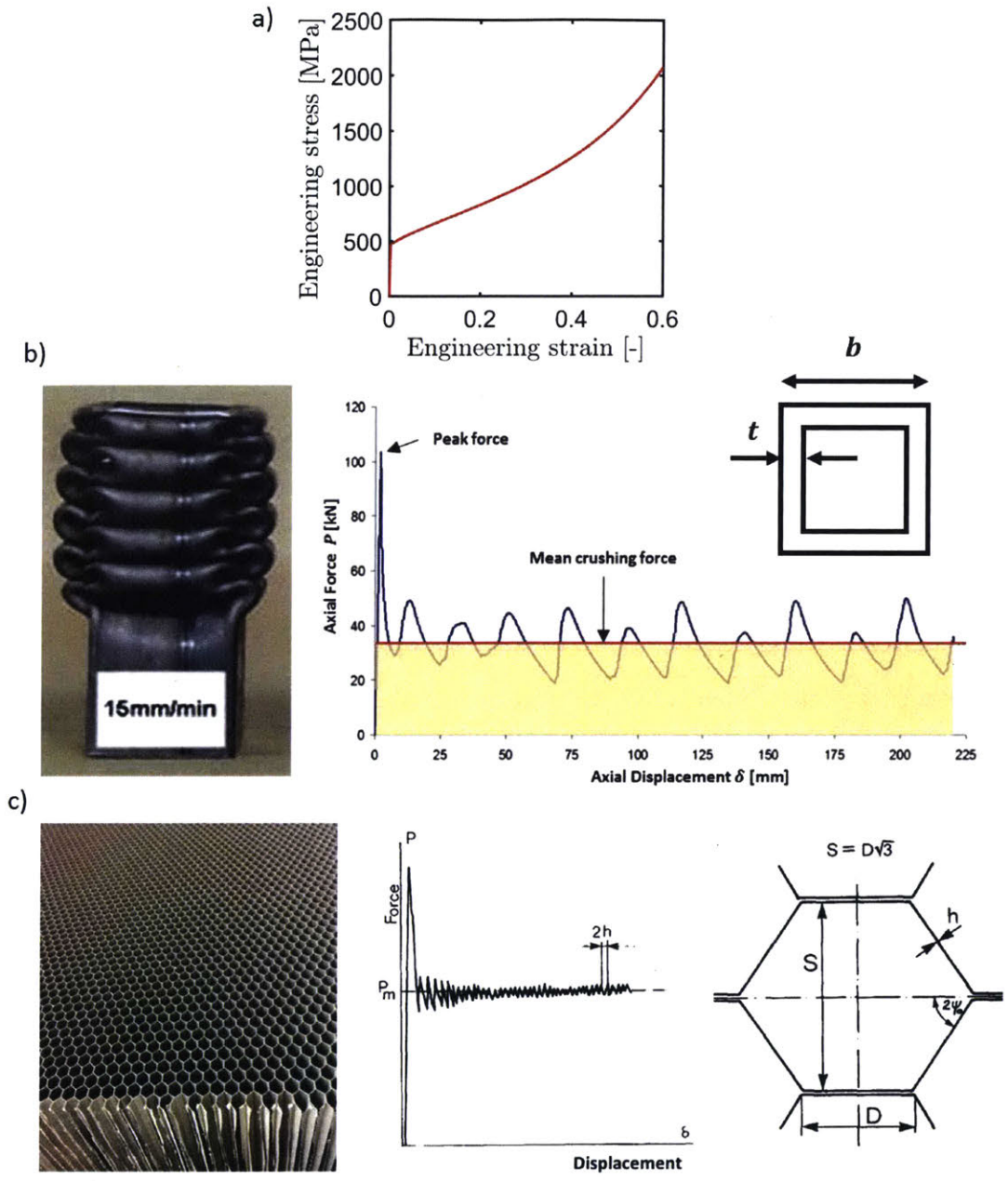

Figure 1.1: a) Stress-strain curve of bulk steel under uniaxial compression. b) View of a compressed prismatic column, typical corresponding force displacement curve, along with diagram of the cross-section. c) View of an aluminum honeycomb, corresponding stress-strain curve, and diagram of cross-section.

1.3.3.2 A few words on energy absorption

Cellular materials have uniaxial behavior that that fall between the extreme examples presented in the previous paragraph. At large relative densities, they present a bulk-like response, with hardening throughout. At low relative densities, the engineering stress quickly reaches a peak, after which it drops to a plateau value around which it oscillates. Deterministic structures such as the prismatic column, present large and repeatable oscillations that correspond to a repeated crushing mode of successive layers of the structure, while stochastic structures such as foams (as will be shown later) have small oscillations, given that they present a large number of cells with different topologies and thus a large number of crushing mechanisms and associated forces, which blurs the response.

A difficult point concerns what measure of energy absorption should be used. Aside from cost, two quantities influence the design and choice of material: the energy dissipated per unit mass (specific energy absorption) and the energy dissipated per unit volume (volumetric energy absorption). For any material, as the material gets compressed and compacted, the forces involved will diverge to infinity – in that sense the energy needed to fully compress the material is infinite. For the measure to have meaning, there needs to be a cutoff-strain ε_f. If one neglects elastic energy, the specific energy absorption will then read:

$$\psi = \frac{D}{\rho} = \frac{1}{\rho}\int_{\varepsilon=0}^{\varepsilon_f} \sigma : d\varepsilon \tag{1.13}$$

Where D is the plastic dissipation per unit volume. How should that cut-off strain be defined? This decision oftentimes driven by applications. In energy absorption applications, kinetic energy is absorbed by the structure in order to protect an object or a person from an impact and both the large forces associated. It makes sense, then to define the cutoff strain as the strain for which the maximum acceptable force is first observed. The energy absorbed per unit volume is then maximal if the stress-strain curve presents a long plateau, with a stress corresponding to the maximum acceptable, up to a very large densification strain. As explained above, all geometries will present that desirable plateau for low enough relative densities – however the poor scaling with relative density in that regime will lead to poor specific energy absorption.

In this thesis we not will attempt to estimate the densification strains of the cellular materials investigated. Instead we resort to a simpler definition of specific energy absorption that relies on a fixed cutoff strains for all structures.

1.4. Stochastic foams

Until about two decades ago, stochastic foams with cell sizes at the millimeter level were the only man-made cellular solids with nearly isotropic mechanical properties. Metal foams can be made through a variety of processes from vapor deposition or electrodeposition on a polymer foam (that is subsequently removed) to injecting bubbles of gas in molten metal (for more details, see Ashby et al. 2000). Two categories of foams can be distinguished. Open-cell cellular solids consist in a set of nodes connected by ligaments that exhibit a beam-like mechanical response, while closed-cell foams are composed of thin-walled plate-like elements. In their pioneering work, Gibson and Ashby (1999) provide scalings for the mechanical properties of both categories. Those are based on structural analysis of cells representative of the two architecture types. In what follows the subscripts X_{oc} and X_{cc} correspond to open-cell and closed-cell foams while X_s corresponds to the constituent solid phase.

	Open-cell	Closed-cell	
Young's modulus:	$\frac{E_{oc}}{E_s} = C_1\bar{\rho}^2$	$\frac{E_{cc}}{E_s} \approx \phi^2\bar{\rho}^2 + (1-\phi)\bar{\rho}$	(1.14)
Shear modulus:	$\frac{G_{oc}}{G_s} = C_2\bar{\rho}^2$	$\frac{G_{cc}}{E_s} \approx \phi^2\bar{\rho}^2 + (1-\phi)\bar{\rho}$	(1.15)
Poisson's ratio:	$\nu_{cc} \approx \frac{1}{3}$	$\nu_{oc} \approx \frac{1}{3}$	(1.16)
Elastic collapse:	$\frac{\sigma_{oc}^{el}}{E_s} \approx 0.05\bar{\rho}^2$	$\frac{\sigma_{cc}^{el}}{E_s} \approx 0.05\bar{\rho}^2$	(1.17)
Plastic collapse:	$\frac{\sigma_{oc}^{pl}}{\sigma_{y,s}} \approx 0.3\bar{\rho}^{3/2}$	$\frac{\sigma_{cc}^{pl}}{\sigma_{y,s}} \approx 0.3(\phi\bar{\rho})^{3/2} + 0.4(1-\phi)\bar{\rho}$	(1.18)

Where ϕ is here a geometrical parameter accounting for excess matter in the ligaments bordering the cell walls. In the expressions for closed-cell foams, the contributions of the gas trapped within the cells has been omitted. The typical stress-strain curve for a low-density foam is provided in Fig 1.2, featuring an elastic loading followed by a plateau

region, ended by a densification phase. The energy absorbed corresponds to the grey area under the curve in the plateau regime, up to a cutoff strain (here the densification strain).

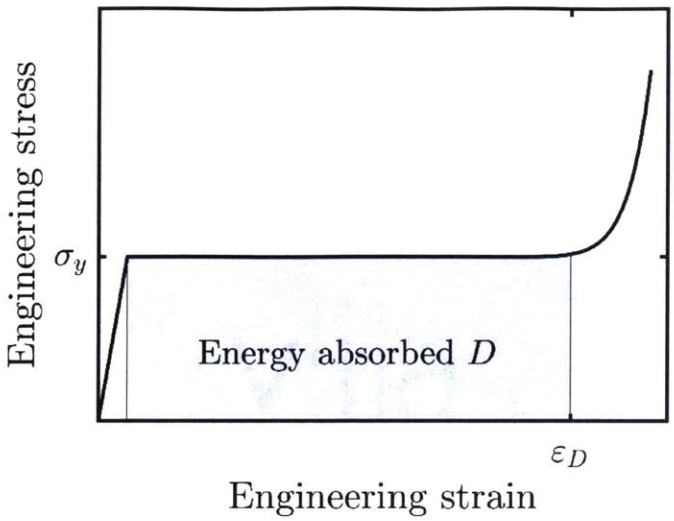

Figure 1.2: Typical stress compression stress strain curve for a low density foam, showing elastic loading, a stress plateau and a densification regime.

In the correlations above, the estimated plastic stress corresponds to the plateau stress. Given our definition of energy absorption, ignoring elastic strains and for a cutoff strain ε_m below the densification strain, the plastic dissipation would read:

$$D = \bar{\rho}\sigma_y\varepsilon_m \tag{1.19}$$

As can be seen above the mechanical properties of idealized closed-cell foams are far superior to those of open-cell foams, with linear scalings of both stiffness and strength (before plastic collapse dominates at extremely low relative densities). Using the more precise example of a tetrakaidecahedron foam, Simone and Gibson (1998) even estimated that at low relative densities:

$$\sigma_{cc} \approx 0.44\bar{\rho}\sigma_{y,s} \tag{1.20}$$

$$E_{cc} \approx 0.33\bar{\rho}E_s \tag{1.21}$$

However these close-to-optimal predicted behaviors are not observed in practice (e.g. Gibson (2000), Ashby et al. (2000)). In *Metal foams: a design guide*, Ashby et al. give the following correlations for experimental data:

$$E \approx \alpha E_s\bar{\rho}^n \text{ with } 1.8 \leq n \leq 2.2 \tag{1.22}$$

$$\sigma_y \approx \alpha\sigma_{y,s}\bar{\rho}^m \text{ with } 1.5 \leq m \leq 2 \tag{1.23}$$

Gibson (2000) notes that experimental data for closed-cell foams is better represented by open-cell foams equations, and attributes the discrepancy to the influence of bending in the response of curved cell walls. Evans et al. (1998) similarly attributes this knockdown in properties to morphological defects. Ashby (2006) summarizes that the actual behavior of open- and closed-cell stochastic foams is bending dominated (with the associated sublinear scaling).

1.5.Lattice-materials

1.5.1 Truss-lattices and plate-lattices

Different from stochastic structures, lattice-materials are deterministic periodic cellular materials. Truss-lattices are the deterministic equivalent of open-cell foams, just as plate-lattices are deterministic closed-cell foams. Perhaps due to manufacturing constraints, truss-lattices have received have been predominantly studied in the past two decades. Deshpande et al. (2001a) showed that stretching-dominated truss-lattice materials significantly higher stiffness and strength than foams, with linear scalings of stiffness and strength properties (see also. Evans et al., 2001).

In engineering practice, metallic truss-lattices can be built from three-dimensionally formed perforated sheets (e.g. Sypeck and Wadley (2002), Wadley et al. (2003)). Alternatively, truss lattice metamaterials with solid struts can be readily obtained through additive manufacturing (e.g. Yan et al. (2012), Gumruk and Mines (2013), Stankovic et al. (2015), Tancogne-Dejean et al. (2016)). The smallest achievable feature size of state-of-the-art selective laser melting with metals is still of the order of about $30\mu m$. Metallic structures with finer structural features can be fabricated by depositing metallic layers onto free-standing polymer scaffolds through electroless-plating, atomic layer deposition or RF sputtering. After removal of the polymeric support, hollow shell-like structures with nanometric wall thicknesses are obtained. It is noted that the same process also applies to making hollow ceramic nanostructures. The fabrication of porous solids with mesostructural features in the submicrometer range is mostly explored to leverage size effects in the solid base constituent. For example, Schaedler et al. (2011) produced a lattice scaffold with strut lengths of a few millimeters using a self-propagating photopolymer

waveguide technique. Using electroless plating, they deposited thin nickel films with an average grain size of a few nanometers. Multiphoton lithography has been employed by Jang et al. (2013) and Montemayor et al. (2014) to produce solid polymer lattice templates with a few microns long struts. Jang et al. (2013) applied about $75nm$ thick ceramic layers onto the octet truss scaffold, thereby producing hollow TiN octet truss metamaterials with a base constituent strength of $1.7GPa$. Bauer et al. (2014) employed 3D laser lithography along with atomic layer deposition to create cellular polymer mesostructures with $10nm$ to $200nm$ thick alumina coatings that exceeded the compressive strength of foams at effective densities below 1g/cm^3.

Perhaps the best-known example is the octet-truss, of which Deshpande et al. (2001b) investigated the elastic and failure response both experimentally and analytically. The octet-truss's properties have been widely studied, including its macroscopic plastic behavior (Mohr, 2005), fracture toughness (O'Masta et al., 2017) and buckling-to-yield failure transition (Carlton et al., 2017). Elsayed and Pasini (2010) elaborated design maps for octet-truss-inspired lattices with simultaneous yield and buckling limits. This accumulated knowledge as well as its popularity make it an ideal candidate for comparisons, and it is the structure of choice for numerous studies on related topics. For example, scale effects in octet truss lattices made from copper with strut diameters of a few microns have been investigated by Wendy Gu and Greer (2015), while He et al. (2017) made use of molecular dynamics simulations in conjunction with theoretical models to assess the compressive response of copper nano-lattices with strut diameters of a few nanometers only, reporting significant property enhancement as compared to bulk copper.

However, the linear scaling of truss-lattice properties often breaks down at low relative densities due to buckling instabilities (Deshpande et al. 2001b). This issue has been partially addressed by the design of hierarchical metamaterials which feature different levels of structure (e.g. Meza et al. (2015), Zheng et al. (2016)). Hierarchical design allows low relative densities to be reached for the overall structure while keeping mesostructural feature-level aspect ratios low enough to retard instability-driven failure. By hierarchically combining octahedral and octet-trusses, Meza et al. (2015) have been able to achieve the linear-scaling of the elastic and elastic limit properties down to relative densities of about 10^{-4}.

It is now known that even optimal truss-lattice materials (Gurtner and Durand, 2014) cannot achieve the theoretical Hashin-Shtrikman stiffness bounds for isotropic cellular solids. At low relative densities, the highest achievable Young's modulus of stretching-dominated isotropic truss-lattice materials is about three times lower than the theoretical upper limit (Tancogne-Dejean and Mohr, 2018a). The latest studies on the stiffness and strength of mechanical metamaterials revealed that plate-lattices can attain the Hashin-Shtrikman and Suquet bounds (Berger et al. 2017, Tancogne-Dejean et al. 2018b). However, the closed-cell nature of optimal plate-lattices complicates their manufacturing through powder-bed or liquid-bath additive techniques. Moreover, similar to closed-cell foams, their lack of permeability limits their potential for multifunctional applications.

1.5.2 Shell-lattices

Another emerging category of metamaterial architectures next to truss- and plate-lattices are shell-lattices, i.e. periodic structures composed of non-intersecting shells (e.g. Han et al., 2015). These open cell shell structures have the particularity of separating two fluid phases. This feature facilitates their production through additive manufacturing techniques that require the extraction of powder or liquids. Moreover, it makes them suitable for applications requiring multi-functionality such as mechanical resistance combined with heat exchange capability. Such surfaces naturally emerge in block copolymers where two macromolecules arrange at equilibrium by forming cocontinuous domains (e.g. Thomas et al. 1988). Constant mean-curvature surfaces, including the best-known Triply Periodic Minimal Surfaces (TPMS), and (mathematically simpler) level-set surfaces have been proposed as an approximation to the separating surface (e.g. Lambert et al. 1996). Following from those findings, cocontinuous composites, i.e. two-phase composites wherein each phase occupies the volume on one of the two sides of the limiting surface, have been proposed and their mechanical properties studied for a range of constituent materials.

Maldovan et al. (2007) studied the stiffness of microframes (solid/air composites) with several interface topologies, including some defined by level-set surfaces approximating the Schwarz P, I-WP and F-RD surfaces. Wang et al. (2011) used the same geometries to print glassy polymer/rubber polymer composites, where the volume fraction of the

respective phases was varied leveraging one degree of freedom in the level set function. They reported enhanced properties as compared to particle-reinforced composites, including increased damage tolerance. Topologically similar carbon/epoxy bicontinuous composites were produced by Lee et al. (2012) via a combination of 3D direct laser writing, pyrolysis and infiltration, and revealed to present specific energy absorptions of up to 720 kg/kJ. A similar approach consists in reinforcing a soft matrix through a uniform-thickness shell with the analytical surface as a mid-surface instead of using "skeletal" truss-structures. Abueidda et al. (2015) analyzed numerically the thermal expansion of such cocontinuous composites, revealing a low coefficient of thermal expansion of interest for applications. Dalaq et al. (2016a, 2016b) studied numerically and experimentally the elastic modulus, strength, strain at failure and toughness of such composites (with varying TPMSs) consisting of a Tango-Plus matrix reinforced by TPMS-shaped Vero-Plus.

Foam-like shell-lattice materials can be obtained by retaining only the non-intersecting shell structures of uniform thickness. With the goal of identifying superior scaffold designs for tissue engineering, Kapfer et al. (2011) designed such shell-lattices and estimated their elastic properties, as well as their fluid permeability, numerically and compared those to TPMS-based skeletal networks of the same porosity, revealing superior mechanical properties. Han et al. (2015) proposed ultra-low density shell-lattices consisting of Schwarz P- and Schwarz D-surfaces. They optimized these structures for stiffness along one direction by reducing the nozzle size between neighboring cells while breaking down the cubic symmetry by elongating the unit-cell along the direction. Lee et al. (2017) investigated the stiffness and yield properties of shell-lattices based on the Schwarz-P minimal surface. Al-Ketan et al. (2017) studied the compressive behavior of steel-based BCC metamaterials, including a BCC truss-lattice, and shell-lattice structures based on a level-set approximation of the I-WP TPMS. They showed that the shell-lattice presented superior mechanical properties as compared to the truss-lattices. Bobbert et al. (2017) fabricated sixteen types of TPMS shell-lattices from Ti-6Al-4V, reporting low elastic properties, high strength, high fatigue resistance, and high permeability, thereby mimicking the properties of trabecular bone.

1.6. The importance of isotropy

As pointed out by Lee et al. (2012), an important aspect of mechanical metamaterials is the ability they give to design for structural anisotropy – giving the example of Damascus steel blades benefitting from an anisotropic microstructure. Metamaterials offer the opportunity to locally tailor the anisotropy to further enhance the performance in given applications. In cases where loadings are expected in one direction or within a plane, the desirable elastic response would likely be transverse isotropic. Given an elastically-isotropic material, a particularly simple way to obtain transverse-isotropic metamaterials is provided by results on foam elasticity (Gibson and Ashby, 1999). Most foams have structural anisotropy where their cells are more elongated in one direction than in the transverse plane. For a foam with an anisotropy ratio R, where R is the ratio of the longest to the smallest cell size in given directions, the ratio of their Young's moduli in the direction of anisotropy E_l to the transverse Young's moduli E_t is given by:

$$\frac{E_l}{E_t} = \frac{2R^2}{1 + (1/R^3)} \tag{1.24}$$

Similarly, one could use elongate the mesostructures of elastically-isotropic metamaterials to tailor their anisotropy to the application. This further enhances the importance of finding high performance isotropic configurations.

However most configurations, even the most studied, are far from isotropic, despite often having cubic symmetry. For example the octet truss lattice is often perceived as an isotropic metamaterial, but it is worth noting that its mechanical response can be highly anisotropic. Two strategies have been used to obtain elastically-isotropic configurations: a superposition approach, and a variation approach.

Isotropic truss- and plate-lattices are typically through the first approach: two mesostructures of opposed anisotropy are combined to obtain an isotropic hybrid. To design isotropic truss lattices materials, Gurtner and Durand (2014) derived topology constraints that guarantee optimal isotropic elastic properties. Aside from introducing a general methodology, Messner (2016) provides selected examples of optimized lattice architectures of high stiffness-to-density ratio that are elastically-isotropic. Isotropic truss-lattices of cubic symmetry have been obtained by Zok et al. (2016) by combining simple cubic, body-centered cubic and face-centered cubic elementary trusses. Similar elastically-

isotropic structures have been obtained by Tancogne-Dejean and Mohr (2018a). A similar approach has been used on plate-lattices (Berger et al. 2017, Tancogne-Dejean et al. 2018b).

The other approach consists in finding a continuous family of topologies that maintains a high level of performance. Given that cubic symmetry materials have anisotropy controlled by only one parameter, it is likely that isotropic configurations can be found. Such an approach has been used recently to obtain SC, BCC and FCC tube-lattices (Tancogne-Dejean and Mohr, 2018c).

1.7.Statement of contents

This thesis is concerned with the development and mechanical characterization of isotropic metallic cellular materials with high performance at both low and large strains with respect to those of the constituent material. A first step towards isotropy is taken by considering only mesostructures with the maximum number of internal symmetries, i.e. metamaterials of cubic symmetry. A second restriction is taken by ignoring the effects of fracture: as a consequence most of the large-strain results developed herein relate only to cellular solids formed with very ductile metals. Given that assumption, the precise modeling of the constituent material is not an issue we need to be concerned with and the current numerical methods offer a fast and convenient way to explore the behavior of vast numbers of geometries. Unfortunately the geometries considered herein are often complex and only defined implicitly. The absence of clearly defined structural elements add to the difficulty of a "pen and paper" analytical approach. As a consequence most of the results presented herein are derived from finite element modeling and analysis of the structures. The results are punctually validated by compression experiments on additively manufactured specimens.

Chapter 2 presents some of the methods used throughout the thesis. First, an account of the consequences of cubic symmetry on both the development of structures and their mechanical behavior is given. Then, the general numerical approached used, involving periodic boundary conditions unit-cell simulations as well as multi-cell simulations, is detailed. Finally useful information on both the experimental methods as well as the constituent metamaterial used for experiments is given. Chapter 3 is concerned with the

comparison of the mechanical properties of ad-hoc structures of relative density 20%: one truss-lattice, one tube-lattice, and two assemblies of spheres linked to one another by tubes, with different aspect ratios. From the quantitative comparison of the four structures' behaviors, but also through careful analysis of the qualitative behaviors, design rules are derived to obtain structures with smooth stress distributions that are less prone to plastic strain concentration at the mesostructural level. In Chapter 4, these guidelines are followed to develop a novel FCC metamaterial. The obtained structure is a shell-lattice with properties very similar to a TPMS with similar boundary conditions. However the scope of the study, which reveals the low and large strain anisotropy of the structure as a major factor, through the careful numerical analysis in a wide range of loading scenarios and relative densities, sets it apart from previous studies on TPMS shell-lattices. The shell lattice's properties are contrasted to those of the octet truss-lattice, revealing far superior stiffness and strength but most of all, a more stable and more energy absorbing large-strain response. Chapter 5 and 6 are concerned with the generality of these findings. Chapter 5 explores the influence of the topology (here, the node connectivity) on the mechanical properties of the shell-lattice. It is shown that the BCC, FCC and SC shell-lattice all show very large anisotropy, with different preferred orientations, which complicates their comparison. However if average directional properties are considered, the structures essentially have the same performance. Chapter 6 considers for a given node connectivity, the influence of the (implicit) definition of the shell mid-surface on the properties of shell-lattices. It is shown that the anisotropy, a major effect for the original configurations, can be tailored without losing the overall mechanical performance, and that isotropic shell-lattices can be found. To the author's knowledge, these shell-lattices are, among open-cell cellular structures, the best mechanically-performing isotropic topologies to date.

2. Methods

Parts of this chapter are adapted from Bonatti and Mohr (2019a, 2019b).

2.1.Structures of cubic symmetry

2.1.1 Primitive unit-cell, and fundamental domain

This thesis is concerned with the design and numerical mechanical characterization of lattice-materials, i.e. of triply -periodic structures. Such structures are represented by a combination of a motif and a lattice. The lattice is an arrangement of regularly spaced discrete points at which the motif is repeated to recreate the lattice-material. The motif is typically represented within a domain of a minimal volume called a primitive unit-cell (e.g. Ashcroft and Mermin 1976). In practice the shape of primitive unit-cells can be complex, and for simulation purposes it is easier to use a non-minimal unit-cell with larger volume but simpler shape.

On top of being triply-periodic, the geometries considered in this thesis all have cubic, that is to say octahedral symmetry (group Oh, see Kittel 1996). As such they have a symmetry order of 48 when reflections are accounted for, meaning that a primitive cell can be decomposed into 48 volumes that can be deduced from one another through a combination of reflections and rotations (reference needed). Such a minimal volume is called a fundamental domain.

The structures fall into either of the three possible categories of Bravais lattices with cubic symmetry (Kittel 1996) simple-cubic (SC), body-centered cubic (BCC) or face-centered cubic (FCC). While there are many ways to choose primitive unit-cells, the Wigner-Seitz cell is a natural choice (e.g. Ashcroft and Mermin 1976). It is centered around one node of the lattice and contains all the points of space closer to this node than to any other lattice node. As such it corresponds to the Voronoï tessellation of the lattice. Unit-cells with their decomposition (through symmetries) into fundamental domains are presented in Figure 2.1 for the three cubic lattices.

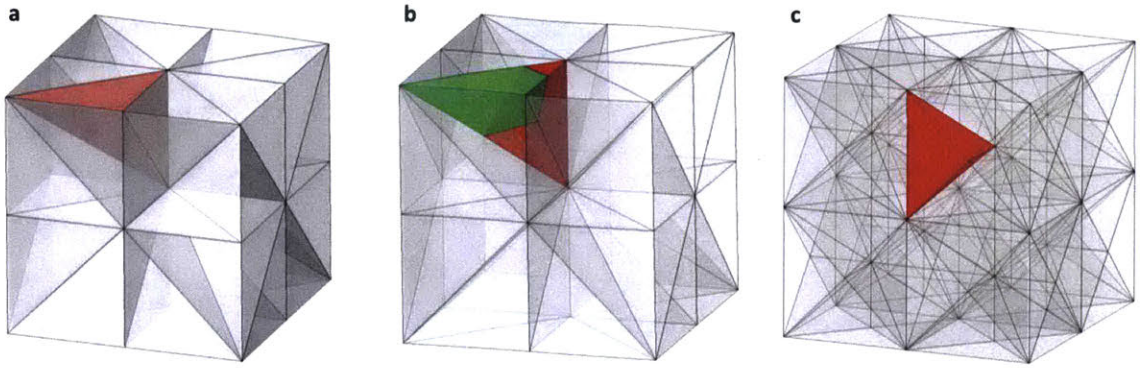

Figure 2.1 Views of a) SC b) BCC and c) FCC unit-cells decomposed by symmetry. Red volumes represent the fundamental domain.

While the SC unit-cell is primitive, it is not the case for BCC and FCC structures: the conventional unit-cell then contains respectively twice and four times the volume of one primitive unit-cell. As a consequence the SC unit-cell contains 48 times, the BCC unit-cell contains 96 times, and the FCC unit-cell contains 192 times the minimal information needed to define the structure.

All structures considered herein take advantage of this simplification. The geometries as well as their discretization (e.g. tessellation, solid-element or shell-element mesh) are always defined on a fundamental domain, and the various models (including unit-cell models) are obtained through a combination of copies, reflections and rotations.

2.1.2 Illustration in the case of FCC structures

Herein we take a closer look at the FCC lattice and its representations. There are many geometric decompositions that can be useful when trying to explain and analyze the behavior of metamaterials that belong in this category. They are presented in Figure 2.2:

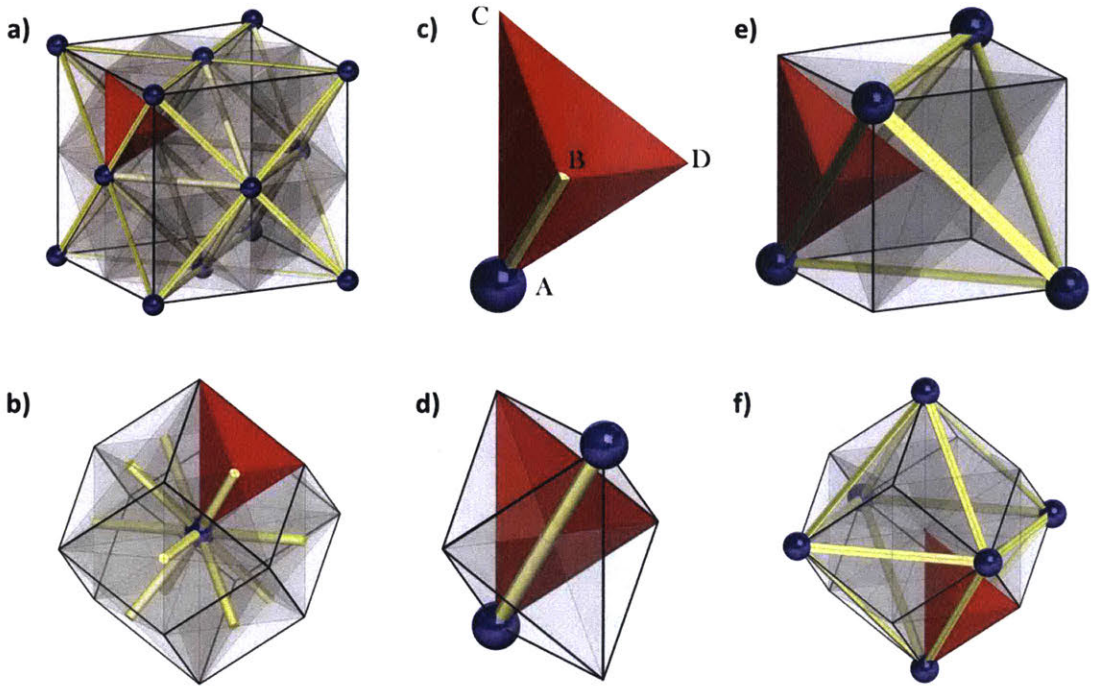

Figure 2.2: Selected decompositions of the FCC geometry. Blue spheres represent the nodes of the lattice, yellow bars represent the links between closest-neighbor nodes. (a) cubic unit-cell, (b) rhombic dodecahedral unit-cell, (c) fundamental tetrahedron, (d) irregular octahedron obtained by collecting all fundamental tetrahedra resting on a midpoint between next-neighbor nodes, (e) cube obtained by collecting all fundamental tetrahedra resting on a tetrahedral site of the lattice, (f) rhombic dodecahedron obtained by collecting all tetrahedra resting on an octahedral site of the lattice.

- **The cubic unit-cell.** Figure 2.2a presents a unit-cell of the FCC lattice with the nodes shown in blue, and the line segments joining closest-neighbors shown in yellow. Once the unit-cell of an FCC metamaterial is defined, the periodic lattice is obtained by translations along the edges of the cubic unit-cell. The cubic unit-cell contains four nodes of the FCC lattice (eight eighth-nodes at the unit-cell corners, and six half-nodes on the unit-cell faces).

- **The rhombic dodecahedral unit-cell.** The Wigner-Seitz cell of the FCC lattice is the simplest volume allowing one to recreate an FCC metamaterial through translations only. It takes the form of a rhombic dodecahedron centered around a single node of the lattice (Fig. 2.2b). As such it is the smallest volume containing all the geometric information necessary for computing the homogenized mechanical behavior of periodic FCC metamaterials.

- **The fundamental tetrahedron.** Taking into account the full set of FCC symmetries (including rotations and mirror transformations in addition to translations), a tetrahedron can be identified as the fundamental domain defining a periodic FCC metamaterial (Fig. 2.2c). Figures 2.2a and 2.2b show how the fundamental tetrahedron (shown in red) integrates into the cubic and the rhombic dodecahedral unit-cells, respectively. In Fig. 2.2c, the four vertices of the fundamental tetrahedron are identified by letters. Vertex A is the only vertex that is situated at a node of the FCC lattice. Vertex B is located at the mid-point between two first neighbors of the FCC lattice, vertex C is situated at an octahedral site and vertex D lies on a tetrahedral site of the FCC lattice. Using Miller notations to describe the FCC lattice directions, we note that the edges [AB] and [BC] are aligned with the [110] direction, [AC] and [BD] are aligned with the [100] direction, and [AD] and [CD] are aligned with the [111] direction. The full FCC metamaterial is then obtained as a collection of copies of this fundamental tetrahedron, each of them translated, mirrored and rotated into a particular configuration.

- Other useful substructures of the FCC lattice are obtained when considering all fundamental tetrahedra around the vertices B, C and D. The collection of all fundamental tetrahedra around the tetrahedral site D form a cube that features eighth nodes at four of the eight cube corners (Fig. 2.2d). Different from the cubic unit-cell described above, the entire FCC structure cannot be composed through translations only when using the smaller cubic cell obtained from collecting all fundamental tetrahedra around a tetrahedral sites of the FCC lattice. Another rhombic dodecahedral unit-cell is formed by the collection of all fundamental tetrahedra around vertex C (Fig. 2.2e), while an octahedron is formed by all fundamental tetrahedra around vertex B (Fig. 2.2f).

Illustrations of the resulting FCC metamaterials for different motifs included in the fundamental tetrahedron are shown in Fig. 2.3. In the case of struts placed on the edges of the tetrahedron, the widely-studied octet truss (FCC) lattice structure is obtained when positioning a straight strut along the edge [AB] (Fig. 2.3a), or equivalently along edge [BC]

(Fig. 2.3d), while a skeletal rhombic dodecahedron (RD) truss lattice is obtained by selecting the opposing edges ([CD] and [AD], Fig. 2.3f and 2.3c). A simple cubic structure is obtained when positioning a straight strut either along the edge [AC] (Fig. 2.3b) or edge [BD] (Fig. 2.3e).

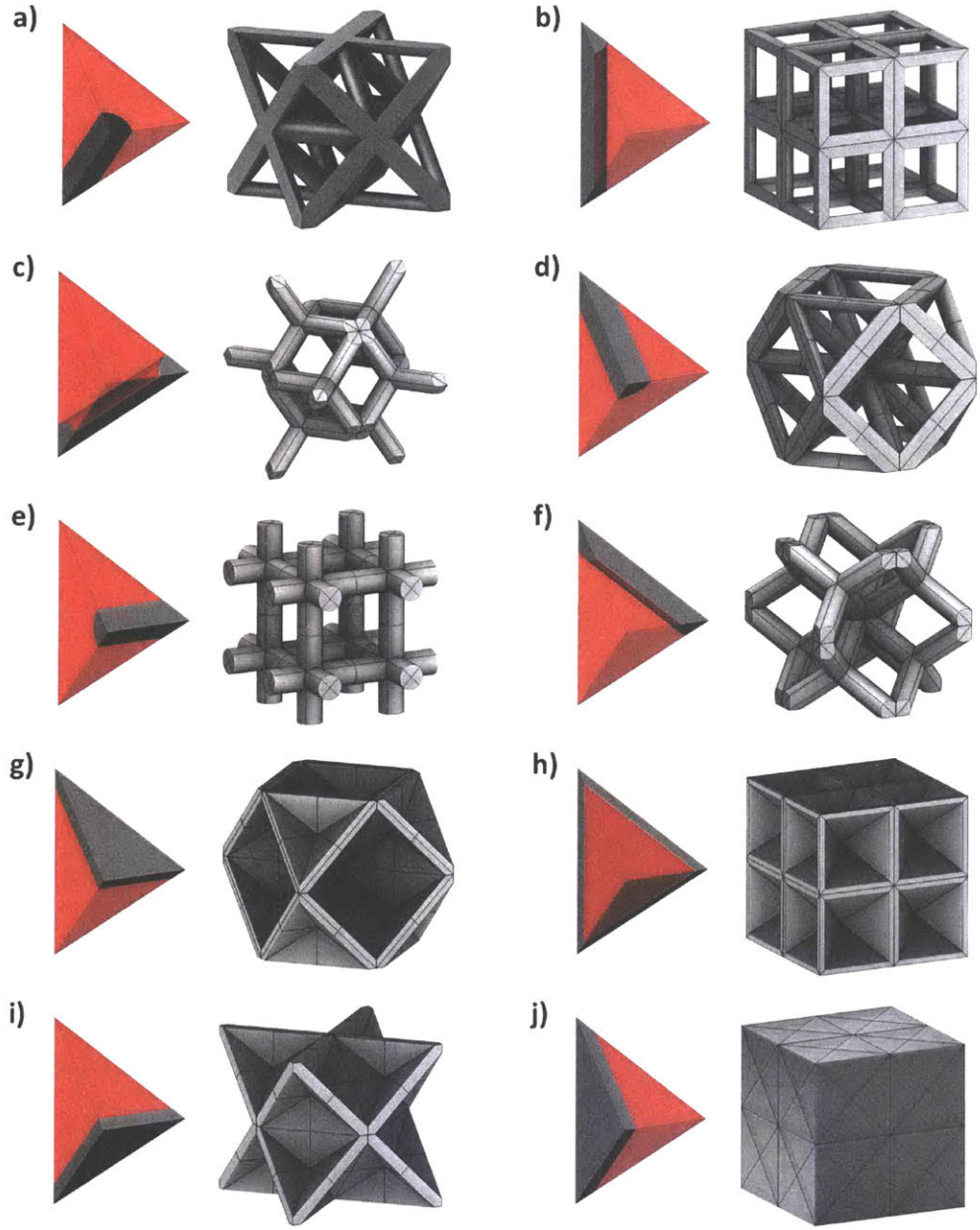

Figure 2.3: Resulting FCC metamaterial architectures for different motifs included in the fundamental tetrahedron: (a) edge AB → octet-truss, (b) edge AC → simple cubic truss, (c) edge AD → rhombic dodecahedron truss, (d) edge BC → octet-truss, (e) edge BD → simple cubic truss, (f) edge CD → rhombic dodecahedron truss, (g) surface A → rhombic dodecahedral foam, (h) surface B → foam with irregular-octahedral cells, (i) surface C → rhombic dodecahedral foam, (j) surface D → simple cubic foam.

2.1.3 *Elastic properties*

The structures' cubic symmetry imposes constraints on their elastic properties, which are recapped in some details in what follows. The stiffness tensor $\boldsymbol{C}$ of cubic structures has only three independent components C_1, C_2, C_3 . In an orthonormal coordinate system aligned with the principal axes of symmetry (i.e. parallel to the edges of the cubic unit-cell), the stress-strain relationship can be written as:

$$\begin{bmatrix}\Sigma_{11}\\ \Sigma_{22}\\ \Sigma_{33}\\ \Sigma_{12}\\ \Sigma_{23}\\ \Sigma_{13}\end{bmatrix} = \tilde{\boldsymbol{C}}\begin{bmatrix}\mathrm{E}_{11}\\ \mathrm{E}_{22}\\ \mathrm{E}_{33}\\ \mathrm{E}_{12}\\ \mathrm{E}_{23}\\ \mathrm{E}_{13}\end{bmatrix}, \qquad \text{with } \tilde{\boldsymbol{C}} = \begin{bmatrix} C_1 & C_2 & C_2 & 0 & 0 & 0\\ C_2 & C_1 & C_2 & 0 & 0 & 0\\ C_2 & C_2 & C_1 & 0 & 0 & 0\\ 0 & 0 & 0 & C_3 & 0 & 0\\ 0 & 0 & 0 & 0 & C_3 & 0\\ 0 & 0 & 0 & 0 & 0 & C_3 \end{bmatrix} \tag{2.1}$$

where Σ_{ij} are the components of the macroscopic stress vector in the natural coordinate system, E_{ij} are the corresponding macroscopic strain tensor components, and $\tilde{\boldsymbol{C}}$ is a matrix representation of the stiffness tensor. To express remarkable quantities it is preferable to invert this relation and reason in terms of compliances:

$$\begin{bmatrix}\mathrm{E}_{11}\\ \mathrm{E}_{22}\\ \mathrm{E}_{33}\\ \mathrm{E}_{12}\\ \mathrm{E}_{23}\\ \mathrm{E}_{13}\end{bmatrix} = \tilde{\boldsymbol{S}}\begin{bmatrix}\Sigma_{11}\\ \Sigma_{22}\\ \Sigma_{33}\\ \Sigma_{12}\\ \Sigma_{23}\\ \Sigma_{13}\end{bmatrix}, \qquad \text{with } \tilde{\boldsymbol{S}} = \begin{bmatrix} S_1 & S_2 & S_2 & 0 & 0 & 0\\ S_2 & S_1 & S_2 & 0 & 0 & 0\\ S_2 & S_2 & S_1 & 0 & 0 & 0\\ 0 & 0 & 0 & S_3 & 0 & 0\\ 0 & 0 & 0 & 0 & S_3 & 0\\ 0 & 0 & 0 & 0 & 0 & S_3 \end{bmatrix} \tag{2.2}$$

Where:

$$S_1 = \frac{C_1 + C_2}{(C_1 - C_2)(2C_2 + C_1)}, \quad S_2 = -\frac{C_2}{(C_1 - C_2)(2C_2 + C_1)}, \quad S_3 = \frac{1}{C_3} \tag{2.3}$$

A direct consequence is that traditional measures of stiffness, such as the Young's modulus or the shear modulus, are direction dependent. Values for important directions, for which Miller indices are used, are given below:

- Bulk modulus:

$$K = 1/(3S_1 + 6S_2) = (C_1 + 2C_2)\,/\,3 \tag{2.4}$$

- Young's modulus:

- Along [100]*: $$E_{100} = 1 / S_1 = \frac{(C_1 - C_2)(C_1 + 2C_2)}{C_1 + C_2} \quad (2.5)$$

- Along [110]: $$E_{110} = 2 / (S_1 + S_2 + S_3) = 2\frac{C_1(C_1 + C_2 + C_3) - C_2^2}{C_3(C_1 - C_2)(2C_2 + C_1)} \quad (2.6)$$

- Along [111]*: $$E_{111} = 3 / (S_1 + 2S_2 + 2S_3) = \frac{3C_3(C_1 + 2C_2)}{4C_2 + 2C_1 + C_3} \quad (2.7)$$

- Shear modulus: with non-zero principal stresses along:

- [110]/[1$\bar{1}$0]*: $$G_{110/1\bar{1}0} = 1 / (2S_3) = C_3 / 2 \quad (2.8)$$

- [100]/[010]*: $$G_{100/010} = 1/(2S_1 - 2S_2) = (C_1 - C_2)/2 \quad (2.9)$$

Where the quantities marked with * are extremal. For linear isotropic we have the relationship:

$$G = \frac{3KE}{9K - E} \quad (2.10)$$

Which provides the isotropy criterion:

$$S_1 - S_2 - S_3 = 0 \quad (2.11)$$

It can be rewritten in different manners to obtain different estimates.

$$S_1 - S_2 = S_3 \quad or \quad \frac{S_1 + 2S_2 + 2S_3}{3} = S_1 \quad (2.12)$$

The community prefers to estimate the anisotropy of cubic structures using a quantity called the Zener ratio, which corresponds to the ratio of extremal values of the shear modulus:

$$\zeta = \frac{S_1 + S_2}{S_3} = \frac{G_{110/1\bar{1}0}}{G_{100/010}} \quad (2.13)$$

Where isotropy corresponds to $\zeta = 1$. However one could prefer using the equivalent in terms of Young's modulus:

$$\frac{S_1 + 2S_2 + 2S_3}{3S_1} = \frac{E_{100}}{E_{111}} \tag{2.14}$$

2.1.4 Other properties

Other properties of the structures than stiffness will in the general case be anisotropic as well, and that even in the event that the elastic isotropy condition is met. However those properties have to respect the cubic symmetry themselves. One interesting case is that of uniaxial properties, such as tensile strength, or even energy absorption in uniaxial compression along one given direction. If one considers a direction as a unit vector in 3D space, one only has to evaluate such a property on a triangle drawn on the unit-sphere, with vertices along one edge of the unit-cell (shorthand [100]), one face diagonal ([110]) and one cube diagonal ([111]). The remaining directional properties can then be deduced from symmetry. The directional dependency of the property can thus be fully described through the use of an inverse pole figure.

2.2.Finite-element Analysis

The mechanical characterization of truss-lattices herein rests mainly on finite-element analysis of the geometries. All finite-element simulations are performed using the commercial software suite Abaqus.

2.2.1 Periodic micro-displacement boundary conditions

In order to describe the behavior of the various structures used herein, we wish to use the vocabulary of continuum mechanics. However the structures are not themselves a continuum as they are heterogeneous, composed of material and void. In this thesis we only resort to a basic application of homogenization theory, for which only an intuitive notion of "averaging" the structure's behavior is needed. The structures considered here are periodic and therefore have an intrinsic length-scale a, which is the side-length of the

unit-cell. The intuitive assumption is that while the structures' behavior remains *stable*, the deformation field resulting from uniform far-field boundary conditions will respect the periodicity of the lattice, and that no phenomena will develop on larger length-scales. As a result the structure's effective behavior can be deduced from simulations performed on just one unit-cell, which is treated as a representative element volume. In the sequel, such simulations are referred to as "unit-cell simulations".

2.2.2 Implementation in Abaqus/Standard

Periodic micro-displacement boundary conditions are applied in the following manner. With $\boldsymbol{E}$ denoting the macroscopic strain, the local displacement field $\boldsymbol{u}$ is decomposed as

$$\boldsymbol{u}(\boldsymbol{x}) = \hat{\boldsymbol{u}}(\boldsymbol{x}) + \tilde{\boldsymbol{u}}(\boldsymbol{x}) = \boldsymbol{u_0} + \boldsymbol{H}.\boldsymbol{x} + \tilde{\boldsymbol{u}}(\boldsymbol{x}) \tag{2.15}$$

where the macroscopic displacement gradient $\boldsymbol{H}$ is equal to $\boldsymbol{E}$ up to a rotation, $\hat{\boldsymbol{u}} = \boldsymbol{u_0} + \boldsymbol{H}.\boldsymbol{x}$ is the macro-displacement that corresponds to the applied strain, and $\tilde{\boldsymbol{u}}(\boldsymbol{x})$ is a micro-displacement. The unit-cell simulations assume that in the bulk of the material, we have

$$\tilde{\boldsymbol{u}}(\boldsymbol{x} + a\lambda_i \boldsymbol{e}_i) = \tilde{\boldsymbol{u}}(\boldsymbol{x}) \tag{2.16}$$

for all integers λ_i and all positions $\boldsymbol{x}$. With a denoting the unit-cell length and $\boldsymbol{e_i}$ denoting the principal directions of the lattice, Eq. (10) ensures that the micro-displacement field shares the periodicity of the lattice. The meshes are designed such that for each node k lying on first face of the unit-cell there exists a node l on the opposite face with normal vector $\boldsymbol{n}$, with the initial position vectors respecting the relations $\boldsymbol{x}_l = \boldsymbol{x}_k + a \cdot \boldsymbol{n}$. The difference in displacements then reads:

$$\boldsymbol{u}_l(\boldsymbol{x}_l) - \boldsymbol{u}(\boldsymbol{x}_k) = \hat{\boldsymbol{u}}(\boldsymbol{x}_k + a\boldsymbol{n}) - \hat{\boldsymbol{u}}(\boldsymbol{x}_k) + \tilde{\boldsymbol{u}}(\boldsymbol{x}_k + a\boldsymbol{n}) - \tilde{\boldsymbol{u}}(\boldsymbol{x}_k) = a\boldsymbol{H}.\boldsymbol{n} \tag{2.17}$$

The periodicity of micro-displacements is enforced by kinematically constraining the difference in the displacements of paired nodes, and setting this difference as equal to the displacement deduced from the macroscopic strain: $\boldsymbol{u}_l - \boldsymbol{u}_k = a\boldsymbol{H} \cdot \boldsymbol{n}$. Three dummy nodes (one per pair of opposing faces of the unit-cell) whose degrees of freedom

correspond to the components of the displacement gradient **H**. Kinematic constraints on the dummy nodes are used to enforce the symmetry of this tensor and make it equal to the macroscopic small strain tensor **E**. As a result, the forces applied to the dummy nodes correspond to the components of the Piola stress tensor **P**. In practice, an additional layer of dummy nodes, with their degrees of freedom kinematically linked to that of the initial layer through linear equations corresponding to the associated rotation matrix, is used to easily change the loading orientation.

2.2.3 Implementation in Abaqus/Explicit

The previous paragraph refers to the implementation of periodic boundary conditions in the implicit solver Abaqus/Standard. However there are cases for which the use of an explicit scheme is preferable: in the case of large models for which large amounts of memory are needed, or for example in the presence of instabilities that provoke a rupture of symmetry, which can lead to non-convergence of the implicit solution. Unfortunately Abaqus/Explicit does not accept large numbers of inter-connected kinematic constraints in the form introduced above, where all surface nodes are interconnected to just three dummy nodes. To resolve this difficulty, a different dummy node is used for every pair of surface nodes. This modification is made at a price, as the ability to control the Piola stress tensor is lost. Such simulations therefore include no stress-free boundary conditions, and are completely strain-led.

2.2.4 Multi-cell specimens

2.2.4.1 Motivation

As explained above, periodic micro-displacement boundary conditions are only realistic if the structure's response does not include features of larger length-scale than that of the unit-cell. However this is an unrealistic assumption in a number of cases.

One of them involves uniaxial compression of structures of relative density sufficiently low (typically $\bar{\rho} \leq 0.1$), for which the stress response obtained through unit-cell simulations will feature a local maximum followed by a phase of softening. Ultimately the

geometry will be compressed enough for internal contact to be initiated and the unit-cell will harden again when compaction occurs. In this case once again, localization will occur in one plane of unit-cells. Once the unit-cells of this plane harden again, another plane starts to localize. In practice the compaction of one plane changes the boundary conditions on the neighboring planes and lowers the force necessary to compact them. What follows in the case of a perfect geometry (and in simulations) is a compaction regime marked by a first peak in stress, followed by lower peaks, revolving around a plateau value. In actual experiments, defects in the specimens lead to an averaging-out of the response which materializes by a stress plateau, much similar to the behavior observed on foams (e.g. Mohr and Doyoyo 2004). Such behavior will be observed during experimental testing of low relative density structures, see for example Fig. 3.15, where a $\bar{\rho} = 0.2$ octet-truss develops compaction zones in the form of shear bands, reflected in the associated stress-strain curves by stress oscillations around a stress plateau.

This behavior, including the level of the stress plateau, cannot be captured by unit-cell simulations which typically have only one layer (and thus only the first peak). To remedy this, larger samples consisting in stacks of several unit-cells are used. Multi-cell simulations are typically realized using Abaqus/Explicit, because of both the large number of elements and the prevalence of contact. Figure 2.4 presents an example for an octet-truss with $\bar{\rho} = 0.1$, comparing the results of a unit-cell simulation under uniaxial compression and a multi-cell simulation consisting in a cubic block of three unit-cells in side under compression between two platens. While the two simulations agree up to the observed first peak in stress, the unit-cell shows strain-softening up to the maximum investigated engineering strain of 0.6. The multi-cell simulation shows multiple peaks corresponding to the successive crushing of the different layers. It is interesting to note the local minima observed do not correspond to the minimum post-peak stress observed for the unit-cell, highlighting the necessity of such an approach.

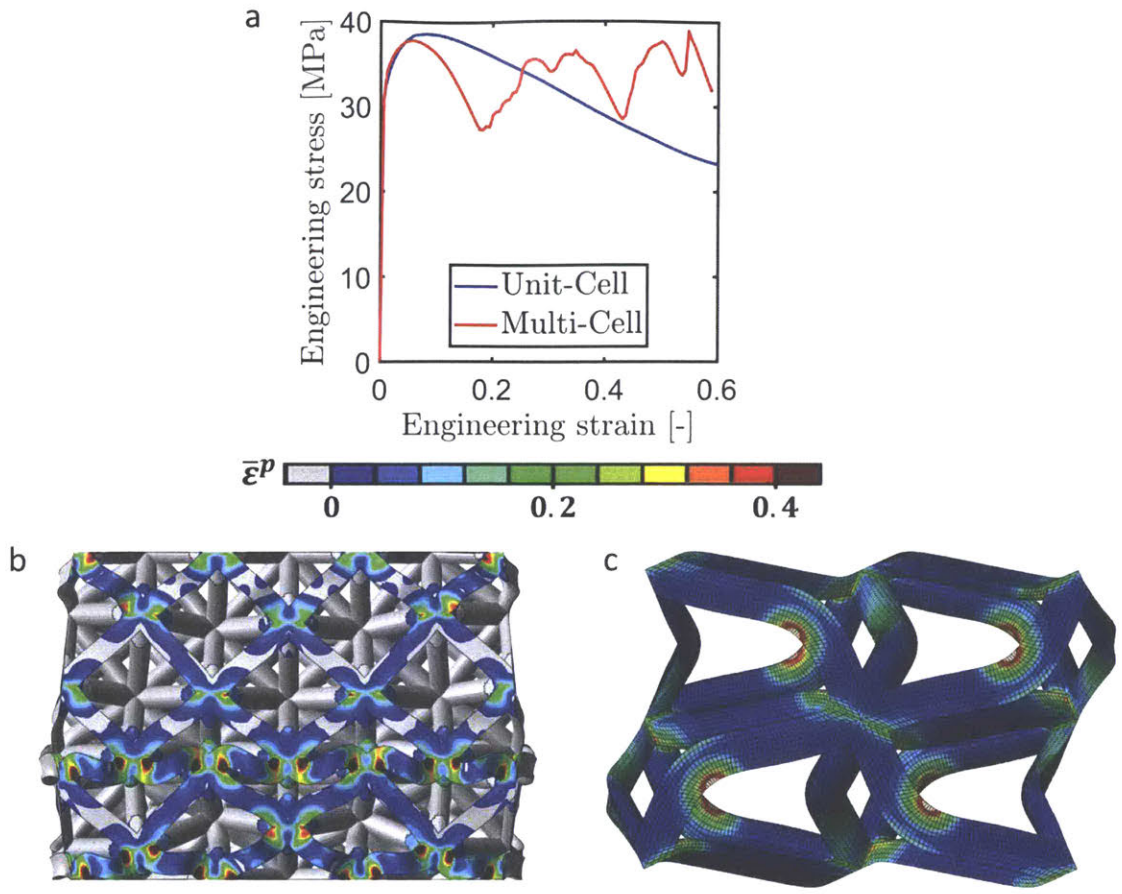

Figure 2.4: Numerical results of the uniaxial compression along [100] of an octet-truss of relative density 10%. a) Comparison of stress-strain curves obtained with unit-cell, and multi-cell simulations. b) Deformation pattern and partial equivalent plastic strain distribution on a multi-cell simulation at engineering strain 0.3. c) Deformation pattern and equivalent plastic strain distribution on a unit-cell simulation at engineering strain 0.3.

2.2.4.2 Oriented multi-cell specimens

To evaluate the large strain response of the metamaterial structures along these three directions, we consider three distinct multi-cell specimens that feature the same shell structure, but with different lattice orientations with respect to the specimen edges (and hence the directions of loading). They are generated from three different parallelepipedic unit-cells whose face normals are given by the following sets of orthonormal vectors.

- The [100]-unit cell is the regular unit-cell:

$$\mathcal{B}_{100} = \left\{ \begin{bmatrix} 1 \\ 0 \\ 0 \end{bmatrix}, \begin{bmatrix} 0 \\ 1 \\ 0 \end{bmatrix}, \begin{bmatrix} 0 \\ 0 \\ 1 \end{bmatrix} \right\} \tag{2.18}$$

- For the [110] unit-cell:

$$\mathcal{B}_{110} = \left\{ \begin{bmatrix} 1 \\ 1 \\ 0 \end{bmatrix} / \sqrt{2}, \begin{bmatrix} -1 \\ 1 \\ 0 \end{bmatrix} / \sqrt{2}, \begin{bmatrix} 0 \\ 0 \\ 1 \end{bmatrix} \right\} \tag{2.19}$$

- And for the [111] unit-cell:

$$\mathcal{B}_{111} = \left\{ \begin{bmatrix} 1 \\ 1 \\ 1 \end{bmatrix} / \sqrt{3}, \begin{bmatrix} 1 \\ -1 \\ 0 \end{bmatrix} / \sqrt{2}, \begin{bmatrix} 1 \\ 1 \\ -2 \end{bmatrix} / \sqrt{6} \right\} \tag{2.20}$$

By selecting proper edge-lengths, namely $(\sqrt{2}, \sqrt{2}, 1)$ for the [110] unit-cell, and $(\sqrt{3}, \sqrt{2}, \sqrt{6})$ for the [111] unit-cell the components of the edge vectors have integer coordinates and the resulting bricks respect the periodicity of the lattice. The three oriented unit-cells for three selected structures are depicted in Fig. 2.5. While this approach is more precise than unit-cell simulations, it is also much more costly both computation-wise and requires much more complex modeling to obtain the structure's mesh.

2.2.5 Summary

The quasi-static mechanical behavior of periodic cubic structures is investigated through means of finite element simulations. The methodology is tailored towards metallic structures. Unit-cell simulations with periodic boundary conditions are used to obtain both the elastic properties and an estimate of the yield surface of the metamaterial. Large-strain behavior is estimated either through similar unit-cell simulations, or using multi-cell models for which no periodic boundary conditions are used. The multi-cell specimens can be cut with different angles to investigate the metamaterial's anisotropy.

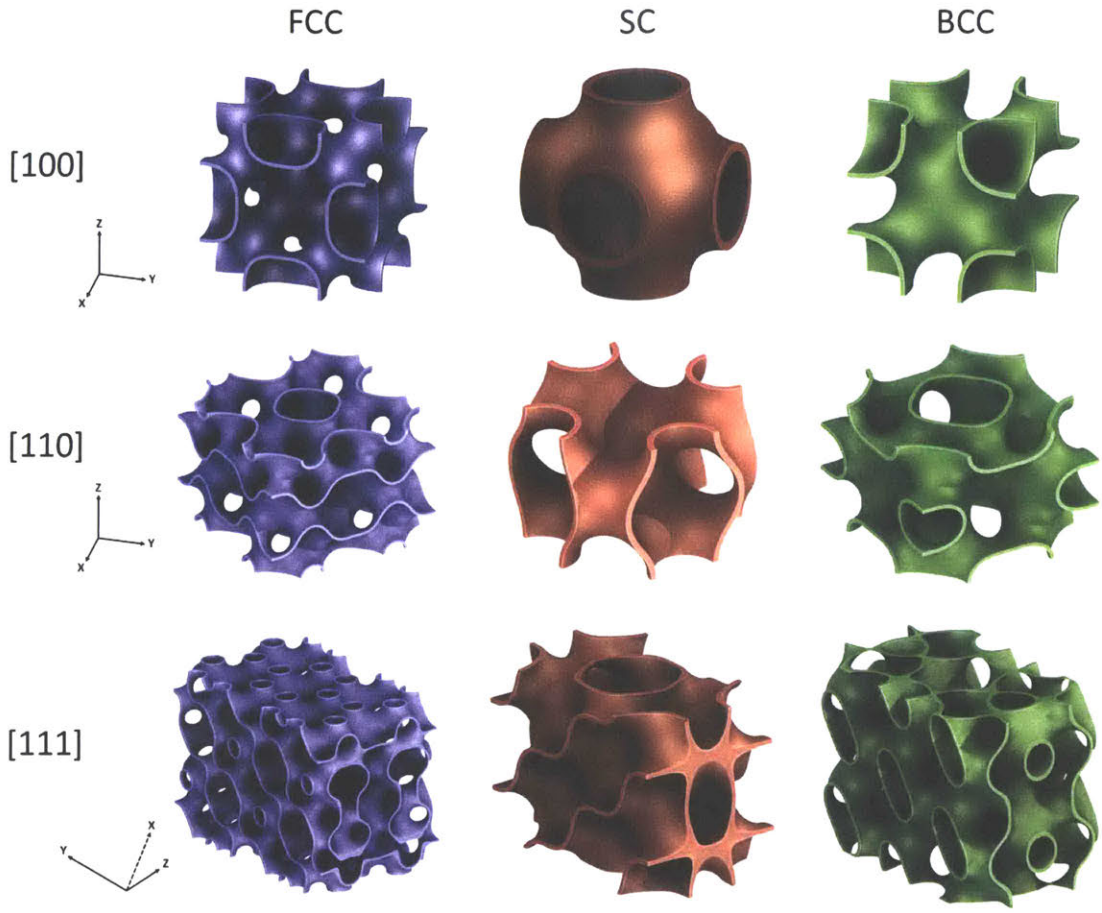

Figure 2.5: View of oriented unit-cells for three types of cell-lattices.

2.3.Experimental methods

All specimens used herein were manufactured using out of a 316L stainless steel powder (CL 20ES, ConceptLaser), with a particle size distribution in the range $20 - 50\mu m$ on a commercial Selective Laser Melting (SLM) machine (ConceptLaser M2). Attempts were made to fabricate specimens using stereolithography (SLA). The manufacturing process involved a post-build curing step involving UV light. Due to the intricacy of the shell specimens this resulted in uneven curing. This suggests that heat-based post-build steps, or even single-step methods, would be better adapted to the manufacturing of shell-lattice geometries.

Specimens usually consist in cubic or nearly-cubic blocks containing several unit-cells of the metamaterial at hand. Those are tested in compression between two rigid platens. Further details are given in each relevant paragraph.

2.3.1 Material behavior

2.3.1.1 Material model

An elastoplastic model is with a simple von Mises yield criterion and isotropic hardening is chosen to model the additively-manufactured 316L stainless steel. We choose a Young's modulus of $E = 200\ GPa$, a Poisson's ratio of $\nu = 0.3$, and a Swift hardening law:

$$k_S(\bar{\varepsilon}^p) = A \cdot \left(\bar{\varepsilon}_p + \varepsilon_0\right)^n \tag{2.21}$$

with the Swift parameters $A = 842.5\ MPa$, $\varepsilon_0 = 0.036$ and $n = 0.176$. These values are chosen based on information provided on the material datasheet for the selected powder, available on Concept Laser's website, specifically at the time of this thesis' writing, at this address:

https://www.concept-laser.de/fileadmin//user_upload/Datasheet_CL_20ES.pdf

For the present constituent material and corresponding to a standard uniaxial tension test, the data sheet indicated in October 2016 a yield strength of $470MPa$, an ultimate strength of $570MPa$ and a ductility of 0.15. The corresponding stress-strain curve is provided in Figure 2.6a. Fracture events are neglected in all simulations – and were not observed experimentally with this constituent material.

It should be noted that updates of the above-mentioned datasheet appeared during the completion of this work, including variations on the above-mentioned numbers. As of October 2018, it reads for the yield stress, 374MPa in the building direction, 650MPa for the ultimate stress and a corresponding elongation of 65%. For the sake of consistency of this thesis the updated values have been ignored herein, and the same stress-strain curve is used in all corresponding simulations. As a consequence numerical results can be compared from one study to another. Experimental curves showed in this thesis are always obtained from specimens printed within the same machine cycle (in the case of large experimental studies, e.g. Part 5, two consecutive cycles with one repeat of each specimen geometry per cycle).

2.3.2 *Experimental validation on a honeycomb-like specimen*

In order to gain insight into the stress-strain response of the as-manufactured cell wall material, uniaxial compression experiments are performed. Given that the material properties of additively manufactured materials usually depend on the wall thickness, a 2D-cellular structure with prismatic cells of triangular section (triangular honeycomb) with the same wall thickness $t_w = 400\mu m$ as that of the manufactured shell-lattice specimens is employed (instead of manufacturing cylindrical compression specimens). Note that despite the complex sample geometry, the stress-state for compression between two flat loading platens is expected to be uniaxial compression in all cell walls. A relative density of 67% is selected to guarantee a high structural stability of the honeycomb specimen for compressive strains of up to 0.2. Preliminary simulations suggested that lower density specimens would respond by cell buckling at lower strains. The resulting honeycomb specimen (Fig. 2.6b) features a truss length of $1.64mm$. The specimen comprises 13×8 triangles for total in-plane dimensions of $11.94mm \times 11.76mm$, and measures $10mm$ in height. For comparison purposes, we also extract standard tensile specimens from $1.5mm$ thick, cold-wrought and annealed, stainless steel 316L sheets (AISI 316L Finish 2B, provided by Aperam, France). The tension experiments with optical strain measurements are performed on a universal testing machine at a strain rate of $10^{-3}s^{-1}$.

The honeycomb specimen is tested on a hydraulic universal testing machine (Instron, model 8801), and one face of the specimen is monitored using a high-resolution digital camera (4240×2824 pixels, Model GS3-U3-120S6M-C, PointGrey). Macroscopic engineering strains are estimated through digital image correlation using software Vic-2D (Correlated solutions), by relying on the natural contrast of the specimen face. Based on the measured force history $F(t)$ and the logarithmic axial strain ε_a (determined through surface DIC), the true axial stress in the cell wall material is computed,

$$\sigma_a = \frac{F}{\bar{\rho}A_0}\exp(\varepsilon_a) \tag{2.22}$$

with the initial macroscopic cross-sectional area A_0 and the relative density $\bar{\rho}$. The identified stress-strain curve is shown by solid dots in Fig. 2.6a. It is in reasonable

agreement with the red stress-strain curve that has been derived from the manufacturer-provided data and used in all numerical simulations. The blue curve in Fig. 2.6a depicts the true strain-strain curve obtained from testing the specimens extracted from $1.5mm$ thick stainless steel 316L sheets. The particular feature of the additively-manufactured stainless steel 316L is that it displays a significantly higher yield point than conventional sheets with the same alloy composition. This yield strength advantage vanishes as the material is deformed. Due to the lower hardening of the additively-manufactured material, the two stress-strain curves (black dots and blue curve) cross at a true strain of about 0.2. The observed superior strength/ductility trade-off is in line with the results from previous studies on additively-manufactured stainless steel (e.g. Hanzl et al. (2014), Suryawanshi et al. (2017), Wang et al. (2018)). It is worth noting that this contrasts with other materials manufactured via SLM, for which the additively manufactured material typically compares unfavorably with conventionally manufactured alternatives (e.g. Mower et al. 2016).

2.3.3 Microscopic analysis

Single unit-cell specimens of an FCC shell-lattice with $\bar{\rho} = 0.3$ and $t_w = 400\mu m$ are manufactured for microscopic analysis. The specimens are embedded in a conductive resin, grinded and polished. Electron Back-Scattered Diffraction (EBSD) analysis is performed with a step size of $0.5\mu m$ in the central part of a cell wall's cross-section. A microscopy specimen is prepared as well from the conventionally manufactured stainless-steel sheet-metal mentioned in the above paragraph. A single unit-cell honeycomb specimen is similarly embedded and polished and to check for internal porosity and surface roughness.

EBSD analysis is performed to gain further insight into the difference between additively-manufactured and rolled stainless steel. The inverse pole figure for a cell wall region of about $300 \times 900\ \mu m^2$ (Figs. 2.6c, 2.6d) shows a highly heterogeneous microstructure with large variations in grain size (ranging from smaller than $1\mu m$ to more than $100\mu m$) and grain aspect ratios (ranging from 1 to greater than 10). The corresponding inverse pole figure for the sheet material (Fig. 2.6e) is very different: a uniform microstructure is observed with predominantly equi-axed grains with grain sizes in the range of 5 to $30\mu m$. As discussed by Suryawanshi et al. (2017), the refinement of

additively-manufactured microstructures due to the high cooling rates during manufacturing is one source of strengthening. However, when comparing the microstructures shown in Figs. 2.6d and 2.6e, refined grains are only seen in small regions. The strengthening can thus not be exclusively attributed to a Hall-Petch effect associated with the EBSD-identified grain sizes. Microstructures with highly unconventional grain shapes and sizes spanning several orders of magnitude have also been observed in additively-manufactured stainless steels by Wang et al. (2018). They argued that solute strengthening and low-angle grain boundaries contribute to the increased yield strength in additively-manufactured stainless steel 316L. Furthermore, they emphasize the potential of strengthening in additively-manufactured stainless steel due to subgrain level structures such as solidification cells.

The microscopic images also show the surface roughness of the additively-manufactured specimens. It is characterized by irregular creases of a depth of about $50\mu m$ (Fig. 2.6c), which corresponds to the particle size of the powder. The surface roughness is partly due to a balling effect, with powder particles attached to the cell wall edges. Defects in the form of porosity are also visible on the polished cross-section of the honeycomb specimen (Fig. 2.6f).

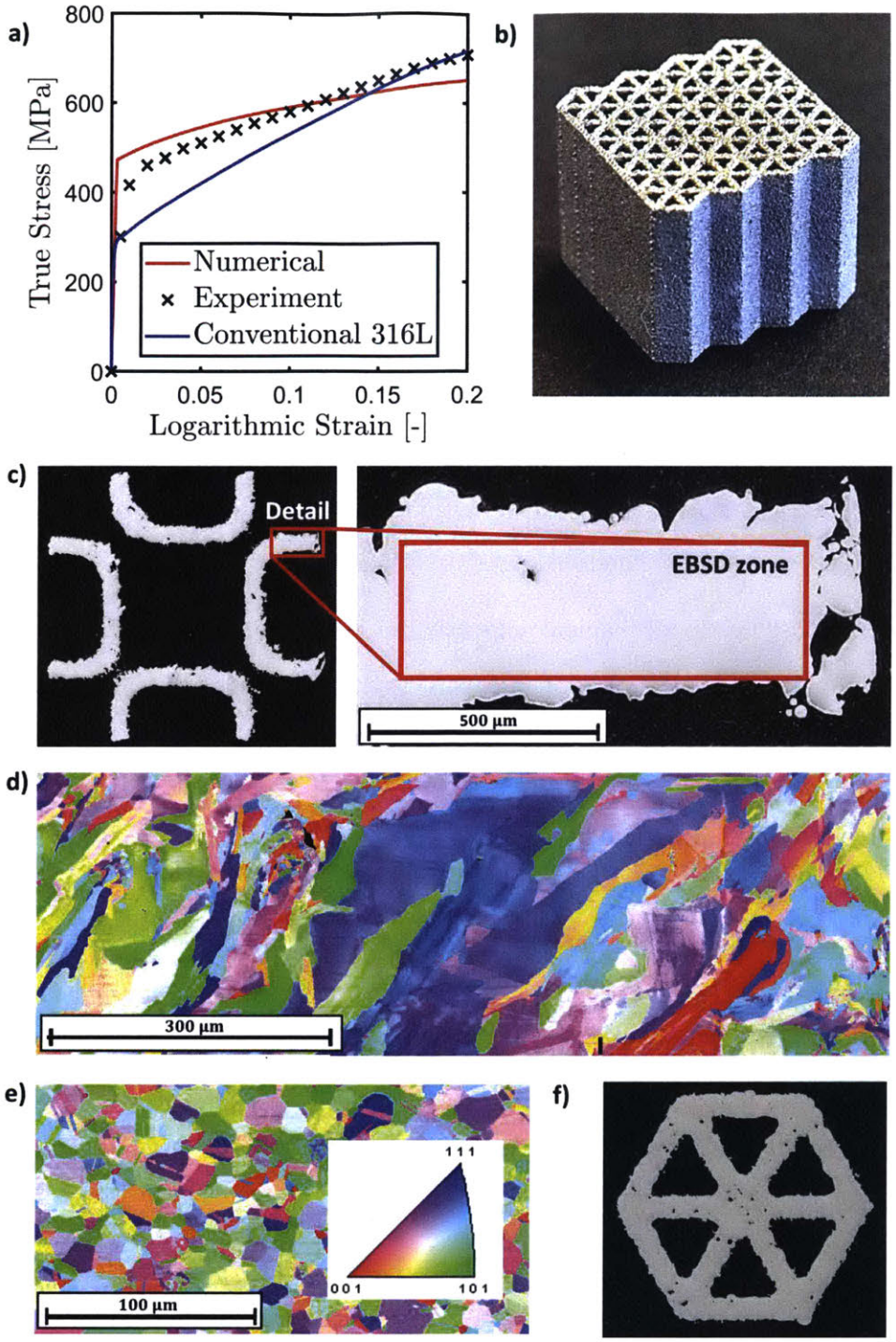

Figure 2.6: a) Experimentally-measured stress-strain curves for additively- and conventionally-manufactured stainless steel 316; b) view of a triangular honeycomb specimen, c) view of the cell-wall of a shell-lattice specimen, d) inverse pole figure obtained through EBSD analysis on a cell wall of an additively-manufactured shell-lattice specimen, and e) for a conventionally-manufactured 316L stainless steel sheet; f) micrograph of a polished section of single-cell triangular honeycomb specimen showing important surface roughness and internal porosity.

3. Compared analysis of several FCC metamaterials

This chapter is adapted from Bonatti and Mohr (2017).

In the present chapter, we explore the mechanical behavior of cellular solids with Face-Centered Cubic (FCC) symmetry. In particular, we consider the octet truss lattice with solid and hollow trusses, hollow sphere assemblies and hybrid truss-sphere structures. The large deformation hydrostatic and confined compression responses of these mesostructures is analyzed for relative densities ranging from 0.2 to 0.6, and for high and low strain hardening base materials. Uniaxial compression experiments are performed on porous stainless steel 316L mesostructures to validate our non-linear finite element models and to demonstrate the superior weight specific energy absorption capabilities of continuous shell mesostructures over the conventional octet truss lattice at 20% relative density.

When discussing the mechanical response of a metamaterial, it is useful to distinguish among three length scales: (1) the macroscopic level, where the porous material is considered as a homogeneous solid, (2) the mesoscopic level, where the porous material is considered as a two phase material composed of a mesostructure made from a homogenous solid base material and a fluid phase (pores), and (3) the microstructural level, where heterogeneities (e.g. polycrystalline grain structure or microporosity) within the base material are considered. In this chapter a particular attention is given to the macroscopic features of the deformation (whether it is homogeneous or displays strain localization) as well as mesoscopic details that reveal insights into the potential weak points of the structures.

3.1.Structures considered

3.1.1 Material used in the experiments

All specimens tested are made from stainless steel 316L powder using Selective Laser Melting (SLM). As shown by Tancogne-Dejean et al. (2016), substantial base material property gradients may prevail within SLM made structures due to locally different temperature histories. As a first approximation, it is expected that the average base material

response in the experiments is similar to the HH material behavior assumed in the simulations.

An attempt has also been made to manufacture polymer specimens through stereolithography (SLA). However we abandoned this approach due to the high number of support structures required to stabilize numerous over-hanging surfaces during the manufacturing process.

3.1.2 Material models considered in the computational analysis

The mechanical stability of plastically-deforming structures is strongly affected by the strain hardening of the base material after first yield. We anticipate that a higher strain hardening capacity of the base material will favorably affect the stability of the mesostructures considered. We therefore carry out all our simulations for two distinct base materials that represent two rather extreme cases (among engineering materials) of high strain hardening and low strain hardening (nearly perfectly plastic) at small and moderate strains,

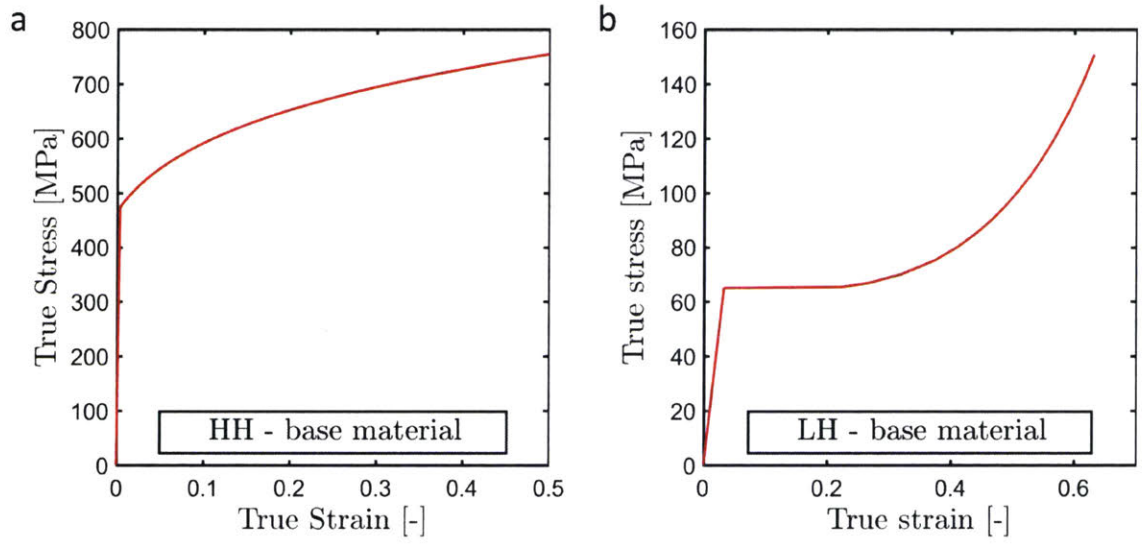

Figure 3.1: Stress-strain responses used in numerical simulations for a) the high strain hardening constituent material corresponding to 316L stainless steel b) the low strain hardening constituent material corresponding to Accura Xtreme, a glassy polymer used in stereolithography.

1. High strain Hardening (HH) base material: the assumed uniaxial stress-strain response for the HH material is shown in Fig. 3.1a. The relationship between the von Mises equivalent stress $\bar{\sigma}$ and the work-conjugate equivalent plastic strain $\bar{\varepsilon}^p$ is described through the Swift law presented in Chapter 2.

2. Low strain Hardening (LH) base material: the uniaxial stress-strain response for the LH material is represented through a piecewise-linear, monotonically increasing function (Fig. 3.1b), while its elastic response is described through the constants $E = 2\text{GPa}$ and $\nu = 0.3$. The assumed response has been adapted from experiments on a PE-like polymer which is used for stereolithography.

Both the HH and LH materials are modeled using the standard finite strain plasticity model of the Abaqus material library (Simulia, 2015), which assumes a von Mises yield function, associated plastic flow and isotopic strain hardening.

3.1.3 Metamaterial architectures

We limit our attention to four mesostructures of FCC symmetry. The fundamental domain of the FCC geometries is a tetrahedron $\mathcal{T}$,

$$\mathcal{T} = \left\{ (x,y,z) \in \mathbb{R}^3 \Big/ \begin{array}{c} x \geq 0 \\ z \geq 0 \\ y \leq L/2 \\ \sqrt{2}x + \sqrt{2}y + 2z \geq 0 \end{array} \right\}, \tag{3.1}$$

with L denoting the closest neighbor distance in the FCC lattice. In particular, we investigate the mechanical behavior of the following FCC mesostructures:

1. Solid Octet Truss (SOT) lattice: The SOT is obtained by connecting the closest neighbors in an FCC lattice through cylindrical solid struts (Fig. 3.2a). As shown by Deshpande et al. (2001b), the relative density $\bar{\rho}$, i.e. the ratio of the density of the porous solid and the solid base material, is controlled by the strut diameter-to-length ratio D/L,

$$\bar{\rho}_{SOT} = \frac{3\pi}{\sqrt{2}}\left(\frac{D}{L}\right)^2 - C\left(\frac{D}{L}\right)^3 \tag{3.2}$$

where the cubic correction coefficient $C = 13.6$ has been identified by Tancogne-Dejean et al. (2016) from fitting Eq. (3) to CAD calculations.

2. Hollow Sphere Assembly (HSA): this configuration is obtained by placing hollow spheres at the vertices of the FCC lattice (Fig. 3.2b). The outer diameter of the spheres is equal to the closest neighbor distance L. The relative density of the HSA material is then controlled by the sphere wall thickness-to-diameter ratio t/L. In our simulations and experiments, hollow cylindrical joints are included between adjacent spheres, with outer diameter $L/5$ and of wall thickness t. These joints ensure the cohesion of the assembly while being compatible with the use of powder-bed and liquid-bath additive manufacturing techniques (as the non-molten material inside the spheres can still be extracted through these joints). Neglecting the mass contribution of the joints between adjacent spheres, the theoretical estimate of the relative density reads

$$\bar{\rho}_{HSA} = \frac{\pi}{\sqrt{2}} \cdot \left(2\left(\frac{t}{L}\right) - 4\left(\frac{t}{L}\right)^2 + \frac{8}{3}\left(\frac{t}{L}\right)^3 \right) \tag{3.3}$$

A derivation for equation (1.3) is provided in Appendix 1. In addition to these two extreme cases of solid struts and hollow spheres, we consider two intermediate configurations:

3. Hollow Octet Truss (HOT) lattice: when substituting the solid struts of the SOT by hollow struts, the HOT configuration is obtained (Fig. 3.2c). In addition to the D/L ratio, the relative density of the HOT lattice depends on the inner-to-outer strut diameter ratio d/D,

$$\bar{\rho}_{HOT} = \frac{3\pi}{\sqrt{2}}\left(\frac{D}{L}\right)^2 \left(1 - \left(\frac{d}{D}\right)^2\right) - 13.6\left(\frac{D}{L}\right)^3 \left(1 - \left(\frac{d}{D}\right)^3\right) \tag{3.4}$$

Equation (3.4) is readily obtained when subtracting an SOT of strut diameter d from an SOT of strut diameter D.

4. Hybrid Truss-Sphere (HTS) assembly: Hollow spheres are placed at the vertices of the FCC lattice and connected by hollow struts (Fig. 3.2d). The relative density of the HTS is then controlled by four ratios: (i) the normalized strut outer diameter d_{out}/L, (ii) the strut inner to outer diameter ratio $d_{in}/$

d_{out}, (iii) the normalized sphere outer diameter D_{out} / L, and (iv) the sphere thickness to the strut thickness ratio $t_{SPH} / t_{STR} = (D_{out} - D_{in}) / (d_{out} - d_{in})$. For the particular case of $D_{in}/L = 2/3$, $d_{in}/d_{out} = 1 / \sqrt{2}$ and $t_{SPH} = t_{STR} = t$, the theoretical estimate of the relative density reads

$$\bar{\rho}_{HTS} \approx 1.975\left(\frac{t}{L}\right) + 57.7\left(\frac{t}{L}\right)^2 - 4469\left(\frac{t}{L}\right)^3 \tag{3.5}$$

when neglecting terms of higher order in *t/L*.

A solid sphere-based assembly is not considered due to its high relative density ($\bar{\rho} = \pi / 3\sqrt{2} \cong 0.74$). It is worth noting that the SOT features a single continuous porous phase while all other architectures (HSA, HOT and HTS) each feature two separate porous phases.

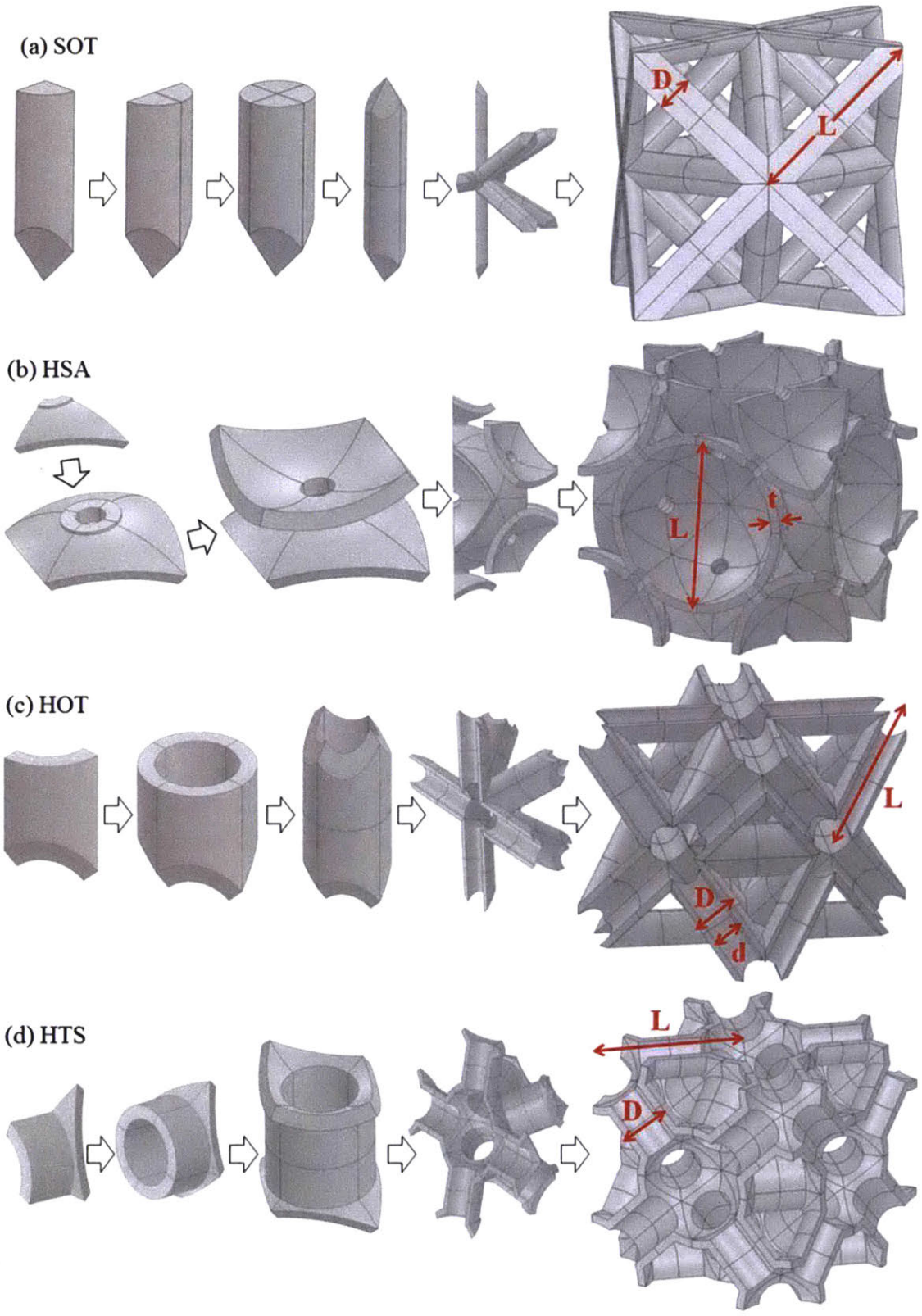

Figure 3.2. Composition of metamaterial architectures: (a) solid octet truss, (b) hybrid sphere assembly, (c) hollow octet truss, and (d) hybrid truss sphere assembly.

3.2. Finite element analysis

Three basic types of simulations are performed to investigate the mechanical behavior of porous solids:

(1) Estimation of the macroscopic elastic moduli: Implicit small-strain analysis of the unit cell subject to uniaxial tension, hydrostatic tension and pure shear loading (using Abaqus/Standard solver);

(2) Determination of the large strain response: Explicit finite-strain analysis of the unit cell subject to hydrostatic and confined compression (using Abaqus/Explicit solver);

(3) Determination of specific energy absorption: Explicit finite-strain analysis of cubic specimens comprised of 27 unit cells subject to uniaxial compression (using Abaqus/Explicit solver);

3.2.1 Unit-cell models

An automated meshing scheme has been developed to generate solid element meshes of the respective FCC unit cells. Starting from a mesh of the primitive cell (Fig. 3.3), the full unit-cell mesh is generated through a series of mirror operations (see Fig. 3.2 or paragraph 2.2 for details):

- SOT unit cell meshes are created for three relative densities, $\bar{\rho} = 0.2, 0.4, 0.6$. The SOT meshes feature three first-order elements along the radial strut direction. Maintaining an element aspect ratio close to one, the respective total number of elements per unit cell are 57.600, 37,440 and 28,800.
- HSA unit cell meshes are created for three relative densities, $\bar{\rho} = 0.2, 0.4, 0.6$. The HSA meshes feature eight first-order elements along the sphere thickness direction. Maintaining an element aspect ratio close to one, the respective total number of elements per unit cell are 276,864, 104,256 and 66,240.
- HOT and HTS unit cell meshes are created for a relative density of $\bar{\rho} = 0.2$ only. A minimum of three elements through thickness is used in the respective

meshes. For element aspect ratios close to unity, this results in a total number of elements per unit cell of 165,888 and 266,304, respectively.

Implicit analyses are performed to compute the macroscopic elasticity constants. To estimate the macroscopic Young's modulus E, the shear modulus G and the bulk modulus K, three distinct sets of boundary conditions are applied. With $\{\mathbf{e}_1, \mathbf{e}_2, \mathbf{e}_3\}$ defining a Cartesian coordinate frame that is aligned with the unit cell edges, the respective boundary conditions read

$$\text{Uniaxial tension:} \quad \begin{cases} F_{11} = 1 + \varepsilon_{\max} \\ P_{ij} = 0 \ \forall \ (i,j) \neq (1,1) \end{cases} \tag{3.2}$$

$$\text{Simple shear:} \quad \mathbf{F}_S = \varepsilon_{\max} \mathbf{e}_1 \otimes \mathbf{e}_2 \tag{3.3}$$

$$\text{Hydrostatic:} \quad \mathbf{F}_H = \frac{\varepsilon_{\max}}{3} (\mathbf{e}_1 \otimes \mathbf{e}_1 + \mathbf{e}_2 \otimes \mathbf{e}_2 + \mathbf{e}_3 \otimes \mathbf{e}_3) \tag{3.4}$$

In the explicit finite-strain simulations, we define self-contact with a friction coefficient of 0.2 within the unit cells. The gradient $\mathbf{F}_H$ is also applied to determine the large deformation response under hydrostatic compression, while the macroscopic deformation gradient

$$\mathbf{F}_{CC} = -\varepsilon_{\max} \mathbf{e}_1 \otimes \mathbf{e}_1 \tag{3.5}$$

is applied to assess the material response to confined compression. In the large deformation simulations, $\varepsilon_{\max}$ is chosen such that about half of the unit cell porosity is absorbed at the end of the simulation. Mass scaling is used to solve the quasi-static boundary value problems with about 200,000 stable explicit time steps. The reported macroscopic stresses are computed from the work-conjugate forces at the master nodes. Note that we always report true strains and stresses when showing unit cell simulation results.

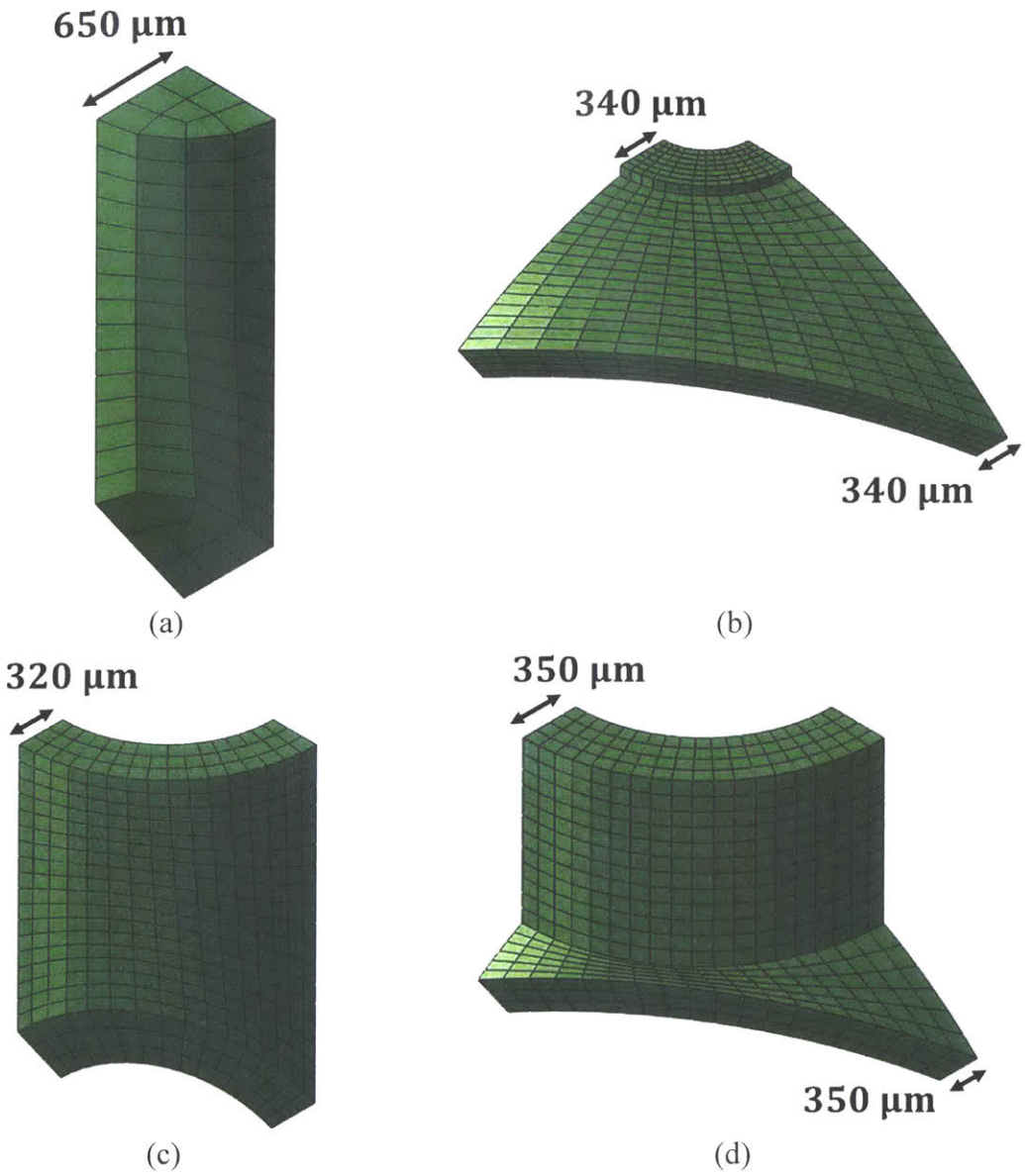

Figure 3.3: Details of the building blocks of the meshes used to discretize the geometries. Each unit-cell model consists in 96 rotated and translated copies of the shown details, combined with 96 copies of its mirror mesh. a) SOT b) HSA c) HOT d) HTS.

3.2.2 Uniaxial compression specimens

As explained in Paragraph 2.2, the periodic boundary conditions imposed onto the unit cell models are potentially confining as far as the localization under uniaxial compression is concerned. We therefore generated uniaxial compression specimens comprising multiple unit cells. With regards to the limitations of the high performance computing infrastructure, cubic specimens comprised of $3 \times 3 \times 3 = 27$ unit cells are generated based on the unit cell

meshes for a relative density of $\bar{\rho} = 0.2$. Note that the largest specimen model included about 7.5 million solid elements. The virtual specimen is placed between two parallel flat surfaces (analytical rigid surface). A friction coefficient of 0.2 is assumed between the specimen and the rigid surfaces. The lower surface is kept stationary, while the upper surface is moved downward at a constant velocity. Using automatic mass scaling, the base material density is adjusted such that a maximum macroscopic compressive engineering strain of 0.6 is reached after about 500,000 time steps. As in the explicit unit cell simulations, self-contact with a friction coefficient of 0.2 is defined within the cellular structures.

3.2.3 Simulation results

3.2.3.1 Elastic moduli

Recall that we created models of different relative densities for the SOT and HSA configurations only. Consequently, the relative modulus versus relative density plots are only provided for these two materials (Figs 3.4a to 3.4c). It is worth noting that the curves are not in hierarchical order. For example, the Young's modulus of the SOT is lower than that of the HSA material at low relative densities, while the shear and bulk moduli of the SOT are always higher irrespective of the relative density. The differences are most pronounced at a relative density of 0.6, where the SOT shear and bulk moduli are about 60% higher. The comparison of the moduli of all four mesostructures (Fig. 3.4d) at a relative density of shows that the HTS structure exhibits the highest Young's and bulk moduli, while its shear modulus is 30% lower than that of the shear stiffest material (SOT). Overall, the HOT architecture exhibits the lowest elastic properties, in particular its shear modulus is 40% lower than that of the SOT. The widest spread in moduli among different structures is observed for hydrostatic loading. Here, the bulk modulus of the HSA is only half that of the HTS material.

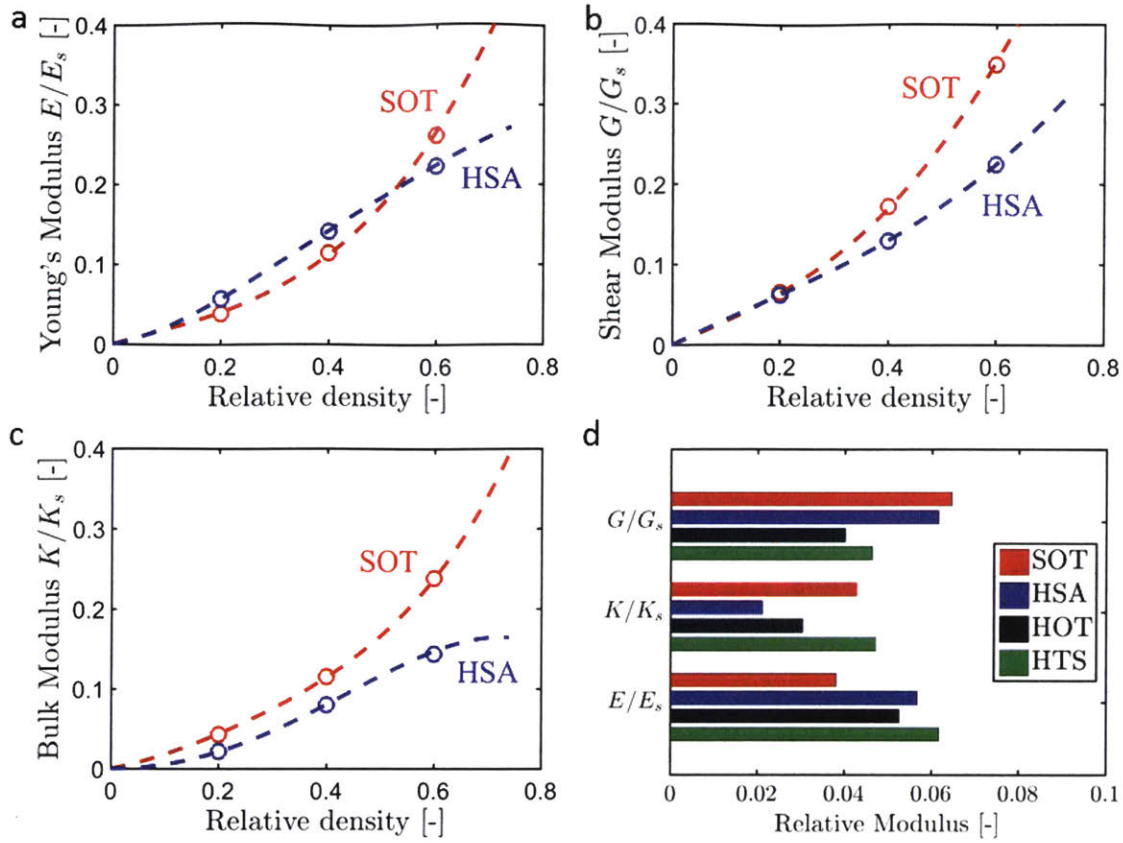

Figure 3.4: Comparison of the computed macroscopic elastic properties: (a) Relative Young's modulus, (b) relative shear modulus, and (c) relative bulk modulus of the Solid Octet Truss (SOT) and the Hollow Sphere Assembly (HSA) as a function of the relative density. Each open symbol highlights a simulation result, while the dashed lines indicate the trends. (d) Comparison of the moduli for all four metamaterial architectures at a relative density of 0.2.

3.2.3.2 Large strain response to hydrostatic compression

Simulations are performed for all four mesostructures {SOT, HSA, HOT, HTS} for a relative density of $\bar{\rho} = 0.2$, while the mechanical response of the first two structures is also analyzed for $\bar{\rho} = 0.4$ and $\bar{\rho} = 0.6$. The simulations are stopped when the initial porous volume is reduced by 50%. In the sequel, we discuss selected simulation results in detail.

- *Solid Octet Truss (SOT) lattice*: Figures 3.5a and 3.5b show the computed macroscopic pressure versus volumetric strain relationships for the high strain hardening (HH) and low strain hardening (LH) base materials, respectively. In addition, selected contour plots of the equivalent plastic strain distribution at the mesostructural level are shown. The hydrostatic loading condition at the

macroscopic level puts all struts under uniaxial compression. The stress state within the 'nodes', i.e. the joints connecting 12 struts, is almost perfect hydrostatic compression as long as the struts are straight. The plastic deformation is therefore confined to the struts as the von Mises base material does not deform plastically in the regions of locally hydrostatic stress states. For small strut length to diameter ratios (e.g. Figs. 3.5c and 3.5d), the struts remain straight even at large plastic strains. Slender struts buckle plastically (e.g. Figs. 3.5e and 3.5f). As a result, plastic hinges form within the struts and the nodes undergo a rigid body rotation (so-called 'twist mode', see Tancogne-Dejean et al. (2016)). The pressure versus volumetric strain curves are monotonically increasing for 'stable' mesostructures, while it exhibits a more or less pronounced peak for 'unstable' mesostructures that respond through strut buckling. The stability of the mesostructure is not only a function of the relative density; it also depends on the strain hardening capacity of the base material. For example, at a relative density of $\bar{\rho} = 0.4$, the computed response of the SOT made from the HH material is still stable (Fig. 3.5d), while that made from the LH material is unstable (Fig. 3.5e).

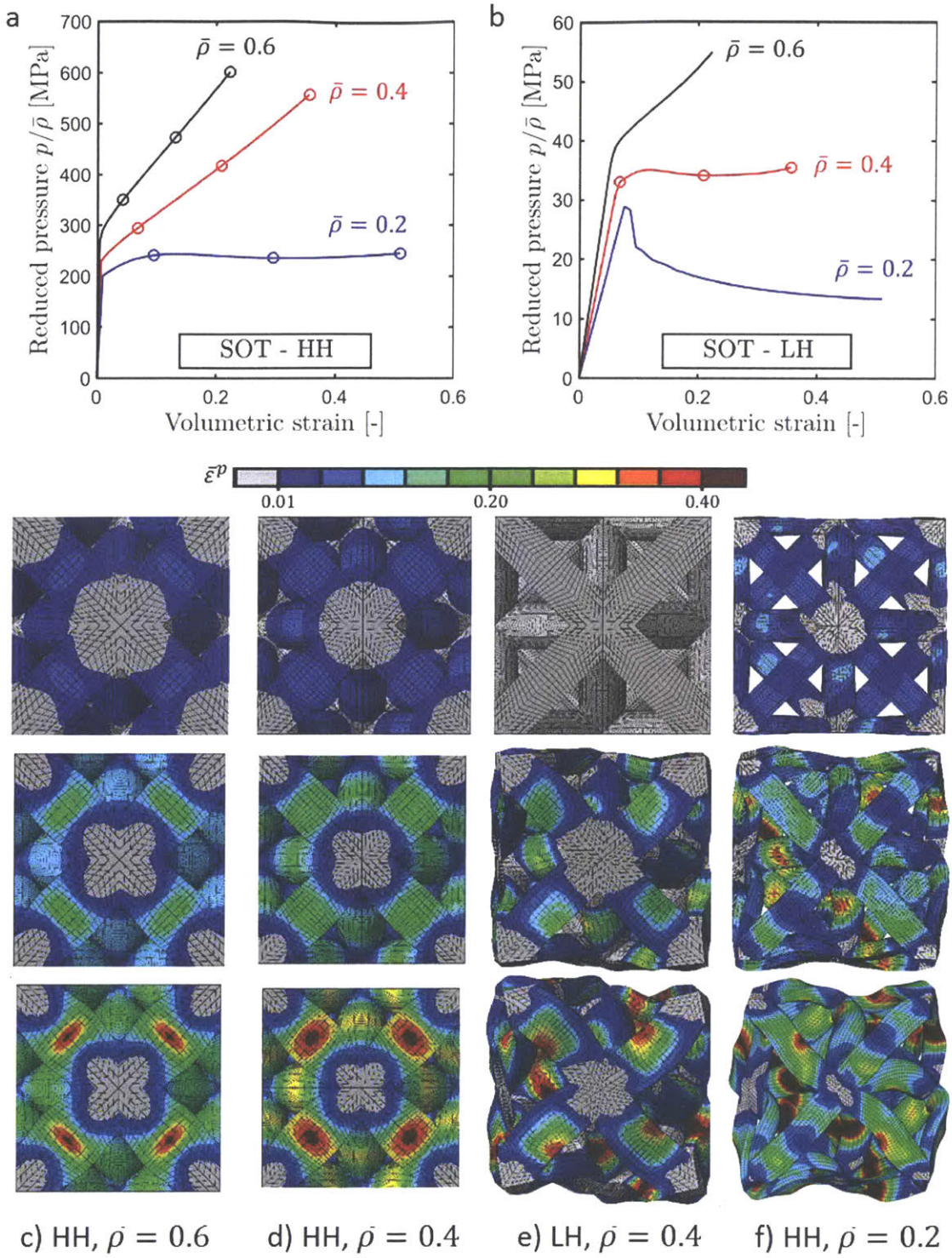

Figure 3.5: Solid Octet Truss (SOT) subject to hydrostatic compression: Stress-strain response for the (a) high, and (b) low strain hardening base material. (c)-(f) selected deformed configurations with equivalent plastic strain contour; the macroscopic stress and strain corresponding to each subplot have been highlighted by an open dot in (a) and (b).

- *Hollow Sphere Assembly (HSA)*: Figure 3.6 summarizes the simulation results for the HSA. All macroscopic pressure-strain curves exhibit a low and a high strain hardening phase. In the low hardening phase, the geometry of the mesostructure changes dramatically. The hollow spheres are progressively transformed into a hollow dodecahedron (Fig. 3.6f). In the two-dimensional section views shown in Figs. 3.6c to 3.6e, this mesostructural evolution corresponds to the transformation of a circular central pore to a square pore. The contact area between two neighboring spheres increases throughout this bending-dominated transformation. Once all spheres surfaces are in contact, the high hardening phase sets in. For the $\bar{\rho} = 0.2$ ($\bar{\rho} = 0.6$) structures, this change occurs at a volumetric strain of about 0.23 (0.11). As compared to the SOT material, the response of the HSA is initially much softer, but it quickly exceeds the macroscopic deformation resistance of the SOT as soon as the high hardening phase sets in.

- *Hollow Octet Truss (HOT) lattice*: As compared to the SOT, the strut cross sections of the HOT lattices have a significantly higher moment of inertia for the same relative density. As a result, we did not observe any buckling when subjecting the HOT unit cells to hydrostatic loading. The macroscopic pressure versus volumetric strain curves for all HOT lattices (high and low strain hardening base materials) are monotonically increasing for a relative density of $\bar{\rho} = 0.2$ (Figs. 3.7a and 3.7b). As opposed to the highly pressure-resistant solid nodes of the SOT, the hollow nodes of the HOT mesostructure are weak. Plastic deformation initiates early at the nodes. As a consequence, the macroscopic pressure resistance of the HOT material is even lower than that of the SOT material at small volumetric strains (Figs. 3.7a and 3.7b). However, due to its positive strain hardening at the macroscopic level, it can carry higher pressures than the unstable SOT lattice of the same weight at large strains.

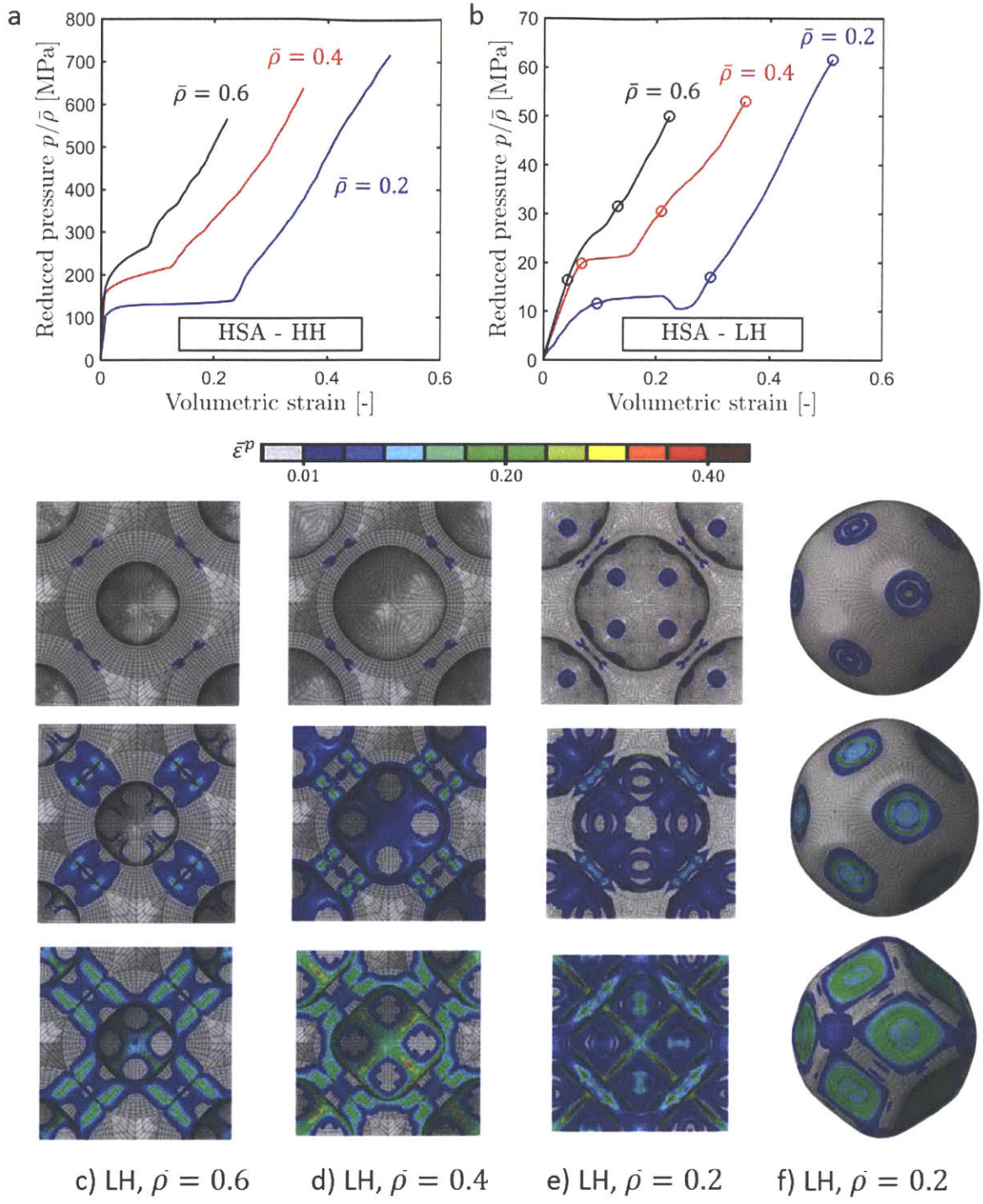

Figure 3.6: Hollow Sphere Assembly (HSA) subject to hydrostatic compression: Stress-strain response for the (a) high, and (b) low strain hardening base material. (c)-(f) selected deformed configurations with equivalent plastic strain contour; the macroscopic stress and strain corresponding to each subplot have been highlighted by an open dot in (a) and (b). (f) presents the view of an individual sphere.

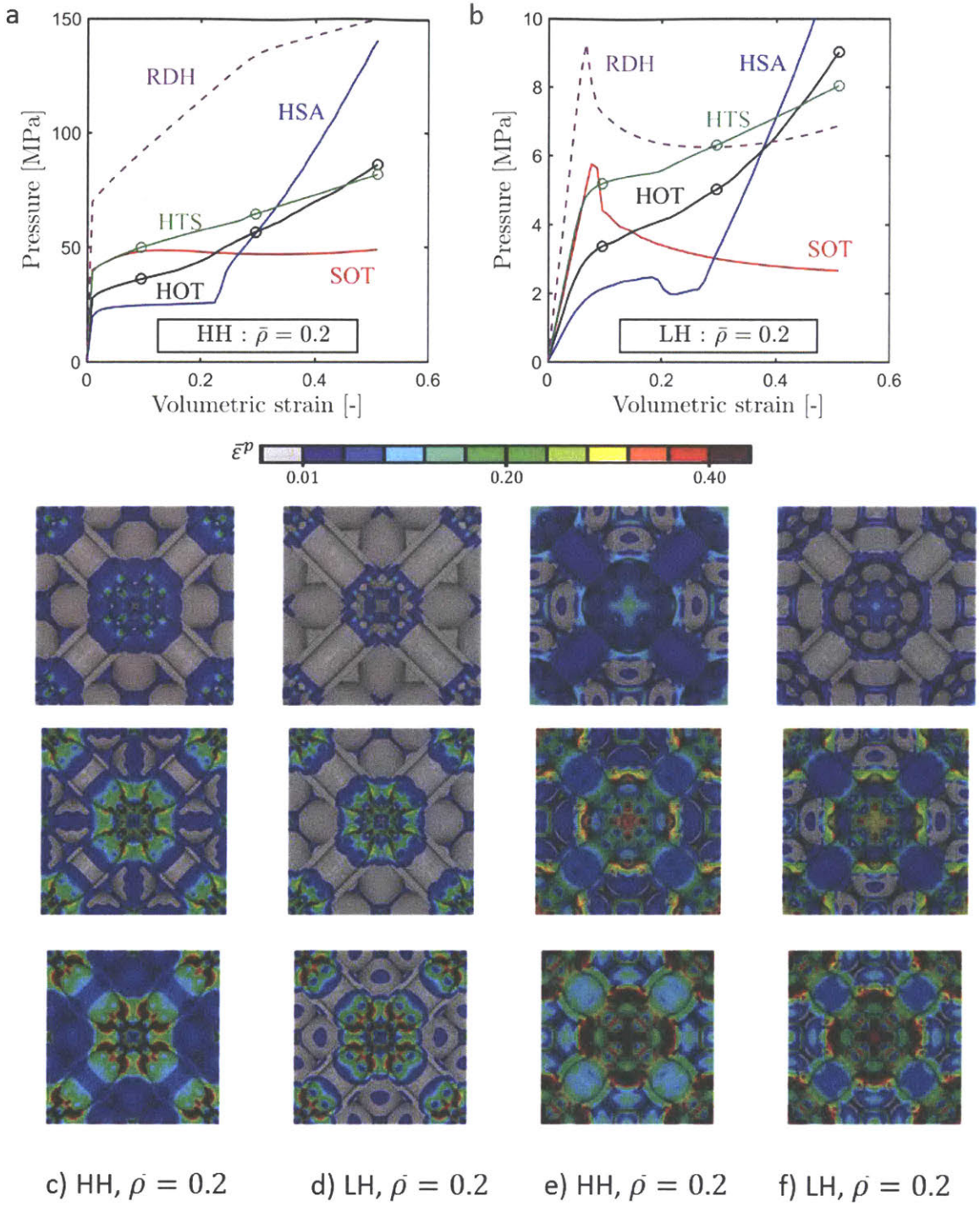

Figure 3.7: Metamaterials of 20% relative density subject to hydrostatic compression: Stress-strain responses for the (a) high, and (b) low strain hardening base materials. Selected deformed configurations with equivalent plastic strain contour for the (c)-(d) Hollow Octet Truss (HOT), and (e)-(f) Hybrid Truss-Sphere (HTS) assembly; the macroscopic stress and strain corresponding to each subplot have been highlighted by an open dot in (a) and (b).

- *Hybrid hollow Truss-Sphere Assembly (HTS)*: The HTS material architecture is very similar to that of the HOT material. The main modification is an increase of the size of the nodes, which leads to both an overall reduction in surface area (and corresponding increase in wall thickness) and a reduction of the angle sharpness. The former explains this structure's higher elastic properties (Fig. 3.4d), while the smoother node geometry reduces plastic strain concentration at the nodes, providing a significantly higher pressure resistance at small volumetric strains (for a same relative density of $\bar{\rho} = 0.2$). The large deformation response of the HTS mesostructure remains stable irrespective of the strain hardening capacity of the base material (Figs. 3.7e and 3.7f) which results in a monotonically increasing macroscopic pressure-strain response.

3.2.3.3 Large strain response to confined compression

The hydrostatic loading condition is special in the sense that the struts of octet trusses (SOT and HOT) are all subject to axial compression only. In other words, the mechanical loading includes the symmetries of the mesostructures. We therefore repeated our simulations for confined compression, i.e. a loading condition where the material is compressed along a first direction while the macroscopic deformation must be zero along the other two orthogonal directions. Despite the change in the loading condition, most of the previously reported deformation mechanisms for hydrostatic compression are also observed for confined compression. However, the following differences are worth noting:

- *Solid Octet Truss (SOT)*: for all relative densities and base materials considered, the nodes of the SOT deform elastically only and do not contribute to the plastic dissipation (Fig. 3.8). In the case of the high density structure ($\bar{\rho} = 0.6$), the sturdy struts are primarily sheared (Fig. 3.8c). For lower relative densities, the increased strut slenderness shifts the strut deformation mode from shear-dominated (Figs. 3.8c and 3.8d) to bending-dominated (Figs. 3.8e and 3.8f). Due to the evolution of the mesostructural geometry (strut rotation with respect to the loading direction), the overall load carrying capacity is reduced. Base material strain hardening can partially compensate for this

geometric softening. The HH-SOT therefore still exhibits macroscopically positive strain hardening, while the LH-SOT material is already at the limit to macroscopic softening. The latter is observed for both base materials at a relative density of $\bar{\rho} = 0.2$. The LH-SOT responds in a twist-mode, while the bending deformation localizes in one half of the unit cell for the HH-SOT.

- *Hollow Sphere Assembly (HSA)*: As for the hydrostatic loading, the macroscopic stress-strain response of the HSA material is characterized through two positive hardening phases that are related to the initial growth of contact area between neighboring spheres (Figs. 3.9a and 3.9b). As illustrated in Fig. 3.9e, the shape of the spheres still transforms towards a dodecahedron, but with non-congruent faces due to the deviatoric loading. The plastic deformation is highly localized in the vicinity of the joints between spheres.
- *Hollow Octet Truss (HOT)*: The high second moment of the hollow cross-sections is also advantageous under confined compression, while the hollow nodes are flattened (Figs. 3.10c and 3.10d). At the macroscopic level, all HOT structures exhibit a positive strain hardening response (Figs. 3.10a and 3.10b).
- *Hybrid Truss-Sphere Assembly (HTS)*: Its deformation response is very similar to that of the HOT material except that the flattening of the nodes is less pronounced while the node walls respond by bending (Figs. 3.10e and 3.10f). At the macroscopic level, the HTS exhibits positive strain hardening for all densities and base materials considered. It is also the strongest up to an axial strain of about -0.2, beyond which the HOT reaches similar strength, while the hardened HSA material surpasses both for axial compressive strains greater than about 0.3.

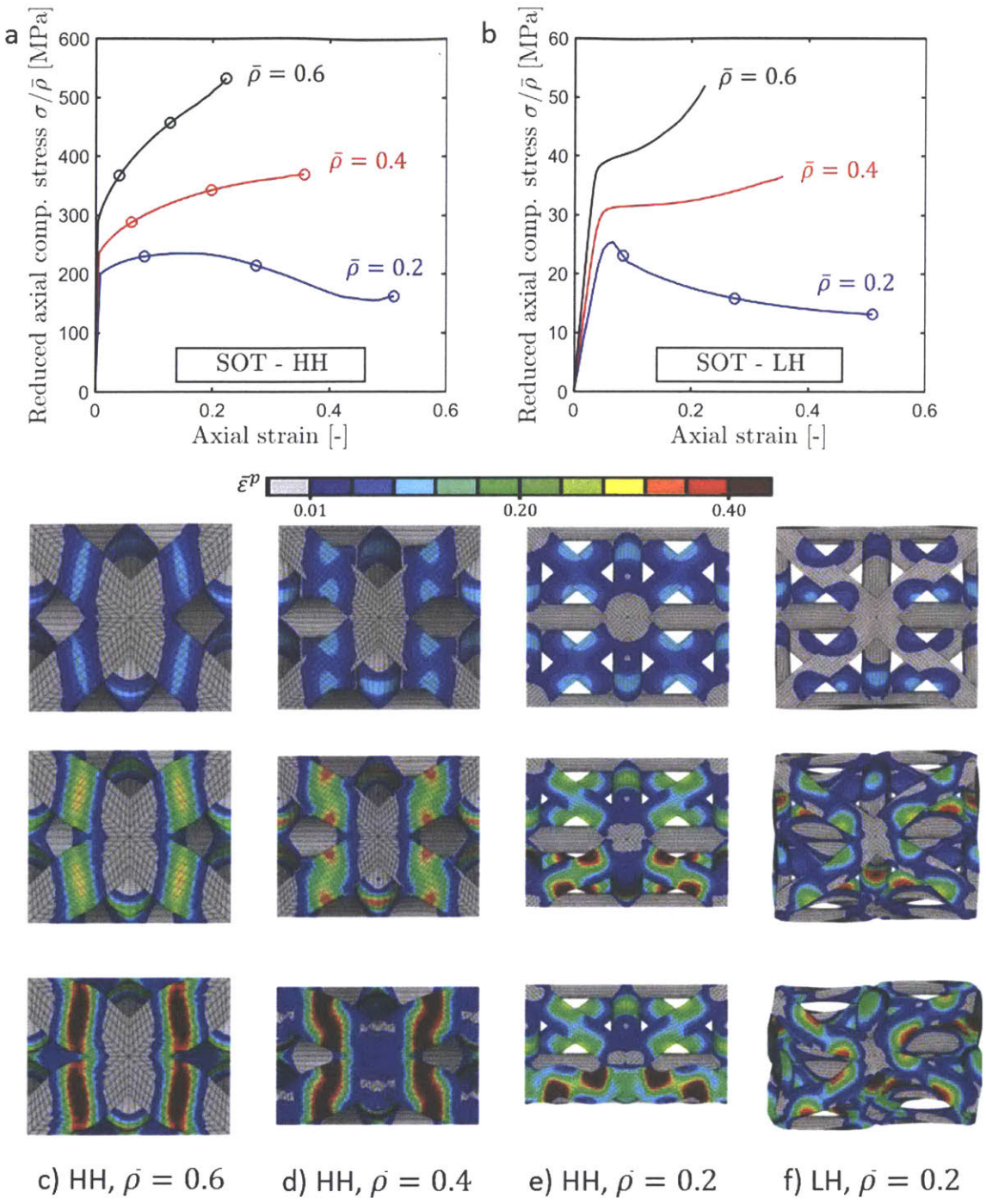

Figure 3.8: Solid Octet Truss (SOT) subject to confined compression: Stress-strain response for the (a) high, and (b) low strain hardening base material. (c)-(f) selected deformed configurations with equivalent plastic strain contour; the macroscopic stress and strain corresponding to each subplot have been highlighted by an open dot in (a) and (b).

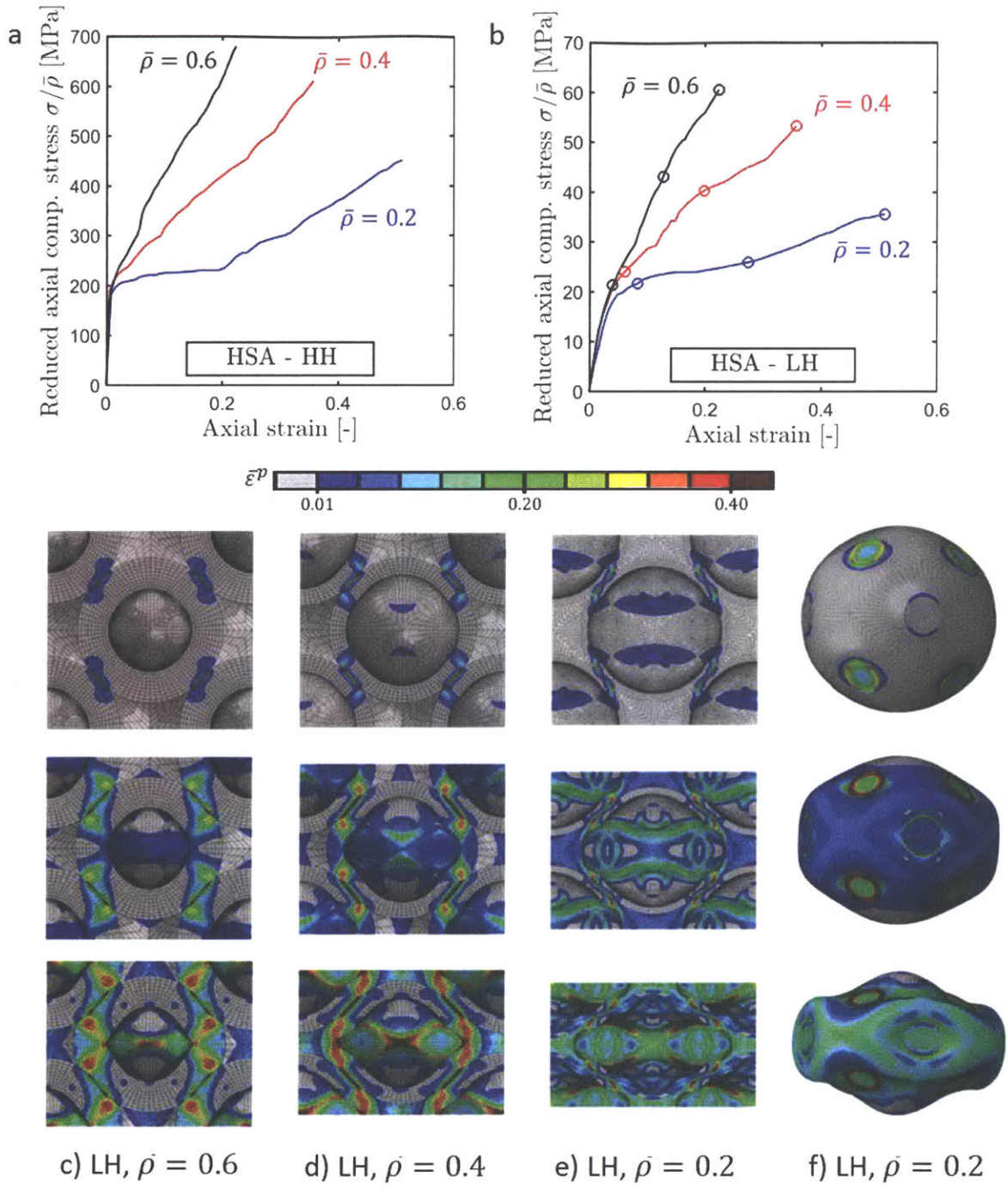

Figure 3.9: Hollow Sphere Assembly (HSA) subject to confined compression: Stress-strain response for the (a) high, and (b) low strain hardening base material. (c)-(f) selected deformed configurations with equivalent plastic strain contour; the macroscopic stress and strain corresponding to each subplot have been highlighted by an open dot in (a) and (b). (f) presents the view of an individual sphere.

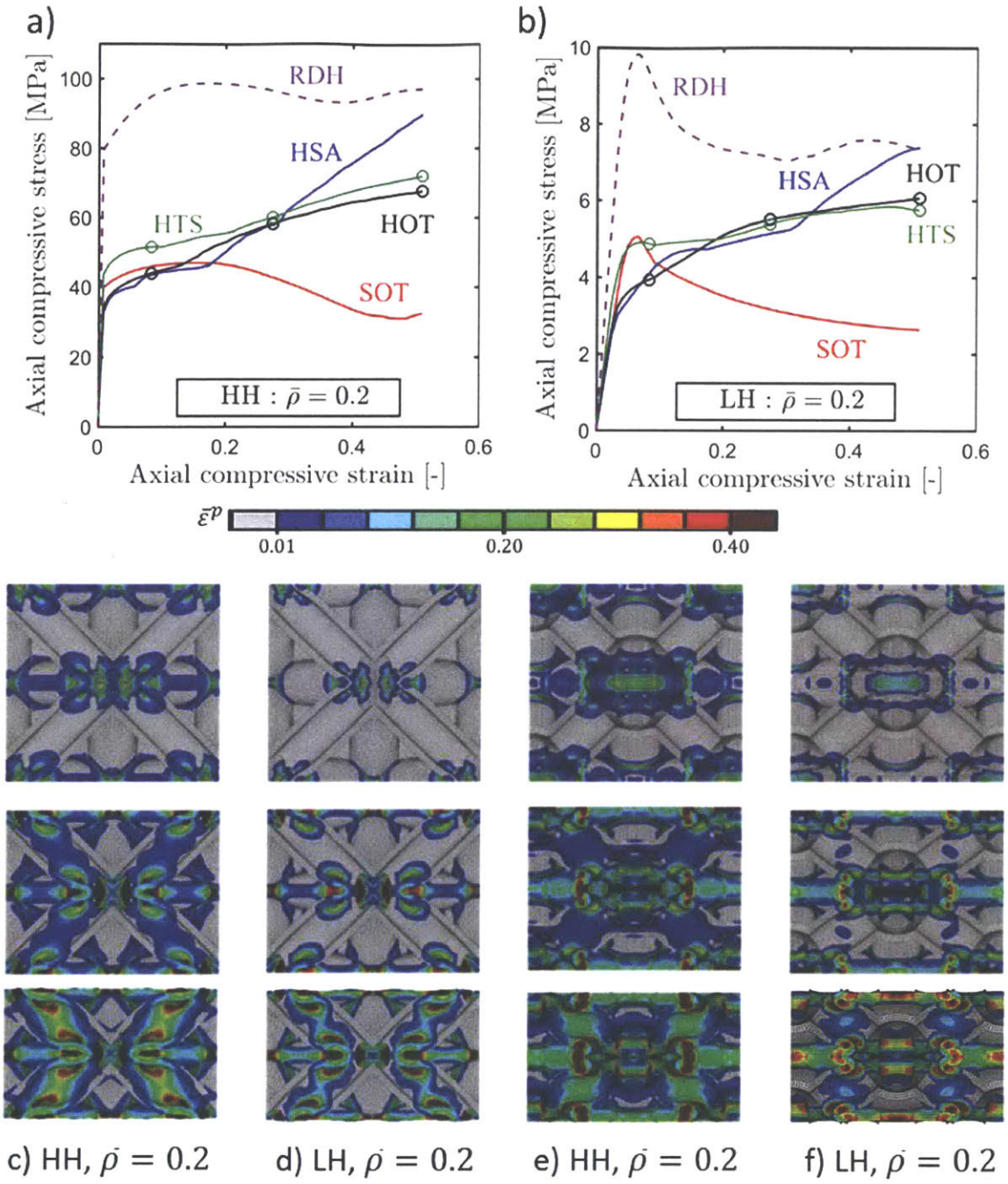

Figure 3.10: Metamaterials of 20% relative density subject to confined compression: Stress-strain responses for the (a) high, and (b) low strain hardening base materials. Selected deformed configurations with equivalent plastic strain contour for the (c)-(d) Hollow Octet Truss (HOT), and (e)-(f) Hybrid Truss-Sphere (HTS) assembly; the macroscopic stress and strain corresponding to each subplot have been highlighted by an open dot in (a) and (b).

3.2.3.4 Large strain response to uniaxial compression

The uniaxial compression simulations are performed to estimate the specific energy absorption capacity of the porous materials. To account for possible far field buckling instabilities, these simulations are performed using cubic virtual specimens composed of $3\times3\times3$ unit cells (close to limit of computational feasibility). Figure 3.11 summarizes the results for uniaxial compression for all materials. The results are reported in terms of the average axial engineering stress and strain. Except for the SOT materials, all other materials exhibit a monotonically increasing engineering stress-strain response under uniaxial compression. Due to the possible lack of macroscopic homogeneity of the deformation fields in the compression specimens, the reported axial strains must be interpreted as average strains or normalized axial displacements.

The oscillations in the stress-strain curve for the SOT material are characteristic for cellular materials such as metallic foams that exhibit true strain softening followed by important hardening during densification. The instability related to the force peak causes the localization of deformation in narrow bands. The width of the localization bands equates to the height of a single unit cell. The equivalent plastic strain contour plots extracted from simulations confirm this mesostructural deformation mechanism (Fig. 3.11c). The other mesostructures remain stable under uniaxial compression. The deformation is therefore uniformly distributed at the macroscopic level. For example, the contour plot of the equivalent plastic strain for the HOT material (Fig. 3.11d) is periodic at the mesoscopic level which corresponds to a homogeneous field at the macroscopic level. The advantage of the HTS over the HOT at small strains is less pronounced under uniaxial compression than for hydrostatic compression. For the HH material at 5% engineering strain, the HTS macroscopic deformation resistance is only 15% higher than that of the HOT (20% for LH, Fig. 3.11), against 20% (30% for LH) for confined compression (Fig. 3.10a) and 40% (60% for LH) for hydrostatic compression.

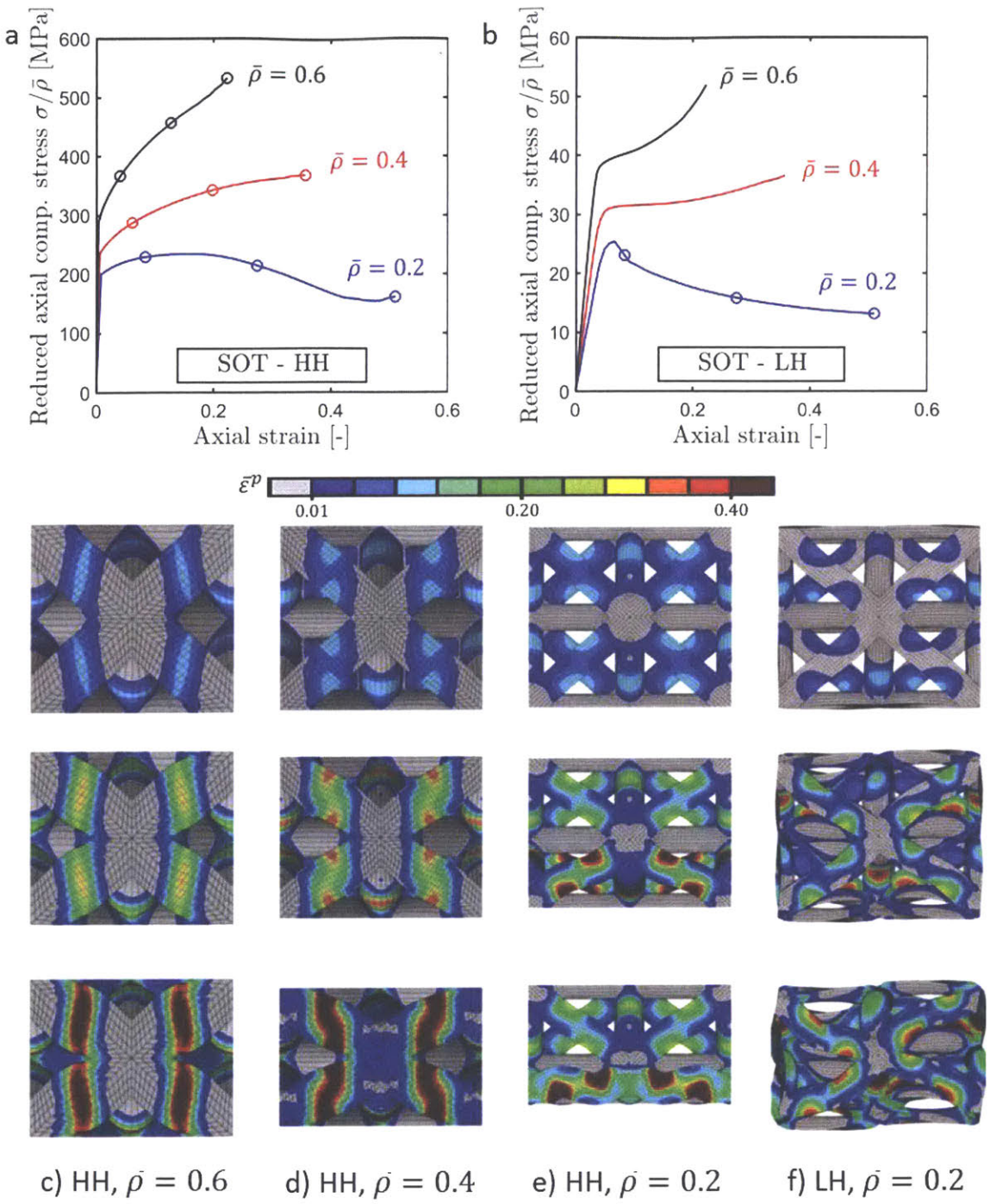

Figure 3.8: Solid Octet Truss (SOT) subject to confined compression: Stress-strain response for the (a) high, and (b) low strain hardening base material. (c)-(f) selected deformed configurations with equivalent plastic strain contour; the macroscopic stress and strain corresponding to each subplot have been highlighted by an open dot in (a) and (b).

The specific energy absorption is defined as the ratio of the mechanical work performed under uniaxial compression up to an engineering strain of -0.5 and the mass,

$$\Psi = \frac{1}{\rho}\int_0^{0.5} \sigma d\varepsilon$$

We find $\Psi_{HH} = 10.6, 14.5, 15.1,$ and 16.3 J / g for the SOT, HSA, HOT and HTS materials made from the high strain hardening steel alloy. For the low strain hardening polymer, the corresponding values are $\Psi_{LH} = 6.15, 8.8, 9.5,$ and 9.3 J / g for the respective meta-materials.

3.3.Experiments

The main purpose of the experiments is to support the conclusions drawn from our computational study. Instead of using experiments as a primary means to investigate the deformation response of additively-manufactured metamaterials, the experiments are just performed here to validate the main qualitative features.

3.3.1 Specimens

Cubic compression specimens are manufactured for all four material architectures for a target relative density of $\bar{\rho} = 0.2$. All cubic specimens are composed of $5 \times 5 \times 5$ unit cells. The specimen edge length is $47.1mm$ which corresponds to a unit cell edge length of $9.43mm$, and an inter-nodal distance of $6.67mm$. Characteristic geometric features of the meso-structures are as follows:

- strut diameter $D = 1.3mm$ for the SOT material,
- sphere wall thickness $t = 340\mu m$ for the HSA material,
- outer and inner strut diameters $D = 2.17mm$ and $d = 1.53mm$ for the HOT material (i.e. a wall thickness of $t = 320\mu m$),
- wall thickness $t = 350\mu m$, sphere outer diameter $5.15mm$, and an outer strut diameter of $D = 2.39\ mm$ for the HTS material.

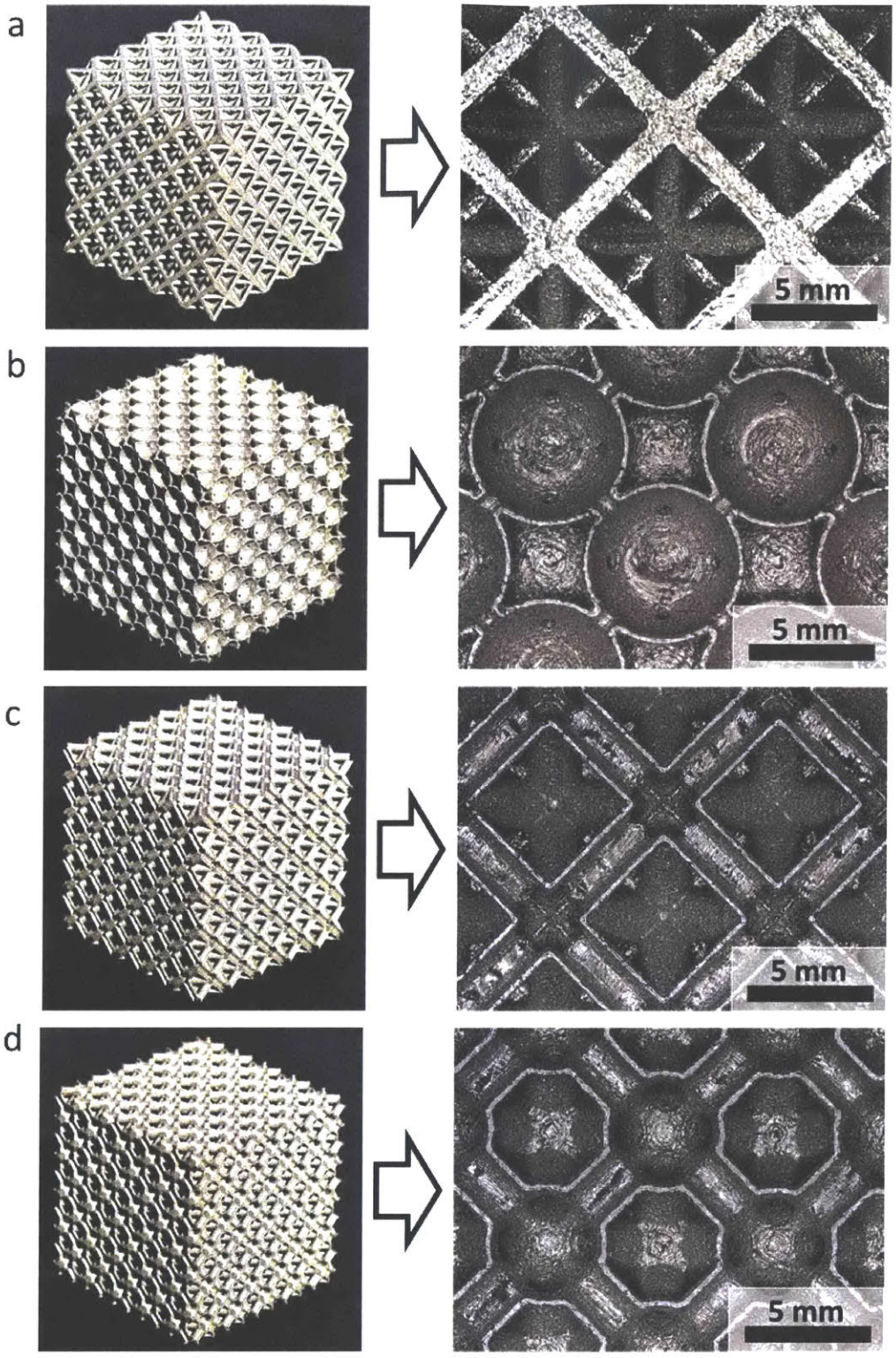

Figure 3.12: Stainless steel compression specimens comprised of 5x5x5 unit cells fabricated through selective laser melting: (a) solid octet truss, (b) hybrid sphere assembly, (c) hollow octet truss, and (d) hybrid truss sphere assembly.

The specimens tested are made from stainless steel 316L using Selective Laser Melting. All specimens except for the SOT are built with layers parallel to two of the cube faces. After manufacturing, all specimens are cleaned in an ultra-sound bath. Figure 3.12 provides a 3D view of representative specimens along with detailed side views of the respective unit cells.

Even though the overall linear specimen dimensions are met with an uncertainty of less than 0.2%, we observe systematic deviations in the specimen weight. The measured relative density of the SOT specimens is only 0.19, while it is 0.21 for all other specimens. The slightly higher weight of the specimens with two distinct porous phases is tentatively attributed to a combination of residual non-molten powder within the structure, and additional material attached to the overhanging, down-facing surfaces of the structures. The powder bed supports the structure during its layer-by-layer build-up. Inevitably some of the supporting powder is partially molten. As a result, we observe residual powder at downward facing cell walls (Figs. 3.13a and 3.13b), while no traces of partially molten powder are seen on upward facing walls (Fig. 3.13c). To facilitate the interpretation of the traces seen on the photographs (Figs. 3.13a-3.13c), the corresponding depths profiles are provided in the subsequent row of figures (Figs. 3.13d-3.13f). In the side view (Fig. 3.13b), the residual powder is only seen on the downward facing walls. Traces of some excess powder in the HTS structure are shown in Fig. 3.13g. We also observed some strut diameter variations in the SOT structure (Fig. 3.13h) and hollow struts of the HOT structure that are obstructed by excess powder (Fig. 3.13i), while in some cases some thin-walls collapsed (Fig. 3.13c).

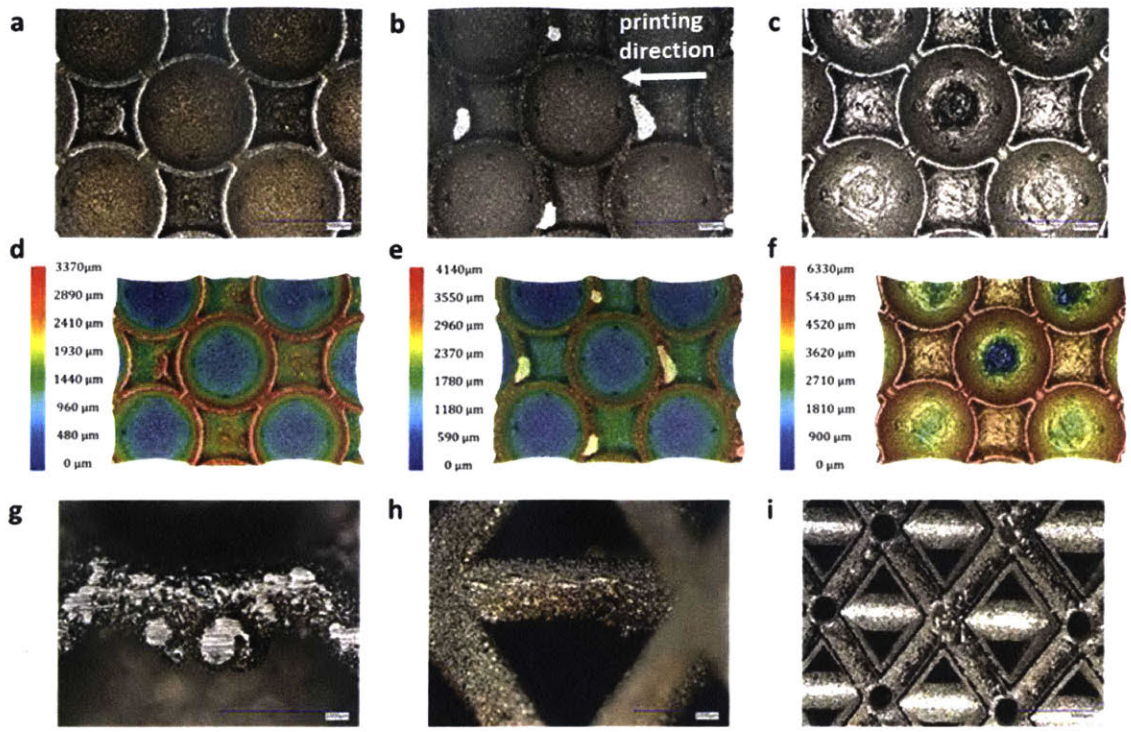

Figure 3.13: Printing defects on SLM-produced specimens. a-c) Surface finish and defects on HSA structure on a) bottom face b) side face c) top face. d-f) Surface defects with elevation measurements on HSA structure on d) bottom face e) side face f) bottom face. g) Detail of excess molten powder on an overhanging, down-facing surface of the HTS structure. h) Detail of uneven cross-section on a strut of the SOT structure. i) Angled view of the top face of the HOT structure: evidence of some obstructed channels.

3.3.2 Experimental procedures

3.3.2.1 Young's modulus measurements

A series of non-destructive compression experiments is performed to measure the effective Young's moduli of the metamaterials. Given that the wave propagation response of the present metamaterials is not known yet, we take a conventional static testing approach instead of measuring wave propagation speeds to deduce the Young's modulus. The specimen is placed between two polished steel platens of a hydraulic universal testing machine (Model 8800, Instron, USA). It is subsequently pre-loaded up to an axial stress of about 9MPa to ensure good contact between the specimen and the loading platens. A sinusoidal force loading history of a frequency of $0.1Hz$ is then applied with an axial stress amplitude of $\pm 6MPa$. Two cameras are employed to monitor the deformation of two

opposing specimen sides (front and back sides). The corresponding strain response is then measured using virtual extensometers. As illustrated in Fig. 3.14a, the virtual extensometers are positioned around the central row of unit cells, where the possibly confining effect due to the friction at the specimen boundaries is the lowest. The weighted average of all virtual extensometers is reported as the axial strain, thereby reducing experimental uncertainty related to the non-parallelism of the top and bottom loading platens. The camera system took images at a framerate of $5Hz$ with 1500 pixels along the vertical frame direction. With the cameras (2448x2048 pixels, Model GS3-U3-51S5M, PointGrey) positioned at a distance of about$0.45m$, the size of one pixel is 30 μm. This corresponds to 300 pixels along one unit cell length. For a stress increment of 12MPa, we expect a relative displacement of at least $9.43mm \times 12 \,/\, 0.2 \times 200000 \approx 2.8\mu m$, i.e. about 0.1 pixels which is still in the range of the subpixel resolution of the VIC2D algorithm. To approach the optimal measurement accuracy of the DIC code, a speckle pattern with an average black speckle size of about 60 μm is applied. Preliminary experiments using an optical microscope (mounted horizontally at a distance of less than $25mm$) were not successful due to significant artificial strains related to the out-of-plane displacements (due to the Poisson's effect).

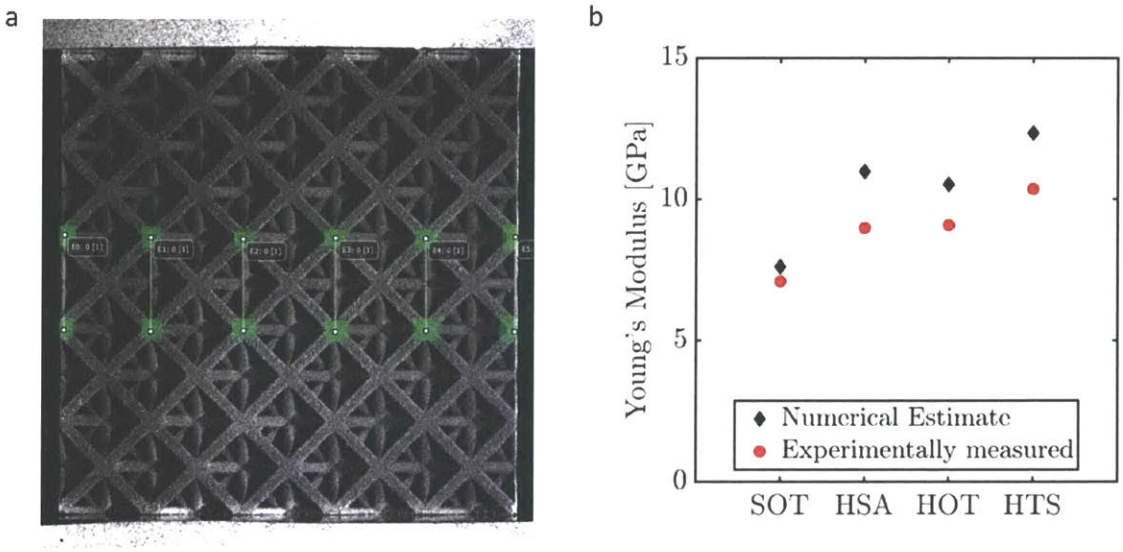

Figure 3.14: Results of experimental measurement of Young's modulus. (a) Face-view of a SOT specimen with virtual extensometers. (b) Comparison of numerical estimates and experimentally measured values of Young's modulus for the four metamaterials considered.

3.3.2.2 Large deformation response

The compression experiments are performed on a screw-driven universal testing machine (Model RME250, Zwick) equipped with two flat loading platens and a 250kN load cell. No grease or lubricant are applied to the polished steel platens. Two high resolution digital cameras (2448x2048 pixels, Model GS3-U3-51S5M, PointGrey) equipped with lenses (Model AF-X M100 Pro D, Tokina) are employed to monitor two orthogonal specimen surfaces at a spatial resolution of about $30\mu m\ /\ pixel$. A constant crosshead velocity of $6mm$ / pixel is applied (which equates to a constant engineering strain rate of about $2.1 \times 10^{-3}\ /\ s$ for specimens with homogeneous macroscopic strain fields). Different from the simulations which were all stopped at a strain of -0.6, we continued the experiments until the maximum machine loading capacity of $250kN$ had been reached. Average engineering stresses are obtained from the force measurements, while average engineering strains are deduced from the top platen displacement measurement after correction for a machine stiffness of $100kN/mm$.

The main purpose of the optical system is to monitor the deformation mode, but we also make use of the natural contrast in the images to estimate surface strains through planar Digital Image Correlation (DIC) with the software VIC2D (Correlated Solutions). Given the depth to the monitored surfaces, only the points located on the closest surface (on the foreground) are extracted and used for DIC. In the DIC algorithm, Gaussian weights are used over a window of 13 pixels in size and one measure every 5 pixels. Strains are calculated using Gaussian derivative estimators of size 5. In all experimental figures, we show the effective surface strain. Contour bars are omitted as the sole purpose of the DIC results is to highlight regions of severe plastic deformation. Higher quality images and 3D correlation would be needed to draw quantitative conclusions from the DIC in the large deformation experiments.

3.3.3 Experimental results

3.3.3.1 Elastic response

After determining the strain history from the vertical extensometers, we verified that it has the same frequency as the applied stress history. Furthermore, the applied stress and measured strain histories are found to be in phase, i.e. possible viscous effects are negligible at a frequency of $0.1Hz$. In other words, we may use the relation

$$E = \frac{d\sigma}{d\varepsilon}$$

to determine the Young's modulus. Due to the noise observed on the strain measurements, sinusoidal signals are fitted onto both force and strain signals. The obtained moduli for the four meta-materials are depicted as red solid dots in Fig. 3.14b. The SOT material exhibited with $7.1GPa$ the lowest modulus. The measured moduli of the HSA and HOT materials are about $9GPa$, while the highest modulus of $10.4GPa$ is observed for the Hybrid Truss-Sphere (HTS) structure. Experiments were performed on one specimen per mesostructure only.

3.3.3.2 Large deformation response

Figures 3.15 to 3.18 summarize the engineering stress-strain curves obtained from uniaxial compression experiments on all four metamaterials at a relative density of 0.2. These figures also include the photographs (with superposed surface strain fields) that show the front and side view of the specimens at different stages of loading. For each of the four geometries, two tests are performed to verify the repeatability of the reported experimental results. The main experimental observations are:

- For the SOT material, an oscillating stress-strain response is observed at the macroscopic level (see red and blue solid curves in Fig. 3.15). After deforming in a linear-elastic manner up to a stress of about $20MPa$, the stress-strain curve becomes non-linear, reaching a first peak in stress at about $35MPa$. The deformation fields are still macroscopically uniform at this point, i.e. the surface strain variations are in phase with the periodicity of the mesostructure. After reaching a first peak in stress, a diagonal localization band forms of the width of approximately one unit cell (stage ①, Fig. 3.15). A minimum stress of $21MPa$ is reached at an engineering strain of about 0.17. A second peak of $33MPa$ is then

observed at a strain of about 0.22. Thereafter, a second localization band becomes apparent (stage ②, Fig. 3.15). After the second peak, the stress-strain curve exhibits shallow oscillations in stress prior to the densification at a strain of 0.6.

- The first two localization bands in the SOT material are not adjacent to each other. Instead they seem to have formed independently, triggered by imperfections at the top and bottom boundaries, respectively (stages ① and ②, Fig. 3.15). They are also not flat. On the front plane, they are composed of segments that are either aligned with the (1,1,1) or the (1,0,0) directions of the FCC structure. After the formation of the first two bands of localization, the truss structure is progressively crushed, i.e. the zones of localization broaden through the collapse of the cells that are located at the interface towards the regions of intact mesostructure (stage ③).
- During crushing, the mesoscopic deformation mode is clearly bending-dominated. In the struts within the interface zones between crushed and intact regions, plastic hinges form near the nodes. The latter are supported by the struts in the intact regions in a way that their rotation is prevented.
- The experimentally-measured macroscopic engineering stress-strain curve for the HOT material (Fig. 3.16) is monotonically increasing. The surface strain fields preserve the periodicity of the mesostructure at all stages of deformation, with no localization visible at the macroscopic level. The only feature that is reminiscent of a cellular solid is the steep increase in hardening rate due to densification, at an engineering strain of about 0.5. The deformed configurations of the HOT material show the change of the unit-cell geometry, which involves the rotation of the struts and the flattening of the nodes.
- The response of the HTS assembly (Fig. 3.17) is very similar to that of the HOT material, i.e. the macroscopic stress-strain response is monotonically increasing and the deformation fields respect the periodicity of the mesostructure. Mesoscopic features of the deformation response include a concentration of plastic deformation at the spherical nodes (see green zones at stage ① in Fig. 3.17) which are compacted by folding.
- The macroscopic stress-strain response of the HSA (Fig. 3.18) is also monotonically increasing. However, the specimen responds in a global shear

mode. This can be clearly seen in the side views of the deformed configurations in Fig. 3.18. Due to the shearing, the normal stress distributions along the specimen boundaries also become non-uniform at the macroscopic level. For example, the compressive stress at the bottom left corner of the specimen (in the side views) is expected to be higher than the normal stress at the top left corner. As a result, the surface strain fields in the front view are graded, with the largest compressive strains near the bottom platen. This gradient effect is potentially amplified in the surface strain field due to artificial strains related to the change in camera to surface distance during shearing.

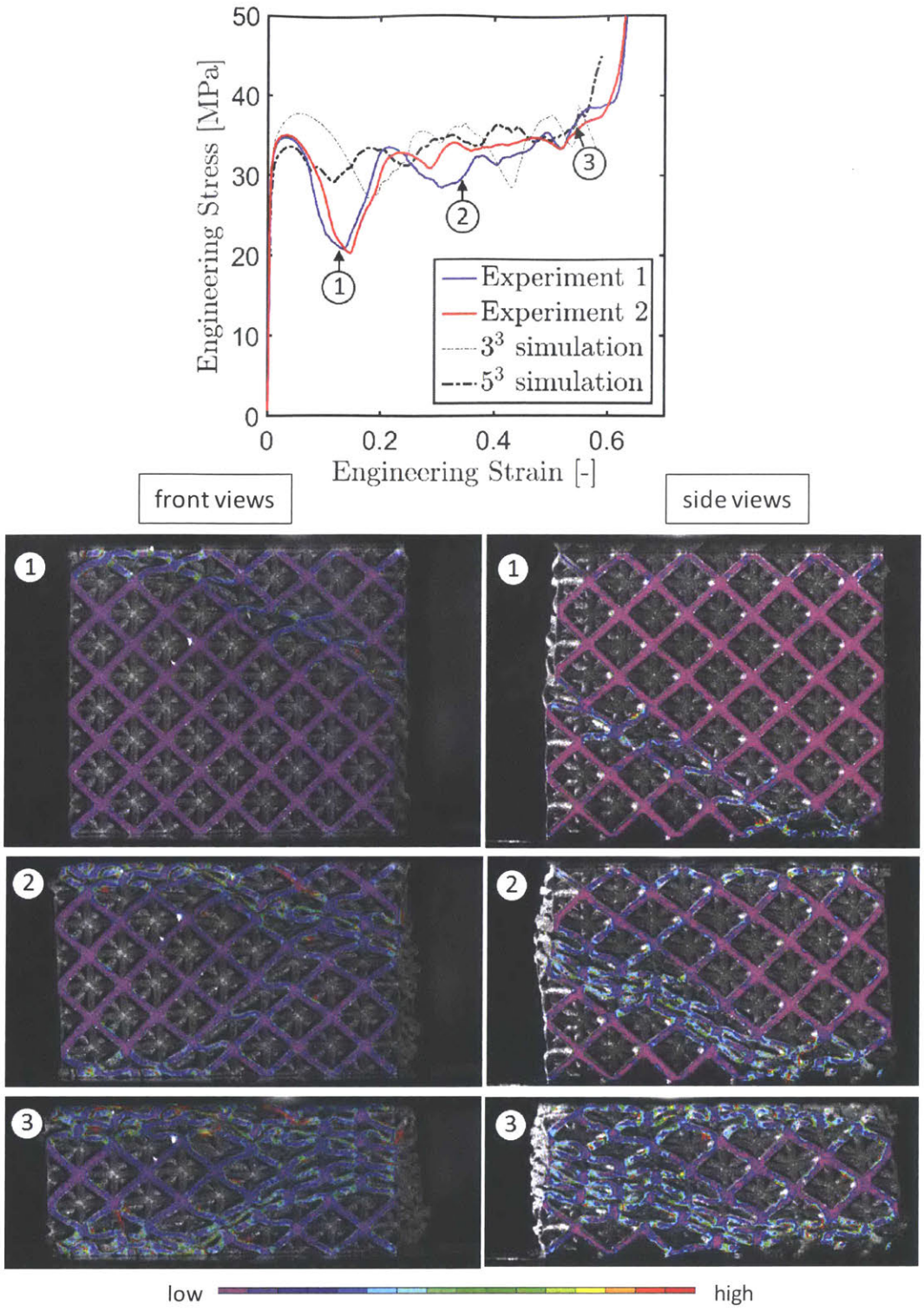

Figure 3.15: Uniaxial compression response of SOT specimens: Engineering stress-strain curve as obtained from experiments (red and blue solid curves) and numerical simulations (dashed lines). The photographs in the left column show the front view of the deforming specimen. The corresponding side views are shown in the right column. The color indicates the deformation intensity as obtained from planar DIC.

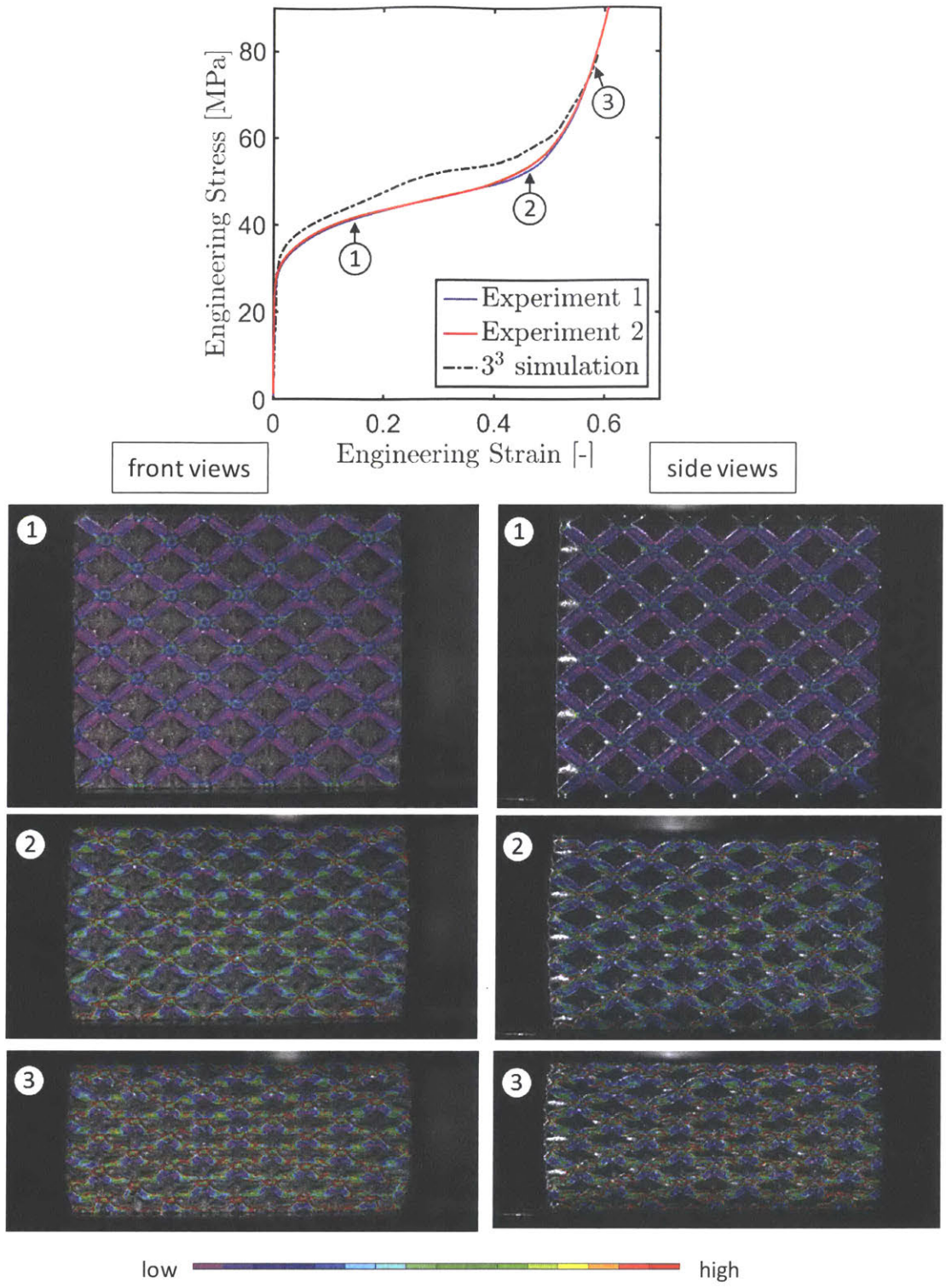

Figure 3.16: Uniaxial compression response of HOT specimens: Engineering stress-strain curve as obtained from experiments (red and blue solid curves) and numerical simulations (dashed line). The photographs in the left column show the front view of the deforming specimen. The corresponding side views are shown in the right column. The color indicates the deformation intensity as obtained from planar DIC.

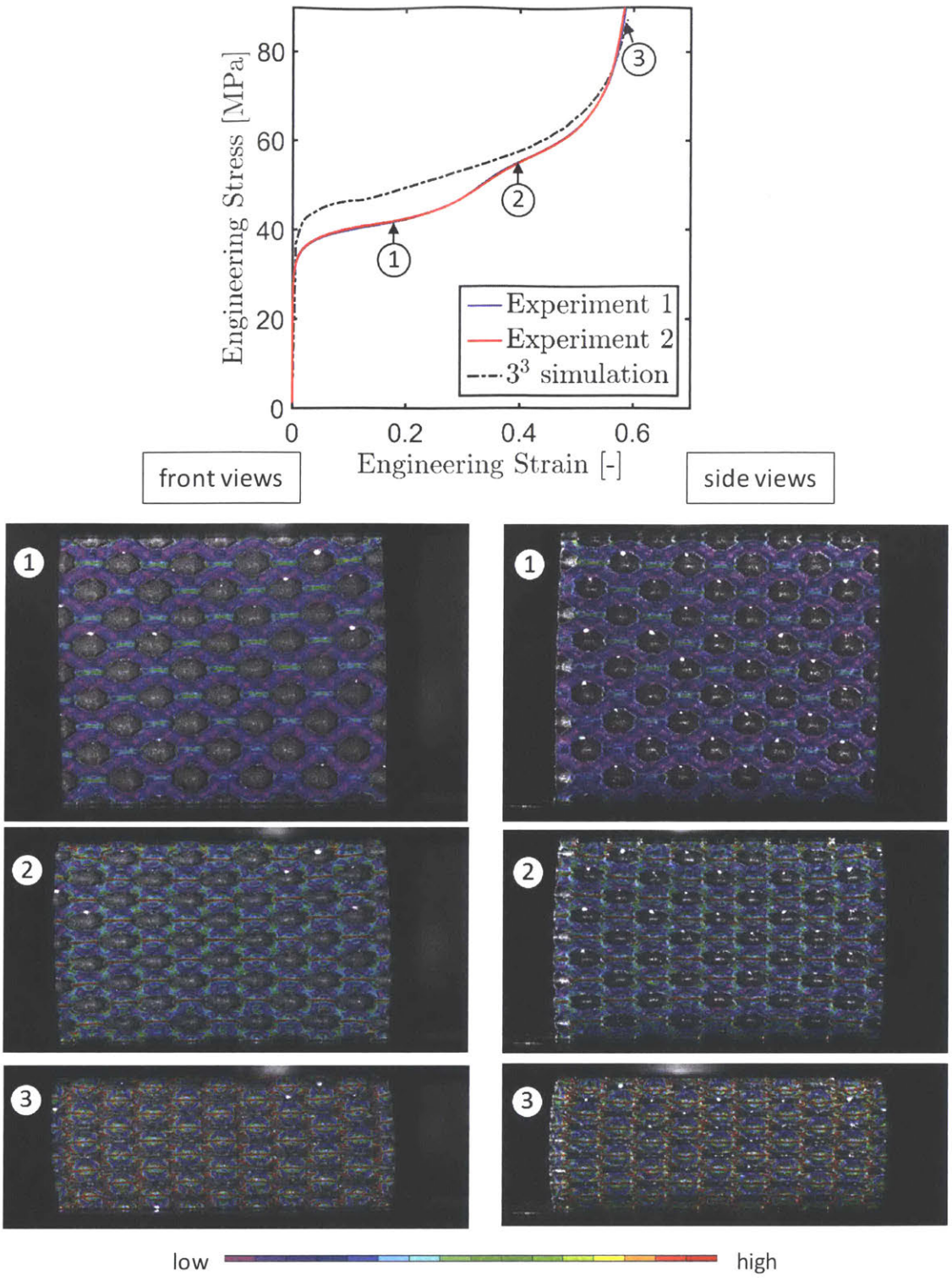

Figure 3.17: Uniaxial compression response of HTS specimens: Engineering stress-strain curve as obtained from experiments (red and blue solid curves) and numerical simulations (dashed line). The photographs in the left column show the front view of the deforming specimen. The corresponding side views are shown in the right column. The color indicates the deformation intensity as obtained from planar DIC.

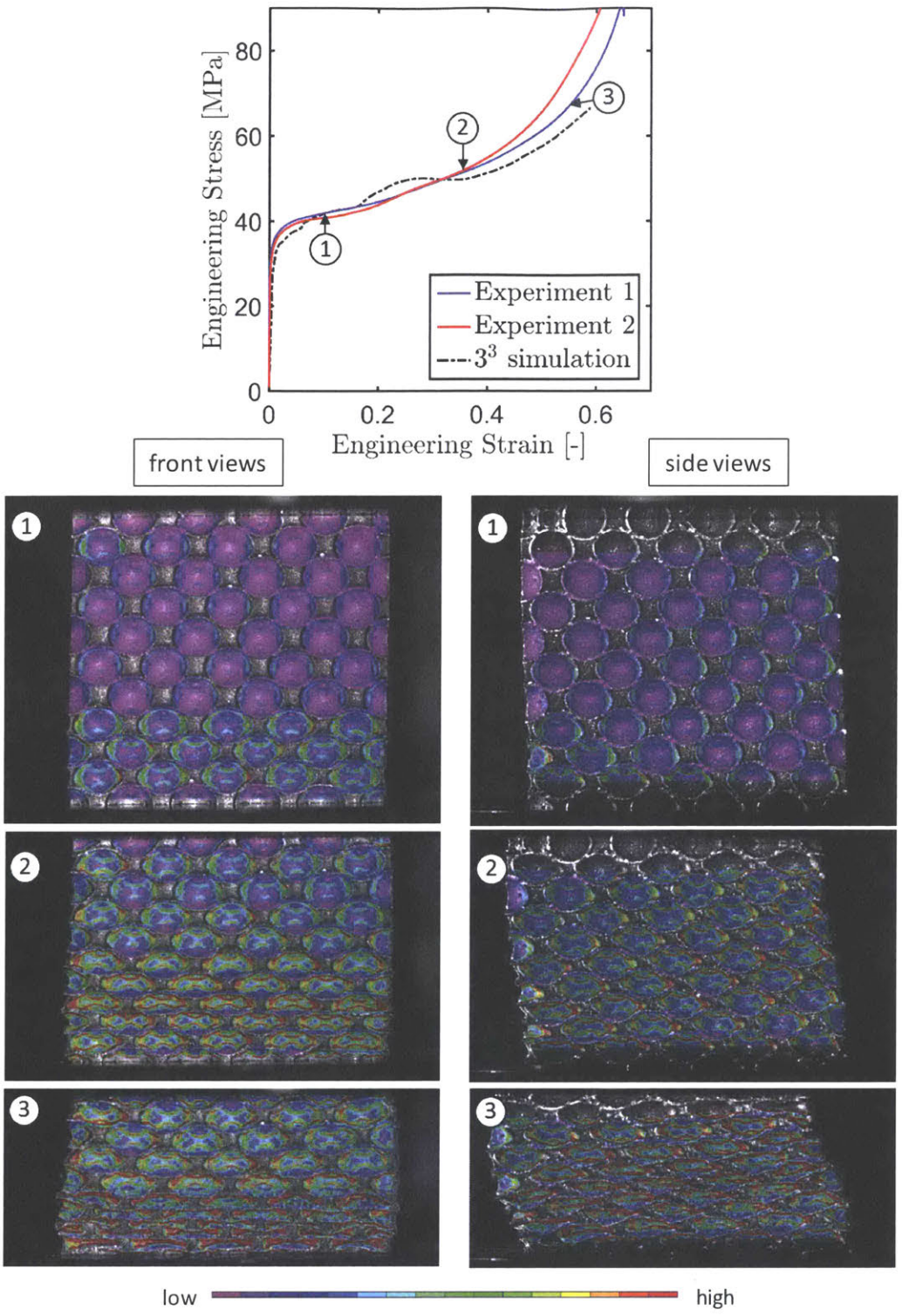

Figure 3.18: Uniaxial compression response of HSA specimens: Engineering stress-strain curve as obtained from experiments (red and blue solid curves) and numerical simulations (dashed line). The photographs in the left column show the front view of the deforming specimen. The corresponding side views are shown in the right column. The color indicates the deformation intensity as obtained from planar DIC.

3.3.4 Comparison of experiments with simulations

Figure 3.14b shows the comparison of the Young's modulus estimates obtained from experiments and finite element simulations. The experimental results are systematically lower than the simulation results, with a maximum difference of 18% for the HSA structure. However, the same trends are observed in the experiments and simulations, with the SOT and HTS structures being the softest and the stiffest, respectively.

For large deformations, the experiments confirm the main qualitative conclusions drawn from our computational study. In both the simulations and experiments, the deformation in the SOT structures localizes at the macroscopic level when subject to uniaxial compression, while all other structures exhibit a macroscopically homogeneous deformation mode. Differences are the 3D nature of the crushed regions (localization bands) in the SOT experiments (Fig. 3.15) which reduce to a planar band of growing width in the simulations (Fig. 3.11c). Boundary imperfections clearly affected the formation of the first two localization bands in the experiments. Larger specimens would be needed to reduce the effect of boundary imperfections on the crushing of the SOT structure. Different from the simulations (Fig. 3.11f), the HSA structure goes into a shear mode in the experiments which is also attributed to imperfections. It is striking in both the simulation and experimental results that the deformation fields in the HOT and HTS structures follow the periodicity of the mesostructure at all stages of deformation. The comparison of the surface deformation fields (e.g. compare Fig. 3.11d with configuration ② in Fig. 3.16 for the HOT structure, and Fig. 3.11e with the configuration ② in Fig. 3.17) shows qualitative agreement of the simulations and experiments with regards to the strain concentration patterns at the mesoscopic level. It is also worth noting that the macroscopic stress-strain curves lie perfectly on top of each other for repeat experiments.

The experimentally-measured stress-strain curves (colored solid curves) also agree reasonably well with the numerical predictions (dashed back curves). The quantitative agreement is surprisingly good given that the hardening response of the base material had just been estimated based on rudimentary material data provided by the manufacturer. The simulations systematically overestimate the stress level for the HOT and HTS configurations by up to 12% (see Figs. 3.16 and 3.17). Even smaller differences are

observed for the HSA (Fig. 3.18), where the simulation curve meanders around the measured stress-strain curves. Aside from the uncertainty in the base material behavior, quantitative differences are due to the assumption of a spatially-uniform base material property distribution, the absence of imperfections in the simulations, and the difference in the size of the compression specimens. Recall that the simulation models included only 3x3x3=27 unit cells while the experiments comprised 5x5x5=125 unit cells.

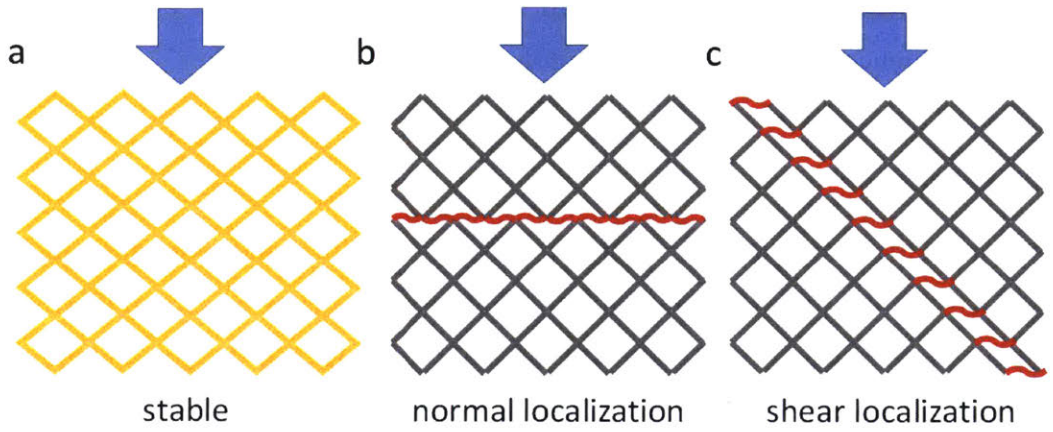

Figure 3.19: Schematic illustration of possible deformation modes of the Solid Octet Truss (SOT) structure when subject to uniaxial compression: (a) stable response with uniformly distributed macroscopic strains throughout the entire specimen, (b) normal strain localization band, and (c) shear localization band.

The influence of the specimen size on the macroscopic stress-strain response is expected to be most pronounced for the SOT structure because of the localization of deformation at a length scale that is set by the unit cell size. We therefore repeated the simulations for the SOT structure using a FE model with 5^3 unit cells. The 3^3-simulation (thin dashed curve) overestimates the initial peak stress, while an improved estimate is obtained with the 5^3-model (thick dashed curve). Knowing the localization mechanism in the SOT structure, the width of the first peak is expected to be monotonically related to the ratio of the unit cell size and specimen height. Consequently, the macroscopic strain (or normalized displacement, which is the more appropriate term in the case of the SOT specimens) at the first valley is smaller and closer to the experiment for the 5^3-model than the 3^3-simulation. The minimum stress in the first stress valley is significantly lower in the experiments ($21 MPa$ versus $30 MPa$ in the simulations). This is attributed to the difference in the mesostructural deformation mode (inside the localization bands). In the experiments,

the unit cells predominantly respond in a shear localization mode (see Figs. 3.15 and 3.19b), while a normal localization mode is observed in the simulations (see Figs. 3.11c and 3.19c). Kinematic constraints due to the small specimen size and non-planarity of the initial bands of localization prevent the progressive crushing of the SOT structure in a shear mode only. As a result, the initially pronounced quantitative differences between the simulations and the experiments vanish at large macroscopic strains. Densification also sets in earlier in the simulations than in the experiments which is consistent with the reported differences in the mesostructural deformation modes.

3.3.5 Discussion

The numerical simulations and the experimental results elucidate the poor mechanical performance of the conventional octet truss architecture at large macroscopic strains. The initial small-strain strength of the SOT is among the highest of the 20%-relative density metamaterials considered, but its mesostructure collapses in the plastic range. This behavior is observed for hydrostatic compression, confined compression and uniaxial compression. Overall, the large strain response of the SOT material at a relative density of 20% is still reminiscent of that of conventional cellular solids such as metallic foams or low density honeycombs. (e.g. Jang and Kyriakides, (2009a, 2009b)). The response of the SOT structure becomes stable at larger relative densities. At the mesoscopic level, the 3D connections of the SOT struts (nodes) are usually subject to stress states close to hydrostatic loading. In the case of incompressible base materials (such as most metals), the nodes will thus not deform plastically which is a major drawback of the SOT structure as far as weight efficient energy absorption is concerned.

The other three metamaterials exhibit a stable mesostructural response within the range of relative densities considered. All structures feature FCC symmetry, but the mesostructural configuration of the HSA, HOT and HTS materials is fundamentally different from that of the SOT material. The first three fall into the class of continuous shell structures. As compared to foams, their continuity order is still low, i.e. the surface curvatures are still discontinuous. However, despite their discontinuous surface curvature, the low order shell structures exhibit already a significantly higher stability under

compression than the solid octet truss lattice. The simulation results also show that the plastic deformation concentrates near sharp angles (i.e. at curvature discontinuities) within the mesostructures, which is particularly inefficient from a specific energy absorption point of view.

As compared to the SOT material, the hollow sphere assembly (HSA) exhibits almost the opposite qualitative features: its small strain strength is low, but due to the progressive increase in internal contact within its compressed mesostructure, the HSA shows a macroscopically stable large deformation response that is accompanied by high macroscopic strain hardening under hydrostatic and confined compression. Since the high hardening commences after transforming the spheres into dodecahedra, we also repeated the unit cell simulations for $\bar{\rho} = 0.2$ assuming a Rhombic DodecaHedron (RDH) as initial mesostructure. As shown by the dashed lines in Figs. 3.7a, 3.7b, 3.12a and 3.12b, the dodecahedron shell mesostructure is by far the strongest. The estimated small strain strength of the RDH is at least 75% higher than that of the other metamaterials. At large strains the RDH is prone to cell wall buckling which reduces its load carrying capacity, in particular in case of the low strain hardening base material. However, the overall stress level still remains high which makes it an attractive alternative to the metamaterial architectures studied in the previous sections. Unresolved issues encountered during the additive manufacturing of RDH specimens prevented the experimental confirmation of the exceptional mechanical performance of the dodecahedron shell mesostructure.

It is reemphasized that results from compression experiments on cellular solids are potentially specimen size dependent. In the hypothetical case of zero friction between the specimens and the loading platens, a free lateral boundary is less constraining than another column of unit cells, i.e. the formation of macroscopic localization bands is more prone to occur in small specimens. In the case of non-zero friction, the specimen cannot expand freely in the lateral direction and lateral compressive stresses are expected to build up. This friction boundary effect leads to the macroscopic barreling which we observed in our experiments. The friction effect is expected to stabilize the specimen response. The comparison of the simulation results for 3x3x3 and 5x5x5 SOT specimens suggest that the specimen size effect is not significant for the SOT structures, while the experimental demonstration for all structures is deferred to future research.

The development of analytical models is also deferred to future research. Possible starting points are Gurson's (1977) approximate solution of the plastic response of a thick-walled hollow sphere. It will provide a valuable basis for developing an analytical model for the Hollow Sphere Assembly (HSA). There exists also an approximate analytical expression for the macroscopic yield surface of the SOT material (Mohr, 2005) which could also be extended to HOT materials.

3.4. Conclusions

The large deformation response of four different mesostructures of FCC symmetry are analyzed. The analysis includes the widely-used octet truss lattice material with solid and hollow trusses, a closed-packed hollow sphere assembly and a hybrid hollow truss sphere assembly. The unit cell simulations for hydrostatic compression reveal that the conventional octet truss lattice is prone to buckling failure for relative densities below about 0.3, with the exact transition density depending on the base material hardening capacity. As a result, the twisting mode, i.e. the rotation of the connecting nodes is observed at low relative densities due to the excessive plastic bending of individual struts. The mesostructures of the hollow sphere assembly turned out to remain stable for all relative densities considered (from 0.2 to 0.6), but it underwent substantial geometric changes. Individual spheres actually transformed into rhombic dodecahedra. This transformation maximized the contact surface between the constituent spheres which is accompanied by step increase in the hardening rate at the macroscopic level.

Both the simulations and experiments on stainless steel metamaterials made through selective laser melting demonstrated that the solid octet truss lattice material is the weakest among all 20%-relative density configurations considered. Its specific energy absorption capacity is 35% lower than that of the hybrid hollow truss sphere assembly. It is also shown computationally that the hollow dodecahedron shell mesostructure provides the highest specific small-strain strength and energy absorption capability among all metamaterials considered. This leads to the tentative conclusion that periodic shell structures provide superior strength and energy absorption capacity for the same weight.

It is also noted that mesoscopic localization of the deformations is associated with an overall decrease in the energy dissipated by the structures, with notably softening in the case of the solid octet-truss. Despite the high stress-values observed, the rhombic dodecahedron structure shows unstable behavior, marked with peaks in the observed force reminiscent of those of the octet-truss, suggesting that the straight plates it is composed of do not provide much more stability than the straight beams of the octet-truss. Moreover, the intersections presented by those structures did not contribute to plastic dissipation. More stable responses are observed when utilizing curved shells with no intersections, which is exemplified by the two hollow-octet-truss architectures presented herein. However those structures presented localization of mesoscopic level deformations around sharp angles, limiting the overall energy absorption. A strategy to address this concern is investigated in Chapter 4.

4. From Octet-Truss to FCC shell-lattice

Parts of this chapter are adapted from Bonatti and Mohr (2019a).

Based on our conclusions from the previous chapter that plastic deformation often localizes at corners and non-smooth intersections instead of distributing the plastic dissipation in a uniform manner throughout the entire structure, we develop new family of shell-lattices. It is obtained through the smoothening of the geometry of a hollow FCC truss (octet-truss). . The elastic, yield and large deformation properties of this Smooth Shell FCC (SSF) metamaterial are investigated numerically through finite element analysis. For reference, all computed mechanical properties and scaling laws are contrasted with those of octet truss lattice material. Furthermore, the simulation results are partially validated through compression experiments on cubic stainless steel specimens manufactured through selective laser melting.

4.1. Generation of smooth-shell structures

4.1.1 Method outline

Our objective is to design a porous FCC metamaterial by embedding a smooth curvature shell surface in the fundamental domain (tetrahedron). For this we need to an optimization problem, with boundary conditions and a functional:

- **Boundary Conditions.** The shell structure of the hollow octet truss lattice, which rests on all four faces of the fundamental tetrahedron (Fig 4.1a), is taken as starting point. The defining surface Ω of a smooth shell-lattice shall rest on the faces (opposite to vertex) A, B, C and D of the fundamental tetrahedron, in that order and with no hole, separating the tetrahedron into two volumes with edge [AB] on one side and edge [CD] on the other. The intersections with the tetrahedron's faces (which correspond to the borders of the surface) are submitted to orthogonality to the face they lie on, in order to ensure smooth connections (C_1-continuity) after applying the mirror transformations required to recreate the FCC lattice material. Recall from Fig. 2.2 that the octet truss

lattice structure is obtained by placing a strut along the edge [AB] of the fundamental tetrahedron, while placing a strut along the edge [CD] yields a skeletal rhombic dodecahedron. Similar to the F-RD (FCC-Rhombic Dodecahedron) minimal surface, the structures defined herein will be generated by a surface (see Fig. 4.1c to 4.1f) that can at the same time be seen as a smoothened hollow-truss FCC network (Fig. 4.1d), and a smoothened hollow-truss RD network (Fig. 4.1e). The exact shape of the motif inside the fundamental tetrahedron of the novel smooth shell structure (Fig. 4.1b) is determined by the choice of a functional that will be minimized.

- **Basic functional.** We choose to minimize the surface integral

$$\int_{\Omega} (k_1^2 + k_2^2)^2 dA \tag{4.1}$$

with k_1 and k_2 the principal curvatures at any given point on the surface Ω. It is noted that the integrant has an interpretation in mechanics: for an elastic material of zero Poisson's ratio, it represents the square of the strain energy required to bend an initially flat platelet into the shape of the smooth shell surface.

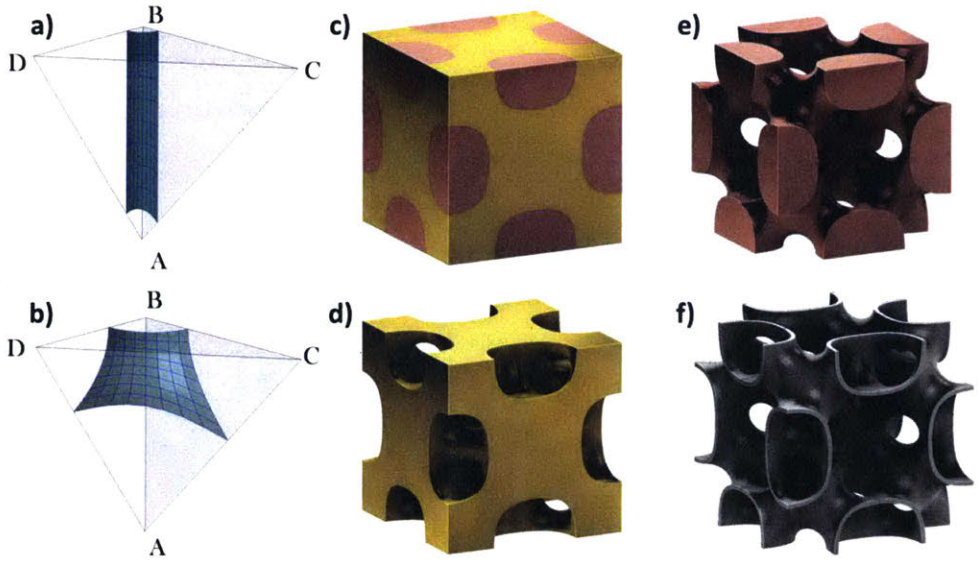

Figure 4.1: Proposed Smooth Shell FCC (SSF) metamaterial architecture: (a) shell structure inside the fundamental tetrahedron used as initial guess (hollow octet-truss), (b) double-curvature surface of the SSF minimizing the function in Eq. (1), (c) cubic unit-cell of the SSF, (d) fluid phases separated by the shell structure, (e) first fluid phase, (f) second fluid phase.

The minimization problem defining the surface geometry is solved approximately using an in-house Matlab script.

4.1.2 Implementation

4.1.2.1 Mapping definition

In a first step a 2D square mesh is defined and projected into the fundamental tetrahedron (Fig 4.2).

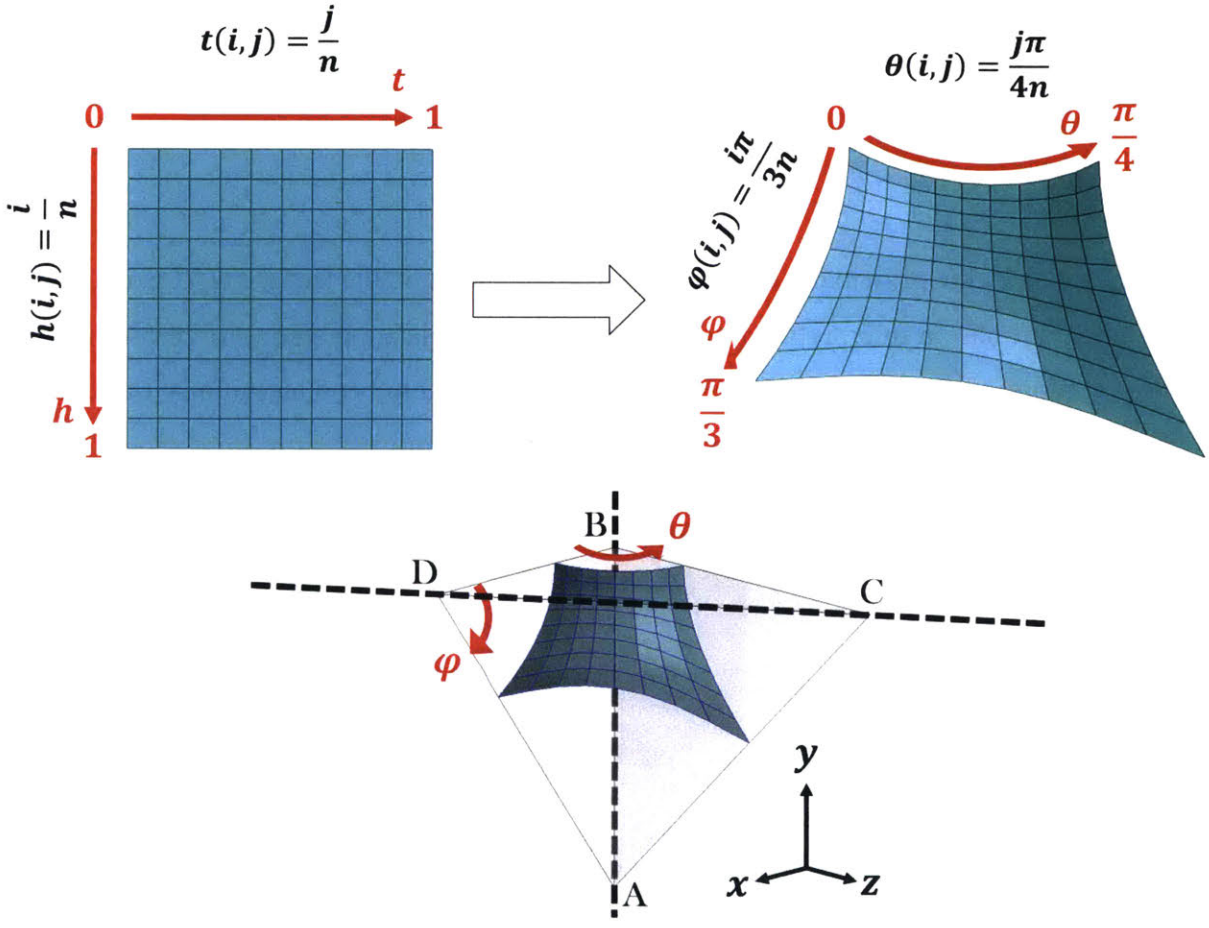

Figure 4.2: a) A 2D square grid is projected onto a surface embedded in the fundamental domain of the FCC lattice. b) Choice of coordinates within the fundamental tetrahedron.

Similar to Chapter 4, we specialize the definition given in Chapter 3 and take our fundamental tetrahedron $\mathcal{T}$ with the following coordinates:

$$\mathcal{T} = \left\{ (x,y,z) \in \mathbb{R}^3 \middle/ \begin{matrix} x \geq 0 \\ z \geq 0 \\ y \leq 1 \\ \sqrt{2}x + \sqrt{2}y + 2z \geq 0 \end{matrix} \right\} \tag{3.2}$$

The original grid is parameterized with two coordinates $0 \leq t \leq 1$ and $0 \leq h \leq 1$. In practice a $n \times n$ grid is used, with n an integer (typically $6 \leq n \leq 100$). The coordinates in the grids are then for $(i,j) \in \{1,2,\dots,n\}^2$, $h(i,j) = i/n$ and $t(i,j) = j\ /\ n$. We define a temporary set of coordinates within the tetrahedron, of which the first two are the angles θ around axis (AB) and φ around axis (CD), as depicted in Figure 4.2. Due to the definition of $\mathcal{T}$, θ varies between 0 and $\pi\ /\ 4$ while φ varies between 0 and $\pi\ /\ 3$. In the natural coordinate system, planes of constant θ are defined by equation:

$$\mathcal{P}_\theta : \{\cos(\theta) \cdot x - \sin(\theta) \cdot z = 0\} \tag{3.3}$$

While planes of constant φ are defined by equation:

$$\mathcal{P}_\varphi : \left\{ -\frac{\sin(\varphi)}{\sqrt{3}} \cdot x + \cos(\varphi) \cdot y - \frac{\sqrt{2}\sin(\varphi)}{\sqrt{3}} \cdot z = \cos(\varphi) - \frac{\sin(\varphi)}{\sqrt{3}} \right\} \tag{3.4}$$

A point $\boldsymbol{x} \in \mathcal{T}$ of coordinates θ_x and φ_x has to lie on the segment of vertices P_1 and P_2, where P_1 is at the intersection of (AB) and $\mathcal{P}_\varphi$:

$$P_1 = \begin{bmatrix} 0 \\ 1 - \tan(\varphi)\ /\ \sqrt{3} \\ 0 \end{bmatrix} \tag{3.5}$$

And P_2 lies at the intersection of (CD) and $\mathcal{P}_\theta$:

$$P_2 = \begin{bmatrix} \sin(\theta)\ /\ (\sqrt{2}\cos(\theta) + \sin(\theta)) \\ 1 \\ 2\cos(\theta)\ /\ (\sqrt{2}\cos(\theta) + \sin(\theta)) \end{bmatrix} \tag{3.6}$$

We therefore choose our last coordinate λ such that:

$$\boldsymbol{x} = (1 - \lambda_x)P_1(\varphi_x) + \lambda_x P_2(\theta_x) \tag{3.7}$$

We choose to constrain our mapping by assuming that the surface's θ coordinate evolves linearly with t, and φ linearly with h through the mapping, as expressed in Figure 4.2a. In other words we have $\theta_{ij} = j\pi \,/\, 4n$ and $\varphi_{ij} = i\pi \,/\, 3n$, and there is only one free parameter λ_{ij} per point in the grid. As stated above the surfaces we are looking for form at the same time, a tube around axis (AB), and a tube around axis (CD). Given that the surfaces we are interested in are obtained through some form of curvature minimization, we don't expect them to form unnecessary loops and meanders. Therefore this assumption seems reasonable. Additionally the continuity boundary conditions on the different faces are now embedded into the parameterization of the surface.

Now that we have chosen a parameterization we can summarize the situation. Given a choice of n^2 scalars $0 \leq \lambda_{ij} \leq 1$ with $(i,j) \in \{1,2,\dots,n\}^2$, we can express matrices X, Y and Z of surface coordinates, with:

$$X_{ij} = \lambda_{ij} \sin\left(\frac{j\pi}{4n}\right) / \left(\sqrt{2}\cos\left(\frac{j\pi}{4n}\right) + \sin\left(\frac{j\pi}{4n}\right)\right) \tag{1.8}$$

$$Y_{ij} = \lambda_{ij} + (1 - \lambda_{ij})\left(1 - \tan\left(\frac{i\pi}{3n}\right)/\sqrt{3}\right) \tag{3.9}$$

$$Z_{ij} = 2\lambda_{ij} \cos\left(\frac{j\pi}{4n}\right) / \left(\sqrt{2}\cos\left(\frac{j\pi}{4n}\right) + \sin\left(\frac{j\pi}{4n}\right)\right) \tag{3.10}$$

4.1.2.2 Computation of the cost-function

First order derivatives, surface normal and curvatures are estimated using a finite difference scheme.

- **Symmetric boundary conditions:** In a first step, extended coordinate matrices of size $(n + 2)^2$: X_2, Y_2 and Z_2 are defined by mirroring the second next row (resp. column) through the corresponding surface. This ensures that the curvatures computed on the edges of the grid reflect the symmetries of the final surface.

- **Calculation of first and second order derivatives:** In a second step, first and second order derivatives of the mapping are estimated, through the use of matrix convolution (symbol $*$). For example, the derivative $dx\,/\,dt$ is represented by:

$$dXdT2 = X_2 * dT2 \tag{3.11}$$

Where $dT2$ is the kernel corresponding to second order differentiation with respect to grid parameter t. A chosen kernels are:

$$dT' = n\begin{bmatrix}-1 & 1\\ 0 & 0\end{bmatrix}, \tag{3.12}$$

$$dH' = n\begin{bmatrix}0 & -1\\ 0 & 1\end{bmatrix}, \tag{3.13}$$

$$dT2 = n^2\begin{bmatrix}0 & 0 & 0\\ 1 & -2 & 1\\ 0 & 0 & 0\end{bmatrix}, \tag{3.14}$$

$$dH2 = n^2\begin{bmatrix}0 & 1 & 0\\ 0 & -2 & 0\\ 0 & 1 & 0\end{bmatrix}, \tag{3.15}$$

$$dTdH = \frac{n^2}{4}\begin{bmatrix}1 & 0 & -1\\ 0 & 0 & 0\\ -1 & 0 & 1\end{bmatrix}. \tag{3.16}$$

The first order derivatives are not properly defined yet - the quantities of the form $dXdT'$ have size $(n+1)^2$ and have a half-grid point offset. Proper derivatives are obtained by applying two further steps, for example the quantity:

$$\frac{1}{2}dXdT' * \begin{bmatrix}1\\ 1\end{bmatrix} \tag{3.17}$$

Yields $dXdT$ through cutting off the surplus column (resp. line for dH).

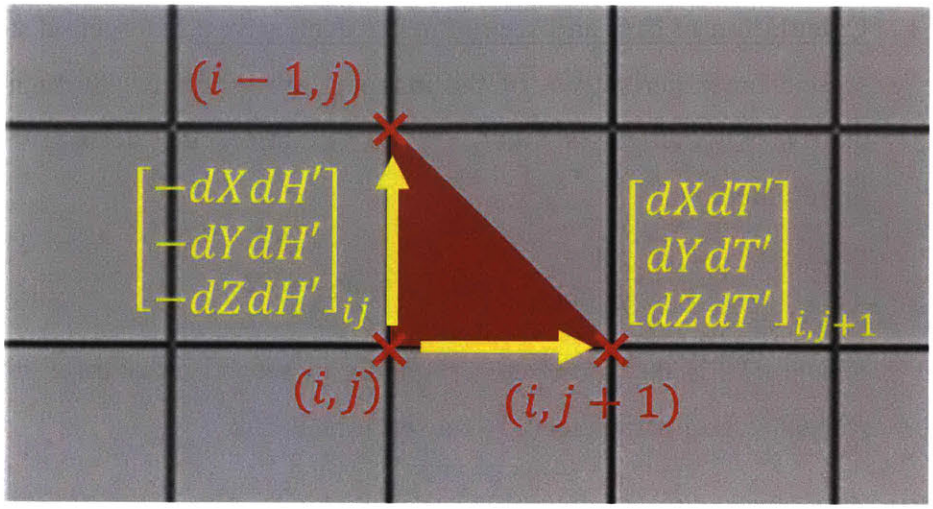

Figure 4.3: The area vector of the red triangle's image on the surface is estimated using the calculated offset derivatives. The same is performed at each point for each of the four triangles lying on the point.

- **Calculation of the surface vectors:** The quantities of the form $dXdT'$ are used to estimate at each point the surface vectors of the four triangles lying on the grid point. This is done as shown in Figure 4.3. As a result twelve matrices in the form $N_1X, N_1Y, \ldots, N_4Z$ are determined at each point. The surface vector at each point is the average of the four corresponding triangles' surface vectors, divided by half (since every point on the surface is counted twice). It is decomposed in surface normal $\boldsymbol{n_{ij}}$, and local area a_{ij} .

- **Estimation of curvatures:** The operations to obtain the principal curvatures is best expressed formally. We compute the coefficients as of the first fundamental and second form according to the following definitions:

$$E = \frac{\partial \boldsymbol{x}}{\partial t} \cdot \frac{\partial \boldsymbol{x}}{\partial t}, F = \frac{\partial \boldsymbol{x}}{\partial h} \cdot \frac{\partial \boldsymbol{x}}{\partial h}, G = \frac{\partial \boldsymbol{x}}{\partial h} \cdot \frac{\partial \boldsymbol{x}}{\partial t} \tag{3.18}$$

$$L = \frac{\partial^2 \boldsymbol{x}}{\partial t^2} \cdot \boldsymbol{n}, M = \frac{\partial^2 \boldsymbol{x}}{\partial t \partial h} \cdot \boldsymbol{n}, N = \frac{\partial^2 \boldsymbol{x}}{\partial h^2} \cdot \boldsymbol{n} \tag{3.19}$$

We compute the following quantities at each point:

$$F_1 = \begin{bmatrix} E & F \\ F & G \end{bmatrix} \text{ and } F_2 = \begin{bmatrix} L & M \\ M & N \end{bmatrix} \tag{3.20}$$

To finally obtain the shape operator at each node (i,j):

$$A = F_1^{-1} \cdot F_2 \tag{3.21}$$

- **Cost function:** The local cost function can then be calculated:

$$e_{ij} = \left(\kappa_{1,ij}^2 + \kappa_{2,ij}^2\right)^2 = \left(\mathrm{Tr}(A^2)\right)^2 \tag{3.22}$$

From which the global quantity is derived:

$$J = \sum_{i,j} e_{ij} a_{ij} \tag{3.23}$$

The obtained approximation of the cost-function is then minimized by alternating between a Nelder-Mead algorithm and a gradient-descent.

4.1.3 Structure description

The unit-cell of the obtained shell-lattice is shown in Fig. 4.4f. The corresponding coordinates for an 8×8 element mesh of the surface ($n = 9$), are provided in Table 2.1. The fluid volumes separated by it have roughly equal volume, and it resembles the TPMS alternative (Schoen F-RD). As a matter of fact, their mechanical properties are also very similar – this point will be addressed in further detail in Chapter 6. In the sequel, the structure will thus be referred to as the "TPMS-like" shell-lattice. The thickness of the obtained shell structure is varied to achieve different relative densities.

4.2. Computational models

In order to gain insight into the mechanical behavior of shell-lattice materials over a wide range of relative densities, finite element simulations are conducted on unit-cells using the non-linear finite element software Abaqus/Standard. The same procedure is

applied to the widely-used octet truss-lattice metamaterial for both comparison and validation purposes.

	1	2	3	4	5	6	7	8	9
1	[0.0000 1.0000 0.2328]	[0.0463 1.0000 0.2328]	[0.0922 1.0000 0.2225]	[0.1366 1.0000 0.2044]	[0.1781 1.0000 0.1781]	[0.2149 1.0000 0.1436]	[0.2442 1.0000 0.1012]	[0.2633 1.0000 0.0524]	[0.2696 1.0000 0.0000]
2	[0.0000 0.9559 0.2388]	[0.0468 0.9596 0.2352]	[0.0929 0.9620 0.2244]	[0.1376 0.9631 0.2059]	[0.1794 0.9626 0.1794]	[0.2165 0.9604 0.1447]	[0.2465 0.9561 0.1021]	[0.2665 0.9497 0.0530]	[0.2743 0.9411 0.0000]
3	[0.0000 0.9119 0.2480]	[0.0482 0.9192 0.2424]	[0.0953 0.9241 0.2300]	[0.1406 0.9262 0.2105]	[0.1832 0.9253 0.1832]	[0.2215 0.9208 0.1480]	[0.2533 0.9123 0.1049]	[0.2761 0.8994 0.0549]	[0.2880 0.8822 0.0000]
4	[0.0000 0.8678 0.2636]	[0.0507 0.8788 0.2547]	[0.0993 0.8861 0.2397]	[0.1459 0.8893 0.2183]	[0.1899 0.8879 0.1899]	[0.2302 0.8813 0.1538]	[0.2650 0.8684 0.1097]	[0.2922 0.8490 0.0581]	[0.3104 0.8234 0.0000]
5	[0.0000 0.8238 0.2862]	[0.0542 0.8384 0.2724]	[0.1051 0.8481 0.2538]	[0.1536 0.8524 0.2298]	[0.1997 0.8505 0.1997]	[0.2428 0.8417 0.1622]	[0.2817 0.8245 0.1167]	[0.3146 0.7987 0.0626]	[0.3410 0.7645 0.0000]
6	[0.0000 0.7797 0.3165]	[0.0590 0.7980 0.2964]	[0.1131 0.8101 0.2731]	[0.1643 0.8154 0.2458]	[0.2133 0.8132 0.2133]	[0.2601 0.8021 0.1738]	[0.3040 0.7807 0.1259]	[0.3434 0.7484 0.0683]	[0.3789 0.7056 0.0000]
7	[0.0000 0.7357 0.3547]	[0.0652 0.7576 0.3280]	[0.1239 0.7722 0.2991]	[0.1788 0.7785 0.2675]	[0.2316 0.7758 0.2316]	[0.2830 0.7625 0.1891]	[0.3322 0.7368 0.1376]	[0.3784 0.6981 0.0753]	[0.4233 0.6467 0.0000]
8	[0.0000 0.6916 0.4016]	[0.0733 0.7172 0.3685]	[0.1383 0.7342 0.3339]	[0.1985 0.7416 0.2970]	[0.2563 0.7384 0.2563]	[0.3126 0.7229 0.2089]	[0.3671 0.6929 0.1520]	[0.4195 0.6478 0.0834]	[0.4735 0.5879 0.0000]
9	[0.0000 0.6476 0.4579]	[0.0834 0.6767 0.4195]	[0.1577 0.6962 0.3808]	[0.2261 0.7047 0.3384]	[0.2904 0.7011 0.2904]	[0.3513 0.6833 0.2348]	[0.4093 0.6491 0.1695]	[0.4663 0.5974 0.0927]	[0.5290 0.5290 0.0000]

Table 2.1: Coordinates of approximate solution for a 9×9 node grid.

4.2.1 Constituent material

All simulations are conducted using the high hardening material model described in Chapter 2 and corresponding to the additively-manufactured 316L stainless steel (CL20ES powder, Concept Laser) used for experiments. Recall that it is a simple elastoplastic model with J2-plasticity, a Young's modulus of $E = 200\ GPa$, a Poisson's ratio of $\nu = 0.3$, and isotropic hardening described by a Swift law

$$k_S[\bar{\varepsilon}_p] = A\left(\bar{\varepsilon}_p + \varepsilon_0\right)^n \tag{3.24}$$

with the Swift parameters $A = 842.5\ MPa$, $\varepsilon_0 = 0.036$ and $n = 0.176$.

4.2.2 Unit-cell models

Cubic unit-cells are considered due to the simplicity of boundary condition implementation they offer. The meshes are generated directly in Matlab, based on the 2D mesh within the fundamental tetrahedron. Solid elements are created by thickening the smooth shell structure along the local surface normal directions. The total volume of the mesh is estimated and compared to that of the tetrahedron, and the Newton-Raphson method is applied to find the appropriate thickness for the desired relative density.

$\bar{\rho}$	**0.01**	**0.02**	**0.05**	**0.1**	**0.2**	**0.3**	**0.4**	**0.5**	**0.6**
t_w/l_s	$2.09 \cdot 10^{-3}$	$4.18 \cdot 10^{-3}$	$1.05 \cdot 10^{-2}$	$2.09 \cdot 10^{-2}$	$4.21 \cdot 10^{-2}$	$6.39 \cdot 10^{-2}$	$8.64 \cdot 10^{-2}$	$1.10 \cdot 10^{-1}$	$1.36 \cdot 10^{-1}$

Table 2.2: Wall-thickness to unit-cell side-length ratio of the FCC TPMS-like shell-lattice as function of the relative density.1.

Once the appropriate thickness is determined for a given relative density (Table 2.2), the 2D mesh is copied, mirrored and translated to produce a shell mesh filling the unit-cell. Using the same method as above to convert from 2D to 3D elements, five elements through thickness are used in all meshes. The number of 2D elements used in the tetrahedron varies with the target relative density. A grid of 25×25 elements is used for relative densities of 0.01, 0.02 and 0.05 (Fig. 4.4a), 15×15 elements for relative densities of 0.1 and 0.2 (Fig. 4.4b), and 8×8 elements for relative densities of 0.3, 0.4, 0.5 and 0.6 (Fig. 4.4c). C3D8I elements are used in simulations. Given the slenderness of the lightest shell structures and the resulting high element aspect ratios, the elastic results are compared to those obtained with a mesh featuring 50×50 elements (2'400'000 elements in the unit-cell). The mean elastic properties with both discretizations are within 1% of each other. Meshes of the octet-truss lattice unit-cell are similarly deduced from automatic meshes of the tetrahedron contents (see previous Chapter).

Periodic micro-displacement boundary conditions are applied as described in Paragraph 2.2.1.

4.2.3 Elastic small-strain simulations

Elastic simulations are performed to determine both the homogenized elastic response, and the local stress field. The basis material is modeled as purely elastic without any plasticity. For both the shell- and truss-lattice unit-cells, six simulations are performed. In each simulation, one component of the small strain tensor is set to reach a value of 10^{-4}, while the other components are kept equal to 0. Those simulations are performed for relative unit-cell densities of 0.01, 0.02, 0.05, 0.1, 0.2, 0.3, 0.4, 0.5 and 0.6.

From these simulations, all components of the macroscopic elastic stiffness matrix are readily obtained from the computed macroscopic stress-strain response. An estimate of the structures' yield surface is also determined using the procedure described in Paragraph From these simulations, all components of the macroscopic elastic stiffness matrix $\mathbf{A_{tot}}$ are readily obtained from the computed macroscopic stress-strain response. In addition, the stress response is recorded at integration points of each element n. This linear localization relationship, i.e. the relation between the local stress tensor $\boldsymbol{\sigma}_\mathbf{n}$ and the applied macroscopic strain tensor, is described by the matrices $\mathbf{A_n}$. The local stress response can then also be related to the applied stress $\mathbf{P}$ at the macroscopic level,

$$\boldsymbol{\sigma}_\mathbf{n} = \mathbf{A_n A_{tot}^{-1} P} \tag{3.25}$$

We note that the macroscopic Piola stress is equal to the macroscopic Cauchy stress for small strains.

We make use of (6) to estimate the macroscopic yield stress. To obtain a high resolution pole figures of the macroscopic yield stress of FCC metamaterials, a correspondingly high number of directions $\mathbf{a}^{(i)}$ needs to be considered. With the availability of (6), we can then compute the local stress field for any arbitrary macroscopic stress tensor $\mathbf{P}$ without running additional elasto-plastic finite element simulations. Based on the elastic solution of the unit-cell problem, the macroscopic yield stress for a direction $\mathbf{a}^{(i)}$ is then defined as the minimal value of $\left|P^{(i)}\right|$ for which the local von Mises equivalent stresses $\bar{\boldsymbol{\sigma}}_\boldsymbol{n}$ due to the macroscopic loading by the stress tensor $\boldsymbol{P}^{(i)} = P^{(i)}\mathbf{a}^{(i)} \otimes \mathbf{a}^{(i)}$ exceeds the basis material yield strength within 5% of the volume of the solid phase. The

pole figures shown in the present paper have all been generated based on data for about 21'000 directions of loading.

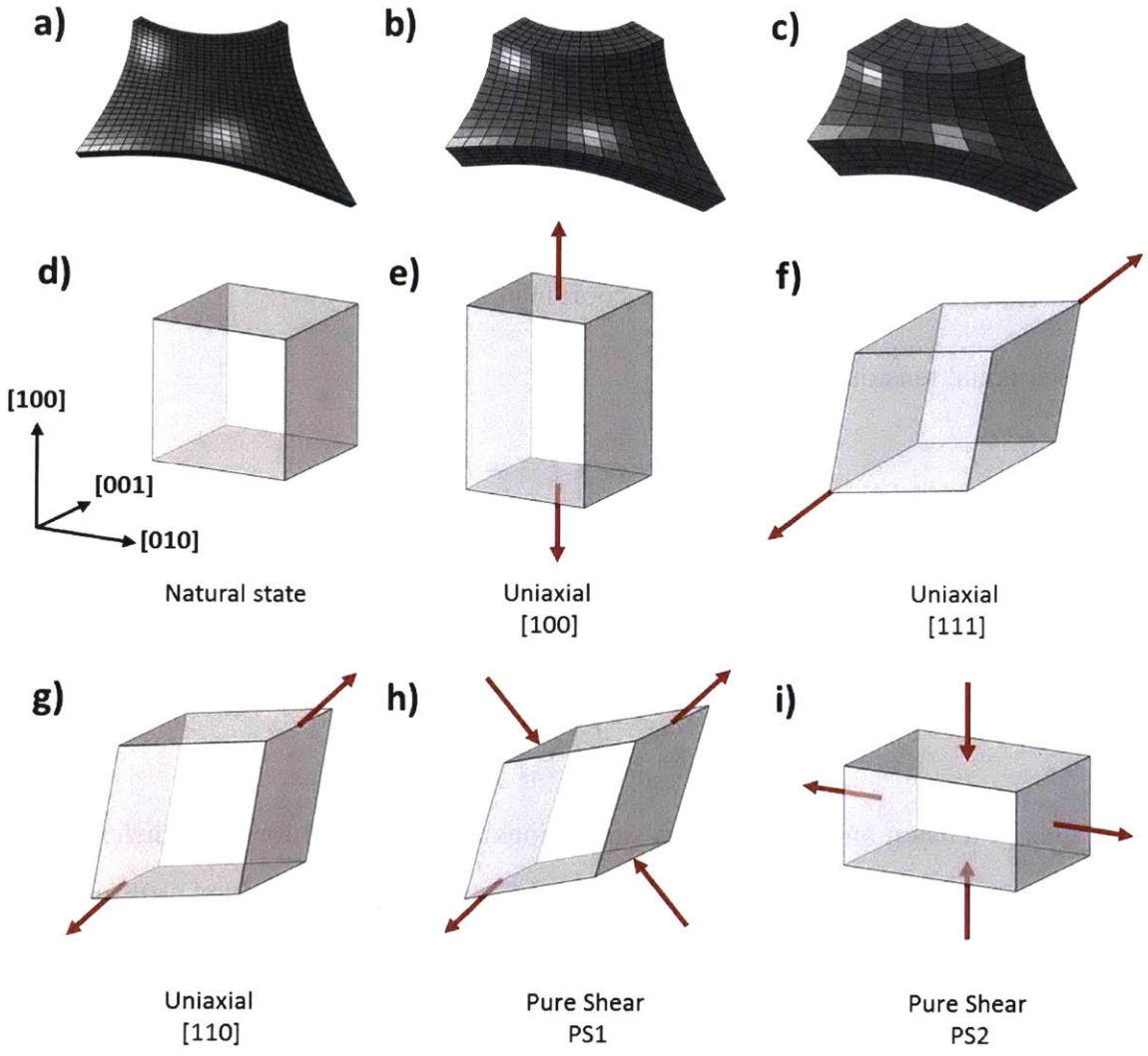

Figure 4.4: a-c) 3D mesh contents of the fundamental tetrahedron for $\beta = 1$. a) 25×25 grid, $\overline{\rho} = 0.05$ b) 15×15 grid, $\overline{\rho} = 0.2$ c) 8×8 grid, $\overline{\rho} = 0.4$. d-i) Loading scenarios corresponding to the extrema of the stiffness and yield strength in uniaxial tension and pure shear. d) reference configuration, e) uniaxial tension/compression loading along the $[100]$ direction, f) uniaxial tension/compression loading along the $[111]$ direction, g) uniaxial tension/compression loading along the $[110]$ direction, h) pure shear loading (PS1) with principal stress directions along the $[110]$ and $[1\bar{1}0]$ axes, i) pure shear loading (PS2) with principal stress directions along the $[100]$ and $[010]$ axes.

4.2.4 Elastoplastic finite-strain simulations

Large strain simulations assuming an elasto-plastic material behavior are performed on all unit-cell models (covering relative densities of 0.1, 0.2, 0.3, 0.4, 0.5 and 0.6). Three basic loading scenarios are considered: uniaxial tension, uniaxial compression and pure shear, to be understood in the sense of the Piola stress $\boldsymbol{P}$ (engineering stress). Introducing a scalar parameter λ that evolves from 0 to λ_{max} during the simulations, the loading conditions may be written in terms of the components of the macroscopic displacement gradient $\mathbf{H}$ and the stress tensor $\mathbf{P}$ in the coordinate frame $\{\mathbf{e}_1, \mathbf{e}_2, \mathbf{e}_3\}$:

- Uniaxial tension:

$$\begin{cases} H_{11} = \lambda \\ P_{12} = P_{13} = P_{23} = P_{22} = P_{33} = 0 \end{cases} \tag{3.26}$$

- Uniaxial compression:

$$\begin{cases} H_{11} = -\lambda \\ P_{12} = P_{13} = P_{23} = P_{22} = P_{33} = 0 \end{cases} \tag{3.27}$$

- Pure shear:

$$\begin{cases} H_{12} = H_{21} = \lambda \\ P_{11} = P_{13} = P_{23} = P_{22} = P_{33} = 0 \end{cases} \tag{3.28}$$

Uniaxial tension and compression simulations are performed for three different unit-cell orientations, i.e. with the $\mathbf{e}_1$-direction being parallel to the [100], [110] and [111] directions. Pure shear simulations are performed in the unit-cell's natural coordinate frame (case PS1), as well as with a rotation of 45 degrees around the 3rd coordinate axis (case PS2). All loading scenarios are illustrated in Fig. 4.4.

To evaluate and compare the specific energy absorption capability of metamaterials, the plastic dissipation is computed up to the same applied macroscopic strain. In particular, we chose the loading parameter λ such that a von Mises material would exhibit the same energy dissipation for all loading cases, with a final equivalent plastic strain of $\bar{\varepsilon}^p = 0.36$. This lead to maximal values of λ of 0.3 in uniaxial compression, 0.43 in uniaxial tension and 0.32 in pure shear.

The specific energy absorption ψ is then defined as the total plastic dissipation per unit mass,

$$\psi = \frac{D}{\rho} \tag{3.29}$$

with D denoting the plastic dissipation density, and ρ denoting the mass density.

4.3.Experimental procedures

The main purpose of the experiments is to validate the computational results. Given the high level of confidence in the reliability of non-linear finite element analysis, only a small subset of the computational results is reproduced experimentally.

4.3.1 Specimens

In order to confirm the numerically-estimated scaling of large-deformation properties of the shell-lattices, uniaxial compression experiments are performed on shell-lattice specimens oriented in the [100] direction, for relative densities of 0.1, 0.2, 0.3 and 0.4. The specimens are tested along the building direction. Cubic specimens consisting each of $5 \times 5 \times 5$ unit-cells are produced. All specimens have been manufactured out of 316L stainless steel using a selective laser melting system (Model M2, Concept Laser) using CL 20ES powder (Concept Laser). In an attempt to minimize variations of the basis material properties related to the manufacturing process, the same wall thickness of $400\mu m$ is chosen for all specimens. This leads to cube edge lengths of $95.6\,mm$, $47.5\,mm$, $31.4\,mm$, and $23.2\,mm$, respectively. Figure 4.5a shows a photograph of the manufactured specimens. The external overall dimensions of the produced specimens are found to be within 1% of the prescribed ones. The measured masses of the specimens are within 2% of the prescribed ones assuming a basis material density of $8g\,/\,cm^3$.

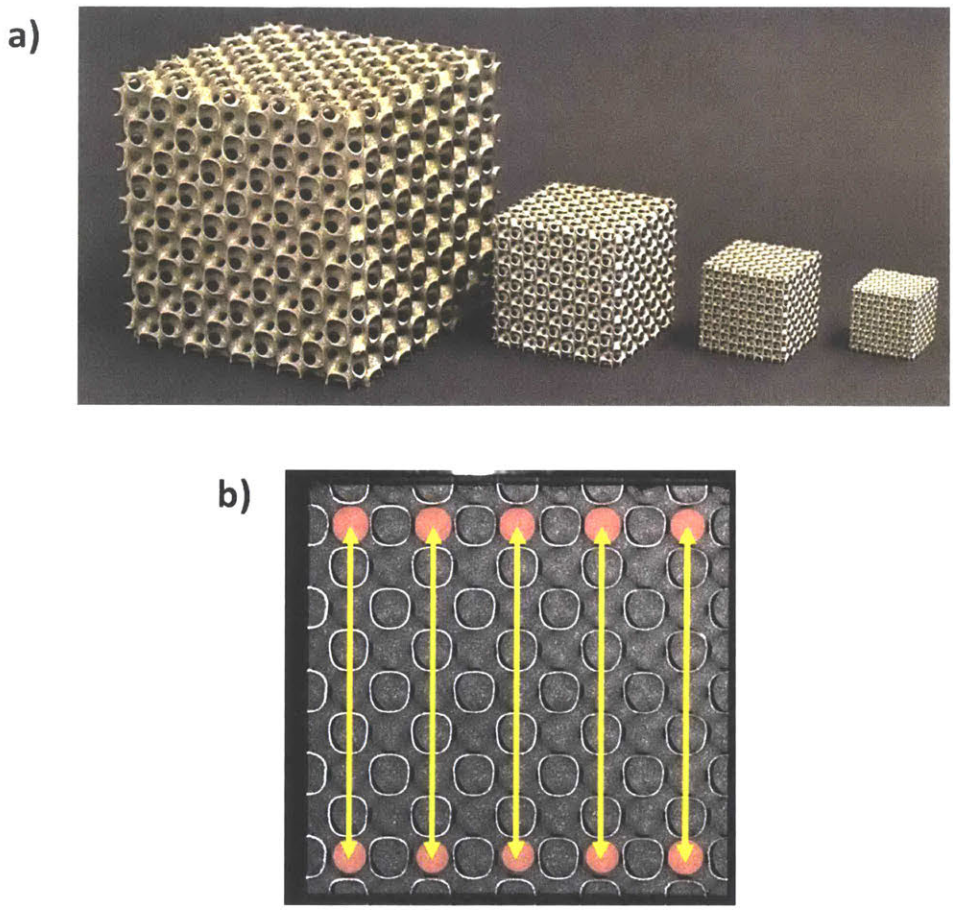

Figure 4.5: (a) View of untested uniaxial compression specimens produced via selective laser melting using a 316L stainless steel powder. Each specimen consists of 5*x*5*x*5 unit-cells with 400μm wall thickness, with relative densities from left to right: 0.1, 0.2, 0.3 and 0.4. (b) Position of virtual extensometers used to determine compressive strains via digital image correlation.

4.3.2 Macroscopic compression experiments

The shell-lattice specimens are tested using a screw-driven universal testing machine (Model RME250, Zwick) equipped with two flat steel loading platens and a 250kN load cell. No grease or lubricant is applied to the platens. For each specimen a crosshead velocity corresponding to a constant engineering strain rate of 2×10^{-3} is applied. A high-resolution digital camera (4240 × 2824 pixels, Model GS3-U3-120S6M-C, PointGrey) is installed to monitor one face of the specimen, with a resolution of about 500 pixels per unit-cell. Macroscopic engineering strains are estimated through digital image correlation using the software Vic-2D (Correlated Solutions). Five virtual extensometers are placed

between the centers of the unit-cells of the top and bottom row (Fig. 4.5b). The reported engineering strain corresponds to the average of all five extensometers

4.4.Results

4.4.1 Scaling of the elastic properties

Recall that due to the cubic symmetry of the structures at hand, commonly-used elastic constants such as the Young's modulus E and the shear modulus G depend on the orientation of the loading direction with respect to the cubic unit-cell.

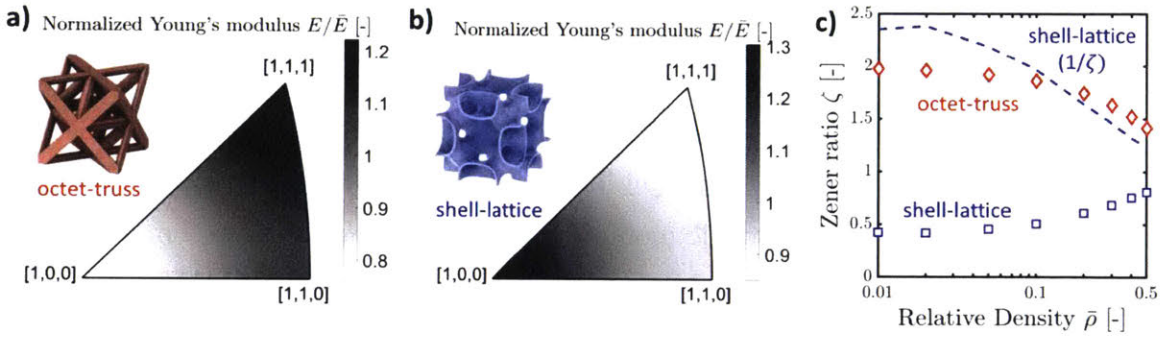

Figure 4.6: Elastic anisotropy: pole figures of the Young's moduli (as normalized by the mean for all directions) at relative density $\bar{\rho}$=0.2 for (a) the octet-truss and (b) the FCC shell lattice; (c) Zener anisotropy ratio as a function of the relative density.

This direction-dependency for the anisotropic shell-lattice and the octet truss-lattice are shown in Fig. 4.6. which includes pole figures of the Young's modulus for both metamaterials at a relative density of 0.2. It becomes immediately apparent from Fig. 4.6 that the octet truss-lattice is stiffest when loaded along the [111] direction, and softest when solicited along the [100] direction. The opposite trend is observed for the TPMS-like shell-lattice (Fig. 4.6b) despite the fact that it features the same FCC symmetries as the octet truss. A similar qualitative difference is observed with regards to shear loading: the octet truss shows the highest shear modulus in the PS1 configuration and its lowest in the PS2 configuration, while the opposite order is observed for the shell-lattice.

The degree of elastic anisotropy of cubic metamaterials can be conveniently measured by Zener's anisotropy ratio:

$$\zeta = \frac{C_3}{C_1 - C_2} = G_1/G_2 \tag{3.30}$$

which corresponds to the ratio of the shear moduli for the loading cases PS1 and PS2. The scaling of the Zener anisotropy ratio with relative density is presented in Fig. 4.6c. For the octet truss, it decreases from a value of 2 at very low relative densities to 1.4 for a relative density of 0.6. A similar trend is observed for the TPMS-like shell-lattice, i.e. the anisotropy decreases as the relative density increases. The ratio of the maximum to minimum shear modulus is 2.4 at low density, i.e. the TPMS-like structure exhibits a slightly higher anisotropy than the octet truss at low relative densities. However, the two curves intersect at relative density of about 0.15. In other words, the shell-lattices are less anisotropic than the truss-lattices at relative densities above 0.15.

The scaling of the elastic moduli, i.e. their evolution as a function of the relative density, is shown in Fig. 4.7. To highlight the scaling and to ensure a good readability of our plots, the computed macroscopic moduli are normalized by the Voigt bounds (basis material modulus times the relative density). To allow for meaningful comparisons of the stiffness of the anisotropic metamaterials, the maximum, minimum, and average values of the Young's and shear moduli are reported for each relative density. It transpires from the results that the shell-lattices exhibit high specific stiffness at high relative densities; it approaches the Hashin-Shtrikman (HS) bounds (Hashin and Shtrikman, 1963) much faster than the stiffness of the octet trusses. At low relative densities, the mean stiffness of the TPMS-like shell-lattice is still slightly higher than that of the octet trusses of equal mass, but it is far from the HS bounds. Moreover, while the octet truss response enters the sub-optimal, but linear scaling regime at low densities (e.g. the theoretical E-Modulus scaling factor is 1/5 when the octet truss is loaded along the [111] direction), the scale factor of the shell-lattices continues to decrease as the relative density decreases.

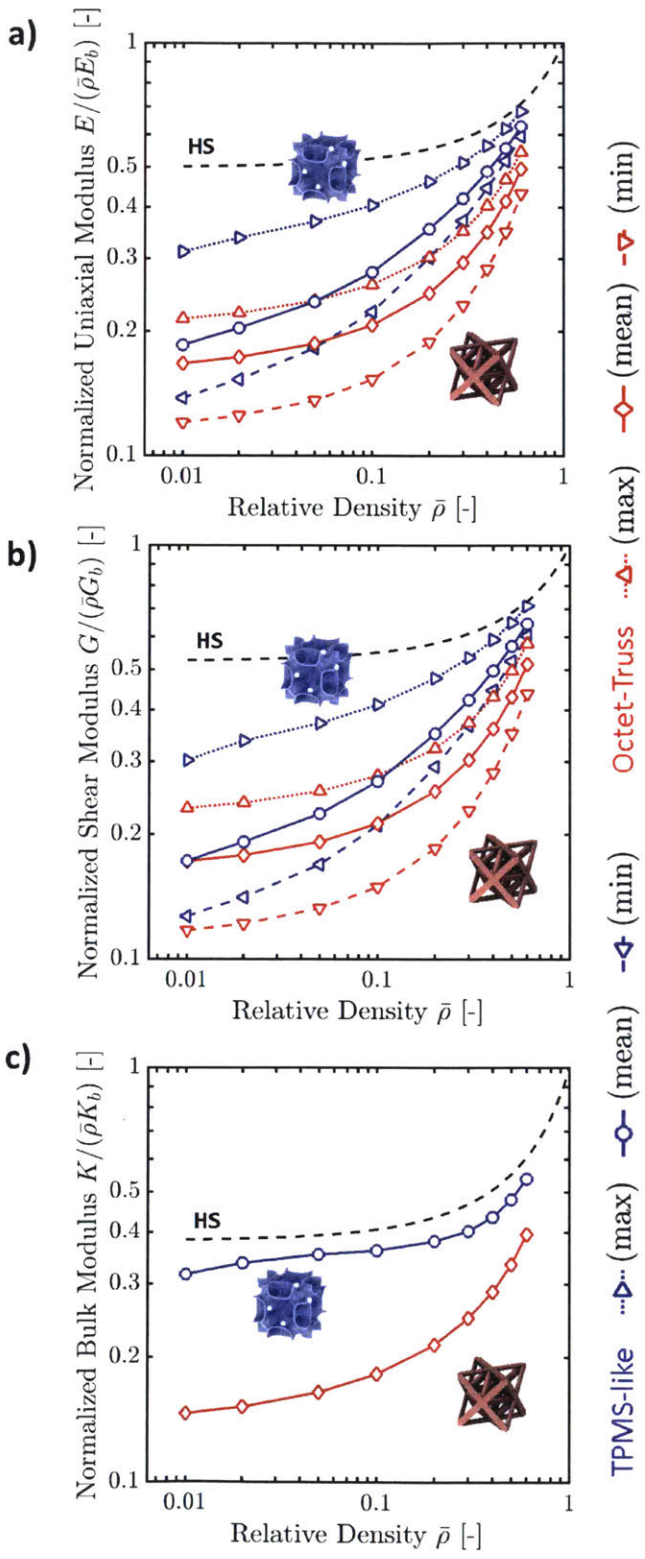

Figure 4.7: Compared scaling of elastic moduli with relative density for the octet-truss and the proposed smooth curvature structure: (a) Tensile modulus, (b) shear modulus, (c) bulk modulus. Dashed lines represent the Hashin-Shtrikman (HS) bounds for isotropic porous structures.

For all relative densities considered, the shear modulus of the TPMS-like shell-lattices is also higher than that of the octet trusses (Fig. 4.7b). The highest mean shear stiffness advantage of more than 40% is observed at relative densities of 0.2 to 0.3. The maximum longitudinal and shear stiffness of the shell-lattices is always higher than the highest stiffness of the octet trusses of the same relative density. The same is observed for the lower bounds: the softest direction of the TPMS-like shell-lattice is always stiffer than the softest direction of the octet truss for the same relative density. The differences are even more pronounced for the bulk moduli (Fig. 4.7c), where the shell-lattice is more than twice as stiff as the octet truss at low relative densities. The bulk modulus of the shell-lattice is actually close to the theoretical HS limit (dashed line) for porous solids.

The above stiffness estimates are partially validated by comparing the computational results for the octet-truss lattice at $\bar{\rho} = 0.01$ with the analytical results by Deshpande et al. (2001b), which apply in the limit of infinitesimal relative densities. It is found that the numerical modulus estimates are close to the analytical values (maximum difference of less than 8%).

4.4.2 Scaling of the initial yield stress

Figure 4.8 shows the direction dependency of the yield stress for uniaxial tension of structures of relative density 0.01 (results for other relative densities are qualitatively similar, while less anisotropic). The results depicted in Fig. 4.8a show that the octet truss exhibits only 80% of the average yield stress when solicited in the [110] direction, while pronounced yield strength peaks ($\approx$ 145% of the mean) are observed for loading along the [111] and [100] directions (the stiffest and softest directions, respectively, see Fig. 4.6a). The TPMS-like shell-lattice (Fig, 4.8b) displays a less pronounced yield strength peak (about 120% of mean) in the [100] direction (that of highest stiffness), while the [110] direction is the weakest with only 88% of the mean yield strength. The yield strength of the shell-lattice for the [111] direction is close to the mean.

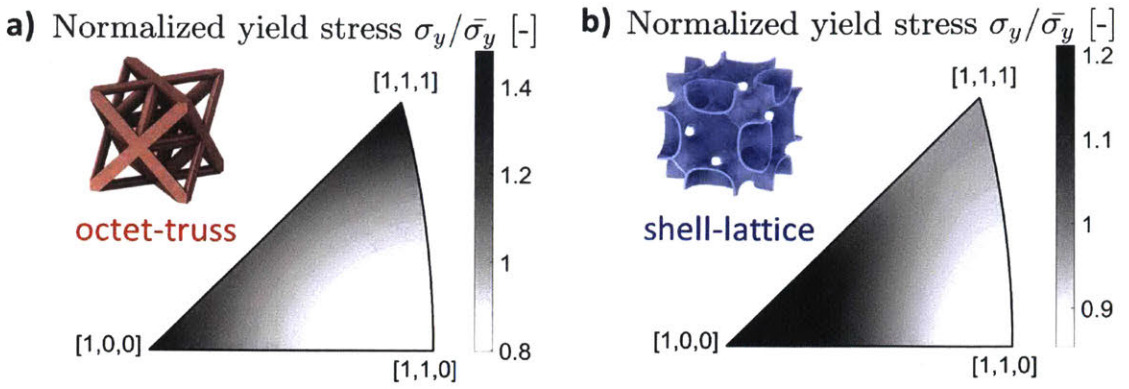

Figure 4.8: Anisotropic yield under uniaxial loading (normalized by the mean for all directions): (a) pole figure of normalized yield stress of the TPMS-like shell-lattice at relative density $\bar{\rho} = 0.01$, (b) pole figure of normalized yield stress of the octet-truss at relative density $\bar{\rho} = 0.01$.

Figure 4.9 provides an overview on the scaling of yield properties for both metamaterials in a variety of scenarios. Similar to the elastic properties, the yield strength of the TPMS-like shell-lattice is higher than that of the octet truss in almost all cases investigated. Figure 4.9a presents the scaling of yield stresses under uniaxial loading with relative density. As already indicated by the pole figures (Fig. 4.8), the directional spread of yield values is more pronounced for the octet truss than for the shell-lattice: for the octet truss, the maximum to minimum value ratio is 1.23 for $\bar{\rho} = 0.6$, and 1.83 for $\bar{\rho} = 0.01$, to be compared with 1.13 and 1.42 for the anisotropic shell-lattice at the same relative densities. Overall the shell-lattice shows higher yield values than the octet truss. Taking the ratio of mean values for yield stress, we find 1.26 for $\bar{\rho} = 0.6$ and 1.15 for $\bar{\rho} = 0.01$.

Figure 4.9b shows the scaling of maximum, mean and minimum yield properties under pure shear loading with relative density. The smooth structure is consistently stronger in these conditions for relative densities above 0.1; for example, its mean value is 1.20 times that of the octet truss for $\bar{\rho} = 0.6$, while its poorer scaling leads to a value of 0.98 that of the octet-truss for $\bar{\rho} = 0.01$. Finally, Fig. 4.9c presents the scaling of yield stress with relative density under hydrostatic pressure. In this case, the TPMS-like shell-lattice is always stronger than the octet-truss lattice: 33% stronger for $\bar{\rho} = 0.6$, and 17% stronger for $\bar{\rho} = 0.01$.

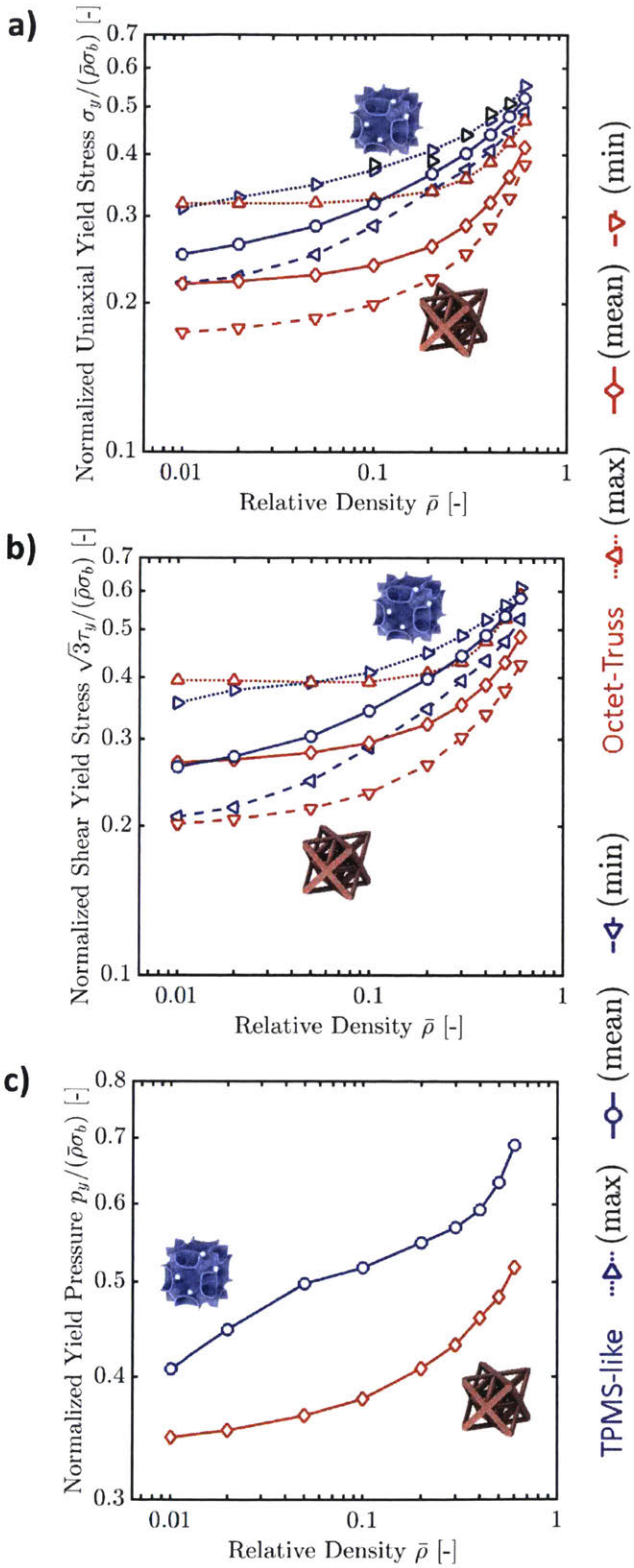

Figure 4.9: Maximum, minimum and average yield properties under (a) uniaxial tension/compression, (b) pure shear, (c) hydrostatic tension/compression as deduced from field elastic response. Black dots represent experimental results.

The above results are partially validated by comparing numerical estimates for the octet truss (at the lowest investigated relative density of $\bar{\rho} = 0.01$) to the analytical pin-jointed truss model proposed by Mohr (2005). Comparing maximum, average and minimum yield strengths under uniaxial, pure shear and hydrostatic loading, the numerical and analytical values are in agreement with a maximum relative difference of 5%.

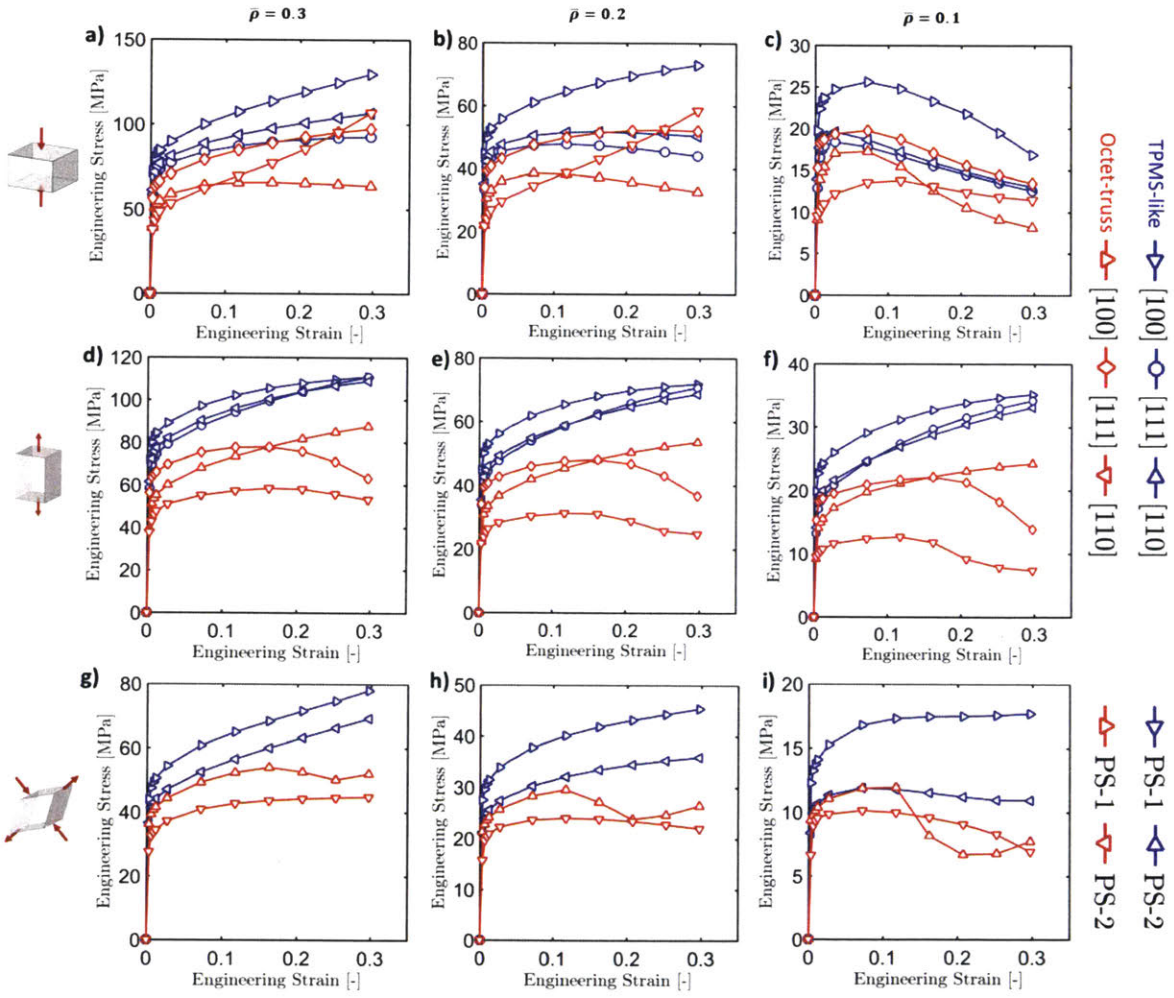

Figure 4.10: Macroscopic engineering stress-strain curves of the TPMS-like shell-lattice and the octet-truss, for different loading scenarios: (a, b, c) uniaxial compression, (d, e, f) uniaxial tension, (g, h, i) pure shear; and different relative densities: (a, d, g) $\bar{\rho} = 0.3$, (b, e, h) $\bar{\rho} = 0.2$, and (c, f, i) $\bar{\rho} = 0.1$.

4.4.3 Large strain response

Figure 4.10 presents the macroscopic engineering stress-strain curves obtained from elastoplastic simulations, for three scenarios (with different orientations) and the three relative densities (0.3, 0.2 and 0.1) at which the metamaterials start exhibiting unstable behavior. Stability is understood here in the non-conservative sense of sustained hardening in a given loading scenario. When unit-cell simulations display a peak in the macroscopic stress, localization bands are expected to form in structures containing multiple unit cells. While the elastic and elastic limit properties presented above are fairly general (for an isotropic elasto-plastic basis material with J2 yield criterion), the large strain response is not. In particular, the stability of metamaterials is expected to depend on both the geometry of structure, and on the hardening behavior of the basis material. It is safe to assume that for a basis material with lower hardening modulus the two metamaterials considered herein would present a transition from stable to unstable behavior at higher relative densities.

The simulation results (Fig. 4.10) show that the TPMS-like shell-lattice is stronger and more stable than the octet truss, and confirm the loading direction dependency of the initial yield stress. For the shell-lattice, the hardening rates rank in the same order as the yield stresses. The [100] direction displays the highest hardening rate and appears stable at densities of 0.3 and 0.2, but unstable at 0.1. The weakest [111] direction is still stable with positive but very low hardening up to a compressive strain of 30% at a relative density of 0.3, and expectedly displays unstable behavior for lower relative densities. The same is true of the slightly-higher hardening [110] direction, which loses stability at a relative density of about 0.2. The initially stronger [111] and [100] directions of the octet truss show qualitatively similar (but quantitatively weaker) behaviors, with the former displaying unstable behavior starting at a relative density of 0.2, and the latter at 0.3. In all of these cases, as relative density diminishes the stress-strain curve gradually displays less hardening, until stability is lost. A remarkable exception to that rule is the stress-strain curve obtained when loading the octet truss along the [110] direction: some struts are then perfectly aligned with the loading direction, leading to a behavior that is up to a factor that of the bulk material, with important increase in force, as seen for relative densities of 0.3 and 0.2. Although this direction displays the lowest yield point, it has the highest hardening

rate for the octet truss at those relative densities. The transition to unstable behavior (as seen for $\bar{\rho} = 0.1$) is sudden, as it is triggered by buckling at the strut level.

The advantages of the TPMS-like shell-lattice become even more pronounced for uniaxial tension (Figs. 4.10d-f). All engineering stress-strain curves for the shell-lattice exhibit a monotonically increasing response well past the basis material's maximum elongation (15% strain), and, up to a multiplicative factor, the response at different relative densities remains notably unchanged. A similar qualitative response is also observed when loading the octet truss along the [100] direction, but at a significantly lower stress level. For the two other loading directions, the tensile response exhibits an engineering stress peak at a strain of about 0.15, which corresponds to the peak force for the base material, associated with necking at the strut level, with the [110] direction lying at much lower stress levels (about 25% less at $\bar{\rho} = 0.3$ and 40% less at $\bar{\rho}$=0.4) than the [111] direction, and both of them well below the stress-levels shown by the shell-lattice.

The shear stress-strain responses are depicted in Figs. 4.10g-i. The shell-lattice shows monotonically increasing stress for $\bar{\rho} \geq 0.2$, with lower relative hardening and larger stress difference between the two directions as the relative density decreases. Its response stays well above that of the octet truss for any of the two orientations considered. At $\bar{\rho} = 0.1$ it exhibits unstable behavior as a peak stress is reached around 10% strain. The octet truss displays an unstable response in its strongest orientation (PS1) at all relative densities shown (and already at $\bar{\rho} = 0.4$). The weaker orientation (PS2) is stable at $\bar{\rho} = 0.3$ and unstable at lower relative densities.

The blue macroscopic stress-strain curves shown in Figs. 4.10a, 4.10d, 4.10g are representative for the shell-lattice response at relative densities above $\bar{\rho} = 0.3$. Note that all curves increase monotonically, irrespective of the loading scenario. For $\bar{\rho} = 0.2$ the material response becomes instable in compression in the [110] and [111] directions, in the sense that the macroscopic stress-strain response for uniaxial compression exhibits a stress peak followed by a softening phase. And for $\bar{\rho} = 0.1$, all loading cases considered lead to an early (<30% strain) peak force except for uniaxial tension. The comparison with the results for the octet truss (red curves in Fig. 4.10) reveal the higher stability of the large deformation response of the TPMS-like shell-lattice. For the octet truss architectures, all force-displacement curves exhibit stress peaks for $\bar{\rho} = 0.2$, and some already for $\bar{\rho} = 0.3$.

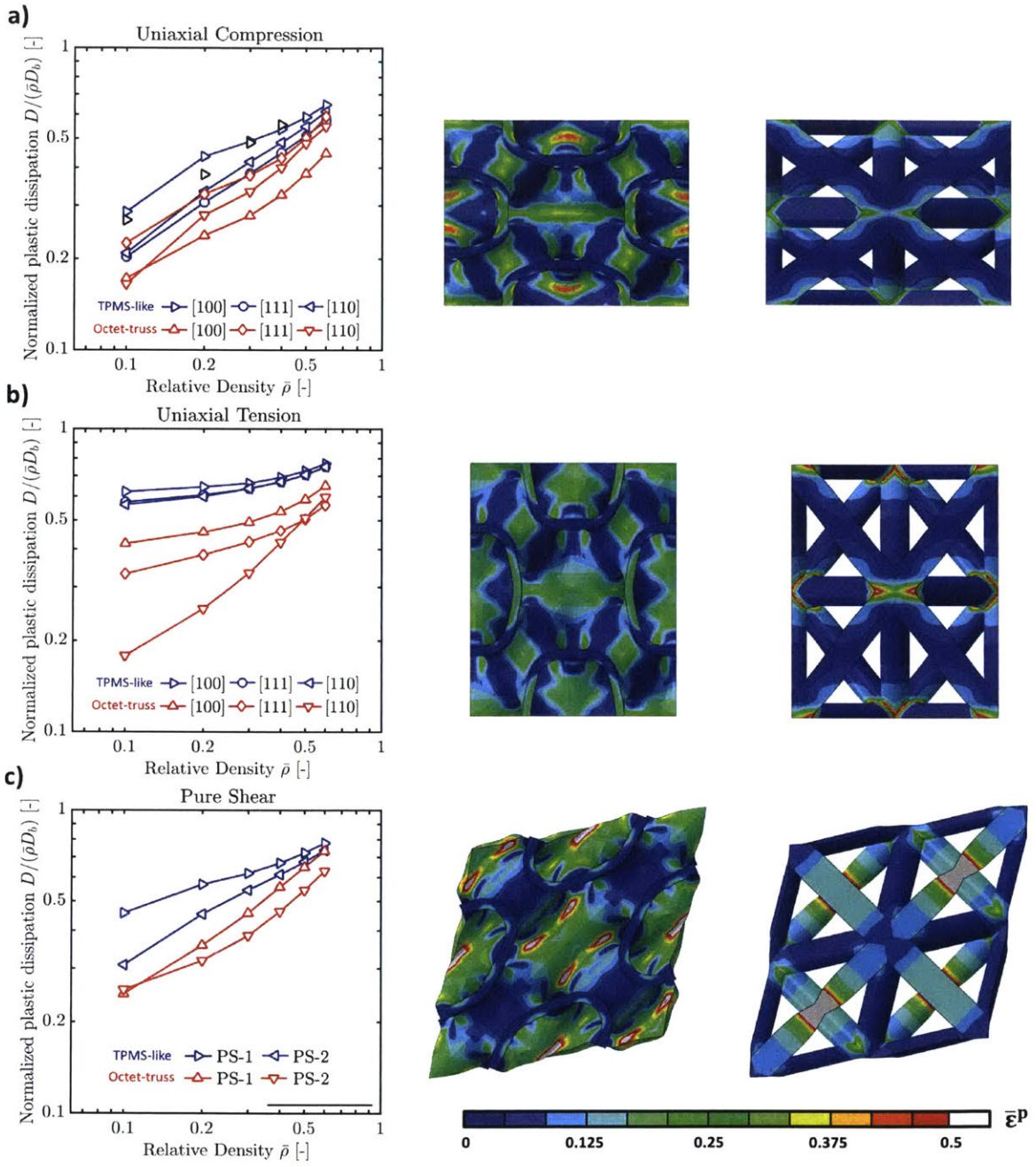

Figure 4.11: Compared scaling of normalized plastic dissipation of the octet-truss and the TPMS-like shell-lattice for different loading scenarios and orientations, and associated deformation with color-coded equivalent plastic strain at 18% engineering strain. (a) uniaxial compression, pattern in compression along [100] (b) uniaxial tension, pattern in tension along [100] (c) pure shear, deformation pattern under loading PS1. Black open symbols in (a) represent experimental results.

4.4.4 Scaling of the specific energy absorption

To evaluate the Specific Energy Absorption (SEA) capability of the proposed metamaterials, we computed the plastic dissipation from the simulations for different relative densities. In Fig. 4.11, the plastic dissipation per unit volume (as normalized by the plastic dissipation of the basis material times the relative density) is plotted as a function of the relative density. This measure is identical to the ratio of the specific energy absorption of the metamaterial and that of the basis material,

$$\frac{D}{D_s\bar{\rho}} = \frac{D\rho_s}{D_s\rho} = \frac{\Psi}{\Psi_s} \tag{3.31}$$

For uniaxial compression (Fig. 4.11a), it can be seen that the SEA of the TPMS-like shell-lattice is almost always higher than that of the octet truss – irrespective of the loading direction and relative density. The SEA for the weakest direction of the shell-lattice structure is approximately equal to the SEA for the strongest direction of the SOT structure. It is worth noting that the overall structural efficiency increases as the relative density increases. For a relative density of $\bar{\rho} = 0.5$, we have $D_{TPMS} \approx 0.55\bar{\rho}D_s$, while it is only about $0.2\bar{\rho}D_s$ at a relative density of $\bar{\rho} = 0.1$. Moreover it is expected that for configurations that show a local peak in force, the overall response of larger scale structures comprising several unit-cells would differ slightly: localization bands, shear bands, and a resulting plateau in force that would impact the SEA of the structure.

In the case of uniaxial tension (Fig. 4.11b), the energy absorbed by the shell-lattice is significantly higher than that of the octet truss for all directions of loading. Moreover, the scaling is more stable (nearly linear) for uniaxial tension than for uniaxial compression. It should be noted that the comparison point is beyond the maximum force of the bulk material: the bulk dissipation value assumes uniform strain and would be an overestimate in the case of an actual component loaded in tension, where the necking and fracture are likely to limit the energy absorption capability. The same is true of un-stable directions for the metamaterials (here, for the octet truss only). At a relative density of $\bar{\rho} = 0.5$, we have $D^{UT}_{TPMS} \approx 0.75\bar{\rho}D_s$, which drops only slightly to $D^{UT}_{TPMS} \approx 0.6\bar{\rho}D_s$ at $\bar{\rho} = 0.1$. As for uniaxial compression, the specific energy absorption under uniaxial tension is the highest for loading along the [100] direction of the shell-lattice structure. The octet truss has widely

different energy absorption depending on the loading direction, due to localization within the struts depending on their alignment with the loading direction, and in any case much lower absorption capability in tension.

At a relative density of $\bar{\rho} = 0.5$, the scaling of the energy absorption capability of the shell-lattice for shear (Fig. 4.11c) is comparable to that for uniaxial tension, i.e. $D_{TPMS}^{PS} \approx 0.7\bar{\rho}D_s$. However, it decreases to $D_{TPMS}^{PS} \approx 0.3\bar{\rho}D_s$ for loading a TPMS-like shell-lattice of $\bar{\rho} = 0.1$ in the PS1 plane. In any case, it is always higher than that of the octet truss, in particular at low relative densities.

4.4.5 Experimental validation

Figure 4.12a shows the measured engineering stress-strain curves for uniaxial compression along the [100] direction of the additively-manufactured TPMS-like shell-lattice specimens. The experimental results for $\bar{\rho} = 0.3$ and $\bar{\rho} = 0.4$ are in reasonable agreement with the unit-cell simulations. For strains between 5% and 30%, the experimentally-measured and numerically-predicted stresses are within 10% of each other. The simulation for $\bar{\rho} = 0.2$ consistently overestimates the stress by 15% over that range, which is attributed to a larger sensitivity to imperfect boundary conditions. Switching from unit-cell models with periodic boundary conditions to models of cubic specimens composed of $3 \times 3 \times 3$ unit cells (blue curves in Figure 4.12a) reduces the maximum difference in stress to less than 9%. The overall stress level for $\bar{\rho} = 0.1$ is also similar for the experiment and the simulation, but the specimen size-dependent oscillation of the stress-strain curve is not captured by the unit-cell simulation (as expected). Photographs taken during the compression experiments (Fig. 4.12b) confirm that shell-lattice structures remain stable at relative densities above 0.2. As anticipated from the simulation results, the response of the $\bar{\rho} = 0.1$ specimen is unstable, i.e. the deformation localizes within a narrow band at the unit-cell level. In the photographs shown in Fig. 4.12c, the void phase of the specimen becomes apparent as black spots within those unit-cells that experienced the highest deformation.

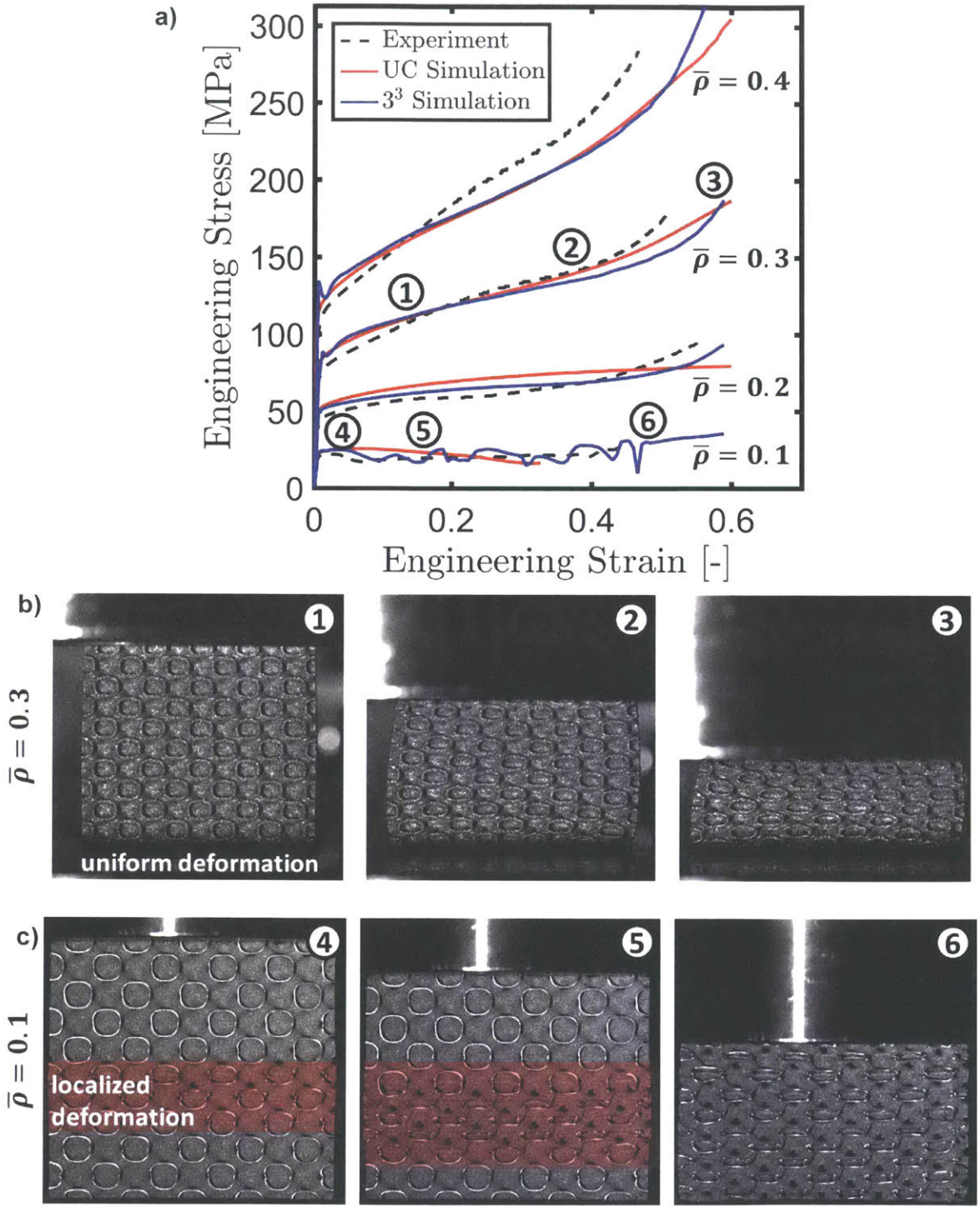

Figure 4.12: Results from uniaxial compression experiments of the TPMS-like shell-lattice along the [100] direction: a) experimental and computational stress-strain curves. b) selected photographs of the deformed specimen for $\bar{\rho} = 0.3$ c) selected photographs of the deformed specimen for $\bar{\rho} = 0.1$.

The yield strengths are estimated through a 0.2%-offset definition using the theoretical elastic modulus. All experimental results (black open triangles in Fig. 4.9a) fall within 5% of the estimated initial yield values. Black open triangles are also included in Fig. 4.11a to show the experimentally-measured plastic dissipation at 30% strain next to the simulation results. For the largest relative densities ($\bar{\rho} = 0.3$ and 0.4), these measurements fall within 3% of the numerically predicted ones. The experimentally determined SEA at 30% engineering strain is 7.3, 10.5, 13.2 and 15.3 J/g for the $\bar{\rho} = 0.1, 0.2, 0.3$ and 0.4 specimens, respectively.

The Young's modulus estimates fall within 30% of the theoretical values. However, these are not presented as a model validation since the experiments were not designed for measuring elastic properties. As described in Bonatti and Mohr (2017), the combination of cyclic elastic loading along with local optical strain measurements appears to be more appropriate for obtaining reliable Young's modulus estimates from experiments on porous metamaterials.

4.5. Conclusions

Smooth shell structures of FCC symmetry are obtained by locally smoothening the geometry of thin-walled hollow octet trusses. Even though the surfaces are defined through a function that minimizes the total curvature, the resulting surface turns out to be similar to a Triply-Periodic Minimal Surface (TPMS). We compare the effective mechanical properties of the TPMS-like shell-lattice with those of the widely-used octet truss-lattice. Paying special attention to anisotropy, the elastic stiffness, yield strength and the large deformation response of these metamaterial structures is determined through detailed finite element simulations for relative densities ranging from 1% to 50%. Both structures display an important anisotropy with max-to-min stiffness ratios of up to 2 as a function of the direction of loading. The results reveal that the mechanical properties of the shell-lattices are almost always superior to those of the stretching-dominated octet truss-lattices of equal mass. In particular, the shell-lattices outclass the octet trusses in terms of plastic dissipation ($\bar{\rho} > 0.1$). For example, at a relative density of 20%, the energy absorption (under compression) of the TMPS-like shell-lattice is 80% higher than that of an octet truss-lattice

of the equal mass when comparing the strongest and weakest directions. The computational results are confirmed through compression experiments on additively-manufactured stainless steel 316L shell-lattice specimens.

The good mass-specific mechanical properties observed for high relative densities along with the absence of discrete joints make the anisotropic and isotropic shell-lattices a strong candidate for hierarchical designs. Their open structure also allows the shell-lattices to be fabricated using powder-bed and liquid bath based additive manufacturing techniques, as opposed to the closed-cell structure of plate-lattices. From the point of view of multi-functionality, it is worth noting that the shell-lattices have the particularity of separating two fluid phases of approximately equal volume which is of interest to (heat-, chemical-) exchanger applications.

In the following chapters, we will extend those results. A first question concerns whether and how the choice of topology (or genus, e.g. Grosse-Brauckmann 2012) of the surface affects the macroscopic mechanical properties. This question is partially addressed in Chapter 5. A second question concerns the choice of the functional that defines the middle surface of the shell-lattices. We will begin an investigation of this question in Chapter 6. Finally, some studies (e.g. Lee et al. 2017) comment on the stretching- or bending-dominated nature of shell-lattices. A tentative answer is presented in Appendix 2.

5. Mechanical behavior of cubic shell-lattices

This chapter is adapted from Bonatti and Mohr (2019b).

The present chapter investigates the effect of the type of cubic symmetry on the stiffness and large deformation response of shell-lattices. Numerical simulations are performed to characterize the elastic and plastic properties of shell-lattices of Body-Centered Cubic (BCC) and Simple-Cubic (SC) symmetry, covering relative densities ranging from 1% to 80%. Furthermore, we extend the results of the previous chapter for shell-lattices of FCC symmetry to enable the comparison of the full material property spectra of FCC, BCC and SC shell-lattices. Special efforts are made to account for the important effect of anisotropy of the TPMS-like lattices. Design maps for tailoring the elastic anisotropy of cubic shell-lattice topologies are also developed and used to provide an analytical description of new topologies yielding elastically-isotropic shell-lattices of cubic symmetry. Large strain compression experiments are performed on additively-manufactured stainless steel 316L shell-lattices of FCC, BCC and SC symmetry to validate selected simulation results.

5.1. Metamaterials investigated

5.1.1 Smooth shell-lattices of cubic symmetry

The shell-lattices described herein are obtained from smoothening the topology of tube-lattices (also referred to as hollow truss-lattices). Details on the generation of smooth FCC shell-lattices are provided in in the previous Chapter. The shell-surfaces defined by tube-lattices are meshed and used as an initial condition. Subsequently, the nodal positions of the mesh are adjusted such as to minimize the cost function:

$$J = \left[\int_{\Omega} (k_1^2 + k_2^2)^2 \, dA\right]^{1/2} \tag{5.1}$$

Introduced earlier, where Ω is the surface, and k_1 and k_2 are its principal curvatures. For each of the cubic structures, its symmetryes are leveraged when carrying out the optimization, i.e. instead of meshing the full cubic unit-cells, the shell surfaces comprised

in smaller volumes (see red tetrahedra in Fig. 5,1) are smoothened. This means that the parameterization provided in Paragraph 4.1.2.1 is adapted to the special cases of the SC and BCC shell-lattice, respectively. They follow the same logic and are not presented here for the sake of concision.

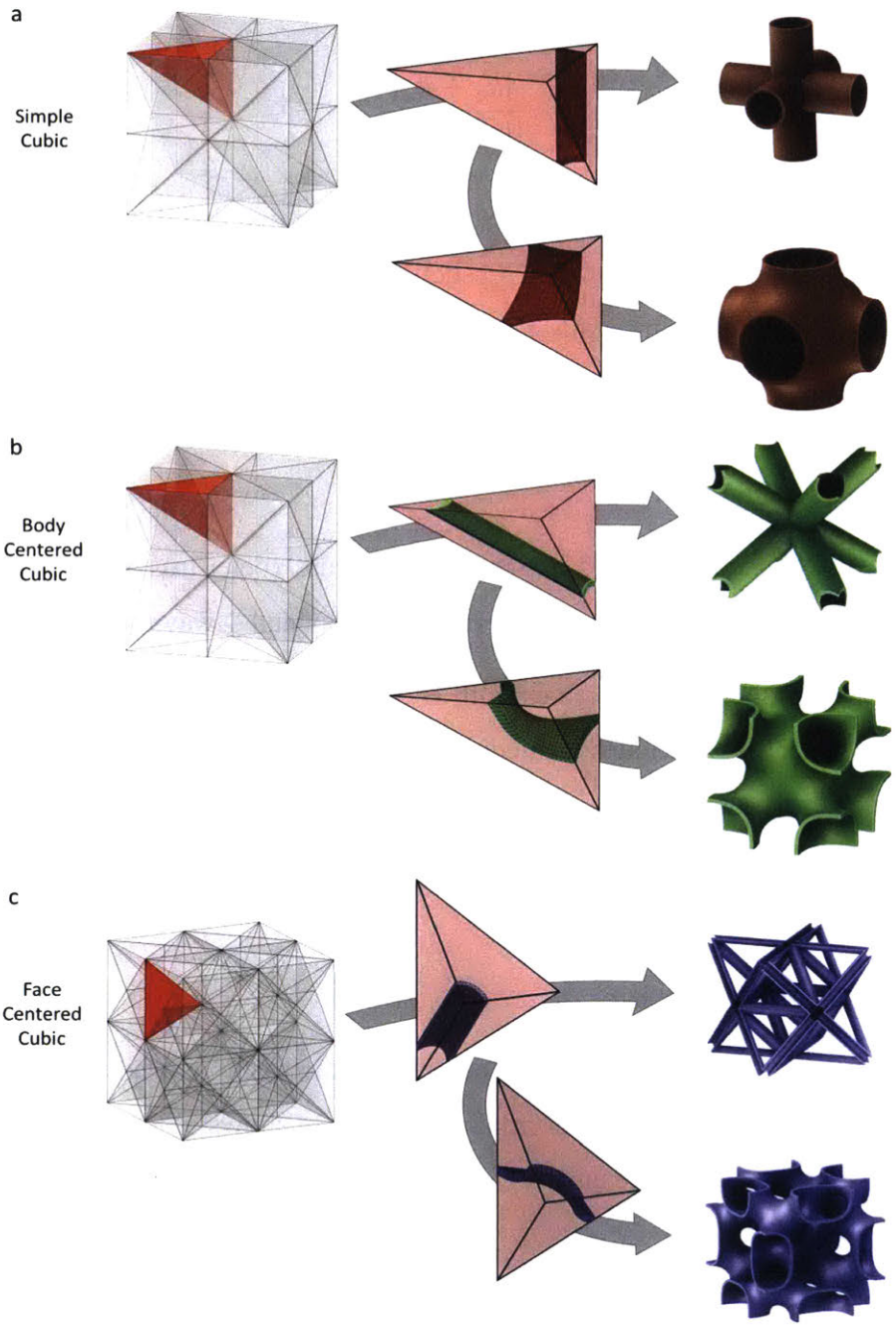

Figure 5.1: Decomposition of the geometries using structural symmetries. a) Simple Cubic structures. b) Body Centered Cubic structures. c) Face Centered Cubic structures.

Figure 5.1 also presents the unit-cells of the obtained smooth-shell structures. They are reminiscent of triply periodic minimal surfaces as they share the same boundary conditions and symmetries. Specifically, the BCC shell-lattice resembles Schoen's I-WP surface, the SC-shell is a modified Schwarz Primitive surface, and the FCC-shell is similar to Schoen's F-RD structure. The differences between the obtained smooth shell structures and their TPMS counterparts become apparent when evaluating the local curvature measure

$$\frac{|k_1 + k_2|}{|k_1| + |k_2|} \tag{5.2}$$

While it is always zero for the TPMS structures, we find that this value has an average of 8% for the SC-shell, 14% for the BCC-shell, and 15% for the FCC-shell. Given that our cost-function aims at eliminating peaks in local principal curvatures, the obtained structures may also be seen as smoothened TPMS structures. It is also worth noting that each of the obtained surfaces separates the unit-cell into two domains of approximately equal volume (see Figure 5.2b):

- The FCC-shell separates a smooth FCC truss (octet-truss) from a smoothened rhombic dodecahedral truss (alternating 8-way and 4-way nodes).
- The BCC-shell separates a smooth BCC truss, from a "wrapping package" truss, with planar 4-way nodes located at the center of the faces and on the middle of the edges of the unit-cell.
- The SC-shell is particular in that it separates two smooth SC trusses.

5.1.2 Shell-lattice metamaterials

Shell-lattice metamaterials are obtained by symmetrically extruding the smooth shell surfaces along their local surface normal. Figure 5.2a shows a detailed plot of the shell thickness t_w normalized by the unit-cell side-length l_s, as a function of the relative density,

$$\bar{\rho} = \rho/\rho_b, \tag{5.3}$$

with ρ and ρ_b denoting the density of the shell-lattice and constituent material, respectively. To avoid overlapping surfaces, the shell thickness must be smaller than twice

the smallest radius of curvature found on the surface. This determines the maximum achievable relative density: 0.85 for the SC-shell, 0.75 for the BCC-shell, and 0.65 for the FCC-shell. The surface area of the mid-plane of the shell structure comprised in a unit cell is $4.80l_s^2$ for the FCC-shell, $3.46l_s^2$ for the BCC shell, and $2.34l_s^2$ for the SC-shell. This implies that for the same relative density and shell thickness, the unit cell of the SC-shell is significantly smaller ($1/8^{th}$ of the volume for low relative densities) than the FCC unit cell. Conversely, for the same relative density and unit cell size, the SC shell is twice as thick as the FCC shell (at low relative densities).

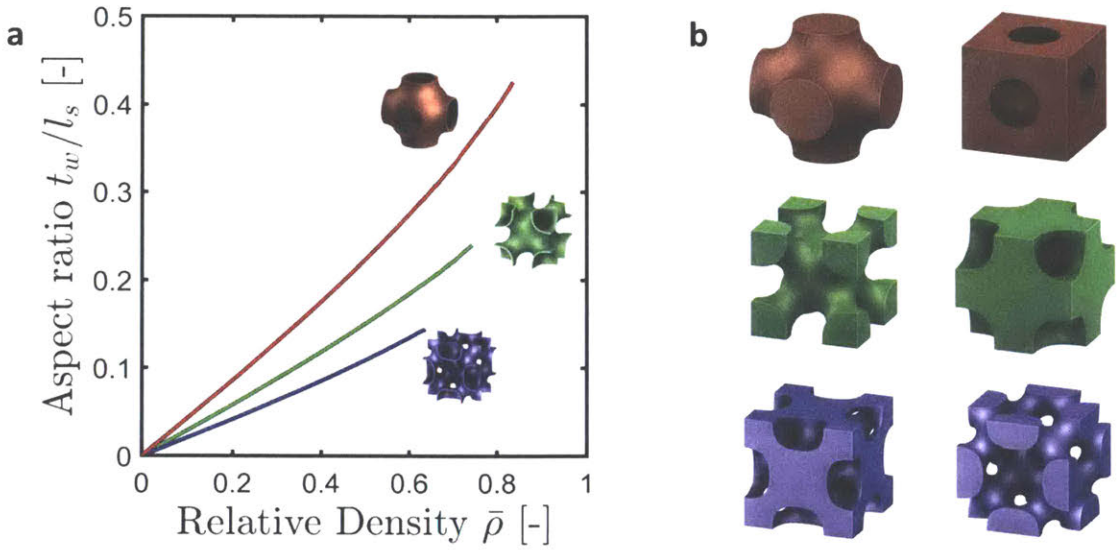

Figure 5.2: a) Ratio of wall-thickness to unit-cell side-length as a function of the relative density. b) View of the two phases separated by the (top-to-bottom) FCC, BCC and SC shell-lattices.

From a manufacturing perspective, it is noted that the proposed shell structures are free from internal low-hanging surfaces in any building direction. Due to the smoothness of the surfaces, the shell walls are always perpendicular to the planes of symmetry of the structure. As a consequence, parts that are cut along those planes do not possess unsupported features that may lead to problems during additive manufacturing (e.g. selective laser melting, stereolithography or binder jetting).

5.2.Numerical

Finite element simulations are conducted to identify the stiffness, yield strength and energy absorption capability of the shell-lattices. The relative density grid considered includes every percent from 1% to 10%, followed by steps of 10% up to the maximum achievable relative density. Two types of simulation models are built: unit-cell models with periodic boundary conditions, and multi-cell specimen models to assess the large strain compression response.

5.2.1 Basis material

The material model used in simulations is the elasto-plastic model used in earlier chapters to model additively-manufactured 316L stainless steel.

5.2.2 Unit-cell meshes

The oriented unit-cell geometries correspond to the ones introduced in Figure 2.4. The shell-lattices are meshed with hexahedral elements C3D8I with five elements through the thickness. The in-plane density of the mesh is chosen so that less than 1% difference in stiffness is observed with a four-times coarser mesh. This results in [100] unit-cell meshes composed of 245'760 elements for the SC-shell, 491'520 elements for the BCC-shell and 600'000 elements for the FCC-shell, respectively. Four times coarser meshes are used for the models of structures featuring relative densities above 10%.

The implicit solver Abaqus/Standard is used to perform the unit-cell simulations. Contact is defined between all surfaces with a friction coefficient of 0.2. Periodic micro-displacement boundary conditions are applied following the methodology detailed in Chapter 2.

5.2.3 Multi-cell specimen models (for large strain compression only)

The results from unit-cell models are expected to become invalid in case the metamaterials exhibit a foam-like crushing behavior under uniaxial compression. In the previous chapter, this materialized through an important difference between numerical and

experimental results on the FCC shell-lattice at relative density 0.1. To obtain more meaningful results, the uniaxial compression response is investigated using full specimen models comprising multiple unit-cells. The multi-cell specimen is then quasi-statically compressed between two platens that are modeled as geometric rigid surfaces. The multi-cell assemblies are meshed by triangular shell elements (type S3 of the Abaqus element library). The commercial software Abaqus/Explicit is used, with semi-automatic mass scaling corresponding to a target number of 500'000 time steps for completing the compression analysis. The multi-cell specimens consist of bricks featuring a side-length of about three times the side-lengths of the corresponding unit cells. The edge lengths and volumes of the multi-cell specimens are

- $3 \times 3 \times 3 = 27$ for the [100] specimens,
- $2\sqrt{2} \times 2\sqrt{2} \times 3 = 24$ for the [110] specimens and
- $2\sqrt{3} \times 2\sqrt{2} \times \sqrt{6} = 24$ for the [111] specimens.

The meshes used contained about 7'000, 14'000 and 12'000 elements per [100] unit-cell (i.e. per unit volume) for the SC-, BCC- and FCC-multi-cell specimens, respectively. The [100] BCC multi-cell specimen therefore features the largest number of shell elements (about 370'000 elements). The contact definition assumes a friction coefficient of 0.2 for both internal and platen-to-specimen contact.

5.2.4 Identification of elastic stiffness tensor and yield stress estimation

For each metamaterial configuration (combination of structure type and relative density), six strain-driven elastic simulations are performed on a [100] solid-element unit-cell in which a small strain increment is imposed. The applied macroscopic strain tensors read

$$\mathbf{E} = \varepsilon_0 \, \boldsymbol{e}_i \otimes_s \boldsymbol{e}_j, \text{ where } \boldsymbol{e}_i \otimes_s \boldsymbol{e}_j = \frac{\boldsymbol{e}_i \otimes \boldsymbol{e}_j + \boldsymbol{e}_j \otimes \boldsymbol{e}_i}{2} \tag{5.4}$$

with $i, j = 1,2,3$. From these simulations, two types of metamaterial properties are determined.

Firstly, the anisotropic macroscopic stiffness tensor is deduced. To visualize the anisotropy of the elastic properties, we compute the direction dependency of the Young's and shear moduli. In addition to the macroscopic moduli, the macroscopic-strain-to-microscopic-stress stiffness tensors are extracted from the results of the unit-cell computations. For each integration point n of the unit-cell mesh, the local strain evolves linearly with the imposed macroscopic strain, which can be summarized by the relation $\boldsymbol{\sigma}_n = \boldsymbol{A}_n : \boldsymbol{E}$, with $\boldsymbol{\sigma}_n$ denoting the average stress in element n, and $\boldsymbol{A}_n$ being a local stiffness tensor. Given that $\boldsymbol{\sigma}_n$ and $\boldsymbol{E}$ are both symmetric, $\boldsymbol{A}_n$ has 36 independent components that are obtained by evaluating the 6 components of the local stress response under each of the 6 loading scenarios. Realizing that $\boldsymbol{\sigma}_n = \boldsymbol{A}_n : \boldsymbol{E} = \boldsymbol{A}_n : \boldsymbol{A}^{-1} : \boldsymbol{\Sigma}$, one can deduce an estimate of a microstructure-based yield stress under any loading condition, which corresponds to the initial yield strength of the material. The elastic limit is herein considered to be reached when elements accounting for 5% of the initial volume of the mesh present a von Mises equivalent stress superior to the bulk material's yield stress. Instead of extracting the entire yield surface, we provide estimates of extremal and mean yield values under uniaxial and hydrostatic loading, as well as the distribution of initial yield strength with loading orientation in the uniaxial loading case.

5.2.5 Identification of the large strain tensile response

For each mesh considered with a relative density above 10%, elastoplastic simulations are performed for uniaxial tension under various loading orientations. Mixed boundary conditions are applied, with the non-zero component of the stress-tensor being strain-driven,

$$\begin{cases} H_{11} = \lambda \\ P_{12} = P_{21} = P_{22} = P_{33} = P_{13} = P_{31} = P_{23} = P_{32} = 0 \end{cases} \tag{5.5}$$

These boundary conditions are applied in the $\mathcal{B}_{100}$, $\mathcal{B}_{110}$ and $\mathcal{B}_{111}$ coordinate systems to identify the large strain tension response for uniaxial tensile loading along the [100], [110] and [111] directions. Recall from Chapter 2:

$$\mathcal{B}_{100} = \left\{\begin{bmatrix}1\\0\\0\end{bmatrix}, \begin{bmatrix}0\\1\\0\end{bmatrix}, \begin{bmatrix}0\\0\\1\end{bmatrix}\right\},$$

$$\mathcal{B}_{110} = \left\{\begin{bmatrix}1\\1\\0\end{bmatrix}/\sqrt{2}, \begin{bmatrix}-1\\1\\0\end{bmatrix}/\sqrt{2}, \begin{bmatrix}0\\0\\1\end{bmatrix}\right\},$$

$$\mathcal{B}_{111} = \left\{\begin{bmatrix}1\\1\\1\end{bmatrix}/\sqrt{3}, \begin{bmatrix}1\\-1\\0\end{bmatrix}/\sqrt{2}, \begin{bmatrix}1\\1\\-2\end{bmatrix}/\sqrt{6}\right\}.$$

5.3.Experimental

Uniaxial compression experiments are performed on FCC-, BCC- and SC- specimens at relative densities of 10%, 20% of 30%. The main purpose of these experiments is to verify the numerical results under large strains.

5.3.1 Specimen description

In a first step, the metamaterials are compressed along their stiffest direction only. To verify our model's capability to capture the directional-dependency of the large strain compression response, compression experiments are also performed along the [100], [110] and [111] directions for 30% relative density BCC-structures. Two specimens of each type are tested. Nearly-cubic specimen geometries in the different orientations are obtained by stacking the respective unit-cells. For BCC and SC specimens, we have

- $7 \times 7 \times 7 = 343$ unit-cells for the [100] specimens,
- $5\sqrt{2} \times 5\sqrt{2} \times 7$=350 for the [110] specimens, and
- $4\sqrt{3} \times 5\sqrt{2} \times 3\sqrt{6} = 360$ for the [111] specimens.

Given their low t_w / l_s ratio, the FCC [100]-specimens are designed with 5x5x5 unit-cells, only.

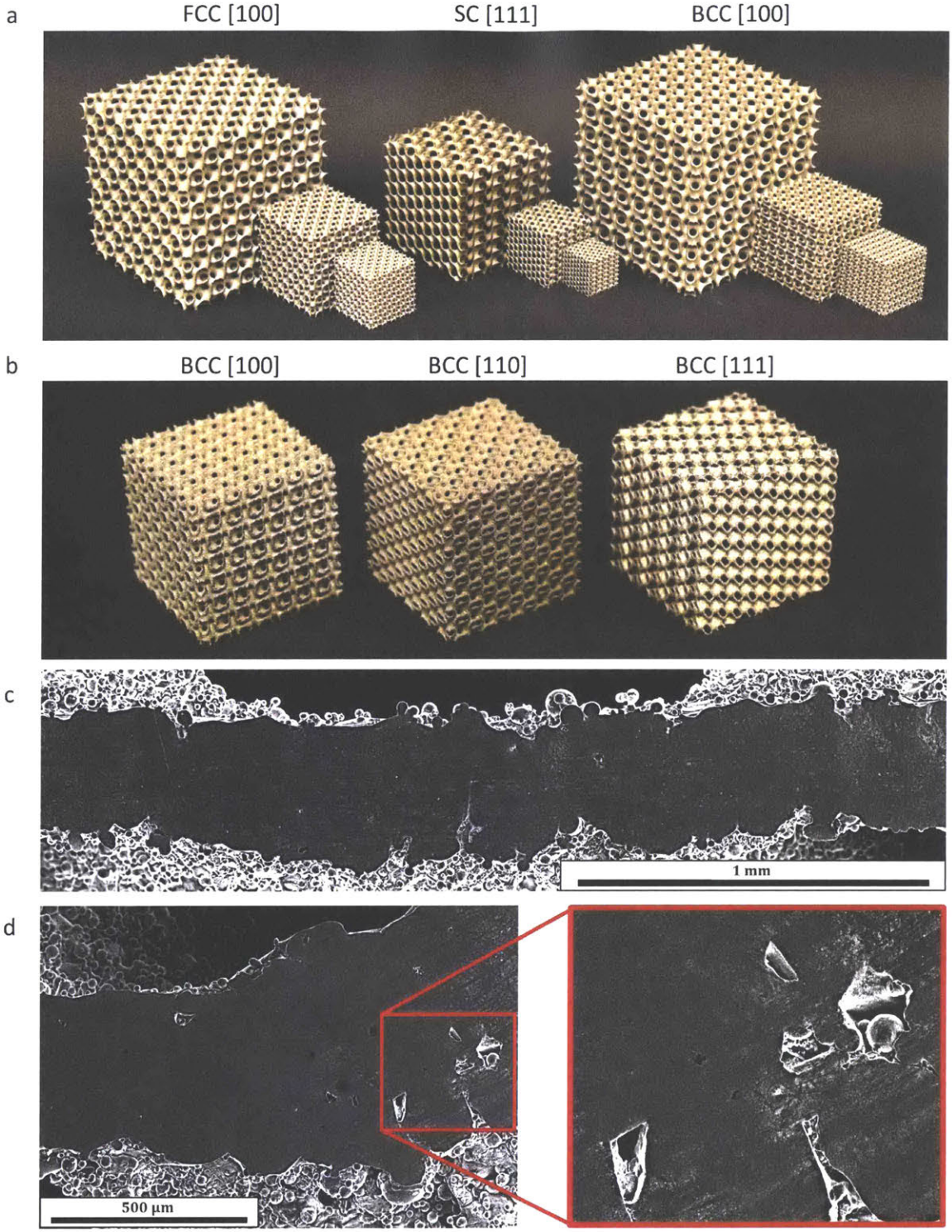

Figure 5.3: a) View of untested specimens of relative densities 10%, 20% and 30%. b) View of untested BCC specimens of relative density 30% with different orientations. c-d) Scanning electron micrographs of a polished cross-section of a BCC shell-lattice specimen of relative density 20%, revealing surface roughness as well as internal porosity.

Type	Relative density	Orientation	Dim. 1 (mm)	Dim. 2 (mm)	Dim. 3 (mm)	Error on mass (%)
FCC	0.1	100	95.53	95.53	95.53	-7.7
SC	0.1	111	64.64	65.96	68	-12.0
BCC	0.1	100	96.12	96.12	96.12	-6.9
FCC	0.2	100	47.50	47.50	47.5	-6.1
SC	0.2	111	32.15	32.82	34.10	-7.2
BCC	0.2	100	47.84	47.84	47.84	-8.2
FCC	0.3	100	31.35	31.35	31.35	-5.4
SC	0.3	111	21.25	21.69	22.54	-7.2
BCC	0.3	100	31.64	31.64	31.64	-7.3
BCC	0.3	110	31.96	31.96	31.64	-6.5
BCC	0.3	111	31.32	31.96	33.22	-10.7

Table 5.1: Dimensions of the specimens and reported error on mass.

All specimens are additively-manufactured from stainless steel 316L using selective laser melting. Specimens are fabricated for three different relative densities: 10%, 20% and 30%. Photographs of the specimens are given in Figs. 5.3a and 5.3b. A summary of the material geometry and the weight properties (as designed and measured) is provided in Table 5.1. All verified outer dimensions are within 1% of those prescribed. However, the specimens have a significantly lower mass than expected (between 5% and 12% lower). This is attributed to the effects of internal porosity (Fig. 5.3d) and high surface roughness (Fig. 5.3c). All specimens featured a targeted wall-thickness of $400\mu m$ while the surface roughness of the additively-manufactured shell-lattices is only one order of magnitude lower.

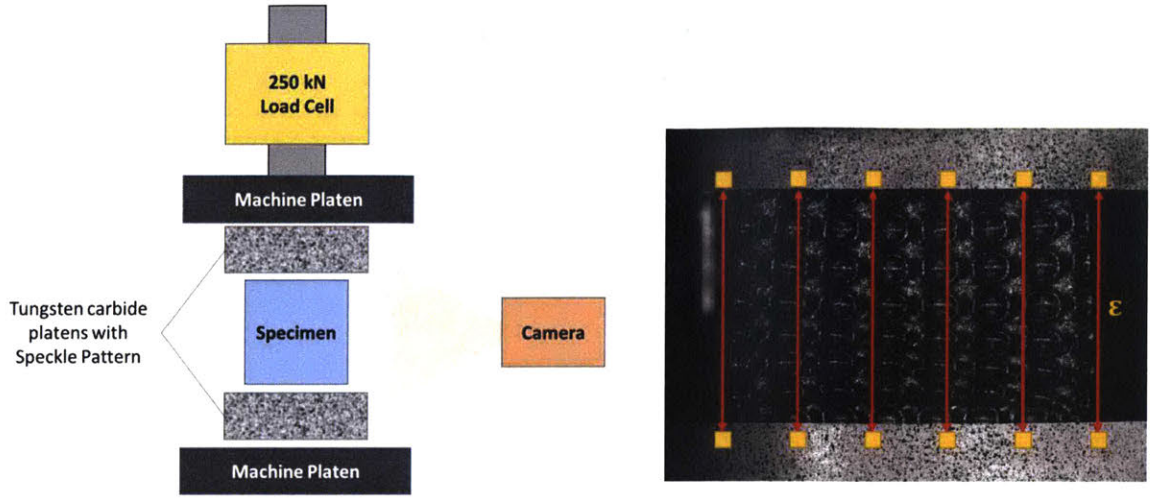

Figure 5.4: Left: diagram of the experimental set-up. Right: experimental picture with position of extensometers.

5.3.2 Experimental set-up

Figure 5.4 provides a diagram of the experimental set-up. Each specimen is loaded using a crosshead velocity corresponding to an engineering strain rate of $1.67 \cdot 10^{-2} s^{-1}$. The specimens are tested using a screw-driven universal testing machine (Model RME250, Zwick), equipped with two flat steel loading platens and a 250kN load cell. Tungsten carbide platens of a diameter closer to the dimensions of the specimens are added in the case of the smaller specimens. No grease or lubricant is applied. A speckle pattern is applied to the side of the platens. A high resolution digital camera (4240×2824 pixels, Model GS3-U3-120S6M-C, Point Grey) is used to monitor both the movement of the platens, as well as one face of the specimen. The displacements of both platens are estimated via digital image correlation. The difference in their displacements is used to estimate engineering strains.

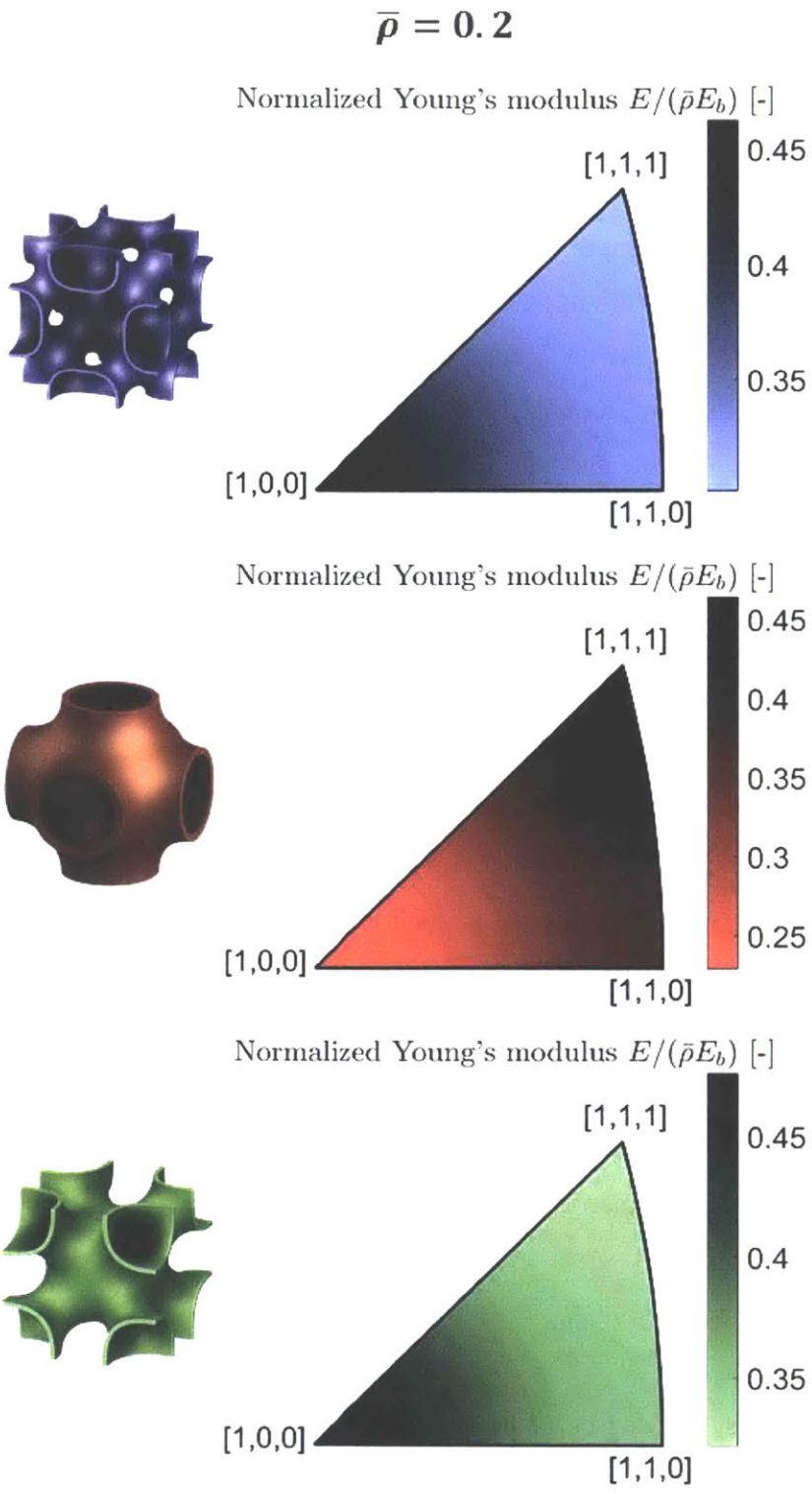

Figure 5.5: Pole figures showing the directional distribution of the Young's modulus of (from top to bottom) the FCC, the SC and the BCC shell-lattices at relative density 20%, reduced by the bulk material's Young's modulus times the relative density.

5.4. Results

5.4.1 Elastic properties

The elastic properties are determined for all three types of shell-lattices (FCC, BCC, SC) covering 15 to 17 different relative densities ranging between 1% and 80%. Given the cubic symmetry of the metamaterials, the directional dependency of the structures is represented by pole figures for the Young's modulus, with the corners of the pole figures representing the moduli for uniaxial stress loading along the [100], [110] and [111] directions.

Figure 5.5 shows the pole figures for all three structures for a relative density of 0.2. Both the FCC and BCC-shells exhibit their stiffest uniaxial behavior when solicited along the [100]-direction, while their softest elastic response is observed for loading along the diagonal direction [111]. The opposite trend is observed for the SC structure. The previous result implies that the FCC and BCC structures have their stiffest shear behavior when changing the angle between the first two base vectors of the $\mathcal{B}_{110}$ frame (modulus $G_{\mathcal{B}_{110}}$), and the softest when changing the angle between the first two base vectors of the $\mathcal{B}_{100}$ frame (modulus $G_{\mathcal{B}_{100}}$); the opposite holds true for the SC shell structures. The pole figures shown in Fig. 5.5 are representative for all relative densities in the sense that the ordering of the strongest and weakest directions is the same irrespective of the relative density. A common measure of a cubic material's anisotropy is the Zener ratio, $\zeta = G_{\mathcal{B}_{100}}/G_{\mathcal{B}_{110}}$. Figure 5.6a presents a plot of the anisotropy level of the structures as a function of the relative density, using a symmetric version of the Zener ratio,

$$\zeta^* = G_{max}/G_{min} = \begin{cases} G_{\mathcal{B}_{100}}/G_{\mathcal{B}_{110}} = \zeta \text{ if } \zeta \geq 1 \\ G_{\mathcal{B}_{110}}/G_{\mathcal{B}_{100}} = \zeta^{-1} \text{ if } \zeta \leq 1 \end{cases} \tag{5.6}$$

For all structures, the degree of elastic anisotropy increases as the relative density decreases. Below a relative density of 40%, the SC structure exhibits the highest degree of elastic anisotropy. It is also worth noting that the FCC structure reaches a plateau at about $\zeta^* = 2.3$ (or $\zeta = 0.43$) as the relative density decreases, while the anisotropy of the other two structures keeps on increasing.

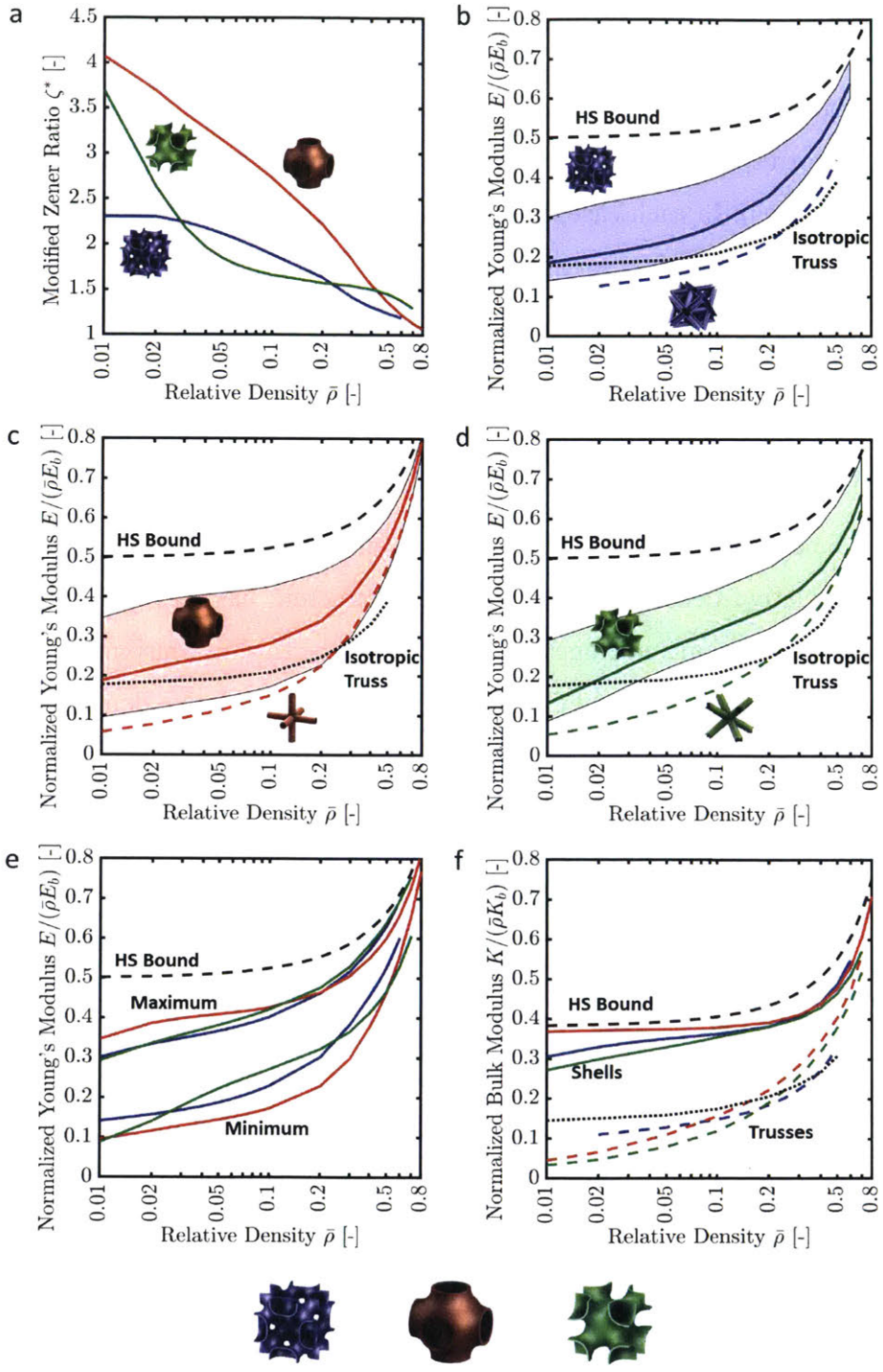

Figure 5.6: a) Modified Zener ratio as a function of the relative density. b-d) Variations with relative density of mean value and range of the normalized Young's modulus of the b) FCC c) SC and d) BCC shell-lattices, as compared to the Hashin-Shtrikman bounds, isotropic tube-lattices of the same kind, and an isotropic truss-lattice. e) Comparison of (normalized) maximum and minimum Young's moduli of the shell-lattices as a function of relative density. f) Variations of the (normalized) bulk moduli of the shell-lattices with relative density, compared to that of isotropic truss-lattices and the Hashin-Shtrikman bound.

Figures 5.6b, 5.6c and 5.6d show the scaling of the maximum, average and minimum (over all directions) Young's moduli with relative density of the FCC, SC and BCC shell-structures, respectively. Those values are compared with the scaling for isotropic tube-lattices of the corresponding kind (dashed colored curves), and for isotropic truss-lattices (dotted black curves). In each case, the minimum directional stiffness remains above the value for isotropic tube-lattices for all relative densities. The average stiffness of the shell-lattices (solid color lines) is always higher than that of the isotropic tube- and truss-lattices for relative densities greater than 2%. At a relative density of 10%, the FCC, SC and BCC shell-lattices have a maximum stiffness exceeding more than two times that of the corresponding isotropic tube- and truss-lattices.

Figure 5.6e compares the maximum and minimum stiffness scaling of all three shell-lattices. At a relative density of 10%, the BCC structure has the best overall uniaxial stiffness, with its directional average attaining 61% of the Hashin-Shtrikman Bound (HSB) compared to 54% for the SC and FCC shell-lattices. At this relative density, the Young's modulus for the stiffest direction of all three metamaterials reaches about 80% of the HSB. However, at a relative density of 1%, the BCC structure performs poorer than the two others (attaining less than 37% of the HSB). In terms of HSB, the ranges obtained over all possible directions at that density are 19%-69%, 18%-58% and 28%-60% for the SC, BCC and FCC shell structures, respectively. At relative densities above 10%, the performances of all three structures are very close to the theoretical limit. At a relative density of 30%, the maximum Young's moduli of all three structures stand between 85% and 90% of the HSB. At 50% relative density these numbers reach 90% (SC) to 96% (BCC) for the maximal values, and 70% (SC and BCC) to 79% (FCC) for minimal values.

For completeness, we show the scaling of the bulk moduli in Fig. 5.6f. All three structures exhibit approximately the same bulk modulus. Most importantly, the scaling for relative densities greater than 10% is such that the bulk modulus is always within 15% of the corresponding HSB. The SC structure even preserves the high structural efficiency when decreasing the relative density to values as low as 1%, while the efficiency of the BCC and FCC structures deteriorate such that the respective bulk moduli reach only 70% and 80% of the HSB at 1% relative density.

5.4.2 *Yield properties*

The results from the 288 unit-cell simulations are also used to estimate the initial yield strength of the metamaterials. Figure 5.7 shows the pole figures for the initial yield stress for the FCC, SC and BCC shell-lattices for selected relative densities. Figure 5.8 presents the variations of yield anisotropy (Fig. 5.8a), uniaxial yield strength (Fig. 5.8b) and yield pressure (Fig. 5.8c) with relative density. Several points are worth noting:

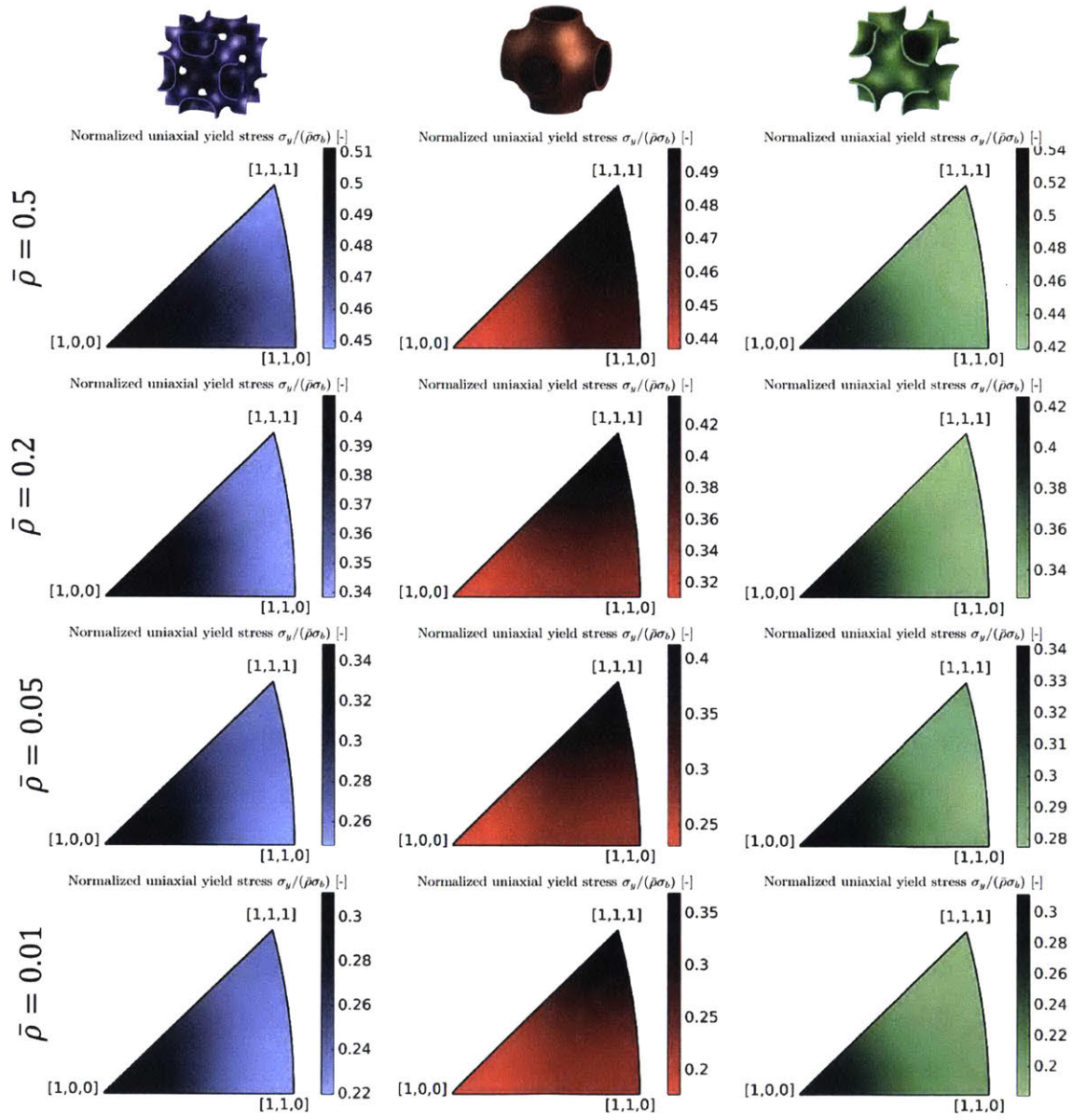

Figure 5.7: Pole figures showing the directional distribution of the uniaxial yield strength of the (from left to right) FCC, SC and BCC shell-lattices at a relative densities of (top to bottom) 50%, 20%, 5% and 1%.

- For the lowest relative density shown, the ranking of the yield strength extremal points is the same as that of the respective Young's moduli. This applies to all three structures.
- For the SC structure, the same holds true for all relative densities considered, i.e. its plastic anisotropy remains qualitatively unchanged. The ratio of maximum-to-minimum yield stress, $\gamma = \max(\sigma_y) / \min(\sigma_y)$, is $\gamma = 2.1$ at 1% relative density. It decreases as the relative density increases (Fig. 5.8a). We have $\gamma = 1.6$ and $\gamma = 1.3$ at a relative density of 10% and 30%, respectively.
- For both the FCC and BCC structures, the highest yield strength is always found for loading along the [100] direction (Fig. 5.7). The weakest direction of either structure is always found between the [110] and [111] directions. However, the exact direction depends on the relative density.
- For the FCC structure, the [110] direction is the weakest for $\bar{\rho} = 0.01$ and $\bar{\rho} = 0.05$ (Fig. 5.7). At 20% relative density, it appears to transition towards the [111] direction, which gives the lowest yield stress at a relative density of 50%. The min-max ratio for the FCC structure (Fig. 5.8a) is only $\gamma = 1.4$ at a relative density of $\bar{\rho} = 0.01$. It then decreases further to 1.3 and 1.15 for $\bar{\rho} = 0.1$ and $\bar{\rho} = 0.3$, respectively.
- For the BCC structure, the weakest direction is usually close to the [111] direction (Fig. 5.7). Here, the yield stress ratio decreases from $\gamma = 1.7$ for $\bar{\rho} = 0.01$ to $\gamma = 1.3$ for $\bar{\rho} = 0.1$.
- Irrespective of their relative density, the shell-lattices have their minimal yield strength on a similar level or above the mean strength of elastically-isotropic tube-lattices (Figure 5.8b). Their mean strength is about 30% higher than that of tube-lattices for $\bar{\rho} = 0.1$, with the difference increasing at lower relative densities.
- The scaling of the hydrostatic yield stress is shown in Fig. 5.8c. The relative scaling is qualitatively similar for all structures. However, as for the bulk

modulus, we observe a superior performance of the SC shell-lattice. Its hydrostatic yield stress is more than 50% higher than that of the FCC and BCC structures at $\bar{\rho} = 0.01$ and about 10% higher at $\bar{\rho} = 0.3$. All structures present far higher yield pressure than the corresponding tube-lattices. The difference increases from about 20% at $\bar{\rho} = 0.5$ to more than 100% for relative densities below $\bar{\rho} = 0.1$.

- For low relative densities, the scaling of the yield stress is well approximated by a power-law fit,

$$\frac{\sigma}{\sigma_b} \approx b\left(\frac{\rho}{\rho_b}\right)^a \tag{5.7}$$

Table 5.2 gives estimates for the fitting parameters a and b for all three shell-lattices. The approximations for parameter a suggest that the behavior of shell-lattices is closer to that of stretching-dominated ($a = 1$) than to bending-dominated ($a = 1.5$) structures.

Property	**FCC**		**SC**		**BCC**	
Model parameter	*a*	*b*	*a*	*b*	*a*	*b*
Minimal yield strength	1.08	0.31	1.17	0.39	1.27	0.65
Average yield strength	1.08	0.37	1.14	0.47	1.20	0.56
Maximal yield strength	1.07	0.43	1.07	0.51	1.06	0.40
Yield pressure	1.13	0.72	1.04	0.66	1.18	0.77

Table 5.2: Parameters of power-law fit for data points between 1% and 10% relative density, for yield properties of the three structures.

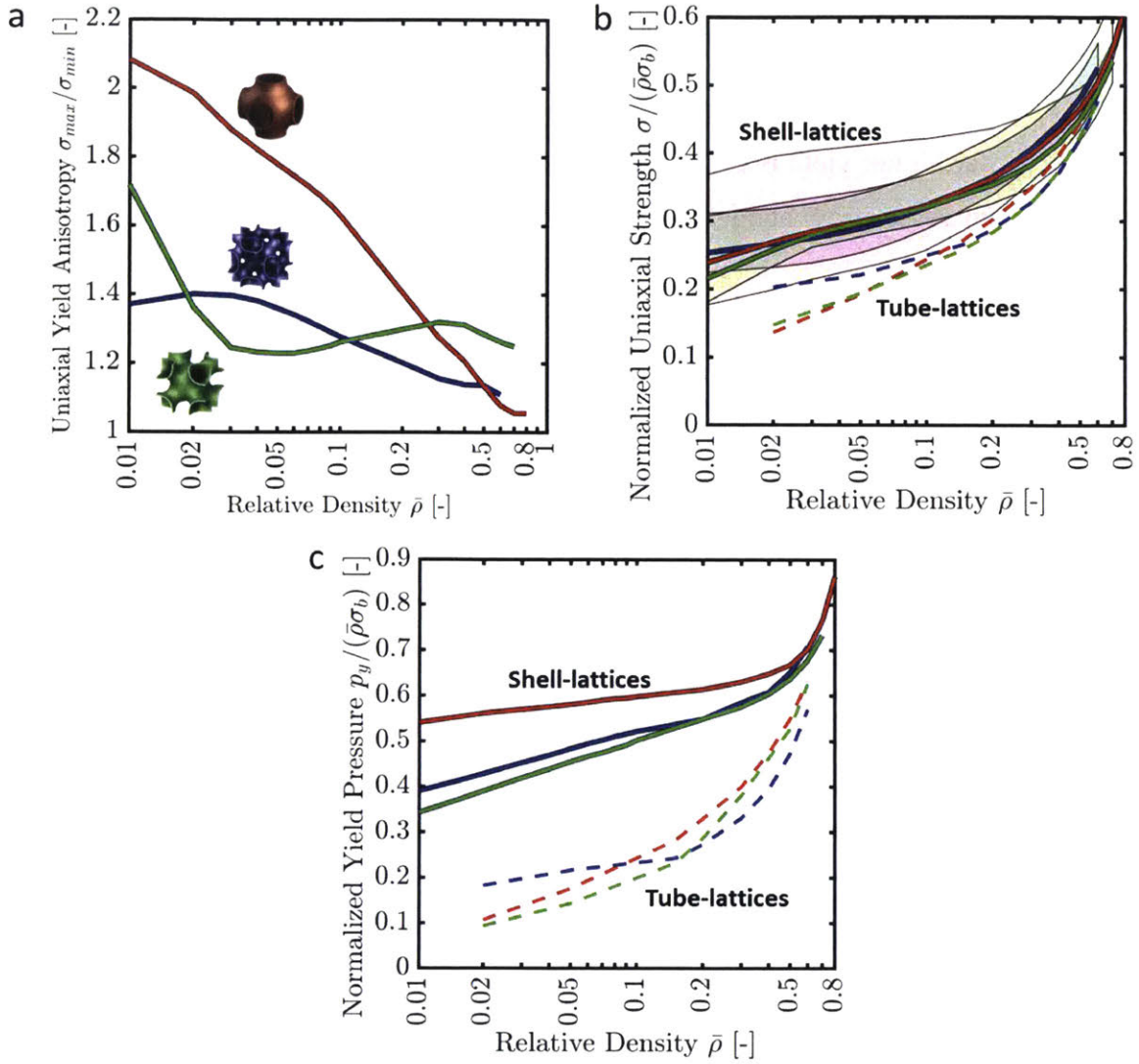

Figure 5.8: a) Variation of the max-to-min ratio of direction-dependent uniaxial yield strengths as a function of relative density. b) Variations of mean values and range of uniaxial yield strength of shell-lattices with relative density, as compared to mean values for isotropic tube-lattices. c) Variations of yield pressure of shell-lattices with relative density, as compared to isotropic tube-lattices.

5.4.3 Large deformation behavior

5.4.3.1 Large strain tension (simulations only)

Figure 5.9 shows the stress-strain curves obtained from unit-cell simulations for uniaxial tension up to an engineering strain of 0.3. The results from large strain unit-cell analysis are in line with the conclusions drawn with regards to the initial yield strength.

The comparison of the upper three curves in Figs. 5.9a ($\bar{\rho} = 0.1$) and 10b ($\bar{\rho} = 0.3$) reveals that the stress-strain response for tension is both qualitatively and quantitatively similar when loading the structures along their strongest direction. At a relative density of 10%, there are still differences of up to 15% in stress level among the stress-strain curves for the weakest material directions. At that density, the SC shell-lattice exhibits the highest degree of anisotropy. Consequently, its stress-strain response for uniaxial loading along the [100] direction corresponds to the lowest curve of all presented in Fig. 5.9.

The maximum of the engineering stress-strain curve for an elasto-plastic material subject to uniaxial tension usually corresponds to the onset of plastic localization. It is worth noting that in Fig. 5.9a and 5.9b, all engineering stress-strain curves exhibit a positive slope until an axial strain of at least 0.3, i.e. twice the ductility of the constituent material. To gain further insight into this phenomenon, we plotted the stress triaxiality field (ratio of hydrostatic and von Mises stress)

$$\eta = -p/\bar{\sigma} \tag{6}$$

for a BCC shell-lattice with $\bar{\rho} = 0.3$ after 30% uniaxial tension along [100] (Fig. 5.9c). At the mesoscopic level, the cell walls are subject to a wide range of local stress states, including generalized shear (blue zones), compressive states (grey zones), uniaxial tension (green) and biaxial tension (orange to red zones). The comparison of exterior (left) and interior (right) views reveals that the stress state varies through the thickness, meaning that bending of the walls plays a crucial role. The corresponding distributions of the equivalent plastic strain are shown in Fig. 5.9d. Most of the plastic dissipation takes place in interconnected bands (in green) that roughly correspond to the zones experiencing uniaxial tension, and in which cell-wall necking is observed (see cross-sections visible in Fig. 5.9d). However, at 30% engineering strain, those are still separated by bands with significantly lower plastic strains (blue bands on interior view in Fig. 5.9d), thereby preventing full structural failure through necking. Peaks (red zones) with $\bar{\varepsilon}^p \geq 0.5$ are observed in the parts of unit-cell subject to generalized shear, as well as uniaxial tension, but are confined to one side of the cell-wall, once again revealing bending action.

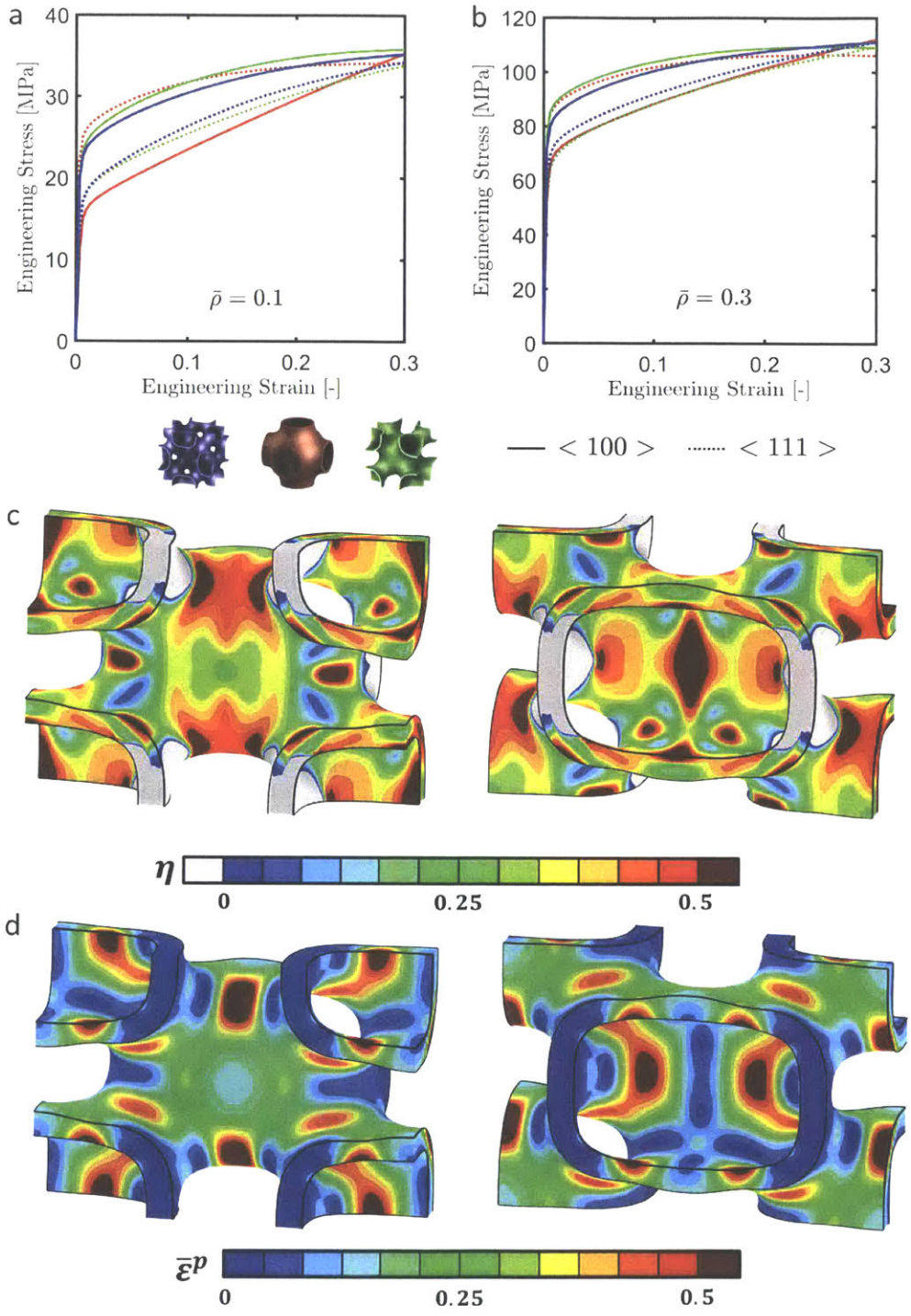

Figure 5.9: a-b) Stress-strain curves from unit-cell simulations of uniaxial tension along the stiffest and softest directions of the FCC, SC, and BCC shell-lattices, at relative densities of 10% (a) and 30% (b). c-d) Deformation pattern of a BCC shell-lattice with $\bar{\rho} = 0.3$ under uniaxial tension (30% strain) along its strongest direction, with color-coded distributions of c) stress triaxiality d) equivalent plastic strain. A cut is made perpendicular to the loading direction and both half-unit cells are presented.

It is also interesting to see that, for all three types of shell-lattices, the macroscopic stress-strain curves for the initially weakest directions exhibit significantly higher strain hardening than the initially strongest directions. At an axial strain between 0.25 and 0.30, we therefore observe the intersection of the stress-strain curves for the respective weakest and strongest directions.

5.4.3.2 Large strain compression (simulations and experiments)

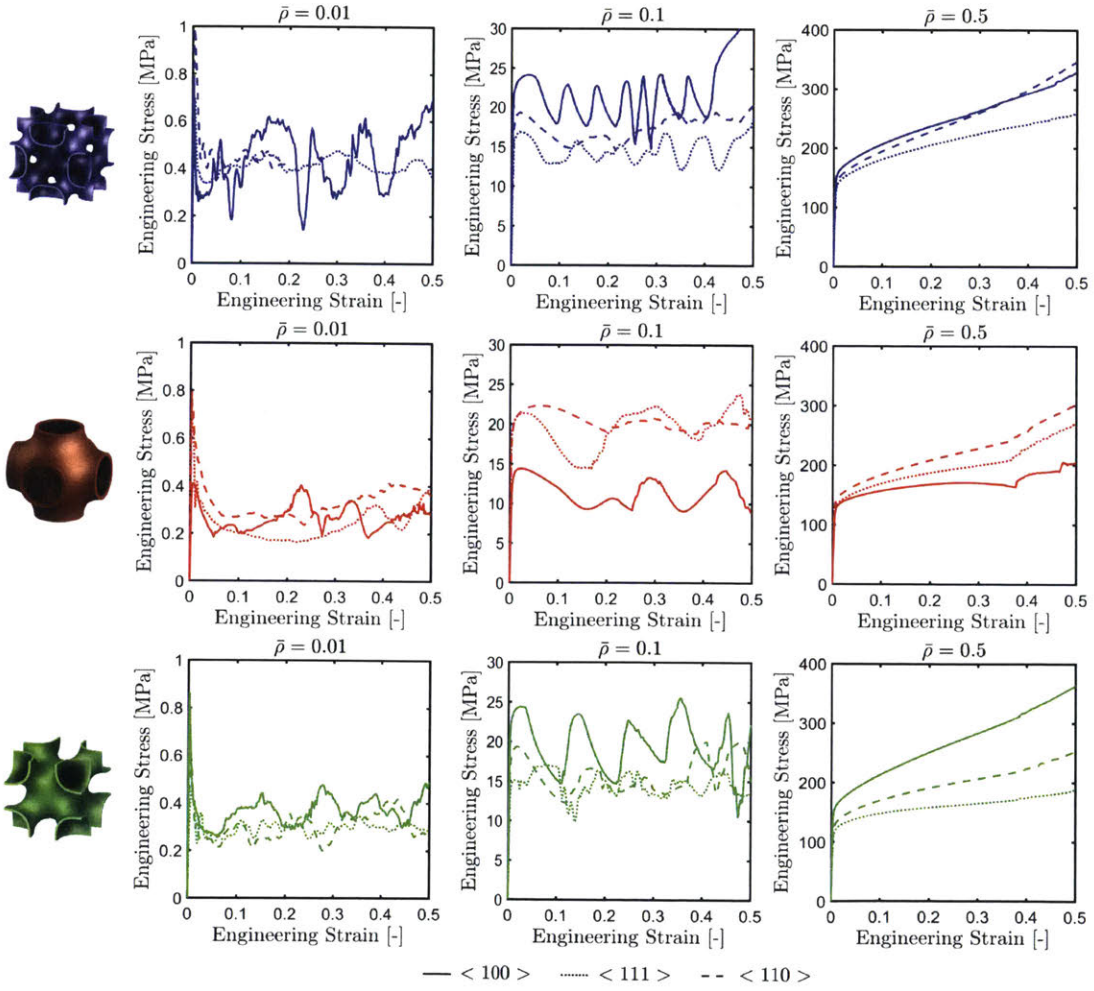

Figure 5.10: Large strain compression: Stress-strain curves obtained from multi-cell shell-element simulations in compression between two rigid surfaces, for three orientations, at relative densities (left to right) 0.01, 0.1 and 0.5. Top-to-bottom: FCC, SC and BCC shell-lattices.

Figure 5.10 provides an overview of the stress-strain response for compression (engineering) strains of up to 0.5 as obtained from multi-cell simulations with shell elements. For relative densities smaller than 10%, the response of all structures is reminiscent of the crushing response of metallic foams and low-density honeycombs (e.g. Mohr and Doyoyo 2004). The stress-strain curve initially shows a high peak stress, followed by oscillations in stress around an approximately constant average stress, with local peaks that are substantially lower than the initial threshold stress. At high relative densities (e.g. Fig. 5.10, right column subplots for $\bar{\rho} = 0.5$), a fundamentally different stress-strain response is seen; it is mostly smooth and monotonically increasing, similar to that of fully-dense metals.

The sequences of deformed configurations in Fig. 5.11 provide more insight into this fundamental difference. The plateau stress (average value was taken) for the SC shell-lattice with $\bar{\rho} = 0.1$ is 80% higher when crushing along the [110] instead of the [100] direction. When loaded along its weak direction, the structure is progressively crushed in a layer-by-layer fashion (Fig. 5.11c). The vertical tube-like sections within such layer respond through tube inversion, a process throughout which the load carrying capacity first decreases and then builds up again through internal contact after partial completion of the inversion. The tube inversion mode cannot be activated when loading the same structure at a diagonal direction (such as the [110] direction). As a result, the deformation is more uniformly spread throughout the entire specimen (Fig. 5.11d). Drops in the macroscopic stress level due localization events at the mesoscale are then also less pronounced (compare dashed and solid curves in Fig. 5.11a). The tube inversion mode becomes also inactive when increasing the relative density, i.e. when increasing the wall thickness. The deformed configuration for the SC shell-lattice of 30% relative density (Fig. 5.11e) at a macroscopic compression strain of 0.3 shows an approximately periodic distribution of the local equivalent plastic strain (i.e. a homogeneous strain distribution at the macroscopic level). The corresponding stress-strain curve (solid line in Fig. 5.11b) is oscillation free and has nearly zero slope while the axial strain increases from 0.1 to 0.5.

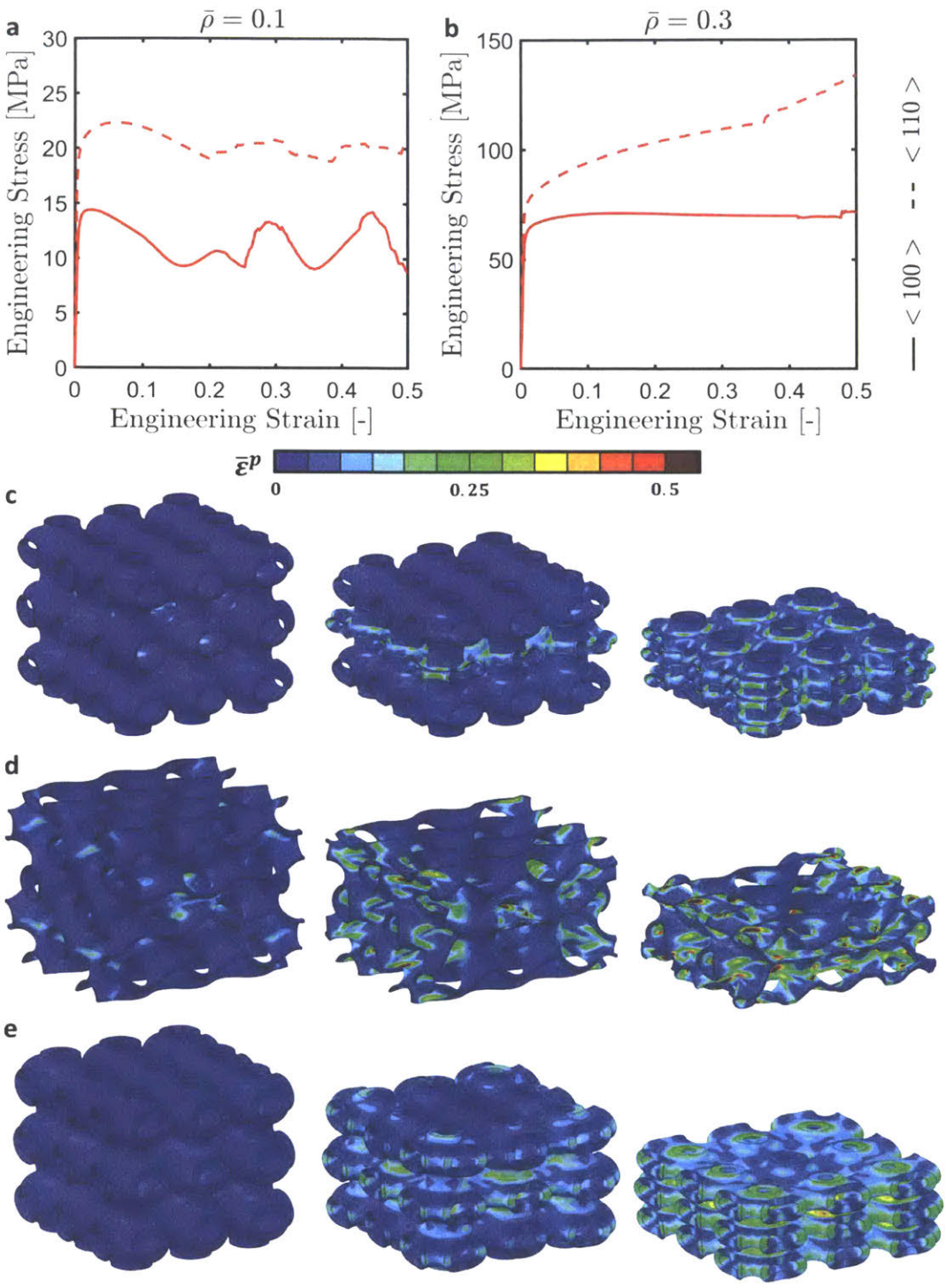

Figure 5.11: Large strain compression simulations of SC shell-lattices. a-b) Engineering stress-strain curves for the least and most energy absorbing orientations at relative density a) 10% and b) 30%. c-e) Deformation pattern and equivalent plastic strain distribution at 0.1, 0.3 and 0.5 compressive strain for compression of c) a $\bar{\rho} = 0.1$ specimen along [100], d) $\bar{\rho} = 0.1$ specimen along [110] and e) a $\bar{\rho} = 0.3$ specimen along [100].

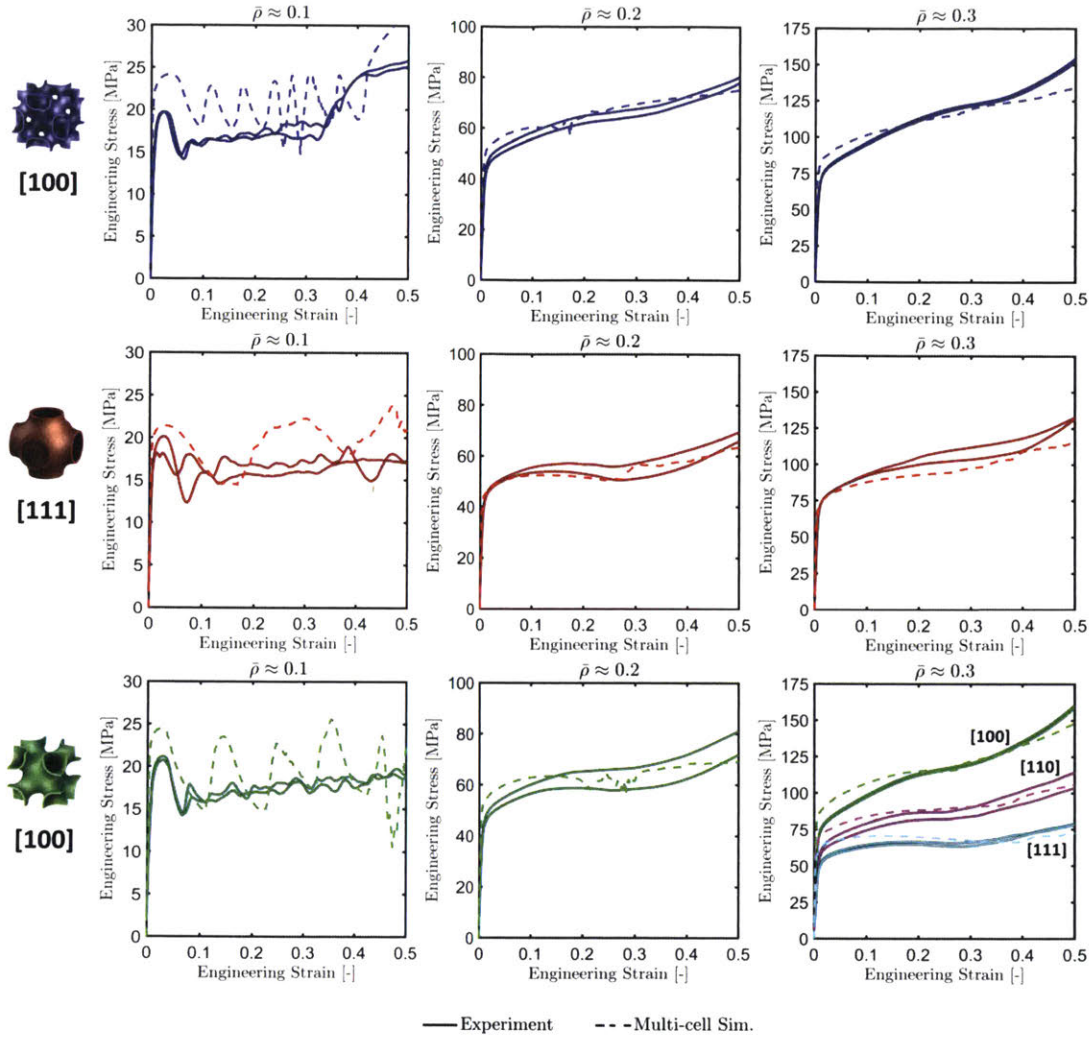

Figure 5.12: Experimental stress-strain curves from compression between two plates, for (left-to-right) densities of about 0.1, 0.2 and 0.3, and of (top to bottom) the FCC, the SC and the BCC shell-lattices. Dashed lines represent numerical results.

The experimental stress-strain curves for large strain compression are shown as solid lines in Figure 5.12. The corresponding multi-cell simulation results are shown as dashed lines. Overall, we observe good agreement of the experimental and numerical results. For the two highest relative densities (20% and 30%), the difference between the experimentally-measured and numerically-predicted curves is comparable to the difference between the two experimental curves. It is particularly reassuring to see that the simulation models agree well for all three orientations of the BCC specimen, thereby partially validating the models' ability to capture the effect of anisotropy. The experimentally-measured stress-strain curve also shows less pronounced oscillations. As discussed by

Mohr and Doyoyo (2004), such differences can be attributed to a combination of differences in specimen size and dimensional imperfections. In the simulation, the specimen is uniformly loaded which results in the simultaneous collapse of all unit-cells within a specimen cross-section, In the experiments, it is impossible to introduce the load with the same degree of uniformity which results in the successive crushing of neighboring cells, leading to the recording of a smeared out stress-strain response when using multi-cell specimens. As far as the plateau stress level over the strain interval [0.1, 0.4] is concerned, the relative difference between the experimental and numerical predictions is less than 15%. The observed deformation modes in the experiments are also consistent with the numerical predictions. An example of the progressive crushing of an [100] BCC specimen of relative density 10% is shown in Fig. 5.13, which confirms the layer-by-layer crushing.

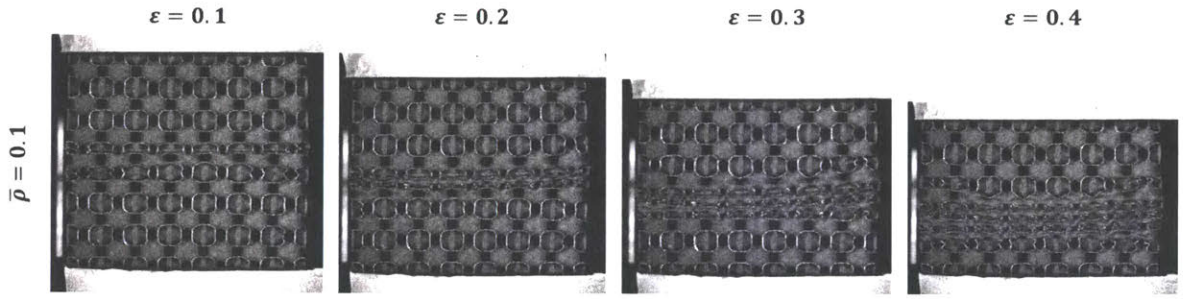

Figure 5.13: Experimental pictures of large strain compression deformation patterns of a BCC shell-lattice [100]-specimen of density 10% under compressive engineering strains of (left to right) 10% to 40%.

5.4.3.3 Specific Energy Absorption (simulations and experiments)

The Specific Energy Absorption (SEA) is defined as the mechanical work performed (per unit mass) when deforming a material up to 30% (engineering) strain under uniaxial loading,

$$\Psi = \frac{1}{\rho} \int_{\varepsilon=0}^{0.3} \frac{\sigma d\bar{\varepsilon}^p}{d\varepsilon} d\varepsilon. \tag{5.8}$$

We evaluate the above integral for simulations and experiments for large strain compression. The resulting plots of the SEA as a function of the relative density are shown

in Fig. 5.14 for all three types of shell-lattices. The anisotropy of the structures also becomes apparent in the SEA plots. For the FCC and BCC shell-lattices, the ordering of directions follows that of their stiffness (and up to a certain degree, yield strength). However, for the SC shell-lattices of high relative densities, the most energy absorbing direction out of the three investigated, is the [110] direction, with the [100] direction the weakest. This result is surprising as this direction is extremal neither in terms of stiffness nor strength.

At a relative density of $\bar{\rho} = 0.5$, the difference between the most and least absorbing directions is 17%, 24% and 54% for the FFC, SC and BCC shell-lattices, respectively. At $\bar{\rho} = 0.3$, the corresponding percentages are 27%, 41% and 55%. The maximum difference is observed for the SC shell-lattice with $\bar{\rho} = 0.1$; here, the difference is 80% when comparing the energy absorbed after loading along the [110] and [100] directions. This large directional dependency of energy absorption capabilities is confirmed by experimental data on the BCC shell-lattice at $\bar{\rho} = 0.3$ (dots on Figure 5.14c). The pronounced difference between the strongest and weakest directions vanishes at low relative densities where a foam-like crushing behavior is observed. The accelerated reduction in SEA starting below a relative density of $\bar{\rho} = 0.2$ is also confirmed by the experimental results at $\bar{\rho} = 0.1$ (solid dots in Fig. 5.14) for all three type of shell-lattices.

For reference, we also computed the SEA for uniaxial tension along the strongest direction, using the same engineering reference strain of 0.3. Due to the absence of mesostructural instabilities, the SEA for tension is significantly higher than that for compression at low relative densities. At high relative densities, the difference between compression and tension decreases. In case of the BCC shell-lattices, the SEA for compression even becomes higher than that for tension at relative densities higher than 40%.

There is little difference between the SEA of the FCC and BCC shell-lattices when these are loaded along their strongest [100] direction (Fig. 5.14d). For the SC structures, the stress level for loading along the weaker [110] direction is 10% to 20% lower in the $\bar{\rho} \geq 0.2$ range, but that gap vanishes at lower relative densities. Despite the narrow scope of the study, it may be concluded that smooth shell-lattices of FCC, SC and BCC symmetry

exhibit a similar energy absorption capacity. The differences observed in specific cases can be mainly attributed to their anisotropy.

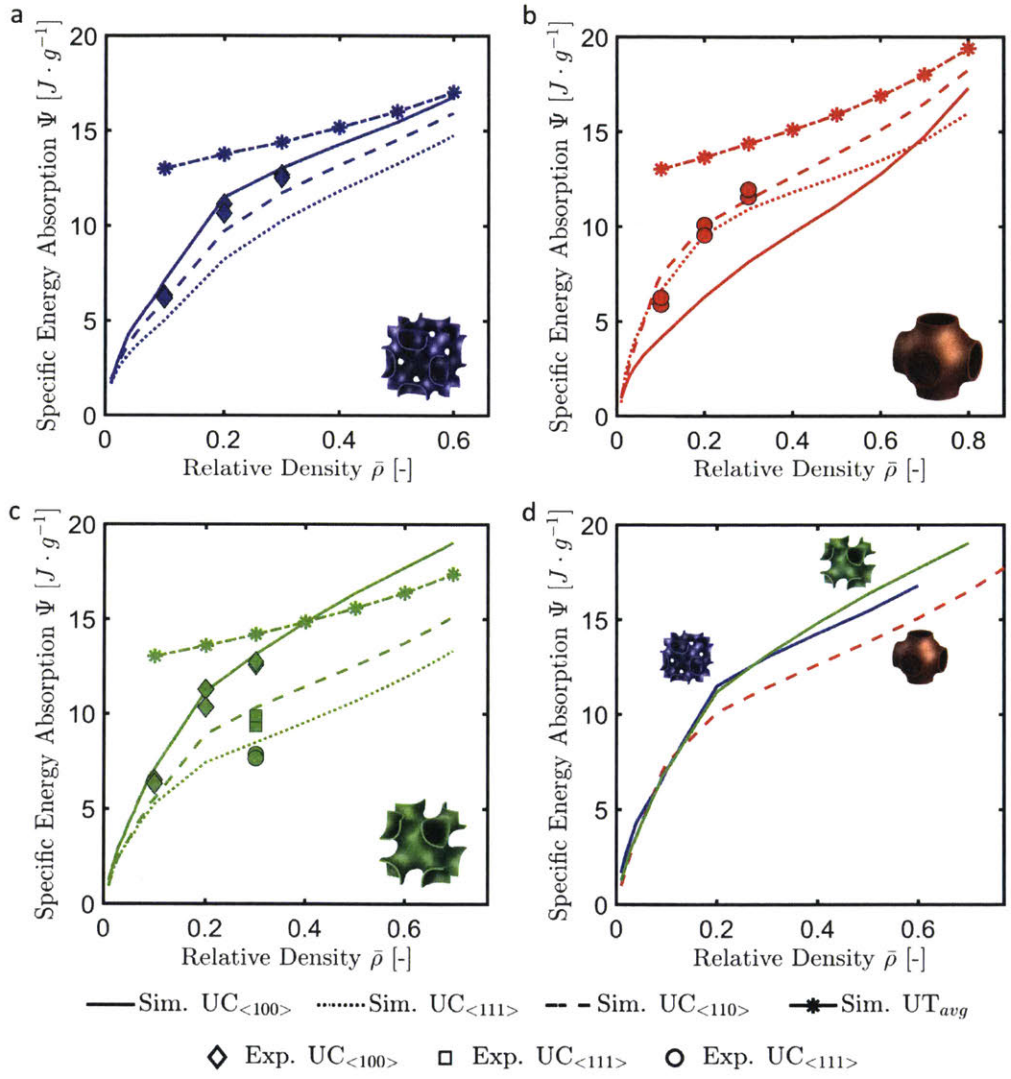

Figure 5.14: Specific energy absorption at 30% strain as a function of relative density, under uniaxial tension (strongest direction only), and uniaxial compression along the [100], [111] and [110] directions for a) the FCC, b) the SC and c) the BCC shell-lattices. d) Comparison of the most absorbing directions of each structure under uniaxial compression.

5.5. Discussion

The stiffness, yield strength and energy absorption capabilities of the three original, TPMS-like shell-lattices are determined for relative densities ranging from 1% to 80%

using detailed finite element simulations. The results are partially validated through compression experiments on additively-manufactured stainless steel 316L specimens.

All three structures achieve remarkable properties, particularly at high relative densities: above 30%, the mean Young's modulus of the smooth shell structures exceeds 70% of the theoretically-achievable highest stiffness (85% for the bulk modulus), 40% higher than that of optimal trusses with solid struts, and 30% higher than that of trusses with hollow struts, see Figs. 5.6b to 5.6d. The high uniaxial stiffness of the smooth shell structures is lost at low relative densities (i.e. below 10%). Similar trends are observed for both yield and energy absorption properties. Above 20% relative density, the structures exhibit a bulk-like, highly efficient large-strain behavior. When compressed, lighter structures show a foam-like crushing behavior, associated with a much poorer scaling of their specific energy absorption. The only exception to this trend is the bulk modulus, which remains close to the theoretical limit at all relative densities.

It is reemphasized that the newly-proposed metamaterial architectures have been identified by smoothening the curvature of the constituent shell surfaces. Different from plate and beam networks, the mechanical fields at the mesoscopic level are therefore free from stress concentrations, which is expected to provide substantial advantages with regards to fatigue life (and brittle fracture for ceramic structures). Smooth shell-lattices offer a combination of high mechanical properties (close to those of closed-cell foams) and a potential for multifunctionality, which was, until recently, a feature of open-cell foams and lattices only.

One striking feature of these structures is their high anisotropy, with differences in energy absorption capability under compression of up to 80% for the same structure depending on the loading direction. This makes the structure-to-structure comparison difficult, particularly when one structure's strongest direction is the other's weakest. When anisotropy is accounted for, our conclusion is that the mechanical performances of all three structures are very similar, both qualitatively and quantitatively. Strategies to reduce the anisotropy of those three shell-lattices will be introduced in the next chapter.

6. Towards isotropic shell-lattices

Parts of this chapter are adapted from Bonatti and Mohr (2019a, 2019b).

In Chapter 4 we developed a methodology to design smooth shell-lattices through a minimization of a the quadratic norm of the bending energy on the surface. In Chapter 5 we examined the effect of the choice of boundary conditions on the surface, revealing that the mean properties of the structure remained unaffected. In this chapter, we are interested in the effect of the functional on the mechanical properties.

As stated in both previous chapters, the structures considered bear an uncanny resemblance to better-known shell-lattices that rest on different definitions, be it a zero mean-curvature or an equation on the coordinates of the surface points (level-set surfaces). We will start by investigating these similarities. As we will see, changing between those three definitions does not affect much the response of the shell-lattices. Despite that fact, the previous chapters' contribution remains, as no investigation of the effect of anisotropy on the large strain behavior of shell-lattices (TPMS or otherwise) had been undertaken elsewhere.

6.1.Smooth-shells, minimal surfaces and level-set approximations

6.1.1 Structure generation

The structures investigated in Chapter 4 and 5 are visually extremely similar to some TPMS. Shell-lattices based on TPMS have emerged in the literature fairly recently (e.g. Bobbert et al. 2011), however most of the work is even more recent (e.g. articles by Abu al Rub, since 2015). Given that no studies on TPMS shell-lattices investigates their anisotropic large-strain behavior, it is of interest to compare the shell-lattices developed herein to these more common topologies. The FCC shell-lattice corresponds to the TPMS known as "Schoen F-RD", the BCC shell-lattice corresponds to the "Schoen I-WP" and the SC shell-lattice to the "Schwartz P" (P for Primitive Cubic). Minimal surfaces are defined by their zero mean curvature, that is:

$$k_1 + k_2 = 0 \tag{6.1}$$

As a consequence we obtain the three TPMS equivalents by relying on the method detailed in Chapter 4, and simply modifying the functional to:

$$J(\Omega) = \int_{\Omega} (k_1 + k_2)^4 dV = \int_{\Omega} Tr(A)^4 dV \tag{6.2}$$

Some studies that refer to the mechanical behavior of TPMS-based composites, prefer to use an alternative definition (e.g. Nguyen et al. 2017) and readily ignore the difference in mechanical behavior (to the author's knowledge, a comparison of the mechanical behavior shell-lattices based on TPMS and corresponding level-set approximations does not exist in the literature). Level-set surfaces, are defined as isocontours of a function of 3D space. Approximations for a number of TPMS have been developed, and for the three structures herein Maldovan et al. (2007) give:

$$\begin{aligned} f_{SC} = {} & cos(x) + cos(y) + cos(z) \\ & -\tfrac{1}{2}(cos(x)\,cos(y) + cos(y)\,cos(z) + cos(z)\,cos(x)) + t \end{aligned} \tag{6.3}$$

$$f_{BCC} = cos(x)\,cos(y) + cos(y)\,cos(z) + cos(z)\,cos(x) + 2t \tag{6.4}$$

$$\begin{aligned} f_{FCC} = {} & 4\,cos(x)\,cos(y)\,cos(z) + cos(2x)\,cos(2y) + cos(2y)\,cos(2z) \\ & + cos(2z)\,cos(2x) + t \end{aligned} \tag{6.5}$$

The surfaces correspond to the domain $f = 0$, and t is a paremeter used to vary the surface (and in practice the volumes of the two phases separated). The structures approximate the corresponding TPMS for $t = 0$. A factor 2 has been added to the last term in the BCC function for numerical convenience. In practice obtaining level-set surfaces is much more convenient than the structures considered so far. The criterion is purely local and, keeping the parameterization expressed in Chapter 4, one can simply optimize separately the last coordinate for each node.

In what follows the comparison we will limit ourselves to the FCC shell-lattice. To preserve clarity of the figures we will separate the comparison in two parts. We will first compare the smooth shell-lattice from Chapter 4 to the corresponding F-RD shell-lattice, then we will compare the smooth shell-lattice to the corresponding level-set shell-lattice. A view of the three middle-surfaces is proposed in Figure 6.1. The TPMS shell-lattice (Fig. 6.1b) presents flat sections along with steep saddle points, while the bending-energy inspired shell-lattice (Fig. 6.1a) is smoothly curved throughout. The level-set surface (Fig. 6.1c) presents larger four-way nodes, and smaller 8-way nodes, than the other two. A comparison is presented in Fig. 6.1d to highlight those differences.

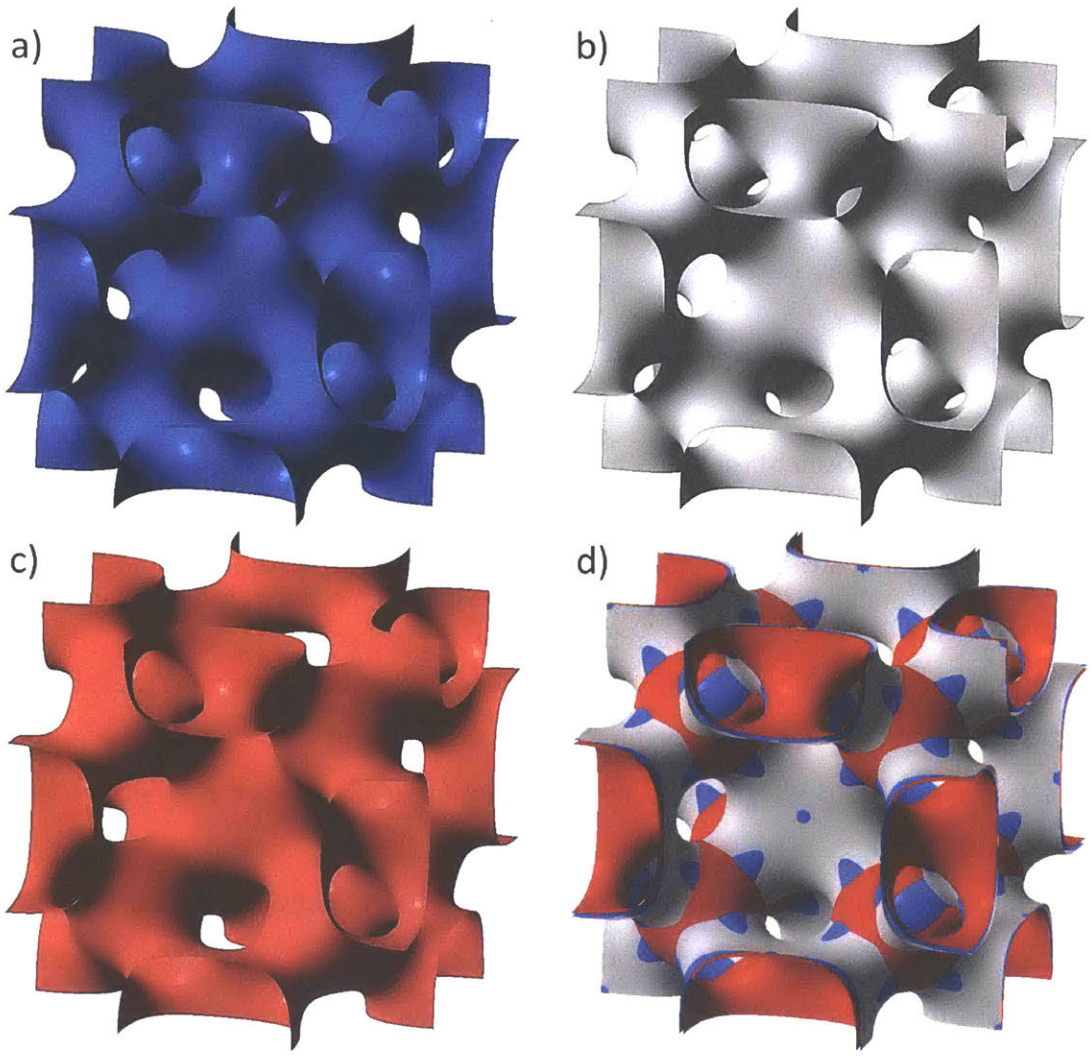

Figure 6.1: View of the middle-surface of FCC shell-lattices. a) Smooth shell FCC. b) TPMS F-RD c) Level-Set FCC d) Superposition of a)-c).

6.1.2 *Comparison: FCC smooth-shell and F-RD minimal surface*

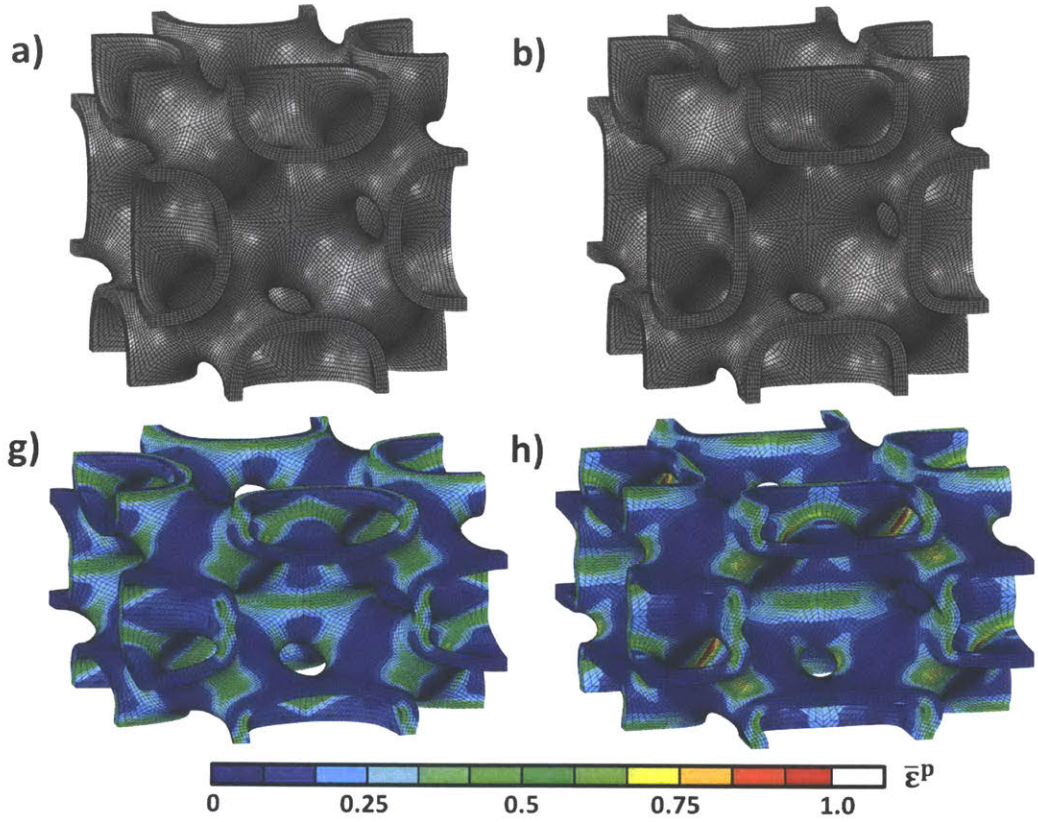

Figure 6.2: Comparison of the smooth shell-lattice and the TPMS Schoen F-RD based shell-lattice. View of the undeformed unit-cell mesh at relative density 0.2 of a) the smooth shell-lattice and b) the TPMS Schoen F-RD based shell-lattice; c-d) Deformed configuration and equivalent plastic strain distribution under uniaxial compression along [100] at an engineering strain of 30% of c) the FCC smooth shell-lattice and d) the F-RD shell-lattice at relative density 0.2.

Numerical simulations are conducted for the F-RD shell-lattices in the exact fashion described for the FCC smooth-shell in Chapter 4. A view of both structures is presented in Figs. 6.2a and 6.2b. Both structures present a similar level of anisotropy, as well as similar directional Young's moduli at all relative densities from 0.01 to 0.5 (Fig. 6.3a). A maximum relative difference of 6% is observed at relative density 0.1. The same is true of both structures' bulk moduli (maximum relative difference of 8%) with once again the F-RD shell-lattice over-performing the smooth shell-lattice slightly, as shown in Fig. 6.3b. The comparison of both materials' response to large strain loadings shows this ranking reversed. While preserving similar levels of anisotropy and very similar responses overall, the smooth-shell structure provides slightly higher macroscopic stress-levels in the cases

investigated. Figures 6.3c and 6.3d provide evidence of such findings for uniaxial compression at relative densities of 0.2 and 0.5, respectively. Figures 6.2c and 6.2d compare the equivalent plastic strain distribution for both structures at relative density 0.2, under uniaxial compression in the [100] direction. At an engineering strain of 0.3, the smooth-shell structure displays a smoother distribution of plastic dissipation ($\bar{\varepsilon}^p_{max} = 0.63$), as the F-RD shell-lattice presents concentration zones around the saddle points in which curvature is concentrated, with a notably higher peak in equivalent plastic strain ($\bar{\varepsilon}^p_{max} = 0.94$). These findings justify the use of "TPMS-like" to refer to the smooth-shell lattices in this document.

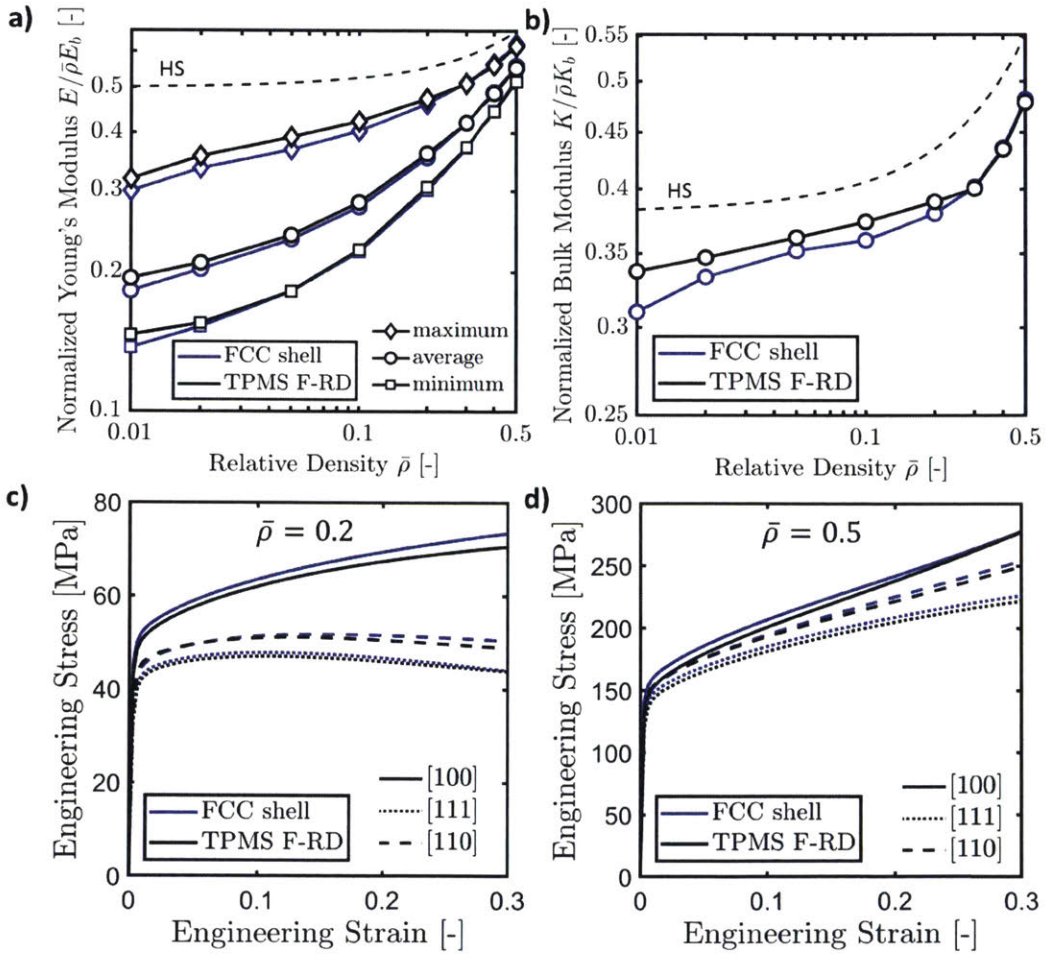

Figure 6.3: Comparison of the FCC smooth shell lattice and the TPMS Schoen F-RD based shell-lattice. a) Scaling of the maximum, minimum and directional average value of Young's modulus with relative density for both structures. b) corresponding scaling of the bulk modulus. c-d) Comparison of stress-strain response under uniaxial compression for a relative density of c) 0.2, and d) 0.5.

6.1.3 *Comparison: FCC smooth-shell and F-RD level-set surface*

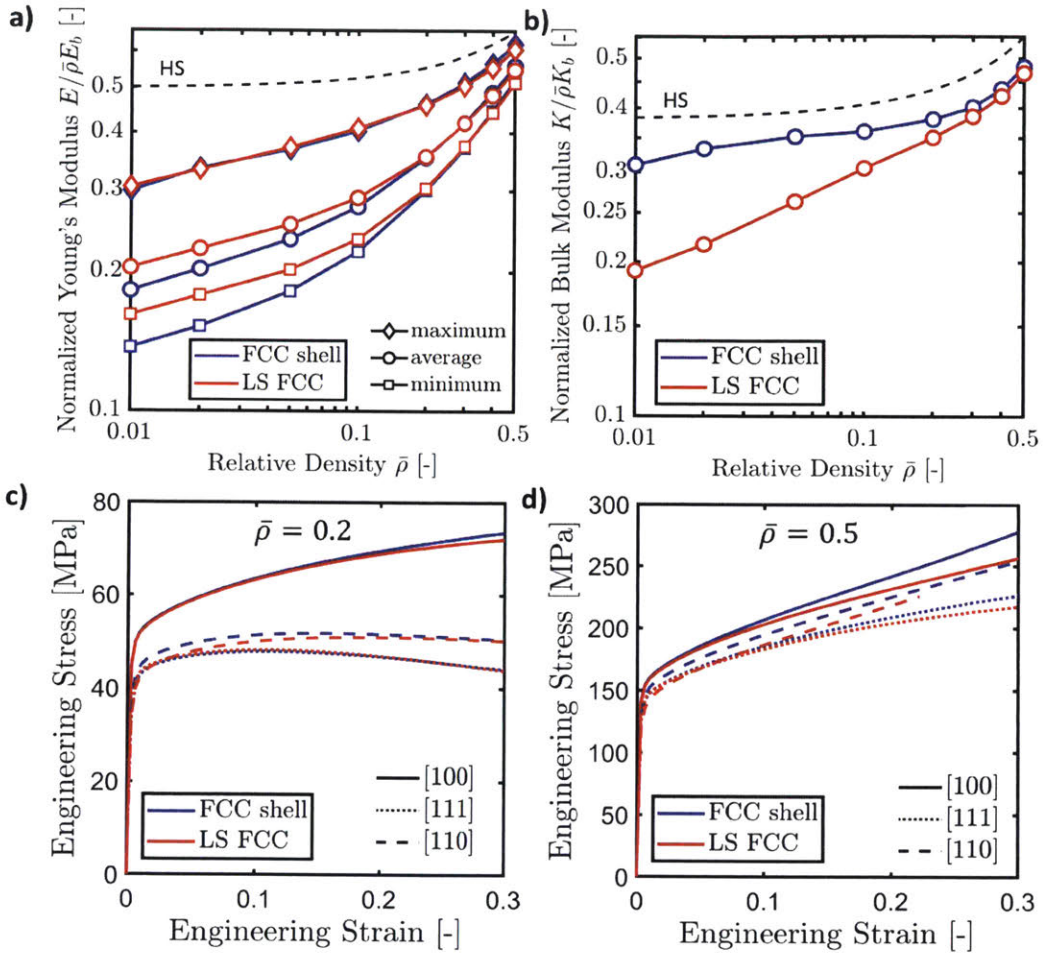

Figure 6.4: Comparison of the FCC smooth shell-lattice and the Level-Set FCC shell-lattice. a) Scaling of the maximum, minimum and directional average value of Young's modulus with relative density for both structures. b) corresponding scaling of the bulk modulus. c-d) Comparison of stress-strain response under uniaxial compression for a relative density of c) 0.2, and d) 0.5.

Numerical simulations are now conducted for the level-set FCC shell-lattices in the exact fashion described for the FCC smooth-shell in Chapter 4. A comparison of its mechanical behavior to that of the smooth-shell lattice of Chapter 4 is presented in Figure 6.4. Both structures present a similar scaling of the Young's modulus (Fig. 6.4a) with near-identical maximum Young's modulus (less than 2% difference), however at small relative densities the minimum Young's modulus of the LS shell-lattice is slightly higher (15% at $\bar{\rho} = 0.01$), leading to a higher mean value (10% at $\bar{\rho} = 0.01$). This also makes the LS shell-lattice less anisotropic than both the TPMS and the smooth shell-lattices. In terms of

the bulk modulus (Fig. 6.4b) this ranking is reversed: the LS shell-lattice has a sublinear scaling of its bulk modulus, leading to increasing differences with the smooth-shell lattice (-40% at $\bar{\rho} = 0.01$): in this particular case using a level-set approximation comes with the cost of losing one of the most striking mechanical properties of triply periodic minimal surfaces. Fig 6.4c-d) present results for uniaxial compression simulations at relative densities 20% and 50% respectively. In all cases, the behavior is essentially the same, with the smooth-shell lattice being slightly more energy absorbent.

6.2. Varying the functional

Given that the anisotropy of cubic structures is represented by one and only one parameter, in order to obtain elastically-isotropic structures one only needs to find a parameterized definition of the structure that affects its anisotropy significantly. It is with this in mind that we explore a continuous variation of the functional.

6.2.1 Anisotropic measures of curvature: the β-parameter

Recall from Chapter 4 the functional used to derive smooth shell-structures:

$$J(\Omega) = \int_{\Omega} (k_1^2 + k_2^2)^2 da \tag{6.6}$$

As explained in §4.1.2.2, this takes the form in our implementation in an estimation of the trace of the square of a tensor A called the shape operator, defined at each node of the original grid. The formulations are equivalent and we can rewrite the functional J to reflect that fact:

$$J(\Omega) = \int_{\Omega} \left(Tr(A^2)\right)^2 da \tag{6.7}$$

Now, recall from Chapter 5, that for all three of the geometries considered (FCC, SC and BCC) the surface separates two sets of trusses, specifically:

- The FCC-shell separates a smooth FCC truss (octet-truss) from a smoothened rhombic dodecahedral (RD) truss (alternating 8-way and 4-way nodes).

- The BCC-shell separates a smooth BCC truss, from a "wrapping package" (WP) truss, with planar 4-way nodes located at the center of the faces and on the middle of the edges of the unit-cell.
- The SC-shell separates two smooth SC trusses.

The shell-lattices can be seen at the same time, as smoothened tube-lattices of both kinds. The idea central to the proposed modification of the functional, is to favor one interpretation over the other. Specifically, we constructed the original functional in order to avoid concentrations of principal curvatures in the directions that carry the stresses. We will now introduce a bias in our measure of curvature, in order to favor one load-bearing direction over the other. In order to effectively do this, two directions on the surface are taken as representative of the direction of the truss.

For clarity we focus now on the case of the FCC shell-lattice. The direction "along the FCC lattice" at point $\boldsymbol{x}$ on the surface is taken as the intersection of the surface and plane P, where P is the plane containing $\boldsymbol{x}$ and edge $[AB]$ of the tetrahedron. It is represented by its direction vector at $\boldsymbol{x}$, $\boldsymbol{e}_F$. Conversely the direction "along the RD lattice" at point $\boldsymbol{x}$ on the surface is taken as the intersection of the surface and plane P, where P is the plane containing $\boldsymbol{x}$ and edge $[CD]$ of the tetrahedron, and is modeled by its direction vector at $\boldsymbol{x}$, $\boldsymbol{e}_R$. The same approach is used for the BCC shell-lattice with respect to the BCC and WP trusses, and for the SC shell-lattice with respect to the two SC-trusses it separates.

To introduce a bias in the measure of the integrand, the respective weights of curvatures along those directions are modulated by a scalar parameter. In order to effect this, we multiply the expression of the shape operator of the surface A taken in basis $\{\boldsymbol{e}_F, \boldsymbol{e}_R\}$. The new cost function is:

$$\int_\Omega Tr\left(\left(\begin{bmatrix}\sqrt{\beta} & 0\\ 1 & 1\end{bmatrix}\cdot A\cdot\begin{bmatrix}\sqrt{\beta} & 0\\ 1 & 1\end{bmatrix}\right)^2\right)^2 da \tag{6.8}$$

Conveniently, due to the choice of parameterization given in §4.1.2.1, our measure of the shape operator is already expressed in that basis, which simplifies the implementation.

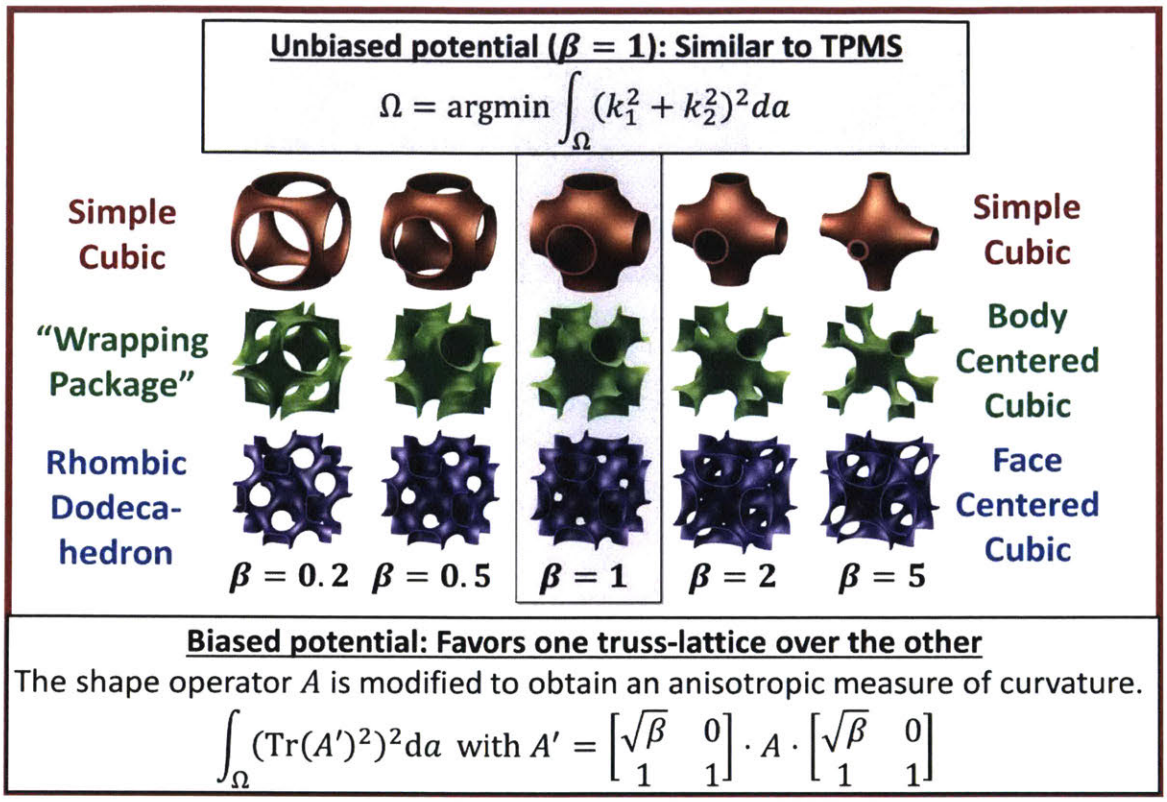

Figure 6.5: Views of the effect of parameter β on the unit-cells of SC, FCC and BCC shell-lattices.

Figure 6.5 presents the effect of parameter β on the unit-cells of the three shell-lattices. Looking at the BCC shell-lattice, when β is large the curvatures along the BCC truss become more costly in the functional, and thus larger. The curvatures in directions normal to the axis of the truss are less weighted and the tubes become narrower. As a result the structure resembles more closely a BCC tube-lattice. The opposite trend is observed for low β values, for which the structure resembles and hollow "Wrapping-Package" truss. The case of the SC shell-lattice is particular in that it separates two similar truss-lattices, and the β-family is therefore symmetric in the sense that β_1 and $\beta_2 = \beta_1$ yield the same structure – only translated by a half cube diagonal in Fig. 6.5.

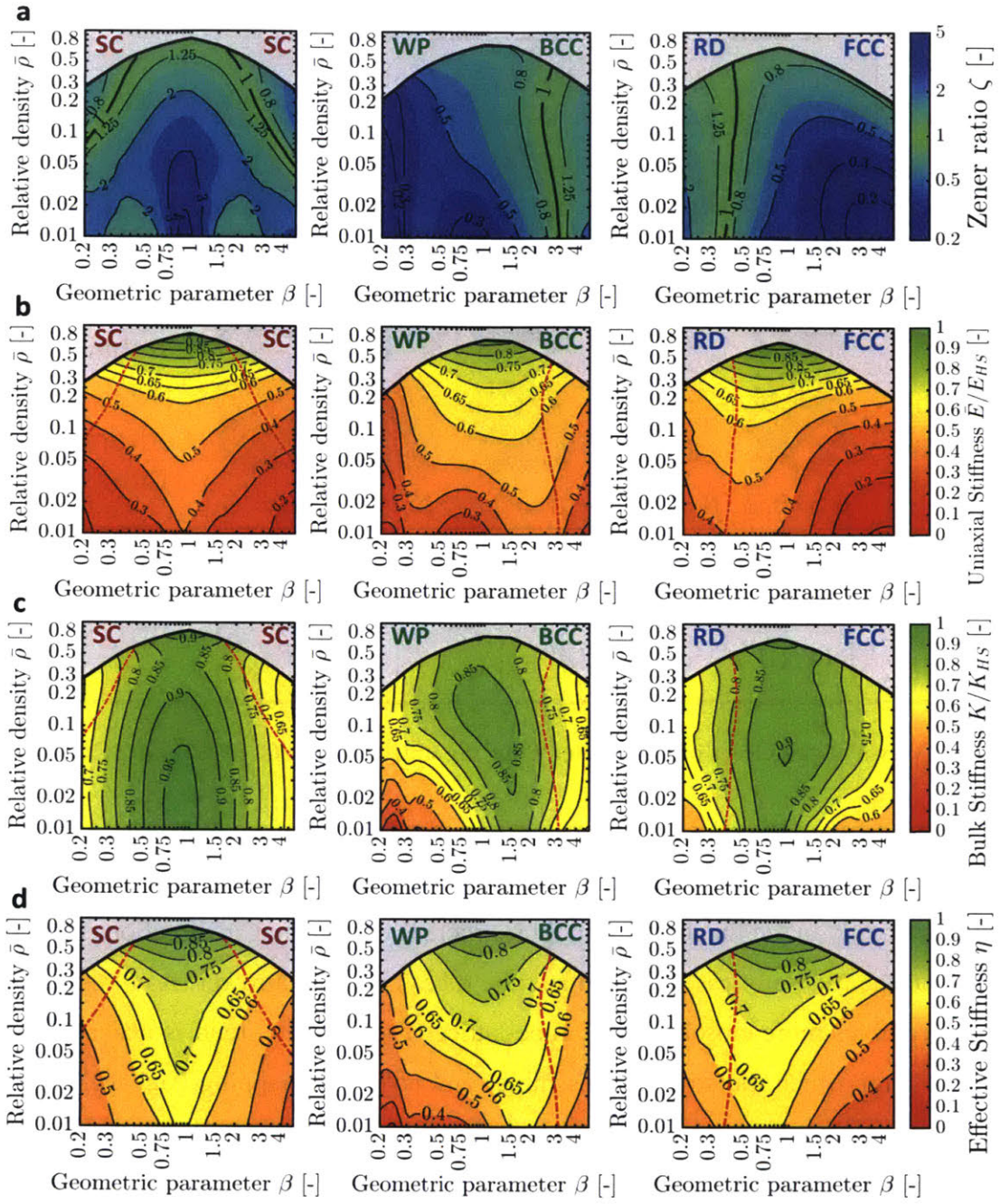

Figure 6.6: Contour plots of various elastic properties of (from left-to-right) the SC, the BCC and the FCC shell-lattices, varying with β and $\bar{\rho}$. a) Zener ratio ζ b) ratio of mean Young's modulus to Hashin-Shtrikman bound c) ratio of bulk modulus to Hashin-Shtrikman bound. d) Measure of overall effective stiffness. Red dashed lines in b-c) correspond to the isotropic solutions ($\zeta = 1$).

6.2.2 Design maps for shell-lattices

6.2.2.1 Simulations

For each type of structure (SC, BCC and FCC), finite element models of shell-lattices are built and their elastic properties estimated, covering the following grid:

- 25 values of β ranging between 0.2 and 5 (by increments of 0.05 from 0.2 to 1, then every 0.5 from 1 to 5), and
- Relative densities 1%, 2%, 5%, 8%, 10%, 15%, 20%, 25%, 30%, 40%, 50%, 60%, 70%, 80% up to the maximum density possible for the structure.

This corresponds to a total of 806 distinct shell-lattices. Five elements through thickness are used, and the unit-cell meshes are composed for $\bar{\rho} \geq 0.1$ of 61440 elements for SC and BCC shell-lattices, and 245760 elements for FCC shell-lattices. For relative densities lower than 0.1, four-times finer meshes are used: 245760 elements for BCC/SC and 983040 elements for FCC shell-lattices. Elastic-step simulations are performed following the method given in Chapter 2, for only two cases (one constrained tension and one pure shear). This is enough to determine three elastic constants per structure and thus the stiffness tensor.

6.2.2.2 Results

From the simulation results, smoothened design maps are derived (Fig. 6.6) where elastic quantities are color-coded as a function of the relative density $\bar{\rho}$ (ordinate) and the shape factor β (absissa). Fig. 6.6a (top row) provides contour plots of the Zener ratio ζ. When considering horizontal paths in Fig. 6.6a (i.e. paths of constant relative density, but varying β), elastically-isotropic shell-lattices ($\zeta = 1$) are found. For example, at a relative density of 0.2, the Zener ratio varies between:

- 0.49 and 2.24 for the SC shell-lattice,
- 0.23 and 1.76 for the BCC shell-lattice,
- 0.57 and 1.59 for the FCC shell-lattice.

The isotropy lines (contour lines corresponding to $\zeta = 1$) are depicted as thick solid lines. For FCC and BCC a single isotropy line is observed that is almost vertical, meaning that the β_{iso} value corresponding to isotropic configurations is approximately independent of the relative density ($\beta_{iso}^{FCC} \approx 0.4$, and $\beta_{iso}^{BCC} \approx 2.5$).The design-maps for the SC shell-lattices are symmetric with respect to the $\beta = 1$ axis, due to the symmetry of the transformation as explained in the previous paragraph. In this case two symmetric isotropy lines are observed. Both of them reveal a strong dependency of the β_{iso} values on relative density, which get out of the investigated range for $\bar{\rho} \leq 0.05$.

The ratios of (directional) average Young's moduli and bulk moduli to the corresponding Hashin-Shtrikman bounds are plotted in Figs. 6.6b and 6.6c respectively. The contour lines are not horizontal, meaning that β influences the stiffness. This effect is more pronounced at low relative densities ($\bar{\rho} \leq 0.1$). For SC structures and for a given relative density, the stiffest configuration is always $\beta = 1$. This is not true for BCC and FCC structures, meaning that in some instances shell-lattices stiffer than $\beta = 1$ ones of same relative density are found.

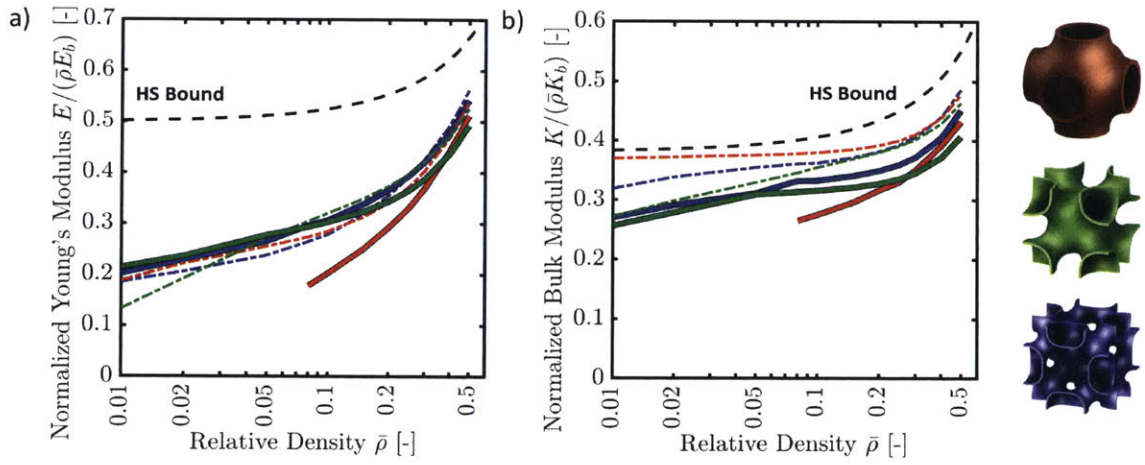

Figure 6.7: Comparison of the elastic properties of isotropic shell-lattices identified from the design maps, to the mean elastic properties of the $\beta = 1$ equivalents. a) Young's modulus b) Bulk modulus.

The solid curves in Fig. 6.7a show the scaling of the Young's modulus of the isotropic shell-lattices (the closest values computed are used) as a function of the relative density. For comparison purposes, we also depict the average moduli for the TPMS-like structures ($\beta = 1$) as dashed lines. SC-isotropic shells are only depicted for the relative densities at

which they have been identified ($\bar{\rho} \geq 0.08$). In that range already, an important drop in stiffness is observed, consistent with Fig. 6.6b. For FCC and BCC structures however, the isotropic shell-lattices are close to the average for the TPMS-like structures for high relative densities, and even perform slightly better at low relative densities. The bulk moduli of the isotropic shell-lattices (Fig. 6.7b) are all substantially lower than those of their $\beta = 1$ equivalents (e.g. by 15% in the case of FCC structures of 2% relative density).

6.3.Behavior of an isotropic shell-lattice

In this section we explore further the comparison between the FCC isotropic shell lattice and the $\beta = 1$ FCC shell-lattice. Once again simulations are repeated for the isotropic shell-lattice following the protocol established in Chapter 4. Additionally uniaxial compression experiments are performed to confirm the findings.

6.3.1 Scaling of stiffness and plastic dissipation

Figures 6.8a,b present the scaling of the Young's and bulk moduli as a function of the relative density. The comparison with the results for the TPMS-like lattice (blue curves) reveals that the Young's modulus of the iso-shell (black lines) of equal density is always higher than the mean stiffness of the TPMS-like structures (Fig. 6.8a). It is also always higher than the stiffness of optimal isotropic truss-lattices (dashed line) and exceeds 60% of the Hashin-Shtrikman bound for relative densities greater than 10%. The bulk stiffness of the iso-shell is also close to that of the TPMS-like structures for relative densities greater than 10%, while it proves less stiff at low relative densities (Fig. 6.8b). In terms of yield strength the iso-shell lattice is strongest along [100] and [111] while [110] is the weakest direction (not shown). The max-to-min ratio of yield stresses (1.28) is reduced as compared to the TPMS-like structure (1.4).

Figure 6.8c depicts the monotonically-increasing stress-strain response of an iso-shell structure of 30% relative density for uniaxial compression along three different lattice directions (black curves). Even though elastic-isotropy does not imply plastic isotropy, we observe a substantially reduced plastic anisotropy as compared to the TPMS-like structure

(blue curves). For example, at a compressive strain of 0.2, the stress level varies by ±5% for the iso-shell, while variations of ±18% are seen for the TPMS-like structure.

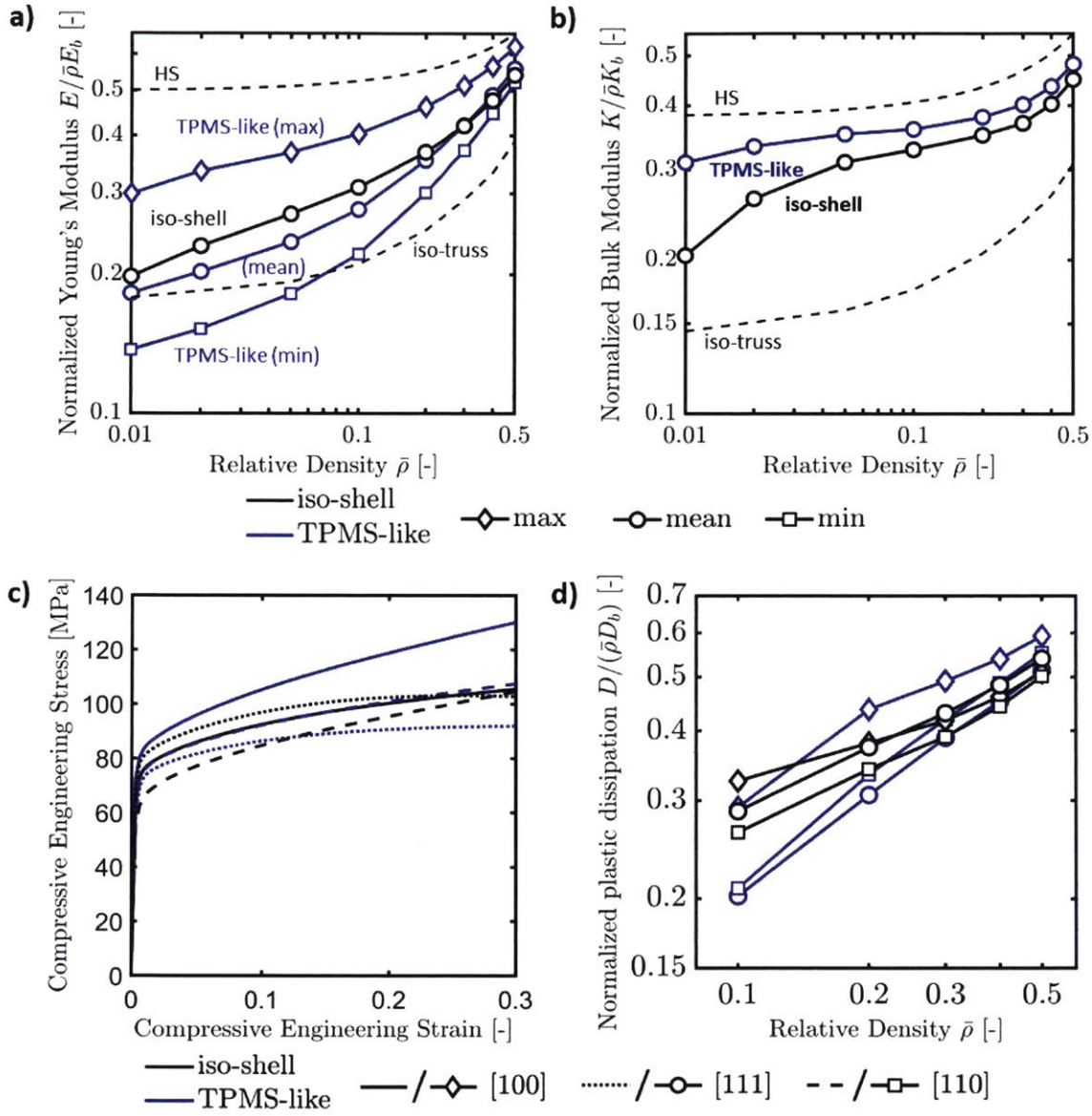

Figure 6.8: a) Comparison of Young's modulus for the smooth shell structure with $\beta = 1$ and the isotropic smooth shell structure. b) Comparison of bulk modulus for the smooth shell structure with $\beta = 1$ and the isotropic smooth shell structure. c) Comparison of uniaxial compression stress-strain curves for the shell-lattice with $\beta = 1$ and the isotropic shell-lattice at a relative density of 30%. d) Comparison of energy absorption under uniaxial compression for the shell-lattice with $\beta = 1$ and the isotropic shell-lattice. Black dotted lines in a-b) represent (top) the Hashin-Shtrikman bounds, and (bottom) the solution for stretching dominated isotropic truss-lattices.

The reduced plastic anisotropy of the iso-shell also becomes apparent when comparing its plastic dissipation per unit volume (for compressive strains of up to 0.3) to that of the TPMS-like structures (Fig. 6.8d). The three black curves for the iso-shell are much closer to one-another than those of the TPMS-like structure (the respective max-to-min ratios are 1.11 and 1.31 for a relative density of $\bar{\rho} = 0.2$). While the curves for the iso-shell are sandwiched between the curves for the strongest and weakest directions of the TPMS-like structures at relative densities greater than 20%, its plastic dissipation for loading along the [100] direction is even higher than that of the TPMS-like structure at a relative density of 10%.

6.3.2 Experimental validation of reduced large-deformation anisotropy

6.3.2.1 Specimens

To confirm and compare the numerically-observed plastic anisotropy of shell-lattices, uniaxial compression experiments are conducted on specimens of relative density 0.3 for $\beta = 1$ (TPMS-like) and $\beta = 0.375$ (iso-shell). For each structure, the experiments are conducted on specimens oriented in the [100] and in the [111] directions. The [100] specimens consist in cubic blocks of $5 \times 5 \times 5$ unit-cells, while the [111] specimens included $4.95 \times 5.2 \times 4.90$ unit-cells. For a wall thickness of $400\mu m$, the TPMS-like and iso-shell specimens feature an edge length of about $31mm$, and $29mm$. To avoid the use of building supports, the [111]-oriented specimens are built with the tested direction transverse to the building direction. To allow for meaningful comparison, all specimens of this batch are therefore tested transversely to the building direction. Two repeats of each experiment are performed to confirm the repeatability of the response. The measured outer dimensions of the specimens are within 1% of the prescribed ones, while the weight measurements suggest relative densities ranging from 27% to 28%.

6.3.2.2 Experimental setup

Similar to compression experiments in previous sections, the specimens are loaded using a crosshead velocity corresponding to an engineering strain rate of $2 \cdot 10^{-2}s^{-1}$. A

hydraulic press (Instron 8801), equipped with two flat tungsten carbide loading platens and a 100kN load cell. Tungsten carbide platens of a diameter closer to the dimensions of the specimens are added in the case of the smaller specimens. No grease or lubricant is applied. A high resolution digital camera (4240 × 2824 pixels, Model GS3-U3-120S6M-C, Point Grey) is used to monitor one face of the specimen. Digital image correlation is used to estimate a measure of the strain, which is taken as the average value of about 10 virtual extensometers spanning the specimen's height.

6.3.2.3 Experimental results

The manufactured iso-shell and TPMS-like specimens all had a measured relative density of about 28%. Quasi-static experiments with two repetitions are performed along the [100] and [111] directions. The recorded engineering stress versus engineering strain curves are shown in Fig. 6.9a. Both structures show a stress-plateau ($\partial\sigma/\partial\varepsilon \approx 0$) at around 15% strain when loaded along the [111] direction. For the [111] direction specimens, we also observe the band-type localization of deformation at the macroscopic level as reflected by the non-periodic surface patterns in the photographs of the specimens at 30% strain (Fig. 6.9b). The [100] specimens show a more uniform deformation pattern at the specimen surface (Fig. 6.9c) and positive strain hardening ($\partial\sigma/\partial\varepsilon > 0$) throughout the entire experiment (solid curves in Fig. 6.9a). As in the numerical simulations, we observe a lower degree of anisotropy in the stress-strain response for the iso-shell specimens than for the TPMS-like specimens. In particular, the elasto-plastic response of the iso-shell is almost the same for the [100] and [111] specimens for engineering strains of up to 15%. The two repeats per testing scenario fall on top of each other, confirming the robustness of the manufacturing and experimental procedures.

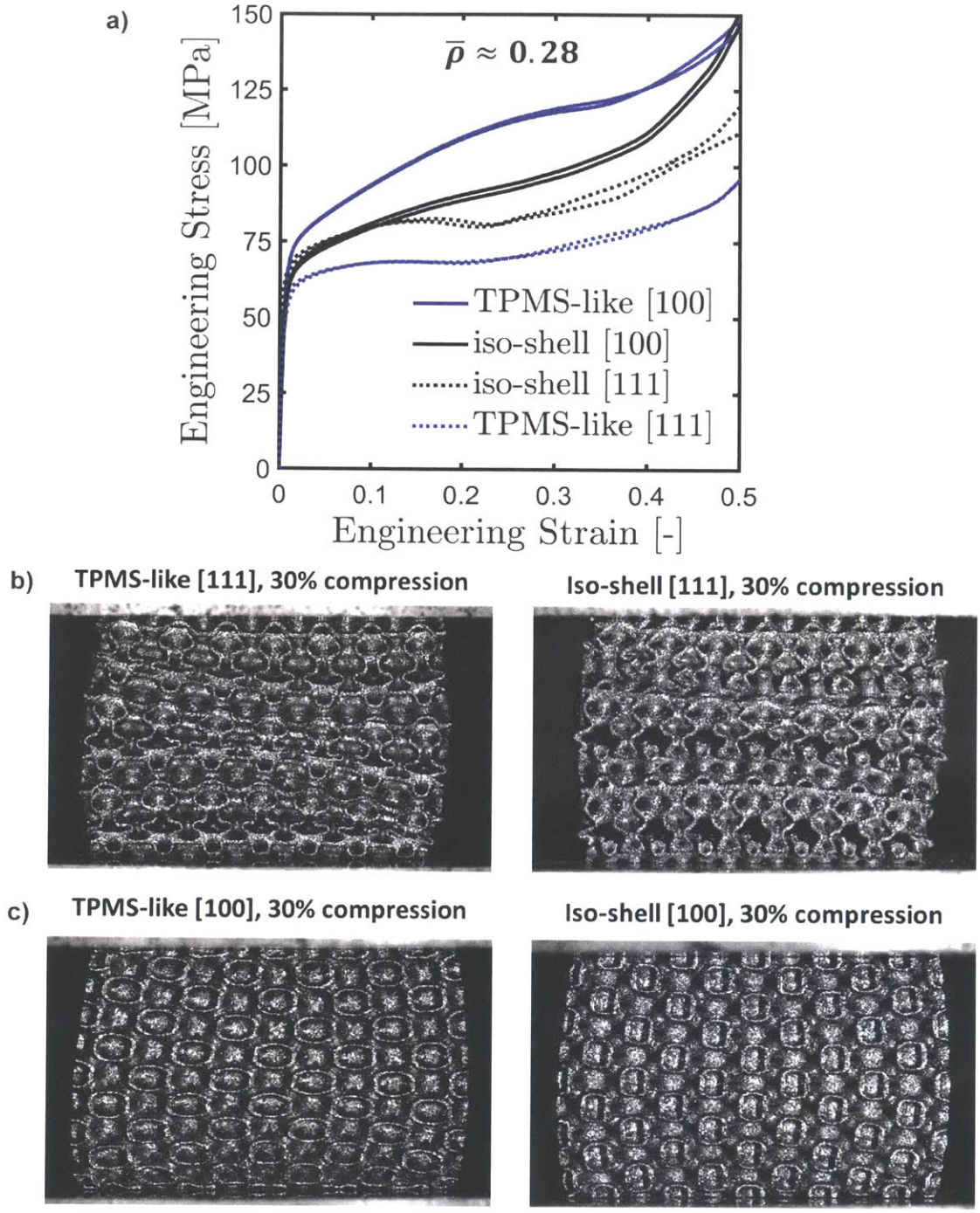

Figure 6.9: a) Comparison of the stress-strain response of TPMS-like and iso-shell structures under uniaxial compression along [100] and [111], at about 28% relative density. b) Pictures of [111]-specimens compressed at an engineering strain of 30% for the TPMS-like (left) and elastically-isotropic (right) shell-lattices. c) Pictures of [100]-specimens compressed at an engineering strain of 30% for the TPMS-like (left) and elastically-isotropic (right) shell-lattices.

6.4. Summary

In this chapter we have explored the influence of the choice of functional on the properties of the shell-lattices. It is found that (at least in the case of the FCC structure) the smooth-shell structures developed in Chapters 4 and 5 have very similar properties to those of the corresponding TPMS, with the smooth-shell lattice distributing stresses better which results in less concentration of the plastic strain at the mesostructural level. It is also found that the popular level-set approximation to triply periodic minimal surfaces leads to different elastic properties. A moderate gain is observed in terms of Young's modulus, at the cost of an important loss in terms of bulk modulus. Both structures (LS and TPMS) showed a similar (slightly inferior) behavior to that of the FCC smooth-shell structure under uniaxial compression.

In a second step, the issue of anisotropy is addressed. Design maps are provided for families of modified shell-lattices of each geometry, based on a modification of the functional that considers anisotropic measures of the surface curvature. They reveal that in all cases elastically-isotropic variants can be found. The identified FCC and BCC iso-shell-lattices each have mid-surfaces almost independent of their relative density. They display average elastic performances close to those of their original, anisotropic counterparts. However the SC family features a much poorer scaling.

The comparison is pushed further in the case of the FCC iso-shell. As compared to the TPMS-like architecture, the elastically-isotropic shell-lattice also features a significantly reduced plastic anisotropy, a property that is preserved even at large strains. The computational results are confirmed through compression experiments on additively-manufactured stainless steel 316L shell-lattice specimens.

7. Summary and outlook

7.1.Summary

Open-cell cellular solids are porous structures with a large variety of applications, from energy absorption to medical engineering. In an attempt to identify isotropic configurations with high low and large strain mechanical properties, detailed numerical simulations are conducted on a wide range of mesostructures of cubic symmetry. Special attention is dedicated to the response to large strain uniaxial compression. The results are partially validated through uniaxial compression of specimens made of 316L stainless steel via selective laser melting.

In order to identify features of mesostructures that impede their mechanical performance, the large deformation response of four different mesostructures of FCC symmetry of relative density 20% are analyzed, including an octet truss-lattice, tube-lattice, a sphere assembly and a tube/sphere hybrid. The numerical simulations reveal that for hydrostatic compression, the octet-truss lattice is prone to buckling failure already at 20% relative density. The effect of the constituent's strain hardening on the metamaterial's stability are highlighted, i.e. a high hardening material leads to increased structural stability. It is shown that the nodes of the octet-truss do not contribute to plastic dissipation. Furthermore, it is shown that for the other three structures plastic dissipation is concentrated in zones featuring sharp angles. It is concluded that periodic shell structures provide superior strength and energy absorption capacity for the same weight, as compared to truss-lattices. Another conclusion is that to avoid concentrations of plastic strains that are detrimental to the overall energy absorption of the structure, it is best to avoid peaks in curvature.

Based on these conclusions, a shell-lattice is developed. Starting from an octet tube-lattice, a novel structure is obtained by minimizing a functional that reduces peaks in principal curvatures. The structure resembles a smoothened Triply Periodic Minimal Surface. Its properties are compared to those of the octet-truss for a range of relative densities from 1% to 60%. The results reveal that the shell-lattice is superior to the octet-truss in almost all cases. However both structures present an important anisotropy.

The FCC shell-lattice is then compared to equivalents obtained by smoothening BCC and SC tube-lattices. It is found that the structures all present highly anisotropic properties. For a given structure, directional difference factors of up to 4.1 in uniaxial stiffness, 2 in yield strength and 1.8 in specific energy absorption are observed. Anisotropy is a major factor and given that one structure's strongest direction is the other's weakest, erroneous conclusions are likely to be drawn when only one direction is considered, as in often the case in the literature. To meaningfully compare the mechanical performance of structures with different degrees of anisotropy, the directional averages of their properties are evaluated. It is found that the differences in average performance of the SC, FCC and BCC shell-lattices are negligibly small. Irrespective of the specific type of cubic symmetry, TPMS-like shell-lattices are remarkably stiff, particularly at high relative densities. For example, at 30% relative density, their average Young's modulus attains 70% and their bulk modulus reaches 85% of the corresponding Hashin-Shtrikman bound. As such their performance stands between those of ideal truss-lattices and those of ideal plate-lattices. Similar conclusions are drawn regarding yield strength. Above 20% relative density, the shell-lattices exhibit a bulk-like large-strain compression response with positive strain hardening at the macroscopic level, associated with high specific energy absorption. Lighter structures show a foam-like crushing behavior, leading to poorer specific energy absorption capabilities.

A family of variations of the shell-lattices is proposed, which make uses of a functional that minimizes an anisotropic measure of the curvature. Design maps are established and reveal that the elastic anisotropy of shell-lattices can be conveniently tailored through the parameterized surface-defining functional. As a result, isotropic topologies of SC, FCC and BCC symmetry could be identified. The Young's modulus of the isotropic BCC and FCC shell-lattices is higher than the average modulus of their original counterparts, while the opposite is observed for the SC structures. As compared to the TPMS-like architecture, the elastically-isotropic shell-lattices also feature a significantly reduced plastic anisotropy, a property that is preserved even at large strains.

To close, we point out that most members of the shell-lattice metamaterial family do not only offer higher average stiffness, strength and energy absorption capabilities than truss- and tube-lattices. The geometric smoothness of shell-lattices and the absence of

intersections prevent stress concentrations. Shell-lattices are expected to provide substantial advantages over truss- and plate-lattices with regards to fatigue life (for metallic structures) and fracture strength (for ceramic structures). Due to their open cell topology, shell-lattices provide multi-functionality (e.g. fluid permeability) and can be conveniently manufactured using powder-bed and liquid-bath based additive manufacturing techniques.

7.2. Outlook

In what follows we explore a few of the possibilities for future research on shell-lattices. Those can be separated into two categories: further characterization of the structures, and further improvements on design.

7.2.1 Investigating the properties of shell-lattices

While the present thesis presents extensive data on the quasi-static behavior of shell-lattices, this represents only one branch of properties relevant to applications. Previous studies on TPMS-based shell-lattices also investigated their permeability, thermal conductivity, or fatigue properties, showing good and sometimes excellent behavior. The extent to which isotropic shell-lattices conserve those qualities remains to be investigated.

From the purely mechanical point of view, an important challenge consists in a proper description of shell-lattices' elastoplastic behavior. The mesostructures of shell-lattices are too complicated to allow their full modeling in applications – an equivalent model is needed. Ideally such a model should be versatile enough to be applied to various mesostructures – as such it is important not to rely on structural analysis of the unit-cell's contents, instead relying on a more general potential energy approach, while leveraging the structure's symmetries. Other challenges concern the large strain dynamic (impact) behavior of these structures, their fracture behavior in the case of less ductile constituent materials, as well as their wave propagation properties.

7.2.2 Opportunities for further design improvement

The design possibilities offered by today's most advanced manufacturing techniques are, to say the least, vast. In what follows we propose three possible projects to develop superior shell-based cellular solids.

7.2.2.1 Optimized topologies

It is almost certain that the shell-lattices developed here are not in any sense optimal. Topology optimization can certainly be used to obtain stiffer, or stronger, isotropic structures. One important constraint we put on shell-lattice topologies was to limit ourselves to the case of uniform thickness shells. However it is not clear that the effect on large-strain properties will be favorable. Unfortunately, large-strain simulations are computationally costly, and their numerical complexity can force the engineer to change strategies before a proper result can be obtained. This makes their combination with optimization techniques unlikely. A less conventional approach could consist in maximizing the (anisotropic) elastic collapse stresses, through Bloch wave analysis, aiming at optimal structural stability.

7.2.2.2 Mitigating fracture in shell-lattices

Uniaxial compression experiments (not shown herein) on shell-lattices made of a less ductile behavior (selective laser melted titanium and aluminum) reveal that when fracture occurs, the fracture path follows a plane of symmetry of the lattice, leading to complete failure of the specimen. In a sense, whenever a periodic material is designed, periodic weaknesses are engineered into it, leading to systematic and thus sudden failure. Three strategies are proposed to remedy this problem.

A first approach rests on arresting cracks through thickness variations. In TPMS-based structures, the lattice is a smoothened version of two locally orthogonal truss-lattices and thickness variations make little sense, as both in-plane directions of the shell are load-bearing. However the isotropic designs. Thickness variations at the mesostructural level, which thicker bands aligned with the load bearing truss-lattice, could be introduced. A first step manageable step could be the study of crack growth on flat sheets with parallel

grooves. A variant approach consists in larger-wavelength variations of thickness, leading to periodic functional grading of the shell lattice density.

A second approach would be based on a recent, thought provoking article. Yoo and Kim (2015) provide an algorithm based on Volumetric Distance Field and Beta Growth Function that allows to model smooth transitions between different TPMS-based lattice-materials. While their work focuses on skeletal TPMS (one side of the shell is solid), it is not hard to imagine adapting this method to the design of shell-lattices, using isotropic shells instead of TPMS to construct the volumetric distance fields. The direct consequence is the development of polycrystalline shell-lattices. The different crystals would not share the same weak planes, preventing complete failure through one plane of the lattice. The interface is a weak point in Yoo and Kim's approach, however it is perfectly possible to locally reinforce it via functional grading (i.e. using a larger thickness at the grain boundary).

The third approach finally, consists in removing periodicity altogether. Scientists have made use of randomly distributed points and the associated Voronoi tessellation, to generate both open and closed random foams. One important advantage is that anisotropy can be tailored through the probability density of the points – an isotropic choice will lead to an isotropic structure. The proposed approach consists in generating random open-cell foams with tubes instead of struts through this method, and subsequently obtaining a random shell-foam by minimizing a function of the curvature on the surface of the tube assembly. While design rules have been established on both truss-lattices and plate-lattice to obtain enhanced properties, those do not exist for shell-lattices. The three examples of shell-lattices treated in this thesis are shown to have similar average properties. Therefore it is not clear to what extent a property loss would be observed.

7.2.3 Hierarchical and composite shell-lattices

The linear scaling of ideal lattice properties often breaks down at low relative densities due to buckling instabilities (Deshpande et al. 2001b). This issue has been partially addressed by the design of hierarchical metamaterials which feature different levels of structure (e.g. Meza et al. (2015), Zheng et al. (2016)). Hierarchical design allows low

relative densities to be reached for the overall structure while keeping mesostructural feature-level aspect ratios low enough to retard instability-driven failure. By hierarchically combining octahedral and octet-trusses, Meza et al. (2015) have been able to achieve the linear-scaling of the elastic and elastic limit properties down to relative densities of about 10^{-4}.

The above approaches rely on the combination of truss-lattices within truss-lattices. However even ideal truss-lattices have lower-than ideal behavior. This knockdown is multiplied at every hierarchical level. As seen in this thesis, shell-lattices of relative density above 1% fare better. Additionally, shell-lattices have the advantage that the neighborhood of every material point is similar: it is a shell. This allows the integration of a second level of hierarchy without the trouble of designing for intersections. The natural way to perform this is to transform the shell cross-section into a sandwich panel. Preliminary simulations (not shown) show that an increase in stability, and thus in energy absorption, can be expected. For the same reason, shell-lattices are particularly suited to the design of composite cellular solids via conformal deposition techniques.

8. Appendix

8.1.Relative density derivation for the HTS structure

The volume is separated into struts and spherical shells. We note V_t the volume of one strut, V_s the volume of one hollow-sphere, V_{tot} the material volume occupied, and V_{cube} the total volume of the unit cell. As explained in the submitted article, we have taken the arbitrary constraints:

$$\begin{cases} r_o = \sqrt{2} r_i \\ r_o - r_i = R_o - R_i = t \\ R_i = L\,/\,3 \end{cases} \quad \text{(A1.1)}$$

Where r_o is the outer truss radius, r_i is the inner truss radius, R_o is the outer sphere radius, R_i is the inner sphere radius, t is the shell thickness.

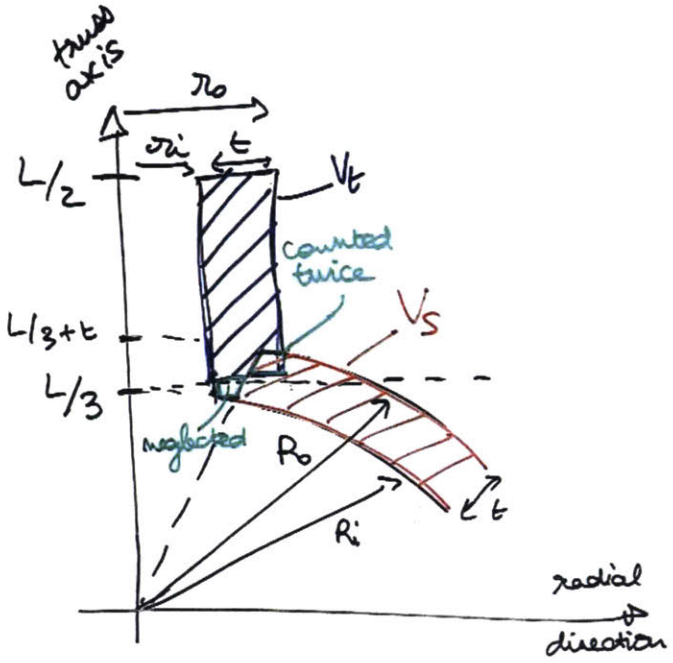

Figure A1.1: HTS geometry and its decomposition for the analytical derivation of a relative density estimate.

- Step #1: Individual half-strut volume

Given our choices of geometry, the volume of a half-strut reads:

$$V_t = \pi(r_o^2 - r_i^2)l = \frac{\pi r^2}{\left(\sqrt{2}-1\right)^2} l \tag{A1.2}$$

With l the length of the half-strut, which corresponds to half the internode distance to which is substracted the inner sphere radius:

$$l \approx L/2 - L/3 = L/6 \tag{A1.3}$$

Corrections to l depend on the cosine of the angle θ, and the first correcting term will be in $(t/L)^2$. Given that V_t already scales in $(t/L)^2$, those correcting terms (which correspond to the volume in green in the supporting drawing) are in $(t/L)^4$ and are thus neglected. Thus we have:

$$V_t = \frac{\pi}{6\left(\sqrt{2}-1\right)^2} L r^2 + O\left(\left(\frac{r}{L}\right)^4\right) \tag{A1.4}$$

- Step #2: Individual sphere volume

The sphere volume reads:

$$V_s = \eta \cdot \frac{4\pi}{3}(R_o^3 - R_i^3) \tag{A1.5}$$

Where η corresponds to the solid angle left after the spherical caps corresponding to the truss connectors are taken out.

$$\eta = 1 - 12 \cdot \frac{2\pi(1-\cos(\theta))}{4\pi} \tag{A1.6}$$

Different choices of θ lead to neglecting different volumes – we chose it arbitrarily as corresponding to the intersection of the inner shell of the sphere to the medium-plane of the half-strut.

$$\cos(\theta) = \sqrt{1-\sin^2(\theta)} \approx \sqrt{1 - \left(\frac{3(r_o + r_i)}{2L}\right)^2} = \sqrt{1 - \frac{\left(\sqrt{2}+1\right)^2}{\left(\sqrt{2}-1\right)^2}\left(\frac{3t}{2L}\right)^2} \tag{A1.7}$$

$$\cos(\theta) = 1 - \frac{1}{2} \cdot \frac{\left(\sqrt{2}+1\right)^2}{\left(\sqrt{2}-1\right)^2} \cdot \frac{9}{4} \cdot \left(\frac{t}{L}\right)^2 + O\left(\left(\frac{t}{L}\right)^4\right) \tag{A1.8}$$

Which leads to:

$$\eta = 1 - \frac{27}{4} \cdot \frac{\left(\sqrt{2}+1\right)^2}{\left(\sqrt{2}-1\right)^2} \cdot \left(\frac{t}{L}\right)^2 + O\left(\left(\frac{t}{L}\right)^4\right) \tag{A1.9}$$

The other factor is rewritten:

$$(R_o^3 - R_i^3) = \left(\frac{L}{3} + t\right)^3 - \left(\frac{L}{3}\right)^3 = \frac{1}{3} \cdot L^2 t + L t^2 + t^3 \tag{A1.10}$$

From which we can re-write:

$$V_s = \frac{4\pi}{9} L^2 t + \frac{4\pi}{3} L t^2 + \left(\frac{4\pi}{3} - \frac{3\left(\sqrt{2}+1\right)^2}{\left(\sqrt{2}-1\right)^2}\right) t^3 + O\left(\left(\frac{t}{L}\right)^4\right) \tag{A1.11}$$

- Step #3: Approximate relative density

In one unit-cell, there are 4 nodes, and each node has 12 half-strut connectors. As a consequence:

$$V_{tot} = 4 \cdot V_s + 48 \cdot V_t \tag{A1.12}$$

$$V_{tot} = \frac{16\pi}{9} L^2 t + \left(\frac{16\pi}{3} + \frac{8\pi}{\left(\sqrt{2}-1\right)^2}\right) L t^2 + \left(\frac{16\pi}{3} - \frac{12\left(\sqrt{2}+1\right)^2 \pi}{\left(\sqrt{2}-1\right)^2}\right) t^3 + O\left(\left(\frac{t}{L}\right)^4\right) \tag{A1.13}$$

Given that the volume of the cube is:

$$V_{cube} = 2\sqrt{2} L^3 \tag{A1.14}$$

We have the relative density:

$$\bar{\rho} = \frac{V_{tot}}{V_{cube}} = \frac{4\sqrt{2}\,\pi}{9} \cdot \frac{t}{L} + \left[\frac{4\sqrt{2}\pi}{3} + \frac{2\sqrt{2}\pi}{\left(\sqrt{2}-1\right)^2}\right] \cdot \left(\frac{t}{L}\right)^2 + \left[\frac{8\pi}{3\sqrt{2}} - \frac{6\left(\sqrt{2}+1\right)^2 \pi}{\sqrt{2}\left(\sqrt{2}-1\right)^2}\right] \cdot \left(\frac{t}{L}\right)^3 + O\left(\left(\frac{t}{L}\right)^4\right) \tag{A1.15}$$

Which in turns gives:

$$\bar{\rho} \approx 1.975 \cdot \frac{t}{L} + 57.71 \cdot \left(\frac{t}{L}\right)^2 - 446.9 \cdot \left(\frac{t}{L}\right)^3 \tag{A1.16}$$

A comparison between numerical values obtained from 3D models of the structure, and this approximation, is shown in Figure A1.2.

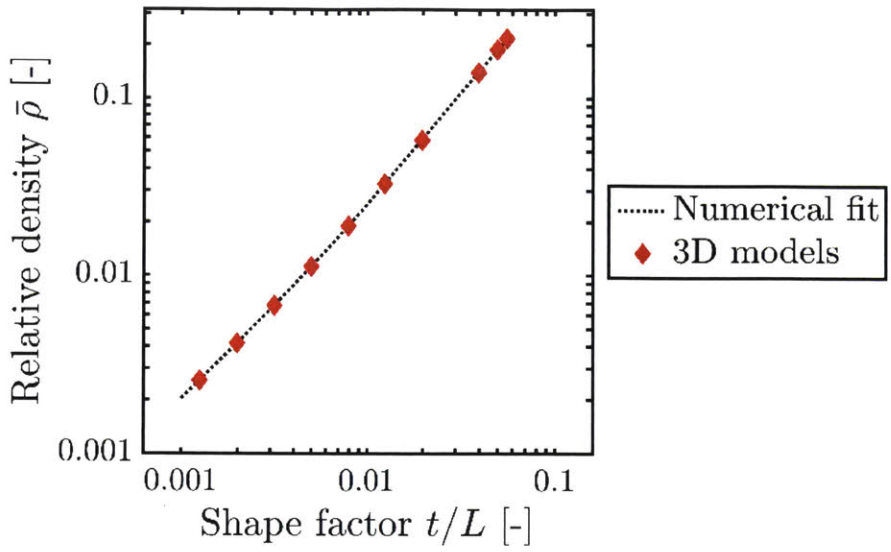

Figure A1.2: Comparison between numerical estimate, and numerical values obtained from 3D modeling, of the relative density of the HTS structure as a function of the thickness to nearest-neighbor distance ratio.

8.2. Shell-lattice materials: bending or stretching dominated?

Following the findings of Deshpande et al. (2010) on the bending or stretching dominated nature of truss-lattice's response to uniaxial compression, a number of studies have used that term to refer to shell-lattices. Are shell-lattices bending or stretching dominated structures? The present study aims at exploring this question quite literally. We will start by introducing some concepts on the behavior of plates and shells. We will then evaluate through numerical simulations the portion of plastic dissipation at large strains that are attributable to bending or membrane action in shell-lattices.

8.2.1 Fundamentals on the plastic theory of shells

The plastic theory of shells is based on the assumption of the plane state of stress. The in-plane components of stress and strain are $\sigma_{\alpha\beta}$ and $\varepsilon_{\alpha\beta}$ where $\alpha, \beta \in \{1,2\}$. In other words, out-of-plane stress components σ_{33} and $\sigma_{\alpha 3}$ are neglected both in the equation of equilibrium and yield conditions. For thin shells it is assumed that the Love-Kirchoff

hypothesis of "planes remain plane" and "normals remain normal" which can be expressed as:

$$\varepsilon_{\alpha\beta} = \varepsilon^0_{\alpha\beta} + z \cdot \kappa_{\alpha\beta} \tag{A2.1}$$

Where $\varepsilon^0_{\alpha\beta}$ is the in-plane (membrane) strain component on the mid-plane, z denotes the through-thickness coordinate, and $\kappa_{\alpha\beta}$ is the component of the curvature tensor. Those two quantities constitute generalized strains, to which the corresponding generalized forces are the membrane forces $N_{\alpha\beta}$ and bending moments $M_{\alpha\beta}$ defined by:

$$N_{\alpha\beta} = \int_{-\frac{h}{2}}^{\frac{h}{2}} \sigma_{\alpha\beta} dz \tag{A2.2}$$

$$M_{\alpha\beta} = \int_{-h/2}^{h/2} \sigma_{\alpha\beta} z dz \tag{A2.3}$$

Neglecting elastic energy, the rate of plastic energy dissipation per unit surface is defined as:

$$\dot{D}_S = \int_{-h/2}^{h/2} \dot{D} dz = \int_{-h/2}^{h/2} \sigma_{\alpha\beta} \dot{\varepsilon}_{\alpha\beta} dz \tag{A2.4}$$

Substituting the Love-Kirchoff hypothesis gives the following expression:

$$\dot{D}_S = N_{\alpha\beta} \dot{\varepsilon}^0_{\alpha\beta} + M_{\alpha\beta} \dot{\kappa}_{\alpha\beta} \tag{A2.5}$$

The first term of the right-hand expression represents the membrane dissipation, while the second term relates to the bending dissipation. During plastic flow, the components of the generalized stresses $N_{\alpha\beta}$ and $M_{\alpha\beta}$ are related through the material's yield condition.

$$3\sigma_{\alpha\beta}\sigma_{\alpha\beta} - \sigma_{\alpha\alpha}\sigma_{\beta\beta} = 2\sigma_y^2 \tag{A2.6}$$

In the specific problem of pure membrane action, the above equation can be integrated over the shell thickness to give:

$$3N_{\alpha\beta}N_{\alpha\beta} - N_{\alpha\alpha}N_{\beta\beta} = 2N_0^2, \tag{A2.7}$$

where $N_0 = \sigma_0 h$ is the fully plastic membrane force. Likewise, the yield condition for the pure bending response is given by:

$$3M_{\alpha\beta}M_{\alpha\beta} - M_{\alpha\alpha}M_{\beta\beta} = 2M_0^2, \tag{A2.8}$$

where $M_0 = \frac{\sigma_0 h^2}{4}$. In the general case of combined membrane and bending deformation, simple expressions for the yield condition $f(N_{\alpha\beta}, M_{\alpha\beta}) = 0$ are not available. Various approximate yield conditions were proposed in the literature and described in Sawczuk (1989).

In the concept of the associated flow rule, the yield condition is the flow potential which allows the components of stresses and strains to be determined in terms of strain rate ratios.

Using the associated flow rules, one can express the rates of membrane and bending energy dissipation in simple cases. In the case of pure membrane action, the rate of membrane plastic dissipation writes:

$$\dot{D}_m = \sqrt{\frac{2}{3}} N_0 \sqrt{\dot{\varepsilon}_{\alpha\beta}\dot{\varepsilon}_{\alpha\beta} + \dot{\varepsilon}_{\alpha\alpha}\dot{\varepsilon}_{\beta\beta}} \tag{A2.9}$$

While in the case of pure bending action, the rate of bending plastic dissipation writes:

$$\dot{D}_b = \sqrt{\frac{2}{3}} M_0 \sqrt{\dot{\kappa}_{\alpha\beta}\dot{\kappa}_{\alpha\beta} + \dot{\kappa}_{\alpha\alpha}\dot{\kappa}_{\beta\beta}} \tag{A2.10}$$

In the general case however, these terms are coupled and no simple expression exists to describe them. In finite element applications, the integration through the thickness is done numerically.

8.2.2 Large strain contributions of membrane and bending action

In order to evaluate the relative contributions of bending action and membrane action in plastic dissipation of shell-lattices under large strains, unit-cell simulations with periodic micro-displacement boundary conditions (see Chapter 5) are performed for a BCC shell-lattice corresponding to the TPMS-like geometry described in Chapter 5, for relative densities 1%, 2%, 5%, 8%, 10%, 15%, 20%, 25%, 30%, 40%, and 50%. The geometries are meshed with shell elements (S4R of the Abaqus element library). The unit-cells are

subjected to uniaxial compression with a maximum compressive engineering strain of 0.5, along directions [100], [111] and [110].

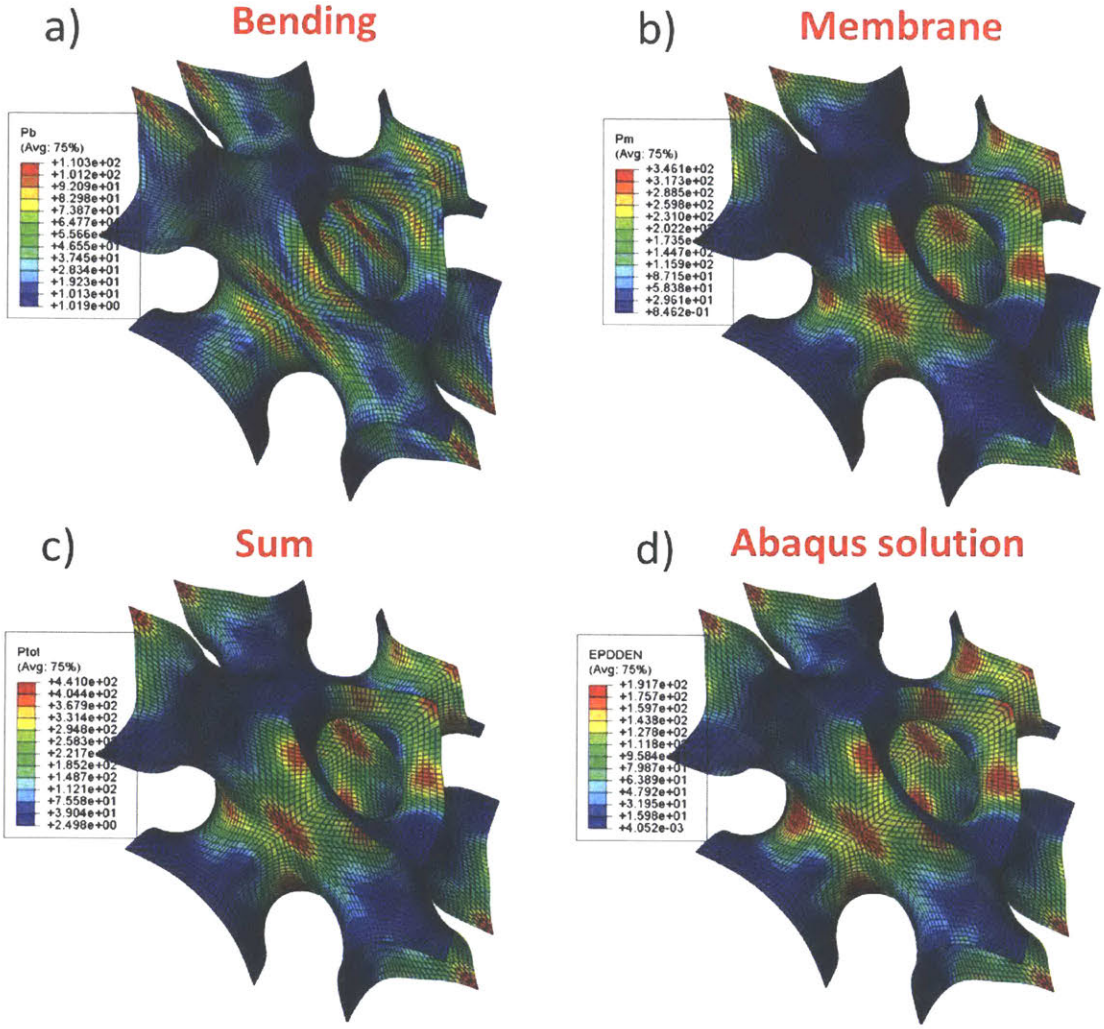

Figure A2.1: Deformed configuration and color-coded distributions of a) bending dissipation b) membrane dissipation c) total dissipation from calculated rates and d) Abaqus solution for the elastoplastic material, corresponding to uniaxial compression at an engineering strain of $\bar{\varepsilon} = 0.25$ of a BCC shell-lattice of relative density 0.25, under uniaxial compression along the [110] axis.

For every frame i corresponding to an engineering compressive strain $i / 100$, the fields corresponding to incremental curvature SK_n^i, and in-plane strains SE_n^i are saved to the file. From these, the respective increments are calculated and serve as an approximation of strain rate and rate of curvature change, as follows:

$$dE_n^i = SE_n^i - SE_n^{i-1} \tag{A2.11}$$

$$dK_n^i = SK_n^i - SK_n^{i-1} \tag{A2.12}$$

From those, are calculated the following increments:

- Rate of bending dissipation:

$$dD_b^i = \sqrt{\frac{4}{3}} M_0 \sqrt{\left(dK_1^i\right)^2 + \left(dK_2^i\right)^2 + dK_1^i dK_2^i + \left(dK_3^i\right)^2} \text{ with } M_0 = \frac{\sigma_y t^2}{4} \quad \text{(A2.13)}$$

- Rate of membrane Dissipation:

$$dD_m^i = \sqrt{\frac{4}{3}} N_0 \sqrt{\left(dE_1^i\right)^2 + \left(dE_2^i\right)^2 + dE_1^i dE_2^i + \left(dE_3^i\right)^2} \text{ with } N_0 = \sigma_y t \quad \text{(A2.14)}$$

Those equations correspond to the plastic dissipation in a rigid perfectly plastic material. However due to numerical issues, such simulations could not be performed. Instead, an isotropic elastoplastic perfectly plastic material model with von Mises plasticity was used, with Young's modulus $E = 200\text{GPa}$, Poisson's ratio $\nu = 0.3$ and yield strength $\sigma_y = 500\text{MPa}$. It is assumed that the curvature changes and strains computed numerically constitute a reasonable approximation of those for a rigid plastic model. However as a consequence, the plastic dissipation in the material is vastly overestimated as compared to the elastoplastic model. Nevertheless the comparison of the distributions of total plastic dissipation density computed through the formulas, to the plastic dissipation reported by the numerical solver, show good qualitative agreement, as exemplified by Figure A2.1. It is therefore possible to compare the relative contributions of membrane action and bending action to the plastic dissipation. Figure A2.2 provides that quantity:

$$\eta = \frac{D_m}{D_m + D_b} \quad \text{(A2.15)}$$

At engineering strains of 0.1, 0.2, 0.3 and 0.5 for all the cases considered. Membrane action contributes between about 50% and 80% of the total dissipation in all cases considered. For each structure, that percentage decreases with increasing compressive strain. For a given loading direction, η increases when $\bar{\rho}$ decreases from 0.5 to about 0.2, then decreases sharply at lower relative densities. Interestingly, this point corresponds to the loss of stability of the material ($0.2 \leq \bar{\rho} \leq 0.3$, not shown).

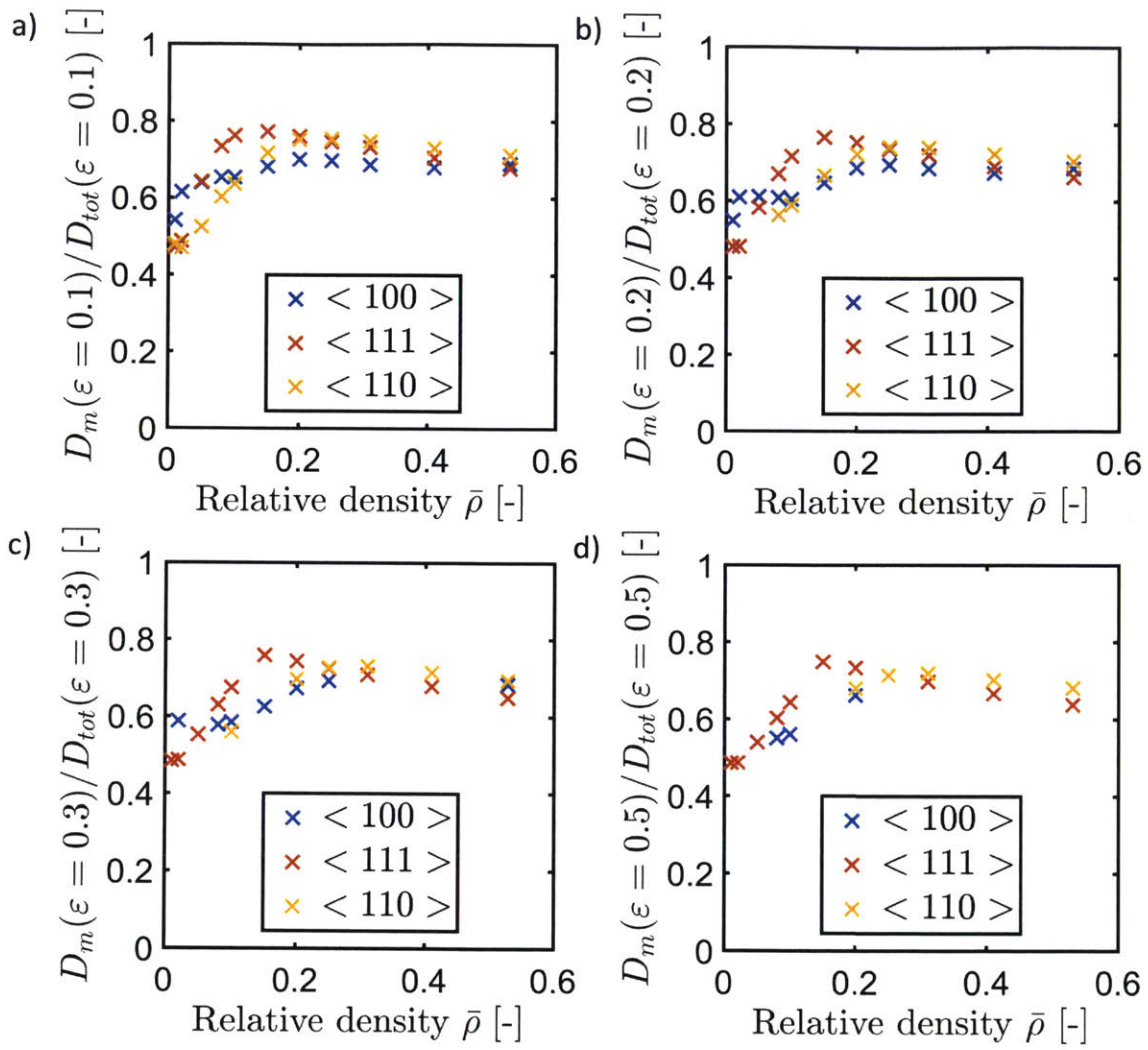

Figure A2.2: Contribution of membrane action to the overall plastic dissipation under uniaxial compression.

Using Eq. A2.9 and A2.10 and introducing a set of approximating assumptions, Wierzbicki and Abramovicz (1989) calculated analytically the relative contribution of the membrane and bending energy. Recall the closed for solution for the mean crushing form of the prismatic column:

$$F = 12\sigma_0 t^{5/3} b^{1/3} \tag{A2.16}$$

For the square prismatic column the ratio is exactly 2 / 3 in the range of applicability of equation A2.16. This result, shown in Fig. A2.2 as a nearly-horizontal line, cuts through the middle of computed points for the BCC shell-lattice. It is therefore hard to design a shell-like structure that relies on membrane action alone. In the best case observed ([111]

orientation, $\bar{\rho} = 0.15$) the ratio of membrane-caused dissipation to total energy dissipation reaches 0.8. This is significant, because for the first time it is shown that the present optimized shells can absorb a larger fraction (by over 0.1) of the total dissipation in the membrane mode than the prototype prismatic column with the same relative density. It is here where optimization of the curvature norm, provided the desired shift towards more membrane action and thus, higher energy absorption.

9. References

Abramowicz, W. and Wierzbicki, T. (1988) 'Axial crushing of foam-filled columns', *International Journal of Mechanical Sciences*, 30(3–4), pp. 263–271. doi: 10.1016/0020-7403(88)90059-8.

Abueidda, Diab W., Ahmed S. Dalaq, Rashid K. Abu Al-Rub, and Iwona Jasiuk. 2015. "Micromechanical Finite Element Predictions of a Reduced Coefficient of Thermal Expansion for 3D Periodic Architectured Interpenetrating Phase Composites." *Composite Structures* 133. Elsevier Ltd: 85–97. doi:10.1016/j.compstruct.2015.06.082.

Ashby, M.F F. 2006. "The Properties of Foams and Lattices." *Philosophical Transactions of the Royal Society A: Mathematical, Physical and Engineering Sciences* 364 (1838): 15–30. doi:10.1098/rsta.2005.1678.

Ashcroft, Neil W., and N. David Mermin. 1976. *Solid State Physics*. Saunders.

Bauer, Jens, Stefan Hengsbach, Iwiza Tesari, Ruth Schwaiger, and Oliver Kraft. 2014. "High-Strength Cellular Ceramic Composites with 3D Microarchitecture." *Proceedings of the National Academy of Sciences of the United States of America* 111 (7): 2453–58. doi:10.1073/pnas.1315147111.

Berger, J. B., H. N. G. Wadley, and R. M. McMeeking. 2017. "Mechanical Metamaterials at the Theoretical Limit of Isotropic Elastic Stiffness." *Nature* 543 (7646). Nature Publishing Group: 533–37. doi:10.1038/nature21075.

Bobbert, F. S.L., K. Lietaert, A. A. Eftekhari, B. Pouran, S. M. Ahmadi, H. Weinans, and A. A. Zadpoor. 2017. "Additively Manufactured Metallic Porous Biomaterials Based on Minimal Surfaces: A Unique Combination of Topological, Mechanical, and Mass Transport Properties." *Acta Biomaterialia* 53. Acta Materialia Inc.: 572–84. doi:10.1016/j.actbio.2017.02.024.

Bonatti, Colin, and Dirk Mohr. 2017. "Large Deformation Response of Additively-Manufactured FCC Metamaterials: From Octet Truss Lattices towards Continuous Shell Mesostructures." *International Journal of Plasticity* 92. Elsevier Ltd: 122–47. doi:10.1016/j.ijplas.2017.02.003.

Bonatti, Colin, and Dirk Mohr. 2019a. "Mechanical Performance of Additively-Manufactured Anisotropic and Isotropic Smooth Shell-Lattice Materials: Simulations & Experiments." *Journal of the Mechanics and Physics of Solids* 122. Elsevier Ltd: 1–26. doi:10.1016/J.JMPS.2018.08.022.

Bonatti, Colin, and Dirk Mohr. 2019b. "Smooth-shell Metamaterials of Cubic Symmetry: Elasticity, Yield Strength and Specific Energy Absorption." *Acta Materialia*, in press.

Carlton, Holly D., Jonathan Lind, Mark C. Messner, Nickolai A. Volkoff-Shoemaker, Harold S. Barnard, Nathan R. Barton, and Mukul Kumar. 2017. "Mapping Local Deformation Behavior in Single Cell Metal Lattice Structures." *Acta Materialia* 129. Elsevier Ltd: 239–50. doi:10.1016/j.actamat.2017.02.023.

Dalaq, Ahmed S., Diab W. Abueidda, and Rashid K. Abu Al-Rub. 2016. "Mechanical Properties of 3D Printed Interpenetrating Phase Composites with Novel Architectured 3D Solid-Sheet Reinforcements." *Composites Part A: Applied Science and Manufacturing* 84. Elsevier Ltd: 266–80. doi:10.1016/j.compositesa.2016.02.009.

Dalaq, Ahmed S., Diab W. Abueidda, Rashid K. Abu Al-Rub, and Iwona M. Jasiuk. 2016. "Finite Element Prediction of Effective Elastic Properties of Interpenetrating Phase Composites with Architectured 3D Sheet Reinforcements." *International Journal of Solids and Structures* 83. Elsevier Ltd: 169–82. doi:10.1016/j.ijsolstr.2016.01.011.

Deshpande, V.S., M.F. Ashby, and N.A. Fleck. 2001a. "Foam Topology: Bending versus Stretching Dominated Architectures." *Acta Materialia* 49 (6): 1035–40. doi:10.1016/S1359-6454(00)00379-7.

Deshpande, V.S. S., N.A. a. Fleck, and M.F. F. Ashby. 2001b. "Effective Properties of the Octet-Truss Lattice Material." *Journal of the Mechanics and Physics of Solids* 49 (8): 1747–69. doi:10.1016/S0022-5096(01)00010-2.

Elsayed, Mostafa S.A. a, and Damiano Pasini. 2010. "Multiscale Structural Design of Columns Made of Regular Octet-Truss Lattice Material." *International Journal of Solids and Structures* 47 (14–15). Elsevier Ltd: 1764–74. doi:10.1016/j.ijsolstr.2010.03.003.

Eshelby, J.D. 1957. "The Determination of the Elastic Field of an Ellipsoidal Inclusion , and Related Problems." *Proceedings of the Royal Society A: Mathematical, Physical and Engineering Sciences* 241 (1226): 376–96. doi:10.1098/rspa.1957.0133.

Evans, A.G., J.W. Hutchinson, N.A. Fleck, M.F. Ashby, and H.N.G. Wadley. 2001. "The Topological Design of Multifunctional Cellular Metals." *Progress in Materials Science* 46 (3): 309–27. doi:10.1016/S0079-6425(00)00016-5.

Evans, Anthony G, John W Hutchinson, and Michael F Ashby. 1998. "Cellular Metals." *Current Opinion in Solid State and Materials Science* 3: 288–303.

Gibson, L. J. 2000. "Mechanical Behavior of Metallic Foams." *Annual Review of Materials Science* 30 (1). Annual Reviews 4139 El Camino Way, P.O. Box 10139, Palo Alto, CA 94303-0139, USA: 191–227. doi:10.1146/annurev.matsci.30.1.191.

Gibson, Lorna J., and Michael F. Asbhy. 1999. *Cellular Solids: Structure and Properties*. Cambridge University Press.

Gibson, Lorna J., Michael F Ashby, and Brendan A. Harley. 2010. "Cellular Materials in Nature and Medicine." Cambridge University Press.

Grosse-brauckmann, Karsten. 2012. "Triply Periodic Minimal and Constant Mean Curvature Surfaces." *Interface Focus* 2 (March): 582–88. doi:10.1098/rsfs.2011.0096.

Gümrük, R., and R.A.W. Mines. 2013. "Compressive Behaviour of Stainless Steel Micro-Lattice Structures." *International Journal of Mechanical Sciences* 68: 125–39. doi:10.1016/j.ijmecsci.2013.01.006.

Gurson, Arthur L. 1977. "Continuum Theory of Ductile Rupture by Void Nucleation and Growth: Part I: Yield Criteria and Flow Rules for Porous Ductile Media." *Journal of Engineering Materials and Technology* 99 (1). American Society of Mechanical Engineers: 2–15.

Gurtner, G., and M. Durand. 2014. "Stiffest Elastic Networks." *Proceedings of the Royal Society A: Mathematical, Physical and Engineering Sciences* 470 (2164): 20130611–20130611. doi:10.1098/rspa.2013.0611.

Han, Seung Chul, Jeong Woo Lee, and Kiju Kang. 2015. "A New Type of Low Density Material: Shellular." *Advanced Materials* 27 (37): n/a-n/a. doi:10.1002/adma.201501546.

Hanzl, Pavel, Miroslav Zetek, Tomáš Bakša, and Tomáš Kroupa. 2015. "The Influence of Processing Parameters on the Mechanical Properties of SLM Parts." *Procedia Engineering* 100 (January). Elsevier B.V.: 1405–13. doi:10.1016/j.proeng.2015.01.510.

Hashin, Z., and S. Shtrikman. 1961. "Note on a Variational Approach to the Theory of Composite Elastic Materials." *Journal of the Franklin Institute* 271 (4): 336–41. doi:10.1016/0016-0032(61)90032-1.

Hashin, Z., and S. Shtrikman. 1963. "A Variational Approach to the Theory of the Elastic Behaviour of Multiphase Materials." *Journal of the Mechanics and Physics of Solids* 11 (2): 127–40. doi:10.1016/0022-5096(63)90060-7.

He, Ze Zhou, Feng Chao Wang, Yin Bo Zhu, Heng An Wu, and Harold S. Park. 2017. "Mechanical Properties of Copper Octet-Truss Nanolattices." *Journal of the Mechanics and Physics of Solids* 101. Elsevier Ltd: 133–49. doi:10.1016/j.jmps.2017.01.019.

Jang, Dongchan, Lucas R Meza, Frank Greer, and Julia R Greer. 2013. "Fabrication and Deformation of Three-Dimensional Hollow Ceramic Nanostructures." *Nature Materials* 12 (10). Nature Publishing Group: 893–98. doi:10.1038/nmat3738.

Jang, Wen Yea, and Stelios Kyriakides. 2009. "On the Crushing of Aluminum Open-Cell Foams: Part II Analysis." *International Journal of Solids and Structures* 46 (3–4). Elsevier Ltd: 635–50. doi:10.1016/j.ijsolstr.2008.10.016.

Jang, Wen-Yea, and Stelios Kyriakides. 2009. "On the Crushing of Aluminum Open-Cell Foams: Part I. Experiments." *International Journal of Solids and Structures* 46 (3): 617–34. doi:10.1016/j.ijsolstr.2008.09.008.

Kapfer, Sebastian C., Stephen T. Hyde, Klaus Mecke, Christoph H. Arns, and Gerd E. Schr??der-Turk. 2011. "Minimal Surface Scaffold Designs for Tissue Engineering." *Biomaterials* 32 (29). Elsevier Ltd: 6875–82. doi:10.1016/j.biomaterials.2011.06.012.

Kittel, Charles. 1996. "Introduction to Solid State Physics, 7th Ed." Wiley.

Lambert, Charla A, Leonard H Radzilowski, and Edwin L Thomas. 1996. "Triply Periodic Level Surfaces as Models for Cubic Tricontinuous Block Copolymer Morphologies." *Philosophical Transactions: Mathematical, Physical and Engineering Sciences* 354 (1715): 2009–23. doi:10.1098/rsta.1996.0089.

Lee, Dong Wook, Kamran A. Khan, and Rashid K. Abu Al-Rub. 2017. "Stiffness and Yield Strength of Architectured Foams Based on the Schwarz Primitive Triply Periodic Minimal Surface." *International Journal of Plasticity* 95 (August). Elsevier Ltd: 1–20. doi:10.1016/j.ijplas.2017.03.005.

Lee, Jae Hwang, Jonathan P. Singer, and Edwin L. Thomas. 2012. "Micro-/Nanostructured Mechanical Metamaterials." *Advanced Materials* 24 (36): 4782–4810. doi:10.1002/adma.201201644.

M.F. Ashby, A.G. Evans, N.A. Fleck, L.J. Gibson, J.W. Hutchinson and H.N.G. Wadley. 2000. *Metal Foams : A Design Guide*. Elsevier.

Maldovan, Martin, Chaitanya K. Ullal, Ji Hyun Jang, and Edwin L. Thomas. 2007. "Sub-Micrometer Scale Periodic Porous Cellular Structures: Microframes Prepared by Holographic Interference Lithography." *Advanced Materials* 19 (22): 3809–13. doi:10.1002/adma.200700811.

Messner, Mark C. 2016. "Optimal Lattice-Structured Materials." *Journal of the Mechanics and Physics of Solids* 96. Elsevier: 162–83. doi:10.1016/j.jmps.2016.07.010.

Meza, Lucas R, Alex J Zelhofer, Nigel Clarke, Arturo J Mateos, Dennis M Kochmann, and Julia R Greer. 2015. "Resilient 3D Hierarchical Architected Metamaterials." *Proceedings of the National Academy of Sciences of the United States of America* 112 (37): 11502–7. doi:10.1073/pnas.1509120112.

Mohr, Dirk. 2005. "Mechanism-Based Multi-Surface Plasticity Model for Ideal Truss Lattice Materials." *International Journal of Solids and Structures* 42 (11–12): 3235–60. doi:10.1016/j.ijsolstr.2004.10.032.

Mohr, Dirk, and Mulalo Doyoyo. 2004. "Experimental Investigation on the Plasticity of Hexagonal Aluminum Honeycomb Under Multiaxial Loading." *Journal of Applied Mechanics* 71 (3). American Society of Mechanical Engineers: 375. doi:10.1115/1.1683715.

Montemayor, Lauren C., Lucas R. Meza, and Julia R. Greer. 2014. "Design and Fabrication of Hollow Rigid Nanolattices via Two-Photon Lithography." *Advanced Engineering Materials* 16 (2): 184–89. doi:10.1002/adem.201300254.

Mower, Todd M., and Michael J. Long. 2016. "Mechanical Behavior of Additive Manufactured, Powder-Bed Laser-Fused Materials." *Materials Science and Engineering A* 651. Elsevier: 198–213. doi:10.1016/j.msea.2015.10.068.

Nguyen, Ban Dang, Seung Chul Han, Yoon Chang Jung, and Kiju Kang. 2017. "Design of the P-Surfaced Shellular, an Ultra-Low Density Material with Micro-Architecture." *Computational Materials Science* 139: 162–78. doi:10.1016/j.commatsci.2017.07.025.

O'Masta, M. R., L. Dong, L. St-Pierre, H. N G Wadley, and V. S. Deshpande. 2017. "The Fracture Toughness of Octet-Truss Lattices." *Journal of the Mechanics and Physics of Solids* 98 (April 2016). Elsevier: 271–89. doi:10.1016/j.jmps.2016.09.009.

Sawczuk, A. 1989. *Mechanics and Plasticity of Structures*. Halsted Press.

Schaedler, T A, A J Jacobsen, A Torrents, A E Sorensen, J Lian, J R Greer, L Valdevit, and W B Carter. 2011. "Ultralight Metallic Microlattices." *Science (New York, N.Y.)* 334 (6058): 962–65. doi:10.1126/science.1211649.

Schoen, Alan H. 1970. "Infinite Periodic Minimal Surfaces without Self-Intersections."

Simone, A E, and L J Gibson. 1998. "Effects of Solid Distribution on the Stiffness." *Acta Metallurgica* 46 (6): 2139–50.

Stankovic, Tino, Jochen Mueller, Paul Egan, and Kristina Shea. 2015. "A Generalized Optimality Criteria Method for Optimization of Additively Manufactured Multimaterial Lattice Structures." *Journal of Mechanical Design* 137 (11): 111405. doi:10.1115/1.4030995.

Suquet, P. M. 1993. "Overall Potentials and Extremal Surfaces of Power Law or Ideally Plastic Composites." *Journal of the Mechanics and Physics of Solids* 41 (6): 981–1002. doi:10.1016/0022-5096(93)90051-G.

Suryawanshi, Jyoti, K. G. Prashanth, and U. Ramamurty. 2017. "Mechanical Behavior of Selective Laser Melted 316L Stainless Steel." *Materials Science and Engineering A* 696 (April). Elsevier B.V.: 113–21. doi:10.1016/j.msea.2017.04.058.

Sypeck, D. J., and H. N G Wadley. 2002. "Cellular Metal Truss Core Sandwich Structures." *Advanced Engineering Materials* 4 (10): 759–64. doi:10.1002/1527-2648(20021014)4:10<759::AID-ADEM759>3.0.CO;2-A.

Tancogne-Dejean, Thomas, and Dirk Mohr. 2018a. "Elastically-Isotropic Elementary Cubic Lattices Composed of Tailored Hollow Beams." *Extreme Mechanics Letters* 22. Elsevier Ltd: 13–18. doi:10.1016/j.eml.2018.04.005.

Tancogne-Dejean, Thomas, Marianna Diamantopoulou, Maysam B. Gorji, Colin Bonatti, and Dir Mohr. 2018b. "3D Plate-Lattices: An Emerging Class of Low-Density Metamaterial Exhibiting Optimal Isotropic Stiffness." *Advanced Materials* 1803334: 1–6. doi:10.1002/adma.201803334.

Tancogne-Dejean, Thomas, and Dirk Mohr. 2018c. "Elastically-Isotropic Truss Lattice Materials of Reduced Plastic Anisotropy." *International Journal of Solids and Structures* 0. Elsevier Ltd: 1–16. doi:10.1016/j.ijsolstr.2017.12.025.

Tancogne-Dejean, Thomas, Adriaan B. Spierings, and Dirk Mohr. 2016. "Additively-Manufactured Metallic Micro-Lattice Materials for High Specific Energy Absorption under Static and Dynamic Loading." *Acta Materialia* 116. Elsevier Ltd: 14–28. doi:10.1016/j.actamat.2016.05.054.

Thomas, Edwin L., David M. Anderson, Chris S. Henkee, and David Hoffman. 1988. "Periodic Area-Minimizing Surfaces in Block Copolymers." *Nature* 334: 598–601. doi:10.1038/334598a0.

Wadley, Haydn N.G., Norman A. Fleck, and Anthony G. Evans. 2003. "Fabrication and Structural Performance of Periodic Cellular Metal Sandwich Structures." *Composites Science and Technology* 63 (16): 2331–43. doi:10.1016/S0266-3538(03)00266-5.

Walpole, L. J. 1966. "On Bounds for the Overall Elastic Moduli of Inhomogeneous Systems-I." *Journal of the Mechanics and Physics of Solids* 14 (3): 151–62. doi:10.1016/0022-5096(66)90035-4.

Wang, Lifeng, Jacky Lau, Edwin L. Thomas, and Mary C. Boyce. 2011. "Co-Continuous Composite Materials for Stiffness, Strength, and Energy Dissipation." *Advanced Materials* 23 (13): 1524–29. doi:10.1002/adma.201003956.

Wang, Y. Morris, Thomas Voisin, Joseph T. McKeown, Jianchao Ye, Nicholas P. Calta, Zan Li, Zhi Zeng, et al. 2018. "Additively Manufactured Hierarchical Stainless Steels with High Strength and Ductility." *Nature Materials* 17 (1): 63–70. doi:10.1038/NMAT5021.

Wendy Gu, X, Colleen N Loynachan, Zhaoxuan Wu, Yong-Wei Zhang, David J Srolovitz, and Julia R Greer. 2012. "Size-Dependent Deformation of Nanocrystalline Pt Nanopillars." *Nano Letters* 12 (12): 6385–92. doi:10.1021/nl3036993.

Willis, J. R. 1977. "Bounds and Self-Consistent Estimates for the Overall Properties of Nonlinear Composites." *Journal of Mechanics and Physics of Solids* 25: 185–202. doi:10.1093/imamat/39.3.215.

Yan, Chunze, Liang Hao, Ahmed Hussein, and David Raymont. 2012. "Evaluations of Cellular Lattice Structures Manufactured Using Selective Laser Melting." *International Journal of Machine Tools and Manufacture* 62: 32–38. doi:10.1016/j.ijmachtools.2012.06.002.

Yoo, Dong-Jin, and Kwang-Hyuk Kim. 2015. "An Advanced Multi-Morphology Porous Scaffold Design Method Using Volumetric Distance Field and Beta Growth Function." *International Journal of Precision Engineering and Manufacturing* 16 (9): 2021–32. doi:10.1007/s12541-015-0263-2.

Zheng, Xiaoyu, William Smith, Julie Jackson, Bryan Moran, Huachen Cui, Da Chen, Jianchao Ye, et al. 2016. "Multiscale Metallic Metamaterials." *Nature Materials*, no. July: 1–8. doi:10.1038/nmat4694.

Zok, Frank W., Ryan M. Latture, and Matthew R. Begley. 2016. "Periodic Truss Structures." *Journal of the Mechanics and Physics of Solids* 96. Elsevier: 184–203. doi:10.1016/j.jmps.2016.07.007.